Investigation of Molten Salt Electrolytes for Low-Temperature Liquid Metal Batteries

by

Brian Leonard Spatocco

B.S., Materials Science and Engineering
Rutgers University, 2008

M.Phil., Micro- and Nanotechnology Enterprise
University of Cambridge, 2009

Submitted to the Department of Materials Science and Engineering
in Partial Fulfillment of the Requirements for the Degree of

Doctor of Philosophy

at the

MASSACHUSETTS INSTITUTE OF TECHNOLOGY

September 2015

Author ……
Department of Materials Science and Engineering
August 7, 2015

Certified and Accepted by …..……...
Donald R. Sadoway
John F. Elliot Professor of Materials Chemistry
Thesis Supervisor
Chair, Department Committee on Graduate Students

Investigation of Molten Salt Electrolytes for Low-Temperature Liquid Metal Batteries

by

Brian Leonard Spatocco

Submitted to the Department of Materials Science and Engineering on August 14, 2015,
in partial fulfillment of the requirements for the degree of
Doctor of Philosophy

Abstract

This thesis proposes to advance our ability to solve the challenge of grid-scale storage by better positioning the liquid metal battery (LMB) to deliver energy at low levelized costs. It will do this by rigorously developing an understanding of the cost structure for LMBs via a process-based cost model, identifying key cost levers to serve as filters for system down-selection, and executing a targeted experimental program with the goal of both advancing the field as well as improving the LMB's final cost metric.

Specifically, cost modelling results show that temperature is a key variable in LMB system cost as it has a multiplicative impact upon the final $/kWh cost metric of the device. Lower temperatures can reduce the total cost via simultaneous simplifications in device sealing, packaging, and wiring. In spite of this promise, the principal challenge in reducing LMB operating temperatures (>400°C) lies in identifying high conductivity, low-temperature electrolytes that are thermally, chemically, and electrochemically stable with pure molten metals. For this reason, a research program investigating a promising low-temperature binary molten salt system, NaOH-NaI, is undertaken.

Thermodynamic studies confirm a low eutectic melting temperature (219°C) and, together with the identification of two new binary compounds via x-ray diffraction, it is now possible to construct a complete phase diagram. These phase equilibrium data have then been used to optimize Gibbs free energy functions for the intermediate compounds and a two-sublattice sub-regular solution framework to create a thermodynamically self-consistent model of the full binary phase space. Further, a detailed electrochemical study has identified the electrochemical window (>2.4 V) and related redox reactions and found greatly improved stability of the pure sodium electrode against the electrolyte. Results from electrochemical studies have been compared to predictions from the solution model and strong agreement supports the physicality of the model. Finally, a Na|NaOH-NaI|Pb-Bi proof-of-concept cell has achieved over 100 cycles and displayed leakage currents below 0.40 mA/cm^2. These results highlight an exciting new class of low-melting molten salt electrolytes and point to a future Na-based low-temperature system that could achieve costs that are 10-15% less than those of existing lithium-based LMBs.

Thesis Supervisor: Professor Donald Robert Sadoway
Title: John F. Elliot Professor of Materials Chemistry

This work is dedicated to my parents,
Robin and Leonard Spatocco,
who have given me all their love
and asked for nothing but my happiness in return.
This is but a small thank you.

Acknowledgements

It is with a profound sense of gratitude that I acknowledge my great fortune and privilege in having been surrounded by some of the most passionate people along the many phases of my life. This work is a direct product of this lucky confluence of family, friends, and mentors and as a result is not a work I can claim full ownership over. In fact, a list of those to whom thanks are owed would likely stretch longer than the work itself. For this reason, this section's listing of supporters work will be necessarily incomplete.

I am so fortunate to have found a mentor and advisor in Professor Sadoway. Great science requires vision, method, and hard work. The latter two are often found in research here at MIT. The former, however, is far more rare. Don has shown me what it means to bring vision to a grand challenge. Specifically, asking the right questions, admitting the sometimes unusual answers, and being confident when others may not agree with your initial conclusions. I am forever grateful for this model of intellectual leadership.

Professor Sadoway's ability to inspire not only drove ground-breaking research but also attracted a peerless team of fellow researchers. Much like the scientific dream teams of former eras, ours was a group replete with experience, intelligence, and passion. Our postdoctoral researchers taught me everything I know about research success and failure, and everything in between. They were also great friends. I am deeply indebted to Dane Boysen, Hojong Kim, Brice Chung, Takanari Ouchi, Paul Burke, Guillaume Lambotte, Huayi Yin, Kai Jiang, and Kangli Wang.

I've also had the great fortune to transit through the materials science doctoral program with some of the most fun and inspiration fellow graduate students in the Sadoway Group and DMSE at-large. Jocelyn Newhouse, Salvador Barriga, John Rogosic, Sophie Poizeau, and Dave Bradwell all made the hardest days passable and the best days possible. I am indebted for their partnership and comradery as we worked to invent for the future. Outside of the group, I recall the dark days of quals, the happy holiday dinners, and everything in between with other friends in the department. Specifically, Max Solar, Neil Patel, Adam Jandl, and Dan Harris served as the most reliable supports during shaky times.

MIT has also afforded me the unmatched opportunity to grow my leadership and management style. Over the last six years I've had the chance to lead and learn from those around me. At Sidney Pacific graduate residence I am grateful for having learned from George Lan, Holly Johnson, George Tucker, Ahmed Helal, Pierre-Olivier LePage, Boris Braverman, William Li, Chelsea He, Amy Bilton, Po-Ru Loh, Tim Curran, and Rosaria Chiang. In addition to creating a fun place to live I also had the chance to fight for student housing and welfare issues with Maokai Lin, Randi Cabezas, and Nathaniel Schafheimer.

More than any other position at MIT, my time in the Graduate Student Council executive officer team has helped me grow and mature. Much of this is thanks to mentors in MIT's administration but perhaps the greatest contributors were the students with whom I had the great fortune to share the burden. Namely, Aalap Dighe, Bomy Lee Chung, and Eric Victor have given more to me than I can repay. The incredible impact we had in that year is principally thanks to our team's trust and cohesivity. I would be unsurprised if our group remains the most effective leadership team I've ever been a part of even as I transition to the working world.

A final group of friends I wish to recognize are those I have lived and worked with on projects external to MIT. Stephen Morgan has been a constant positive force in my life. He has taught me the value of loyalty to one's friends. George Chen has been an inspirational source of courage in my life. George has shown me the value of learning outside my comfort zone. Kendall Nowocin has been an exemplar of what family can and should mean in my life. He has shown me how and why to cherish those around us. Javier Sanchez-Yamagishi has taught me the value of persistence and hard work unlike any other person. You're my role model for how I should set my goals and raise my sights throughout my life. And finally, Kelli Xu has reinvigorated my love of life and the world around me. As my partner you've exposed me to new experiences, challenged my assumptions, and helped me be a more authentic person.

The last group of people I am forever indebted to, and to whom this work is dedicated, is my family. My mother Robin Spatocco and Leonard Spatocco have spent their lives giving me every chance and support I could ask for and asked only for my happiness in return. They did so with a depth of love I can only hope to bring to my future family. You've given me a wonderful life and an even better example to carry forward. You are both incredible people. Similarly, to my brother Peter Spatocco, your humility in the midst of such success inspires me. I can't wait to grow older with you and your family in my life.

Contents

Acknowledgements 7
Table of Figures 11
Chapter 1 - Introduction 15
1.1 The Winds of Change 15
1.2 Cost is King 17
1.3 Objective 19
Chapter 2 - The Liquid Metal Battery as a Grid Storage Solution 20
2.1 Basic Principles 20
2.1.2 Thermodynamic Interpretation 21
2.1.3 Practical Operation 29
2.2 Strengths and Weaknesses 30
2.2.1 Scientific 30
2.2.2 Technological Scale-Up 32
2.2.3 Market 33
2.3 Review of Competitive Technologies 34
Chapter 3 – A Methodology for Research Down-selection 36
3.1 Cost Model of the Liquid Metal Battery 36
3.2 Modeling Results and Discussion 45
3.2.1 Active Cell Material Cost Contributors 49
3.2.2 Inactive Cell Material Cost Contributors 54
3.2.3 Electrical System Component Cost Contributors 56
3.2.4 Other Cost Contributors 58
3.2.5 Conclusions - Key Variables 58
3.2.6 Sensitivities 59
3.3 Down-Selection 64
3.3.1 Cost/Voltage Screening 64
3.3.2 Temperature Screening 66
3.3.3 Scalability 67
Chapter 4 - A Review of Sodium-based Molten Salts 71
4.1 Basic Properties 71

4.2 Molten Salts in Sodium Electrodeposition 74
4.3 Molten Salts during Nuclearization 80
4.3.1 Properties 80
4.3.2 Corrosion 83
4.4 Molten Salts in Energy Storage Devices 87
4.5 The Window of Opportunity 92
Chapter 5 – An in-depth study of the NaOH-NaI System 95
5.1 Choosing a NaOH-NaX system 95
5.2 NaOH-NaI prior art 98
5.3 Experimental Techniques 111
5.3.1 Materials Preparation and Containment 111
5.3.2 Differential Scanning Calorimetry (DSC) Measurements 117
5.3.3 X-Ray Diffraction (XRD) Studies 122
5.3.4 Thermodynamic Modeling 124
5.3.5 Electrochemical Measurements 127
5.3.6 Cell Cycling Study 135
5.4 Results and Discussion 136
5.4.1 Differential Scanning Calorimetry (DSC) Results 136
5.4.2 X-Ray Diffraction (XRD) Results 147
5.4.3 Thermodynamic Modeling Results 157
5.4.4 Electrochemical Measurements – Cathodic Study 164
5.4.5 Electrochemical Measurements – Anodic Study 173
5.4.6 Cell Cycling Study 182
Chapter 6 – Conclusions and Next Steps 190
6.1 Work Summary 190
6.1.1 Cost Modeling and Down-Selection 191
6.1.2 The NaOH-NaI System 193
6.2 Next Steps 198
Works Cited 202
Appendix I – Cost Modeling 212

Table of Figures

FIGURE 1 - OPERATION OF THE LIQUID METAL BATTERY DURING A) DISCHARGING AND B) CHARGING 20
FIGURE 2 - ELECTROMOTIVE FORCE AS A FUNCTION OF CA-MG ALLOY COMPOSITION AT 773, 873, AND 1010 K. THE INTERMETALLIC $CAMG_2$ (T_{MP} = 987 K) IS OVERLAID TO EXPLAIN THE DROP-OFF IN ACTIVITY AT APPROXIMATELY 33 MOLE PERCENT CALCIUM. AN IDEAL VOLTAGE CURVE, ASSUMING IDEAL MIXING, IS ALSO SHOWN TO HIGHLIGHT THERMODYNAMIC DEVIATIONS FROM IDEALITY. 23
FIGURE 3 - MG-CA BINARY PHASE DIAGRAM SHOWING THE PATH TAKEN DURING DISCHARGE AT 773K (500°C) IN BLUE AND 873K (600°C) IN RED. 24
FIGURE 4 - THE ACTIVITY CURVES OF CA AND MG AS A FUNCTION OF COMPOSITION AT 773, 873, AND 1010K. IDEAL SOLUTION CURVE PROVIDED TO DEMONSTRATE DEVIATION FROM IDEALITY. 25
FIGURE 5 - VOLTAGE VERSUS LITHIUM CONCENTRATION FOR A VARIETY OF POSITIVE ELECTRODE COMPOSITIONS. ALLOYS OF PB-SB MUCH MORE CLOSELY FOLLOW THE PROFILE OF LI VS. SB THAN LI VS. PB 27
FIGURE 6 - AT TOP IS A PERIODIC TABLE WITH EXAMPLE CANDIDATE MATERIALS FOR NEGATIVE ELECTRODES PROVIDED IN ORANGE AND POSITIVE ELECTRODES IN GREEN. BOTTOM PRESENTS THESE ELEMENTS PLOTTED BY THEIR REDUCTIVE POTENTIAL AGAINST THE STANDARD HYDROGEN ELECTRODE. 28
FIGURE 7 - MODELED OVERPOTENTIALS AT 100 MA/CM^2 FOR LEFT) MG||SB CELL AND RIGHT) A LI||BI CELL. H_W IN THIS WORK CORRESPONDS TO THE OHMIC OVERPOTENTIAL OF THE ELECTROLYTE. 31
FIGURE 8 - OPEN AIR ASSEMBLY OF A 40 AH LIQUID METAL BATTERY 33
FIGURE 9 - EXAMPLE OF MODULAR GRID-STORAGE DESIGN BY AMBRI 37
FIGURE 10 - HIGH-LEVEL PROCESS FLOW COST MODEL OF AN LMB ASSEMBLY FACILITY. SUB-PROCESSES ARE NUMBERED 38
FIGURE 11 - BREAKOUT OF VARIABLE VS. FIXED COSTS FOR LMB CELL PRODUCTION 45
FIGURE 12 – COST MODEL - CELL VS SYSTEM COSTS. CELL BOM IN BLUE AND SYSTEM BOM IN RED 47
FIGURE 13 – PUBLICLY RELEASED BOM FROM AMBRI. 47
FIGURE 14 - PROMISING ELECTRODE COUPLE COSTS (< $100/COUPLE) WITH VOLATILITY-INDUCED RANGES 52
FIGURE 15 - FUNCTIONALITY OF HIGH-TEMPERATURE WIRE COST ON GAUGE 57
FIGURE 16 - ECONOMIES OF SCALE CURVE FOR LMB PRODUCTION 60
FIGURE 17 - TORNADO PLOT OF SENSITIVITY OF KEY VARIABLES 62
FIGURE 18 - TCOE AS A FUNCTION OF SYSTEM TEMPERATURE 63
FIGURE 19 - THE ENERGY STORAGE POTENTIAL (ESP) FOR STORAGE TECHNOLOGIES BASED ON MATERIAL RESOURCES AND APPROPRIATE GEOLOGIC FORMATIONS. 68
FIGURE 20 - ENERGY STORAGE PRODUCTION ESTIMATES SHOWN VS. 1% OF THE DAILY US ELECTRICITY CONSUMPTION 69
FIGURE 21 - REPRESENTATION OF A MOLTEN NACL SYSTEM SHOWING SHORT RANGE ORDERING (SRO) 71
FIGURE 22 - HISTORICAL TRENDS IN SODIUM MANUFACTURING 76
FIGURE 23 - SCHEMATIC REPRESENTATION OF A DOWNS CELL FOR PRODUCING SODIUM METAL AND CHLORINE GAS 77
FIGURE 24 - EXPERIMENTAL PHASE DIAGRAMS OF NAI-NAOH-NABR AND NAI-NAOH-NACN TERNARY PHASE DIAGRAMS 79
FIGURE 25 - NUMBER OF OPERABLE NUCLEAR POWER PLANTS IN THE UNITED STATES SINCE 1950 80
FIGURE 26 - PLOT OF CONDUCTIVITY VS. TEMPERATURE FOR VARIOUS PURE MOLTEN SALTS 82
FIGURE 27 - THEORETICAL THERMODYNAMIC FREE ENERGIES OF REACTION FOR TWO POTENTIAL NITRATE REACTION PATHWAYS VS. TEMPERATURE 84
FIGURE 28 - SODIUM METAL SOLUBILITY IN NAF, NACL, NABR, AND NAI, CLOCKWISE FROM TOP LEFT, AS DEMONSTRATED WITH LIQUID COEXISTENCE CURVES. 86

FIGURE 29 - CYCLIC VOLTAMMETRIC STUDY AT 100 MV/S WITH A PLATINUM ELECTRODE IN MOLTEN LIOH-NAOH AT 270°C....87
FIGURE 30 - DIAGRAM OF A THERMALLY-REGENERATIVE TYPE BATTERY. 88
FIGURE 31 - RESEARCH PAPERS PUBLISHED THAT FOCUSED ON APPLICATION OF BETA-ALUMINA ELECTROLYTES FOR ENERGY USES. 90
FIGURE 32 - NAOH-NAX PREDICTED BINARY PHASE DIAGRAMS....95
FIGURE 33 - BASIC CASTNER CELL FOR THE PRODUCTION OF NA METAL FROM NAOH FEEDSTOCK 98
FIGURE 34 - THE FIRST BINARY PHASE DIAGRAM OF NAOH-NAI 100
FIGURE 35 - CONDUCTIVITY OF VARIOUS COMPOSITIONS OF NAOH-NAI COMPOSITIONS AS A FUNCTION OF TEMPERATURE. EARLIER DATA BY DEMIDOV IS ALSO OVERLAID TO SHOW GENERAL REPRODUCIBILITY OF CONDUCTIVITY VALUES....102
FIGURE 36 – REPLOTTING OF THE SOLUBILITY OF SODIUM METAL IN TERNARY SALT AS A FUNCTION OF TEMPERATURE. 105
FIGURE 37 - REPLOTTING OF THE NA METAL DIFFUSION EXPERIMENT RESULTS MAPPED TO CORRESPONDING LEAKAGE CURRENTS. 107
FIGURE 38 - LEAKAGE CURRENT ACTIVATION PLOT REPLOTTED FROM OKADA'S DATA 107
FIGURE 39 - NAOH-NAI PHASE DIAGRAM FOLLOWING THE INVENTION OF DSC. 108
FIGURE 40 - SANGSTER'S CALCULATED PHASE DIAGRAM USING FACT METHODS AND EXPERIMENTAL DATA FROM YOSHIZAWA AND SCARPA. 110
FIGURE 41 - EXPERIMENTAL CHAMBER USED FOR DRYING AND ELECTROCHEMICAL EXPERIMENTS. 112
FIGURE 42 - CALCULATED VAPOR PRESSURE OF PURE NAI, NACL, NAOH, LII, AND LICL 113
FIGURE 43 - 80/20 NAOH/NAI SALT IN A NI-201 CRUCIBLE AFTER MELTING AND BEFORE PULVERIZATION 114
FIGURE 44 - PURE NICKEL PROBE AFTER A 1-MONTH EXPERIMENT IN 80/20 NAOH/NAI MOLTEN SALT. A) SHOWS THE PROBE IMMEDIATELY AFTER REMOVAL WHILE B) SHOWS THE PROBE AFTER WASHING AND PICKLING. 116
FIGURE 45 - DIAGRAM OF HOW A DSC EXTRACTS THERMODYNAMIC INFORMATION FROM A SAMPLE. 117
FIGURE 46 - DSC SCAN OF AN INDIUM CALIBRATION MATERIAL. BLUE CURVE SHOWS MELTING UPON TEMPERATURE INCREASE AND PURPLE CURVE TRACKS THE FREEZING PROCESS UPON TEMPERATURE DECREASE. 119
FIGURE 47 – DSC CALIBRATION CURVES FOR A) X-AXIS TEMPERATURE CALIBRATION AND B) Y-AXIS HEAT FLOW CALIBRATION. 120
FIGURE 48 - HIERARCHY OF DSC MEASUREMENTS FOR THE 80/20 SAMPLE. EACH PIECE OF TRANSITION DATA COMES FROM A SINGLE CYCLE. 121
FIGURE 49 - EXAMPLE OF AN EXPERIMENT WITH 3 TEMPERATURE CYCLES. 122
FIGURE 50 - PREDICTABLE LOW-ANGLE BACKGROUND FROM AIR-SENSITIVE SAMPLE HOLDER. SPECTRUM COLLECTED WITH 1000S/STEP FROM 2 THETA RANGING FROM 5° TO 90°. 123
FIGURE 51 - SANGSTER'S OPTIMIZED PHASE DIAGRAM AS GENERATED USING THE FACTSAGE THERMOCHEMICAL SOFTWARE SUITE. THIS PHASE DIAGRAM IS PROVIDED TO DEMONSTRATE THE OPTIMIZATION STEPS FOLLOWED DURING THE CALPHAD METHOD. 126
FIGURE 52 - SCHEMATIC OF A 3-ELECTRODE SETUP. 127
FIGURE 53 - THEORETICAL ELECTROCHEMICAL WINDOW WITH POTENTIAL SIDE REACTIONS OF METALS FOUND TO BE STABLE IN CORROSION TESTS. 128
FIGURE 54 – ON LEFT, AN SEM (SCALE BAR 20UM) IMAGE OF THE PRODUCT ACCUMULATED ON A SILVER WIRE AFTER HOLDING AT 2.2 V FOR 1 MINUTE. THIS MATERIAL WAS FOUND TO HAVE HIGH IODINE CONTENT FROM CHEMICAL MAPPING. ON RIGHT, THE SAME WIRE IMMERSED IN H_2SO_4 BATH. THE YELLOW IS AN INDICATOR FOR IODINE SPECIES. 130

FIGURE 55 - IMPEDANCE BETWEEN TANAB REFERENCE ELECTRODE AND PLATINUM WORKING ELECTRODE. REFERENCE AREA IS ~6 CM^2 AND WORKING ELECTRODE IS ~0.3 CM^2 132
FIGURE 56 - A SUMMARY OF THE ELECTRODES USED IN THE VARIOUS CV EXPERIMENTS. 132
FIGURE 57 - DRIFT BETWEEN TANAB REFERENCE ELECTRODES AFTER ONE WEEK OF EXPERIMENTATION. 133
FIGURE 58 - EXAMPLE CV OF AN UNDRIED NAOH/NAI (80/20) ELECTROLYTE AT 25 MV/S. 134
FIGURE 59 - PROOF-OF-CONCEPT CELL UTILIZING THE EUTECTIC NAOH-NAI BINARY SYSTEM. 135
FIGURE 60 - 1 °C/MIN SCAN OF AN 80% NAOH - 20% NAI SALT SAMPLE. RED SIGNAL CORRESPONDS TO MELTING AND BLUE CORRESPONDS TO FREEZING. 137
FIGURE 61 - 5 °C/MIN DSC SCAN OF 90% NAOH AND 10% NAI MELT. THE MELTING AT 219.9°C IS LATER FOLLOWED BY A SLOW EXIST FROM A 2-PHASE REGION. 138
FIGURE 62 - SCHEMATIC DEPICTING THE PASSAGE THROUGH A 2-PHASE REGION AND THE COMPOSITIONAL CHANGES THAT OCCUR. 139
FIGURE 63 - DSC TEST RUN ON 90% NAOH 10% NAI OVER TWO DAYS WITH TWO DIFFERENT SAMPLES. 141
FIGURE 64 - THREE SUCCESSIVE 5°C/MIN DSC SCANS OF A 60% NAOH / 40% NAI SAMPLE WITH BASELINE ADJUSTMENT MADE TO EMPHASIZE TRANSITIONS. 142
FIGURE 65 - DSC STUDY OF 30% NAOH / 70% NAI ON TWO SEPARATE TEST DAYS. 143
FIGURE 66 - NAOH-NAI BINARY PHASE DIAGRAM WITH EXPERIMENTAL DSC POINTS AND DATA FROM LITERATURE. 145
FIGURE 67 - XRD SCAN OF AN 80/20 EUTECTIC MELT POST CYCLIC VOLTAMMETRY. ONLY TWO PHASES PRESENTED THEMSELVES CLEARLY WITH TRACE AMOUNTS OF $NI(OH)_2$ PRESENT BUT NOT QUANTIFIABLE DUE TO THE BACKGROUND FROM THE AIR-SENSITIVE SAMPLE HOLDER. 147
FIGURE 68 - PROPOSED CRYSTAL STRUCTURE OF $NA_7(OH)_5I_2$. 148
FIGURE 69 - THE RATIOS OF $NA_7(OH)_5I_2$ AND A-NAOH EXPECTED FOR A FROZEN SAMPLE OF EUTECTIC COMPOSITION 149
FIGURE 70 - XRD OF WELL-ANNEALED $NA_7(OH)_5I_2$ SAMPLE. THE TWO EXPECTED PHASES, $NA_7(OH)_5I_2$ AND A-NAOH ARE PRESENT ALONGSIDE A THIRD, UNKNOWN PHASE. 151
FIGURE 71 - EXAMPLE OF AN UNMATCHED PEAK AT 26.7453°. THERE WERE NO COMPOUNDS IN THE ICDD PDF-4+ DATABASE THAT COULD ACCOUNT FOR THIS SIGNAL WITHIN REASONABLE ERROR. 152
FIGURE 72 - XRD RESULTS OF A WELL-ANNEALED $NA_5(OH)I_4$ SAMPLE. SAMPLE QUANTIFICATION IS NOT POSSIBLE DUE TO THE STRONG PRESENCE OF AN UNKNOWN PHASE FOR WHICH THERE IS NO RIR REFLECTIVITY DATA. 153
FIGURE 73 - COMPARISON OF A) $NA_7(OH)_5I_2$ AND B) $NA_5(OH)I_4$ SPECTRA. THE UNKNOWN POINTS CLEARLY IDENTIFIABLE IN SPECTRA “B” ALL COINCIDE WITH UNKNOWNS OR ABNORMALLY LARGE PEAKS IN SPECTRA “A”. 154
FIGURE 74 - PLOT SHOWING THE ORIGINAL XRD OF THE $NA_5(OH)I_4$, THE INDEXED PHASE IN GREEN, AND AN EXAMPLE PM-3M ISOSTRUCTURAL COMPOUND IN BLUE. THOUGH THE HEIGHTS OF THE PATTERN LINE ARE IRRELEVANT, THE SPACING BETWEEN THE VARIOUS LINES IS INDICATIVE OF THE RATIO OF SPACING BETWEEN ATOMIC SITES. 156
FIGURE 75 - OPTIMIZED PHASE DIAGRAM FIT USING CEF SOLUTION MODEL AND OPTIMIZED DATA FOR $NA_7(OH)_5I_2$ AND $NA_5(OH)I_4$ 159
FIGURE 76 - PLOT OF NAOH ACTIVITY FROM THE CEP MODEL AS A FUNCTION OF TEMPERATURE AND COMPOSITION. 162
FIGURE 77 - 2D REPRESENTATION OF THE DATA FROM THE TEMPERATURE-ACTIVITY-COMPOSITION STUDY OF MIXED NAOH. 162
FIGURE 78 - DECOMPOSITION REACTION FOR MODELLED NAOH LIQUID WITH NON-UNITY ACTIVITY. THIS VALUE IS COMPARED TO THE VOLTAGE EXPECTED FOR PURE NAI BREAKDOWN. 164

FIGURE 79 - A PURE NI 0.314 CM^2 WORKING ELECTRODE IS MEASURED AGAINST A TANAB REFERENCE ELECTRODE IN A SERIES OF CATHODIC CV SCANS TO -200 MV (VS. NA) AT 257°C 165
FIGURE 80 - 50 MV/S CVS CONDUCTED AT DIFFERENT TEMPERATURES ON 0.314 CM^2 NI WORKING ELECTRODE AND TANAB REFERENCE.....167
FIGURE 81 - RESISTANCE MEASUREMENT PLOTTED TO HIGHLIGHT ARRHENIUS TEMPERATURE RELATIONSHIP. THOUGH NO CELL CONSTANT WAS MEASURED, THE SETUP GEOMETRY WAS HELD CONSTANT AT ALL TEMPERATURES. 168
FIGURE 82 - INTEGRATION TIMES USED IN THE STRIPPING EFFICIENCY CALCULATION 169
FIGURE 83 - STRIPPING EFFICIENCY OF CATHODIC CVS CONDUCTED AT VARYING TEMPERATURES. 170
FIGURE 84 - RESTRICTED CV DEMONSTRATING THE LINKAGE BETWEEN THE UNDER-DEPOSITION SIGNAL AND THE OXIDATIVE SIGNAL 172
FIGURE 85 - INTEGRATION OF TWO CV STUDIES AT DIFFERENT SCAN RATES. THE SLOWER RATE IS FOUND TO MORE COMPLETELY OXIDIZE THE REDUCED SPECIES, POINTING TO AN INSOLUBLE SURFACE SPECIES.....173
FIGURE 86 - AN ANODIC CV ON A 0.314 CM^2 PLATINUM WORKING ELECTRODE SHOWING THE LOCATION OF ALL FOUR ANODIC PROCESSES DISCOVERED IN THE MELT. 174
FIGURE 87 - INVESTIGATION OF THE 1.5 V OXIDATION SIGNAL VIA NI AND PT WORKING ELECTRODES. 175
FIGURE 88 - REPEATED ANODIC CVS RUN TO SHOW THE DEPLETION OF THE SPECIES THAT DRIVES PEAK III.....177
FIGURE 89 - A TAFEL-TYPE PLOT OF THE ANODIC SCAN OF BINARY EUTECTIC AT VARIOUS TEMPERATURES. DIFFERENT REACTION MECHANISMS ARE CLEARLY VISIBLE AND THEIR ONSETS OCCUR AT THE VOLTAGES SHOWN IN TABLE 35. 178
FIGURE 90 - FUNCTIONALITY OF ECW ON TEMPERATURE STUDY. ECW IS EXTRAPOLATED BACK FROM STAGE IV ANODIC PROCESS. DOTTED ARROW DEMONSTRATES THIS PROCEDURE FOR THE T=328°C VOLTAMMAGRAM. 179
FIGURE 91 - COMPARISON OF THE EXPERIMENTALLY MEASURED OXYGEN PRODUCTION VOLTAGE WITH THAT PREDICTED FROM THE THERMODYNAMIC MODEL. SLOPES ARE PROVIDED NEXT TO CURVES.....180
FIGURE 92 - 112 CHARGE-DISCHARGE CYCLES 182
FIGURE 93 - CYCLES 9 THROUGH 11 OUT OF 112 OF THE CHARGE-DISCHARGE EXPERIMENT 183
FIGURE 94 - CHARGE AND DISCHARGE VS CAPACITY CURVE FOR A SINGLE CYCLE. 183
FIGURE 95 - LEAKAGE CURRENT (SELF-DISCHARGE) MEASUREMENT AFTER A FULL CHARGING STEP.....184
FIGURE 96 - ENERGY AND COULOMBIC EFFICIENCY DATA CALCULATED FOR EACH CYCLE ALONGSIDE EACH LEAKAGE CURRENT MEASUREMENT.....186
FIGURE 97 – SEM (ON PREVIOUS PAGE) OF THE NAOH-NAI SALT AFTER 1 MONTH OF CYCLING (112 CYCLES).....187
FIGURE 98 - SEM OF THE ELECTRODE-ELECTROLYTE INTERFACE WITH SAMPLE POINTS BEING TAKEN AT THE SURFACE OF THE ELECTRODE. THE DARKER REGION REPRESENTS SALT DUE TO ITS LOWER ATOMIC ELECTRON COUNT RESULTING IN LOWER BACKSCATTERING. 188
FIGURE 99 – DESCRIPTION OF THE LOGICAL FLOW USED DURING THIS THESIS WORK.....190

Chapter 1 - Introduction

1.1 The Winds of Change

On the morning of January 31st, 2012 the residents of the west coast seaport town of Esbjerg, Denmark woke to the sound of high winds and thrashing branches. The gusts in the early hours of the morning had been record-setting, with peak recordings at 4:00 AM of 54 mph that maintained strength until noon. With an average annual wind speed of 13.1 mph, Esbjerg is one of the windiest cities in Denmark and would rank in the top five windiest cities were it located in the continental United States[1]. In spite of that morning's anomaly, the city of Esbjerg is not only familiar with such energetic weather, it has come to depend upon it. Since 2010 Esbjerg can lay claim to hosting the largest offshore wind farm in Denmark and the sixth largest in the world with the complementary Horns Rev 1 and 2 rated together at approximately 369 MW generation capacity.

Denmark is no stranger to wind farms or renewable energy – the Danish company, Vestas, is currently the largest producer of wind turbine technology while the country similarly demonstrates a clear lead in wind turbine penetration in its own energy sector with over 30% of electricity production coming from renewable wind resources[2]. For this reason, Denmark is a common planning case-study for countries hoping to integrate intermittent sources like wind and into their existing energy portfolios. A common topic of investigation is in the area of balancing grid inflows and outflows – a challenge resulting from the fact that most power grids maintain virtually no storage and grid operators must therefore maintain in-situ control in order to ensure dispatchable generation can meet demand. Without such minute-to-minute control, oversupply of energy from unexpected generation or undersupply driven by under-predicted demand would equate to economic loss and inefficiency. As a result, integration of intermittent resources like

wind power brings with it legitimate concerns regarding increased variability and asynchronicity between production and demand that could render a poorly planned wind farm a resource sink rather than source.

Though unusual for Danish installations, large perturbations like the one experienced in the early hours of January 31st do result in substantial impacts upon the market. In fact, Esbjerg wasn't alone in its overproduction, as the entire Danish western grid soon became loaded with greater than 2,600 MWh/h production rates for 14 straight hours, 2.6 standard deviations above the hourly wind production mean for this area[3]. Shortly after the initial generation spikes from the local wind turbines, Nordpool's Elspot energy price for the western Denmark power grid dropped to below €0 for over four hours, indicating the need to distribute excess energy so rapidly that the Danish western grid operators were literally paying to have their excess energy exported to neighboring countries. Events like these, though uncommon, have led some researchers to believe that Denmark's national strategic thrust has created a perverse outcome that disproportionately exports tax-supported renewable energy at depressed spot prices to neighbors[4]. On the opposing side, there are just as many researchers that have shown that intermittent exports do not appear to abnormally correlate with periods of peak wind production and that wind-generated electricity goes disproportionately to satisfying domestic demand while higher merit order sources are exported or recouped[5]. In either case, there is agreement that the ability to store excess energy, regardless of its source, provides not only significant economic gain but improved efficiency and reliability. What the case study of Denmark really teaches us is that moving towards a fully renewable future is fundamentally predicated on our ability to intelligently deploy grid-scale storage options to smooth fluctuations implicit with variable demand and intermittent supply.

1.2 Cost is King

Though perhaps the most popular example, wind installations are just one of many integration points where storage could offer economic, efficiency, or reliability benefits. Numerous reports[6, 7] have identified more than a dozen unique, though not mutually exclusive, functional areas in which tandem storage could improve our ability to sustainably supply electricity of approximately 4,100 TWh[8] to US consumers. Though the United States has made great strides in the research and development of renewable energy technologies, it still lags behind several European peers with only approximately 13.1% penetration into the electricity market as of 2014[9]. Of this 520 TWh renewable generation, only approximately 177 TWh comes from intermittent sources like wind and solar[10].

In spite of the fact that the United States electricity grid is not only significantly more physically expansive but also complicated by multiple layers of federal, regional, and local regulation that do not exist in many smaller European counterparts, a majority of states around the country have continued to set competitive targets via renewable portfolio standards (RPS). Though variable across the nation, some geographic areas are aggregately targeting greater than 20% renewable penetration by as early as 2020. One such region, under the purview of the Western Electricity Coordinating Council (WECC), has received attention in a recent study by Pacific Northwest National Lab[11] that investigates the balancing requirements implicit in its RPS target as well as cost-effective technology options. The study found that the anticipated renewable expansion via intermittent wind would require a total of 6.32 GW of balancing power with between 0.07 to 0.22 units of new storage capacity per unit of additional wind power. Such an amount is 25.6% of the total existing storage in the United States[12] and would represent a significant departure from the current storage growth rate. In addition, the report noted that there

are several candidate technologies that are increasingly able to compete with incumbent pumped hydro and compressed air energy storage (CAES) options on the basis of their energy and power outputs.

A more detailed analysis of these technologies[13] has noted that by taking into account the lifetimes of each technology as well as the full cradle-to-gate energy inputs, most modern electrical energy storage[14] technologies fall short of being viable candidates for deployment as load-balancing solutions at the global scale. In fact, in spite of the torrent of research into high-technology solutions the most stringent criteria for comprehensive deployment are likely the severe system cost and material availability metrics. Programs like ARPA-E have set aggressive goals for both cost of energy and power delivery for their grid-storage portfolio with <$100/kWh and <$1000/kW, respectively. Amortized over the range of proposed lifetimes (10 to 20 years), most cost metrics yield levelized energy costs (LECs) of between $0.025/kWh to $0.15/kWh which is well in league with existing gas and oil peaker technologies and the average retail price felt by residential consumers. Many authors[15, 16] have offered similar ranges and placed special emphasis on the global scalability[17] of any candidate technology.

Due to the fact that we are globally trending towards increased representation of renewables in national energy portfolios, because such energy sources are aperiodic and stochastic, and because demand is so large and continually increasing it is proposed that grid-scaled storage is the final bottleneck between our energy landscape today and a renewable and sustainable energy future[18]. Finding this bridge will take more than scientific and technological ingenuity; it requires a process of cost-driven discovery guided by the realities of material availability and the political economy.

1.3 Objective

This thesis hypothesizes that further improving the Liquid Metal Battery's (LMB's) ability to deliver energy at low levelized costs of ownership is highly dependent upon a methodical understanding of the variables that drive cost and a targeted effort towards addressing those that are found to be most impactful. In order to do this, this work will rigorously and quantitatively develop an understanding of the key cost drivers for liquid metal batteries via process-based cost modeling, translate the most promising one into a viable research pathway, and undertake an experimental program with the goal of both advancing the field as well as improving LMB's final cost metric.

Specifically, this work will find that temperature is a key variable in LMB system cost as it has multiplicative impact upon the final $/kWh cost metric of the system. This investigation will therefore target a dramatic reduction of system operating temperature through the investigation and characterization of a novel electrolyte system. Development of such intermediate range molten salts (150 – 300°C) will not only reduce total system cost but will also simultaneously unlock process simplifications in system assembly and sealing. Research will focus on the compositional, thermal, and electrochemical operation windows of the system and thermodynamic modeling will be leveraged to guide future development decisions. The ultimate outcome of this work will be to have rigorously characterized a new low-temperature molten salt system, demonstrated through proof-of-concept battery trials that such systems hold potential for the next generation of LMBs, and made the case for due diligence in designing and undertaking LMB experimental programs in the future.

Chapter 2 - The Liquid Metal Battery as a Grid Storage Solution

2.1 Basic Principles

The liquid metal battery (LMB) is composed of a liquid anode, cathode, and electrolyte that self-segregate into three distinct layers due to density differences and immiscibility. The negative and positive electrodes are electrically isolated from each other by a non-aqueous electrolyte and simple cell geometry designed to separately conduct electrons to or from the electrodes through an external circuit. Upon discharge, the more electropositive metal, A (negative electrode), undergoes an oxidation reaction at the electrode-electrolyte interface to produce ionized A^+ and an electron that is conducted back through electrode A and then collected to be sent around an external circuit. Because only the ionized species is significantly soluble in the electrolyte, A^+ travels across the electrolyte under chemical concentration and electrical potential gradients until it reaches the positive electrode composed of metal B. Once reaching the interface, A^+ reduces back to form an alloy with metal B, and then diffuses away from the interface under a concentration-driven diffusion mechanism. Charging reverses this process and results in an oxidative de-alloying of metal AB and deposition of pure A back at the negative electrode (Figure 1[19]).

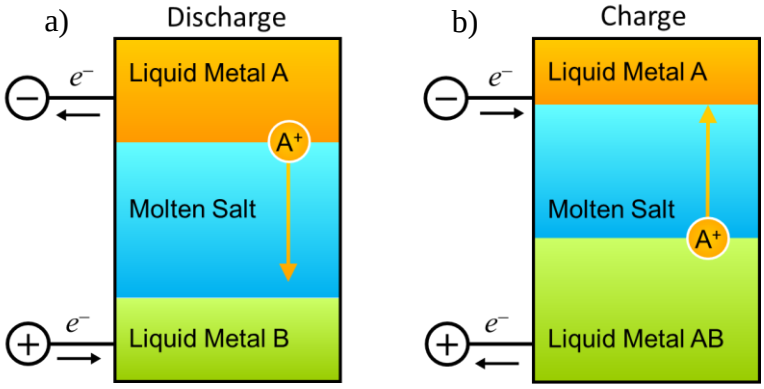

Figure 1 - Operation of the liquid metal battery during a) discharging and b) charging

In this general formulation, the single-cation alloying and dealloying process can be simply represented by the following electrochemical reactions (Equations 1 – 3).

$$\text{Anode: } A_{liq} \rightarrow A^{z+} + ze^{-} \qquad \text{Equation 1}$$

$$\text{Cathode: } A^{z+} + ze^{-} \rightarrow A_{\text{ in liquid B}} \qquad \text{Equation 2}$$

$$\text{Overall: } A_{liq} \rightarrow A_{\text{ in liquid B}} \qquad \text{Equation 3}$$

2.1.2 Thermodynamic Interpretation

Though the driving force behind this reaction is fundamentally linked to the change in partial molar Gibbs free energy, the LMB is unlike most other electrochemical energy storage devices in that the relevant free energies are entirely those of solution mixing as opposed to displacement or intercalation reactions. As a result, the driving force of the cell can be directly linked back to the fundamental thermodynamic properties of mixing through solution model theory (Equations 4-6).

$$\Delta\bar{G}_{cell} = -nFE_{cell,eq} = \bar{G}_{A\ in\ liquid\ B} - \bar{G}_{liquid\ A} \qquad \text{Equation 4}$$

$$\bar{G}_{A\ in\ liquid\ B} = G^{0}_{liquid\ A} + RTlna_{A\ in\ liquid\ B} \qquad \text{Equation 5}$$

$$\bar{G}_{liquid\ A} = G^{0}_{liquid\ A} + RTlna_{liquid\ A} \qquad \text{Equation 6}$$

Where G_i^0 is the standard state free energy, n is the moles of electrons involved in the redox reaction, F is Faraday's constant, $E_{cell,eq}$ is the equilibrium voltage of the cell, R is the gas constant, T is the temperature in Kelvin, and a_i is the activity. In the most common scenario where the negative electrode is composed of pure liquid metal A, the activity of liquid a, $a_{liquid\ A}$, is defined as unity (Equation 7).

$$a_{liquid\ A} = 1 \quad \therefore \quad \ln\left(a_{liquid\ A}\right) = 0 \qquad \text{Equation 7}$$

In scenarios where the anode is not pure but composed of multiple species the activity of interest is complicated by the mixing behavior of the two materials in each other and therefore requires in depth studying and modeling to confidently predict as a function of charge.

By substituting Equations 5-7 for Equation 4, one is able to extract how the voltage of the cell is dependent on the thermodynamic mixing (Equation 8):

$$E_{cell,eq} = -\frac{\Delta \bar{G}_{cell}}{nF} = \frac{RT}{nF}\ln\left(a_{A\ in\ liquid\ B}\right) \qquad \text{Equation 8}$$

Specifically, the voltage of an LMB is fundamentally mediated by the activity of the electropositive metal, A, mixed in the positive electrode environment of B. Because of this, the voltage of an LMB can be very accurately modeled with knowledge of how solution activity is functional on composition and temperature.

There are a variety of experimental methods by which this information can be extracted, including electromotive force (EMF) measurements, vapor pressure measurements, or calorimetry. A recent and instructive example of such an activity study was conducted by Newhouse in which the Ca-Mg couple was explored[20]. In this study, the thermodynamic properties of Ca-Mg alloys were determined using the EMF approach in which different concentrations of Ca-Mg alloy had their open circuit voltage measured against a known/stable two phase Ca-Bi reference alloy[21] at a variety of temperatures (Figure 2[20]). In addition to being an experimental representation of the theoretical discharge profile, this study also gives insights into the storage capacity different positive electrodes can provide on a molar basis.

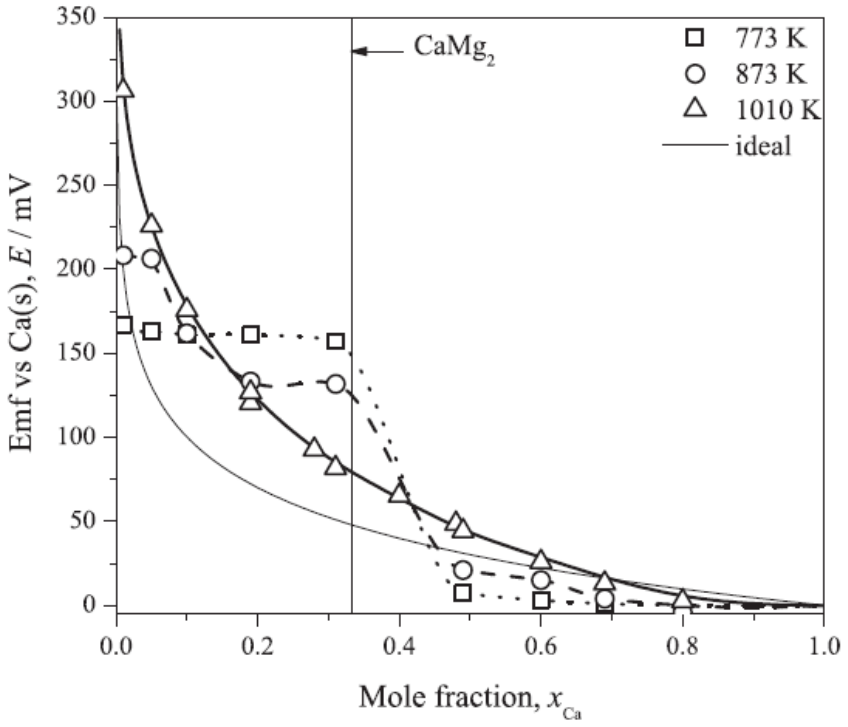

Figure 2 - Electromotive force as a function of Ca-Mg alloy composition at 773, 873, and 1010 K. The intermetallic $CaMg_2$ (T_{MP} = 987 K) is overlaid to explain the drop-off in activity at approximately 33 mole percent calcium. An ideal voltage curve, assuming ideal mixing, is also shown to highlight thermodynamic deviations from ideality.

In this example, the 773 K and 873 K measurements show a precipitous drop-off after crossing over the $CaMg_2$ intermetallic compound composition. In the case of a Ca||Mg system, this information teaches that batteries of this type likely cannot accommodate more than 1 mole calcium for every 2 moles of magnesium. This impacts optimal cell design and overall cost of the device by restricting the capacity.

Another feature worth noting is the voltage plateau observed for the 773 K and 873 K measurements. The plateaus in an LMB system are the result of the positive electrode moving compositionally through a two-phase region in which both end components have equivalent chemical potentials, and thus activities, of the electroactive component. In this binary system this is easy to explain as the increase in calcium composition and corresponding motion across the

binary phase diagram in Figure 3. The transit across the phase diagram involves the entrance and departure of one- and two-phase regions.

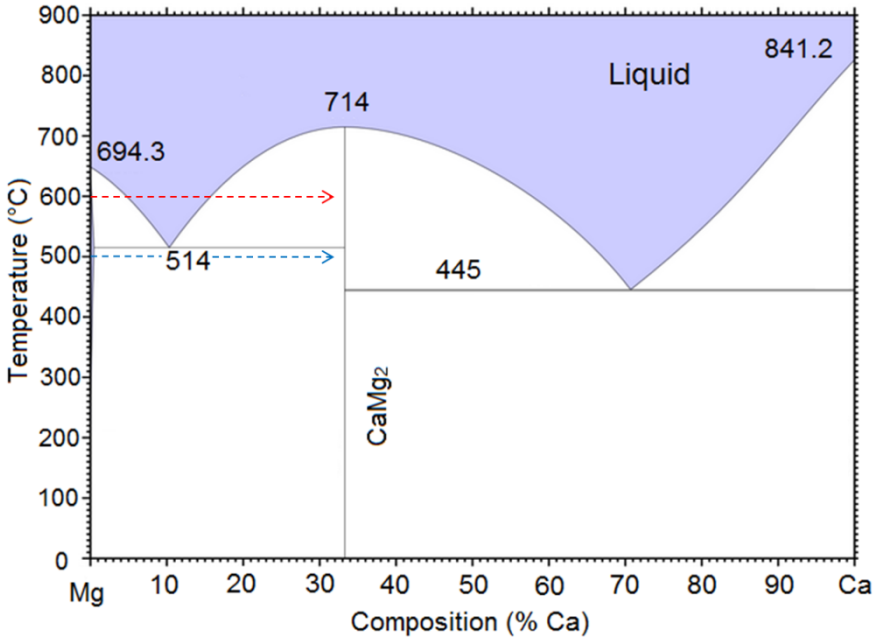

Figure 3 - Mg-Ca binary phase diagram showing the path taken during discharge at 773K (500°C) in blue and 873K (600°C) in red.

By comparing Figure 3 to Figure 2, the passage through a two-phase region is confirmed to correspond to a flat voltage profile. At 500°C (773 K) nearly the entire voltage profile to the left of the $CaMg_2$ compound is flat. This corresponds to passage through a regime where high purity Mg is in equilibrium with $CaMg_2$ (blue line). At the higher temperature, 600°C (873 K), the two plateaus correspond to 1) the passage through high purity calcium and binary liquid two phase and 2) the liquid and $CaMg_2$ two phase region (red line).

Though the EMF vs. composition profile provides some discharge information, it does not allow for a deeper understanding of the thermodynamic phenomena underlying the partial free energy differential. For this, one can extract calcium and magnesium activities and represent these using one of a variety of non-ideal mixing solution models. The activity of calcium, the

itinerant species, can be extracted from the voltage data using a more common form of the Nernst equation (Equation 9) where E_{OCV} is referenced against pure Ca_{solid}.

$$a_{Ca\ in\ Mg} = exp\left\{\frac{-2FE_{OCV}}{RT}\right\} \qquad \text{Equation 9}$$

Activities and their corresponding activity coefficients of calcium in the alloy can then by related to the activities of magnesium via the Gibbs-Duhem relation (Equation 10) such that the thermodynamic properties and functionalities on temperature and composition can be modelled.

$$ln\gamma_{Mg} = -\frac{x_{Ca}}{x_{Mg}} ln\gamma_{Ca} - \int_1^{x_{Mg}} \frac{ln\gamma_{Ca}}{x_{Mg}^2} dx_{Mg} \qquad \text{Equation 10}$$

Where γ_i is the activity coefficient related to activity through $\gamma_i = {a_i}/{x_i}$ and x_i is the mole percent. Figure 4 shows the final product of the EMF study – activity curves as a function of composition.

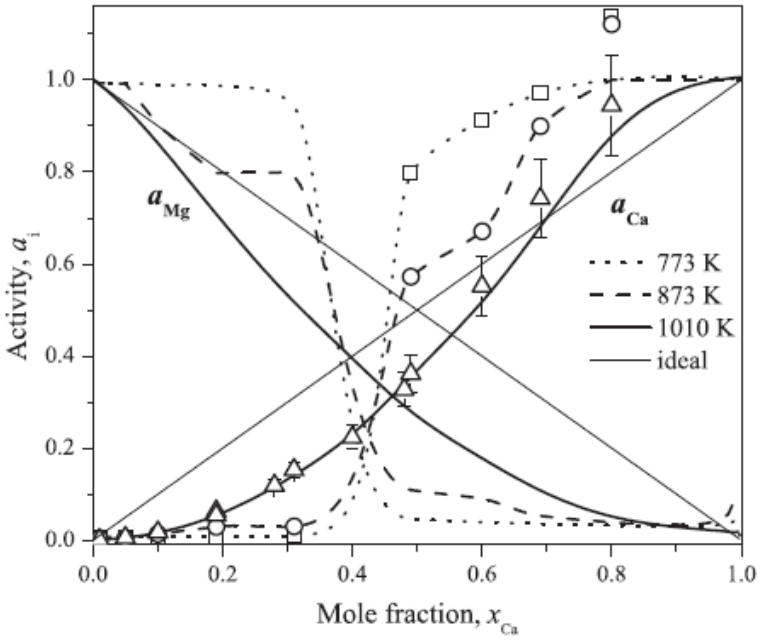

Figure 4 - The activity curves of Ca and Mg as a function of composition at 773, 873, and 1010K. Ideal solution curve provided to demonstrate deviation from ideality.

This information is particularly valuable for LMBs as it is the critical influencing variable in Equation 8, $a_{A\ in\ liquid\ B}$, and can therefore enable proper theoretical modeling of the voltage profile of the device during charge/discharge.

Though the Ca-Mg system is not a strong candidate for a LMB device due to its particularly low voltages (100-300 mV), its behavior is quite illustrative of general behavior between most couples and it also highlights a final, very important point: that useful voltages of LMBs are not only functional on how far apart two metals may be on the electrochemical series but also that LMB voltages are fairly dependent on deviations from ideal and complete mixing between the two end members. In the case of Ca-Mg, it is seen that the actual recorded voltage in the plateau region is approximately twice the value as predicted from ideal solution models. These non-idealities are captured by excess terms in the free energy equations and are embodied by activity coefficients, γ_i, that deviate strongly from unity. Such deviations are physically the result of particular ordering or structuring around the itinerant atom in the positive electrode environment. In the case of a positive electrode with a single metal, this may occur because of the formation of intermetallic compounds (e.g. $CaMg_2$ as above) or simply due to short- or medium-range ordering in the melt that derive from non-random coordinating environments, or associates[22].

In systems where the positive electrode is alloyed with another species, deviations from ideality may additionally derive from a preferential interaction between the itinerant species and one of the alloyed electrode materials over another. An instructive example of this is in the Li||Pb-Sb system in which lithium has been found to preferentially coordinate around antimony atoms rather than lead atoms[23]. This leads to discharge voltages that strongly resemble the Li||Sb

as opposed to the Li||Pb system (Figure 5). This finding[23] has laid the foundation for the first commercial LMBs.

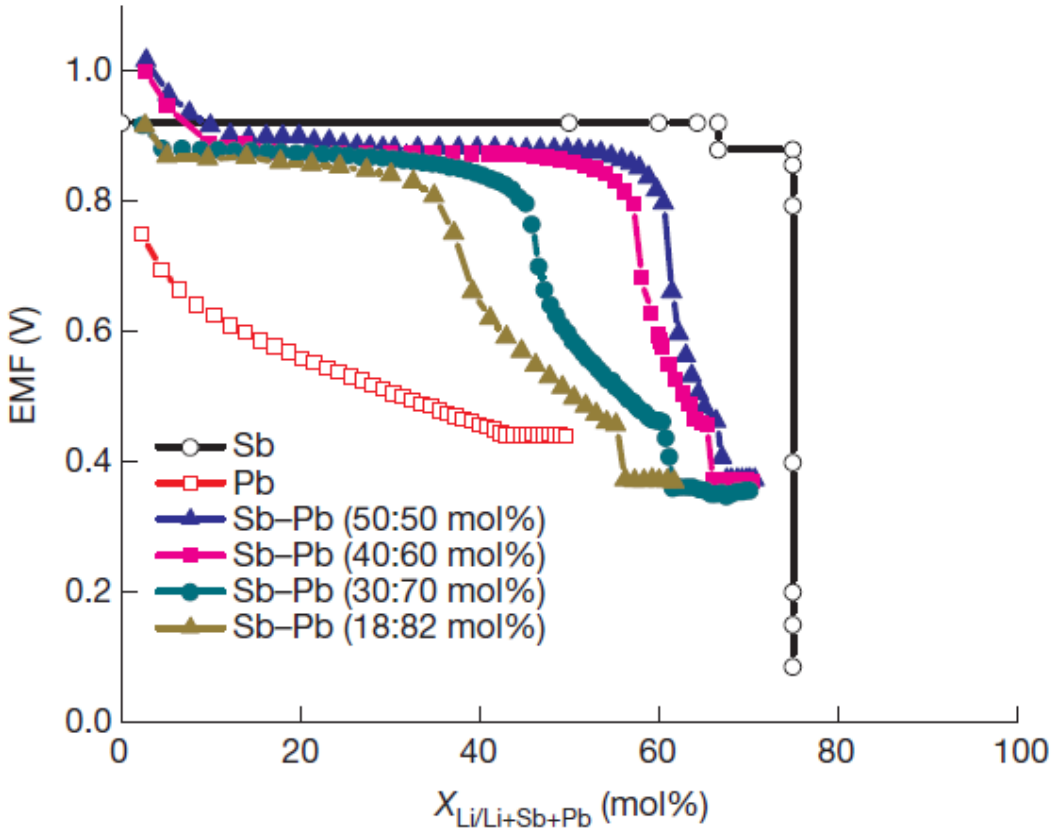

Figure 5 - Voltage versus lithium concentration for a variety of positive electrode compositions. Alloys of Pb-Sb much more closely follow the profile of Li vs. Sb than Li vs. Pb

Similar EMF experiments have been conducted for a large combination of potential negative and positive electrode materials. Fortunately, because the periodic table accurately captures trends in electronegativity, the grouping of negative and positive candidates roughly groups according to Group I and II metals and metals located under the metalloids, respectively. If these metals are similarly visualized as a function of their electrochemical reduction potentials against the standard hydrogen electrode (SHE) there is a clear gap between the two groups that roughly tracks with the EMF between the two metals (Figure 6[19]).

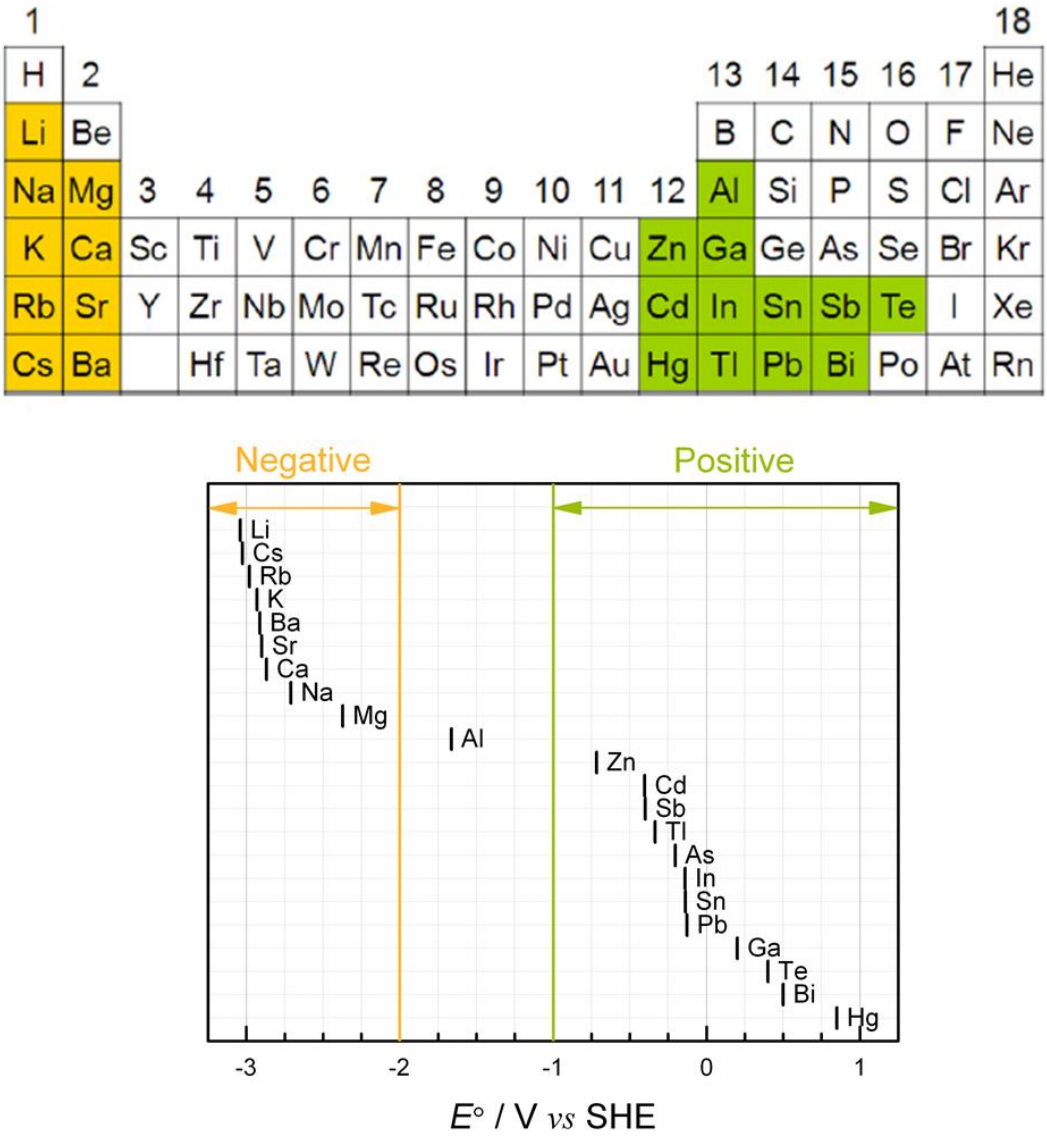

Figure 6 - At top is a periodic table with example candidate materials for negative electrodes provided in orange and positive electrodes in green. Bottom presents these elements plotted by their reductive potential against the standard hydrogen electrode.

With these two groupings, it is easier to review the literature for EMF-type studies and aggregate voltages for the most relevant LMB candidate couples. Fortunately, a great deal of this work has been completed in a review by Kim et al. and is reproduced here (Table 1[19]) to emphasize the extent of the thermodynamic literature as well as areas in which gaps in knowledge exist.

Table 1 - Equilibrium cell voltages estimated from full charge to discharge as defined by phase diagram or occurrence of intermediate compounds. In the absence of phase data, 50/50 mole ratio was used for singly charged cations and 33/66 mole ratio for doubly charged cations.

B / A	Li	Na	K	Mg	Ca	Ba
Zn	0.31-0.07[24]	—	—	0.21-0.08[25, 26]	0.44-0.17[27, 28]	—
Cd	0.56-0.37[29]	0.22-0.02[30, 31]	—	0.21-0.09[32]	—	—
Hg	—	0.67-0.13[33-36]	0.72-0.07[37, 38]	—	—	—
Al	0.30-0.30[39]	—	—	0.20-0.07[40]	0.44-0.41[41]	0.53-0.15[42]
Ga	0.59-0.57[43]	0.20-0.01[44, 45]	—	0.25-0.14[46-48]	—	—
In	0.55-0.50[49]	0.30-0.06[31, 50]	0.24-0.02[51, 52]	0.24-0.11[46, 47]	0.62-0.34[53]	—
Tl	—	0.42-0.11[54]	0.44-0.07[55]	0.23-0.12[56]	—	—
Sn	0.70-0.57[57, 58]	0.45-0.22[31, 50, 59-61]	—	0.35-0.19[62, 63]	0.77-0.51[64]	1.08-0.71[64]
Pb	0.68-0.42[65]	0.47-0.20[66, 67]	0.51-0.15[68, 69]	0.21-0.13[47, 63]	0.69-0.50[64]	1.02-0.66[64]
Sb	0.92-0.92[70]	0.86-0.61[71-73]	1.01-0.54[74, 75]	0.51-0.39[62, 63]	1.04-0.94[64]	1.40-1.15[64]
Bi	0.86-0.77[70]	0.74-0.47[71, 76-78]	0.90-0.45[71, 79]	0.38-0.27[62, 63]	0.90-0.79[64, 80, 81]	1.30-0.97[64]
Te	1.76-1.70[82, 83]	1.75-1.44[84]	2.10-1.47[85]	—	—	—

2.1.3 Practical Operation

Though the discharge voltage is capped at a theoretical thermodynamic limit, $E_{cell,eq}$, all batteries incur operational losses in the form of voltage reductions. These voltage reduction inefficiencies, known as overpotentials, are generated as a result of passing charge and generally increase with increasing current density. The most common overpotential losses batteries face are represented in Equation 11.

$$V_{operational} = E_{cell,eq} - \eta_{ct} - \eta_{ohm} - \eta_{mt} \qquad \text{Equation 11}$$

- Charge transfer overpotential, η_{ct} – also generally referred to as the activation overpotential, this inefficiency arises out of the activation barrier required to facilitate the heterogeneous redox reaction at the electrode interfaces.
- Ohmic overpotential, η_{ohm} - also generally referred to as the resistance overpotential, this inefficiency arises from the linear resistance components implicit with both electronic

and ionic currents. Contributions come from junction potentials, electrical resistivity of electrodes/current collectors/wires, and resistive losses from the passage of ions through the electrolyte.

- Mass transport overpotential, η_{mt} – also generally referred to as the concentration overpotential, this inefficiency arises from local depletion or exclusion (as in the case of bubble generation) of the relevant reactive species or build-up of product species.

Whereas with most battery technologies scientists will work to minimize the aforementioned inefficiencies as much as possible, the LMB's need to remain at a liquid state in order to charge and discharge creates the unusual requirement that heat be available to the device to keep it molten. Though heat can be supplied exclusively from an external source, there is also an option to retain some of the heat generation from the aforementioned inefficiencies to contribute to this required heat content. Doing so reduces the overall system inefficiency by reducing the need to supply external power for heating and cooling systems.

Unpublished work by this lab has shown that given a certain electrolyte resistivity, one can tailor the electrolyte thickness and current density to produce enough IR-based joule heating to keep the cell at operational temperature. The temperature that must be maintained is generally 25°C above the melting point of the highest melting component. As will be discussed, because interatomic bond strengths in ionic solids then to be greater than those in metals, the electrolyte frequently plays the role of setting the operational temperature of the device.

2.2 Strengths and Weaknesses

2.2.1 Scientific

Though LMBs incur penalties from the above overpotential inefficiencies, one of their major strengths is in significantly suppressing the effects of each due to its unique all-liquid

design and material properties. The liquid-liquid interface between the electrolyte and electrode facilitates rapid charge transfer by lowering the potential energy barrier[86], the high conductivities of molten salt at elevated temperatures result in low resistances in the mΩ·cm regime, resulting in minimal resistive loss across the electrolyte and thus high conductivities, and the usage of an all-liquid system improves electrode and electrolyte diffusion and obviates traditional solid-state fade/failure mechanisms characteristic of incumbent technologies and can therefore result in a battery lifetime that is theoretically limited only by corrosion.

Work by Newhouse et. al has quantified these inefficiencies for two archetypal systems, Mg||Sb and Li||Bi (Figure 7[87]). These studies show that for a current density of 100 mA/cm^2 total overpotentials rarely sum to greater than 75 mV and that the largest contribution to this loss is usually related to the electrolyte ohmic overpotential, η_{ohm}[i]. By comparison to existing Na-S systems with β"-Al_2O_3 solid electrolytes (BASE) conducting at around 0.03 S/cm, a comparable discharge current density would yield an overpotential of greater than 1 volt[88].

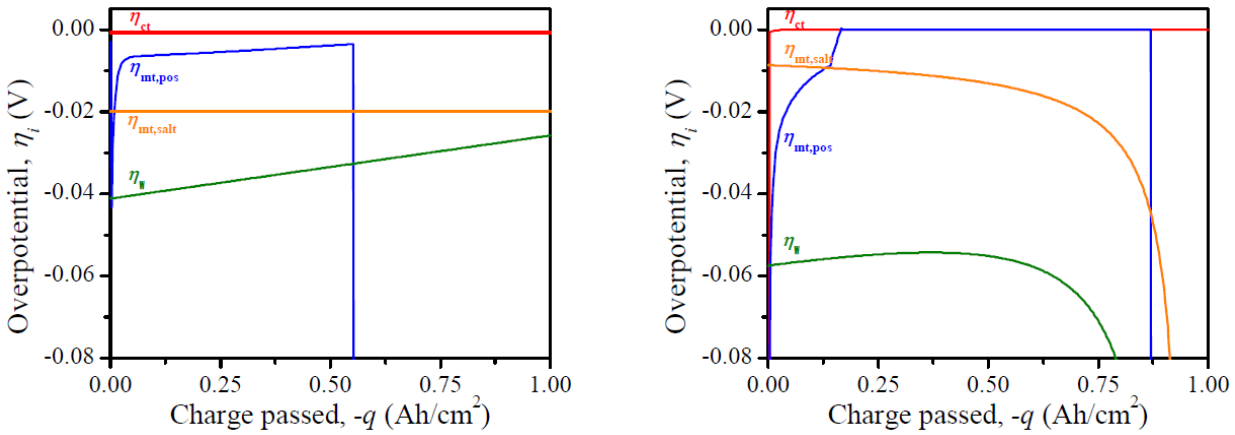

Figure 7 - Modeled overpotentials at 100 mA/cm^2 for left) Mg||Sb cell and right) a Li||Bi cell. η_W in this work corresponds to the ohmic overpotential of the electrolyte.

[i] True in all cases except those experiencing solid intermetallic formation on the electrode surfaces.

LMBs do suffer from distinct disadvantages when compared to existing battery systems. The liquid-architecture that endows the system with rapid kinetics also makes it unsuitable for portable applications and sensitive to motion. For these reasons, LMBs will likely not be competitive in portable or vehicular applications. In addition, because the free energy of the system is derived from a metallic alloying reaction as opposed to a displacement or intercalation-type reaction, the achievable voltages and energy densities tend to be lower. As a result, LMBs are not the best candidates for compact electronic devices. Such devices demand high energy or power capacities per unit volume/mass and therefore are more amenable to Li-type systems. For these three reasons, LMBs will be explored in this thesis to tackle stationary grid storage applications only.

2.2.2 Technological Scale-Up

Unlike many other modern systems that rely upon non-equilibrium or finely-tuned microstructures, LMBs can be produced by simply pouring in the active components, weld-sealing the container closed, and heating it up to temperature (Figure 8). For this reason, mass production or scaling of LMBs should be significantly easier to assemble than existing technologies and the equipment required for scale-up should incur a much smaller CAPEX investment. Specifically, little specialized equipment or labor should be required and as a result LMBs may potentially move outside of the capital intensive cleanroom facility paradigm and empower more capital-constrained regions to domestically produce solutions to their own energy problems.

Depending on the size of the installation and required operational temperature, LMB scale-up requires a more complicated thermal management system than may be required for most other systems. Though systems do not exhibit the same thermal failure or runaway as in some

Figure 8 - Open air assembly of a 40 Ah liquid metal battery

lithium-ion systems[89], uncontrolled temperature swings can reduce output or exacerbate corrosion and erode service lifetime. In addition, because LMBs operate in the molten state, a compromise in the sealing or packaging materials could result in catastrophic failure if the entire system does not maintain some secondary containment. For these reasons, LMB scale-up necessitates additional systems-level considerations to ensure safe operation.

2.2.3 Market

In addition to being simpler to model scale-up system costs, LMBs also present another significant advantage when it comes to addressing grid-scale storage markets. Because of their relative simplicity in design and operation, active components can be interchanged with far fewer complications than with other intercalation- and displacement-type batteries. In other words,

LMB researchers can more easily test and design for various chemistries of active components than would be possible in the case of proposing a new intercalant ion (e.g. sodium) to move away from lithium. This is because the most important information about new chemistries can be determined from phase diagram investigations and basic thermodynamic EMF measurements. The reason this adapts LMBs to diverse markets well has to do with the desire to maintain the flexibility in material down-selection based on cost, energy intensiveness, local availability, and regional security. Depending on whether a country or company wants to provide energy storage at a local minima functional on domestically available materials or a global minima more closely linked to global resource and transport prices then the choice of active components may vary.

2.3 Review of Competitive Technologies

It is important to note that not all storage technologies can easily be compared solely on the basis of energy or power storage metrics as their fitness is highly functional on the application space in which they are to be deployed. For example, though a technology may have a lower energy density or cost, it may have particularly rapid respond times and ramp rates and therefore be the best choice in an application space that prioritizes this power metric above energy cost or density. Choosing the right technology therefore requires first an intimate knowledge of the application space, the potential economic incentives for deployment, and the cost of integrating such a solution into the existing infrastructure. With this caveat in mind, it is still useful and instructive to provide updated information on the most prominent grid-scale EES technologies. Such an analysis not only provides policy makers with a general framework for comparing technologies along well-understood metrics but also doubles as a strategic tool for technologists in identifying fruitful research directions to address unmet needs.

Table 2 - Comparison of competitive technologies for use in grid applications

Type	Energy Efficiency (cycles)	Power Cost ($/kW)	Energy Cost ($/kWh)	Maturity	Embodied Energy (MJ/kg)†	ESOI †
Li-ion	90 – 94 (4,500) 94 – 99 (4,000) 85 (4,000) 85 – 95 (6,000)	1800 – 4100	900 – 1700 600	Demo	454	10
Sodium Sulfur	75 (4,500) 75 – 90 (4,000) 75 (3,000) 75 – 83 (4,700)	3200 – 4000	445 – 555 350	Commercial	488	6
ZEBRA ($Na\|\|NiCl_2$)	80 – 90 (4250)	N/A	100- 350 475	Demo	N/A	N/A
Vanadium Redox	65 – 70 (>10,000) 65 – 80 (5,000) 65 (5,000)	3000-3310	750 – 830 600	Demo	694	3
Zinc Bromide Flow	60 – 65 (>10,000) 70 (3,000)	1670 – 2015	340 – 1350 400	Demo	504	3
Lead Acid	75-90 (4,500) 50 – 75 (1,000) 75 (20,000)	2000-4600	625 – 1150 330	Demo	321	2
LMB (Li||Pb-Sb)	**75** **(5,000 – 10,000)**	**283‡**	**276‡**	**Demo**	**500 - 700**	**5 - 14**

Blue data from 2010 EPRI Report[6], Red data from 2010 Yang Report[16], Green data from various literature compiled in 2011 Sandia Report[90], Orange data from 2010 Argonne Report[91], Purple data from 2013 Hueso Review[92], **Bolded data** from Sadoway Group experiments and calculations

† Embodied Energy and Energy Stored on Investment (ESOI) data from Barnhart Work[13]

‡ Cost model upper projection including full device BOM, labor, and facilities. Excluding distribution costs.

As can be seen, LMB technologies are quite competitive when compared to the current slate of developing technologies. As will be demonstrated in the next chapter, the inexpensive materials, simple fabrication routes, and long life times all contribute to a unique cost structure that allows LMBs to move off of the conventional price trajectory. In spite of this promise, however, a major area of uncertainty that exists compared to other devices is in better understanding how the materials and fabrication play a role in the cost of the final system. Understanding these contributions will allow us to better identify meaningful research directions and push the LMB from the "Demo" state to "Deployed".

Chapter 3 – A Methodology for Research Down-selection

For most mature battery technologies, large companies have spent many years and great expense to optimize the production and operation of their devices. In order to do this they can leverage both the benefit of a production experience curve as well as a strong understanding of where the most sensitive cost levers are that hold the most promise for significantly driving down cost for the overall device. Though liquid metal batteries are exciting because of their potential to disrupt energy storage cost structure limitations, one of the greatest deficits in knowledge about this technology is an understanding of where costs come from and why. In order to identify research directions that can meaningfully improve the LMB's chance at success this thesis has developed a cost model that assists in pinpointing fruitful directions of research must first be created.

To do this, a process-based cost model has been developed to capture the most important cost buckets and functionalities in the liquid metal battery. This is the first known publicly-available cost model of a liquid metal battery and represents work that is entirely independent of those studies that may have been conducted internally at Ambri or other battery companies. As a result, the results from this model represent novel and useful advances to the battery community.

3.1 Cost Model of the Liquid Metal Battery

In order to create a process-based cost model for the LMB, let's first clarify what the finished product is meant to look like. In the case of a grid-tied device, the storage from a single LMB is far too small to create value for the scales most grid customers would operate at. Specifically, for customers working to time-shift for demand or integrate renewables studies have found that device capacities ranging from 1 kW all the way up to 100 MW would be needed

to create economic benefit for the diversity of customers in the space[93]. For common cell sizes (250 Wh) this translates to battery production ranging from 4 to 400,000 LMB cells per product. Because of this large range and potentially huge number of cells required by some customers, it is wise to construct an LMB product as modular blocks of cells to allow for easy manipulation of many cells easily and in standardized forms while also permitting a degree of customization to accommodate different end-users needs. This is, in fact, what the start-up company Ambri has decided to pursue for its own LMB design (Figure 9).

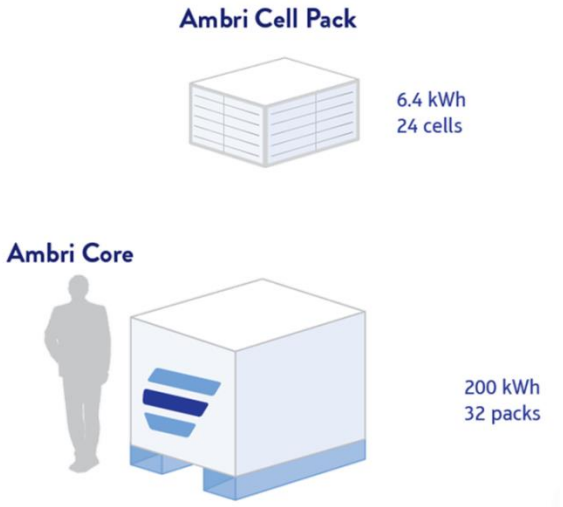

Figure 9 - Example of modular grid-storage design by Ambri

In order to model for this design choice it is important to not only capture the inputs that go into making each individual electrochemical cell but also those that drive the creation of these larger stacks of cells (packs) and stacks of packs (cores). Whereas packs and cores can form the basic unit of value for residential or small commercial customers, cores or groups of cores may constitute a more useful product for large commercial or industrial customers. To this end, a proposed process flow is given in Figure 10. Though each sub-process itself involves multiple steps, the process flow diagram is here shown at a higher level for simplicity and clarify.

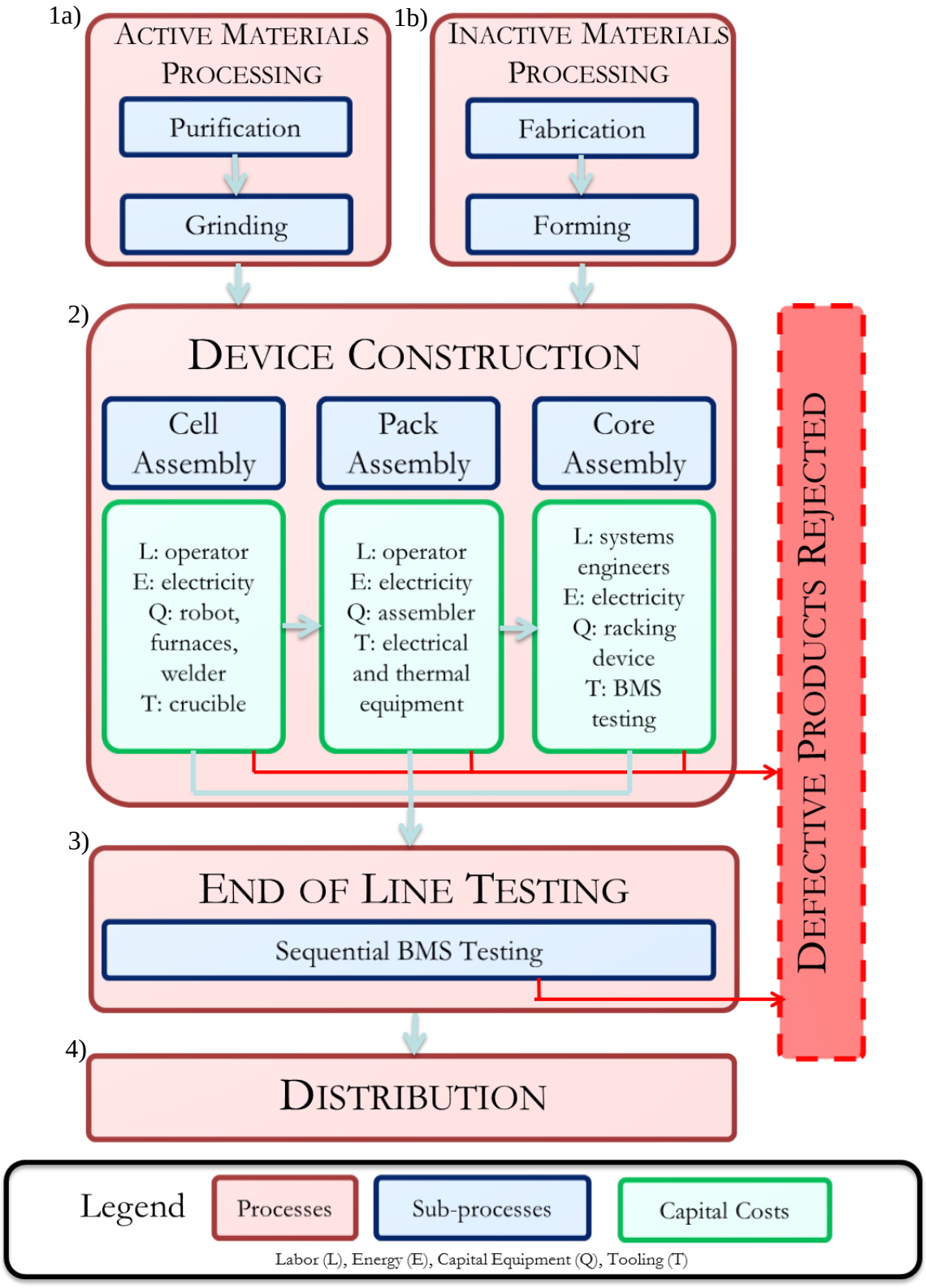

Figure 10 - High-level process flow cost model of an LMB assembly facility. Sub-processes are numbered

Before identifying the sub-processes further, we must first identify the independent variables that can be set by the user to define the specifications of the chemistry, the cell geometry, and the operational parameters. Table 3 shows the parameters that are available for input. Those shown below have been found through public documentation and private communication to best simulate the conditions expected for a commercial LMB cell[i].

Table 3 - Cost model input parameters

Model Inputs		
Active Surface Area	230	cm^2
Battery Capacity	300	Ah
Cells per pack	24	6.4 kWh
Packs per core	32	packs
Cells per core (200 kWh)	768	cells
Temperature	450	°C
Lithium Capacity	50%	
DC-DC Efficiency (System)	93.00%	
C-rate	1/5	(C*fraction)
Alloy Composition (Sb%)	40.00%	mole % M
Cost of Energy (from Grid)	0.15	$/kWh
Electrolyte Thickness	0.75	cm
Container Thickness	0.13	in
Product Life	10	years
Capital Equipment Life	10	years
Staff Wages (w/ benefits)	$20	/hr
Admin wages (w/ benefits)	$50	/hr
Total Storage Requested / year	10,000	kWh

These input parameters set certain dependent parameters and move them outside the space of user configuration. This is the result of either thermodynamic constraints or critical cell design choices. Table 4 shows these key dependent parameters.

[i] A commercial LMB cell assumes a Li-Pb/Sb chemistry. Other assumptions regarding the construction of the LMB cell can be found in Appendix 1.

Table 4 - Dependent parameters that are set once model inputs are selected.

Dependent Parameters		
Cell Volume	565.55	cm^3
Cell Height	4.92	cm
length and width (square)	15.17	cm
Current Density	260.87	mA/cm^2
Voltage	0.789	V
Round Trip Efficiency	83.01%	
Energy per cell	220.25	Wh
Current per cell	60.00	A

Finally, with the input of some other data on administrative labor and building rental costs (Appendix I) the model can be sufficiently specified to allow for calculation of the various process and sub-process costs.

The focus of this cost model will be only on the device construction process. This is because the active and inactive materials processing (process 1a and 1b, respectively) are unlikely to go on at the company, the end of line testing (process 3) for cores is unlikely to involve large sample sets so reject ratios are not available, and because the distribution process (process 4) is highly functional on the business model and catchment area of each manufacturing facility. For these reasons, these three aforementioned processes are unlikely to yield any insightful information regarding true device costs or functionalities and will therefore be ignored in this analysis.

The remaining process, device construction, is in fact made up of a large number of sub-processes and sub-sub-processes that are enumerated in Table 5 along with critical material costs, capital equipment, and labor demands. A full listing of the specific costs and sub-process level assumptions can be found in Appendix I.

Table 5 - Breakout of the Device Construction Process

	Sub-Process	Sub-Sub-Process	Materials	Equipment	Labor
Device Construction	Cell Assembly	Active material melting	Battery metals electrolyte	Furnace crucible	technician
		Active material pouring	Cell container, sheath, argon	robotic	robotic
		Cell alignment	Current collector, argon, dielectric seal	robotic	robotic
		Cell welding and brazing	Filler metal, argon	Laser welder	robotic
	Pack Assembly	Cell racking and wiring	Cell rack and high-T wire	Assembly device	technician robotic
		Insulation and thermal oversight unit	Insulation, thermal management unit	Thermal assembly desk	technician robotic
	Core Assembly	Pack racking and wiring	Pack rack, high-T wire, and bus bars	Core assembly station	technician robotic
		Insulation and thermal management system	Insulation and thermal management system	Thermal assembly desk equipment	technician robotic
		BMS system	BMS device	Core assembly station	technician
		Enclosure	Sheet metal	Bolts	technician

With these processes identified, the next step is to estimate the total average time it takes for each process to produce enough units to form a core. The cell assembly sub-process must create 768 cells, the pack assembly sub- process must take those 768 cells and bundle them into 24 cell

packs, and the core assembly sub-process must bundle 32 packs together to form a core. Different sub-processes require different types of equipment and labor and therefore result in different processing times. Of note, however, is that these three sub-processes may run in parallel and so the time it takes to produce one core, the production line time, is set by the rate-limiting step rather than the summation of all three sub-processes.

With the model inputs in Table 3 combined with reasonable estimations on individual processing times the model predicts that the cell assembly process is the rate limiting step in the device construction process flow.

Table 6 - Time to produce core-equivalent for each step

	Time Required to produce a core equivalent (days)
Cell Assembly	3.33
Pack Assembly	2.00
Core Assembly	2.08

Understanding the rate-limiting step of the production process, cell assembly, grants the ability to calculate the unit production per line per year, the number of production lines needed given a total storage request (Table 3), the maximum number of units that can be produced in a year, and the amount of staffing required for that magnitude of equipment and tooling.

Table 7 - Annual production values from Model Inputs

Production Results		
Number of Production Lines	1	lines
Total Energy Capacity	11,960	kWh
Annual Production Requested	45403	cells
Facility Production Capacity	54299	cells
Number of Cores	60	

With the model inputs from earlier we find that in order to produce 10 MWh of energy storage per year, our production facility must output around 45,000 cells per year and be sized with one line. This line has a maximum energy storage production per year of 12 MWh, or approximately 54,000 cells. The fact that the factory must be oversized by approximately 20% means that a request of 10 MWh is a sub-utilization of equipment and that production closer to 54,000 cells per year will provide for a better amortization of the facilities and CAPEX. Though the cost per unit ($/core) or total cost of energy (TCOE, $/kWh) is not yet available it is now possible to begin modeling each sub-process and its associated steps in terms of their unique contributions to the total cost of cell production. In this cost model, even the costs that are associated with pack or core production are normalized per cell in order to allow for aggregation at the end.

Taking as an example the process of manufacturing battery packs from individual cells (Table 8), the variable costs of each step in the pack assembly are estimated on a per cell basis. In this example, insulation wrapping cost per pack is functional on the dimensions of each cell, the number of cells per pack, and the temperature that the cells are to operate at. This functionality captures both the amount of insulation needed as well as the cost of insulation as thermal requirements become more demanding. This latter variable is derived by sourcing insulation pricing for various types or thicknesses of product and relating to the real operation of the cell. The cost of insulation per pack is then normalized by the number of cells in that pack to yield a cost per cell contribution. Other items in are similarly functionalized and change according to user modifications to the model inputs section (Appendix 1).

Unlike variable costs, the items relating to fixed costs are not consumed per unit production and are instead purchased on loan and amortized over the lifetime of the capital. In this way, capital equipment contributes to unit cost via the annual loan repayment being spread

over the number of units produced per year. In this case, all capital equipment is amortized annually over ten years at an interest rate of 6%.

Table 8 - Example of functionalized costs in the pack assembly process. Bolded prices represent per cell costs.

Pack Assembly Variable Costs				
Material Costs	Insulation Wrapping	Insulation Area (ft^2) per pack	9.69	
		Insulation cost per pack		*$ 11.54*
		Insulation wrapping cost per cell		**$0.48**
	Thermal Oversight Unit	Thermal Management per pack		*$100.00*
		Thermal Management per cell		**$4.17**
	Electrical Wiring	Wiring needed (ft)	1.90	
		Cost of wiring/ft as function of temp	$14.79	
		Total wiring cost per pack		$28.16
		Total wiring cost per cell		**$1.17**
	Unit Racking	Pack Racking Total Cost		*$75.00*
		Pack Racking Cost per cell		***$3.13***
	Electrical Bussing	Bus Cost		*$62.30*
		Bus Cost per cell		**$2.60**
		MATERIALS COST / Cell		**$11.54**
Energy Costs	Battery Assembly Device	Robot Energy consumption (kW)	1	
		All Robots Operational Time (hrs)	1792	
		Reboot Down robots (warmup) hrs	16	
		Total Energy consumed (kWh)	1840	
		Cost of Energy		*$276.00*
		Cost of Energy per cell		**$0.15**
		ENERGY COST / Cell		**$0.15**
Labor Costs	Pack Staffing	Labor and Overhead ($/hour)		*$30.00*
		Battery Management Workers (500 per year)	2	
		Total Hours Worked (hrs)	2880	
		Total Cost Staff		*$86,400.00*
		LABOR COST / Cell		**$1.90**
		VARIABLE COST / Cell		**$ 13.59**

Pack Assembly Fixed Costs					
Item	**Costs**	**# Needed**	**Total costs**	**Annual Cost**	**Cost/Cell**
Battery Pack Assembly Device	$100,000.00	1	$100,000.00	$13,586.80	**$0.30**
Thermal Assembly Desk Equipment	$2,500.00	1	$2,500.00	$339.67	**$0.01**
	FIXED COST / Cell			**$0.31**	

There are a couple of insights that can be derived from the pack assembly process that are, in fact, generalizable about the cost structure of the liquid metal battery. First, variable costs tend to far outweigh labor or fixed costs. This means that any reductions in the price of these inputs should have a strong impact on the total price per cell and TCOE. Further, the amortized contribution of the equipment and tooling is far less than the contribution of labor so the circumstances where labor may be substituted by automation should create savings along the production line. Finally, electrical infrastructure (wiring and busing) and thermal management make up some of the largest contributions to systems-level costs (pack and core) in the LMB. In the case of pack assembly, these two contribute 61% of the total pack assembly cost. Similarly, in core assembly, electrical and thermal components make up 54% of the total cost from that process flow.

3.2 Modeling Results and Discussion

With similar models being developed for the cell and core assembly processes, it is now possible to project total system costs and gain high-level insights into the cost structure of a liquid metal battery. The expected percentages below are those calculated using the model inputs in Table 3. The three processes are first broken out by variable vs. fixed costs.

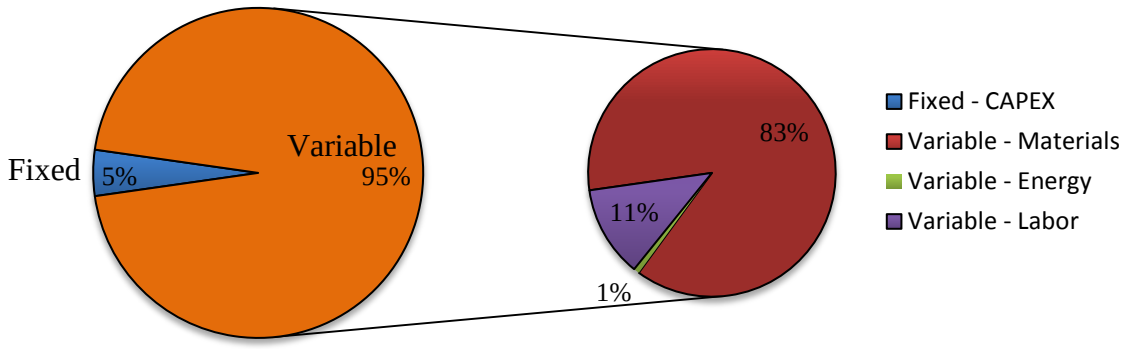

Figure 11 - Breakout of variable vs. fixed costs for LMB cell production

From this representation it is confirmed that the findings in the pack assembly process study are indeed generalizable. Specifically, fixed CAPEX-based costs only make up around 5%. For traditional Li-ion type devices, this cost makes up between 15-30% of total cost[14, 94]. This difference, earlier referred to in Section 2.2.2, is the result of simpler construction and design driving lower-cost facilities and manufacturing methods. In addition, from this presentation of the data, it is clear that battery materials make up the largest percentage cost of a device with 83% of total costs. This area will be explored in further detail shortly to highlight those areas which can be leveraged the most to impart savings to the overall device.

Another manner of viewing the high-level cost structure is to show the various bills of materials for the individual cell vs. system costs (Figure 12). System here refers to the creation of packs and cores. This provides both insights into which process is the most expensive and also provides a point of comparison against ground truth data from an Ambri public disclosure (Figure 13). From this break-out it is first clear that the LMB cost model presented here provides real intuition into the modeling of LMB production costs. Specifically, Figure 12 and Figure 13 differ in their predicted BOMs only marginally[i]. From conversations with members at Ambri, the differences are believed to derive from the degree to which this model under-predicts system-level automation. In final implementation, it is likely that a portion of the 11% labor costs in our model will be shifted over to amortizable capital equipment. These changes will occur mostly in the pack and core assembly process through automated wiring of the electrical infrastructure. Automation, to a lesser extent, may also manifest in reductions to the workers-per-production line ratios in the cell assembly process.

[i] Unlike in Figure 12 where we are able to represent the individual contributions of equipment and energy in the cell and system manufacturing process, in Figure 13 it is subsumed into the relevant slice of the BOM. This is why cell inactive materials and system electricals are much larger in the ground truth data.

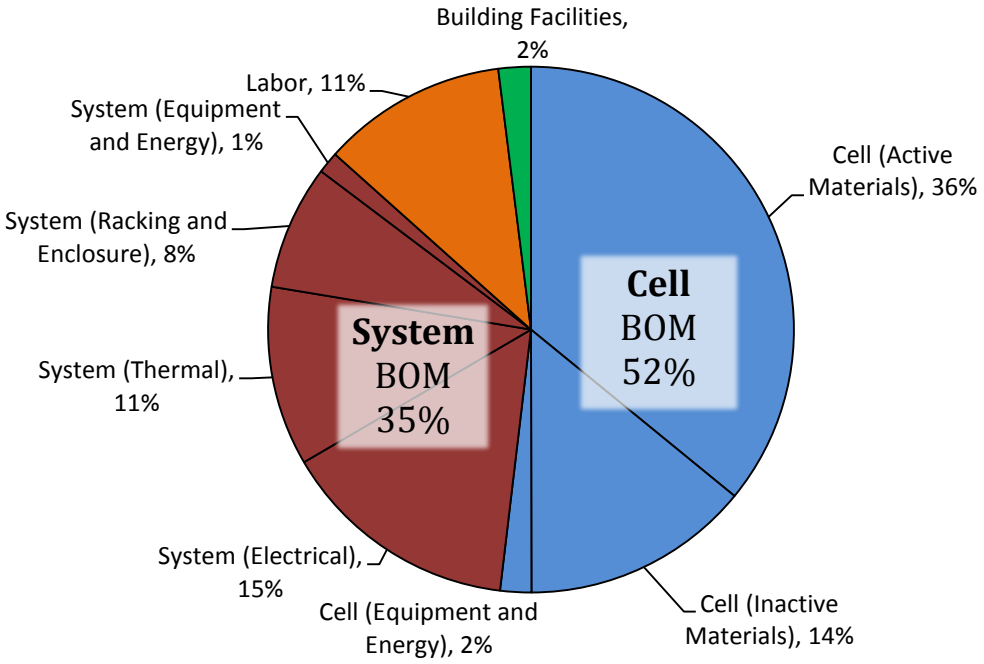

Figure 12 – Cost Model - Cell vs System Costs. Cell BOM in blue and System BOM in red.

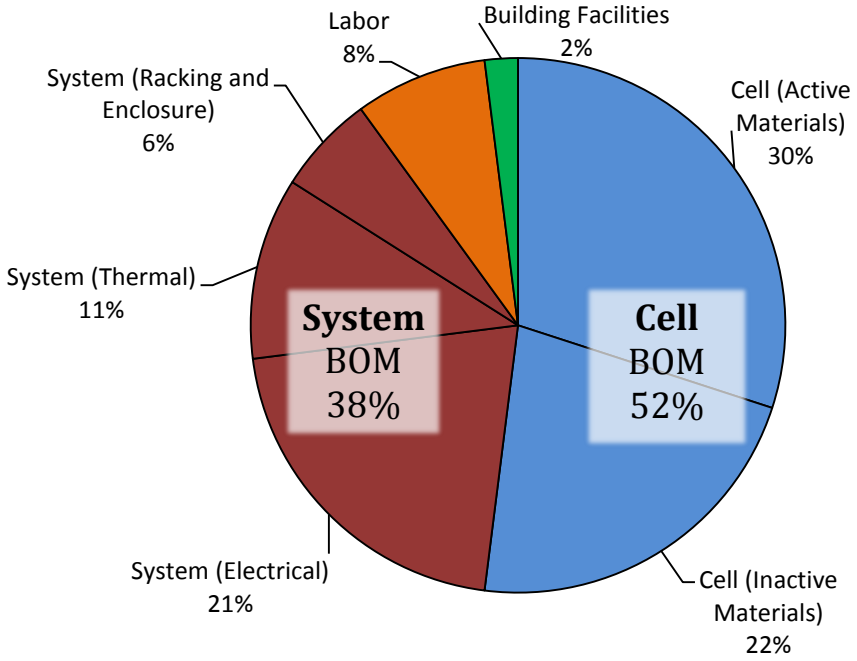

Figure 13 – Publicly released BOM from Ambri.

Having confirmed the relative accuracy of the model, it also helps to look at the absolute results of the modeling as per the model inputs in Table 3. These results provide our first look at the total cost per unit energy (TCOE) of an LMB system.

Table 9 - LMB Cost Model Results

Description		Costs/Cell (USD)
Cell BOM Subtotal		$31.54
	variable	$30.39
	fixed	$1.15
Pack BOM Subtotal		$11.99
	variable	$11.69
	fixed	$0.31
Core BOM Subtotal		$9.12
	variable	$9.05
	fixed	$0.07
Labor		$6.92
Building Costs		$1.21
TOTAL CELL COST		**$60.79**
	Total Pack Cost (24 cells)	$1,458.96
	Total Core Cost (32 packs)	$46,686.73
Energy per cell (Wh)		220.25
TOTAL COST OF ENERGY, TCOE ($/kWh)		**$276.00**

It is important to note that these numbers likely represent a cost ceiling as most of the material prices used in estimating the variable costs are sourced via large one-off orders from large online vendors that partner with MIT. It is unlikely that these prices capture the full economy of scale that a scaled battery producer could leverage with even larger order volumes and supply partnerships.

Of all the numbers in Table 9 the most important value is the TCOE value. This value provides a comparison point with other systems and serves as the value to be amortized over the lifetime of the device. For an expected 10-year lifetime with daily diurnal cycling this device

should operate usefully for approximately 7,300 cycles. Such usage results in a per cycle cost of energy of $0.04/kWh-cycle. This value is well below the retail electricity price of $0.125/kWh and opens up interesting opportunities for numerous markets including, but not limited to, renewables capacity firming and time shift, transmission congestion relief, and demand charge management[7].

With an estimated TCOE in hand and a knowledge that the three largest contributors to device cost are cell active materials (30-36%), cell inactive materials (14-22%) and core/pack electrical components (15-21%) it now makes sense to zoom in on these three processes (59-73%) to further pinpoint how they drive cost.

3.2.1 Active Cell Material Cost Contributors

Active material costs relate to the purchase of ready-to-integrate raw electrode and electrolyte materials. In the case of the Li||Pb-Sb system this corresponds to the purchase of high purity lithium, lead, and antimony metal as well as the bulk acquisition of anhydrous and high purity salt. The costs for this example are shown below.

Table 10 - Cell active materials costs. Bolded dollar values represent per cell costs.

Active Materials Costs			
	Moles of Li (moles)	11.19	
	Mass of Li (g)	77.69	
	Volume of Li (cm^3)	145.49	
	Price of Li per unit (USD)	0.43	
	Total Cost of Li		**$4.79**
	Total Moles of Pb-Sb alloy (moles)	11.19	
	Moles of Sb (moles)	4.48	
	Weight of Sb (g)	545.16	
	Moles of Pb (moles)	6.72	
	Weight of Pb (g)	1391.57	
	Total Cost of Sb and Pb		**$11.69**
	Total Cost Electrolyte		**$5.35**
	ACTIVE MATERIALS COST / UNIT		**$21.83**

This amount can be translated to an actual active materials cost of energy ($AMCOE_{operational}$) according to Equation 12.

$$AMCOE_{operational} = \left(\frac{Cost_{active\ materials}}{Capacity * V_{operational}}\right) * \eta_{DC-DC} \quad \text{Equation 12}$$

Where $V_{operational}$ accounts for the overpotential losses functional on current density and $\eta_{DC\text{-}DC}$ includes generic losses related to system-level DC-DC conversion steps. In the case of a 300 Ah Li||Pb-Sb cell, this value comes out to \$99.10/kWh. This value could also be broken out by base-level theoretical active materials cost (Equation 13) as well as inefficiencies due to the aforementioned voltage and DC-DC losses (Equation 14). Parsing these two contributions provides a better sense of each.

$$AMCOE_{theoretical} = \frac{Cost_{active\ materials}}{Capacity * E_{cell,eq}} \quad \text{Equation 13}$$

$$AMCOE_{operational} = AMCOE_{theoretical} \times \eta_{total} \quad \text{Equation 14}$$

Equation 13 predicts that of the \$99.10 $AMCOE_{operational}$, approximately \$83.25 (84%) comes from theoretical material costs, $AMCOE_{theoretical}$, while the remaining \$15.85 (16%) results from inefficiencies specific to this battery, η_{total} . Drilling down further into the $AMCOE_{theoretical}$, approximately 75% comes from the electrodes while 25% is expected to come from electrolyte salts. The electrode costs are therefore the largest contributor to active material costs (63%) and are also the most well-studied part of the device.

Though these numbers are particularly useful when evaluating this particular Li||Pb-Sb system with a LiCl-based electrolyte, they are less helpful when trying to create cost estimates for a wider array of couples. Many of these couples are still in the development stage and therefore do not have well-known electrolyte costs or properties. As a result, the best way to

avoid including this electrolyte-related uncertainty when generalizing to other systems is to create a cost metric that compares only the metallic couples and an estimate of their discharge voltage according to existing EMF studies. In fact, this estimated couple price metric, C_{est}, is widely used in the research community as a preliminary measure of the economic competitiveness of a grid storage solution.

$$C^{est} = \frac{\sum_i x_i \hat{P}_i}{x_{A,d} z F \hat{E}_{cell,lin}} \qquad \text{Equation 15}$$

Where x_i is the mole or mass fraction of component *i* in the cell, $\hat{P}_i$ is the average monthly bulk metal market price per mole of component *i*, $x_{A,d}$ represents the estimated positive electrode full-discharge composition, z is the valence of the ion in the redox reaction, F is Faraday's constant, and $\hat{E}_{cell,lin}$ is the linearized average equilibrium cell voltage over the relevant discharge range. This calculation ignores the roughly 20% electrolyte material cost impact but does account for the sloping discharge curve through the selection of an averaged voltage upon discharge.

Table 11 - Theoretical prices ($/kWh) for various battery chemistries.

	A (T^{MP}/°C)	**Li (181)**	**Na (98)**	**K (64)**	**Mg (650)**	**Ca (842)**	**Ba (727)**
B (T^{MP}/°C)	**$/mole**	**$0.444**	**$0.064**	**$5.080**	**$0.069**	**$0.140**	**$0.822**
Al (660)	**$0.056**	$62	N/A	N/A	$24	$11	$51
Si (1414)	**$0.067**	$32	N/A	N/A	$18	$11	N/A
Zn (419)	**$0.127**	$104	N/A	N/A	$23	$23	N/A
Ga (30)	**$30.875**	$2,015	$10,994	N/A	$5,766	N/A	N/A
Ge (938)	**$101.372**	$6,607	N/A	N/A	$11,128	N/A	N/A
Cd (321)	**$0.269**	$57	$103	N/A	$73	N/A	N/A
In (157)	**$66.390**	$4,750	$13,775	$20,513	$14,162	$4,959	N/A
Sn (232)	**$2.496**	$173	$285	N/A	$343	$147	$118
Sb (631)	**$1.648**	$85	$87	$324	$139	$65	$60
Hg (-39)	**$0.422**	N/A	$46	$520	N/A	N/A	N/A
Pb (327)	**$0.420**	$59	$54	$622	$97	$30	$36
Bi (271)	**$4.974**	$248	$311	$556	$575	$223	$176
Te (450)	**$27.886**	$611	$654	$689	N/A	N/A	$2,223

By applying this cost equation to the full spectrum of metal couples, it is possible to generate Table 11 to visualize estimated couple prices for potential battery chemistries. Couples lacking sufficient EMF curve data or showing immiscibility in their phase diagrams are noted as "N/A" to avoid having errors of different orders of magnitude represented in the same table. In addition, because prices for various metals fluctuate differently due to different market drivers and changing scarcity, it is also able to quantify the volatility of the estimated couple price by calculating a standard deviation of molar price over an annualized period for each component (Equation 16).

$$Volatility_{\,i} = \frac{100}{\hat{P}_i}\sqrt{\frac{\sum_j \left(p_j - \hat{P}_i\right)^2}{n-1}} \qquad \text{Equation 16}$$

This calculation provides additional insights into which battery chemistries are the most stable in cost and which are the most likely to fluctuate in time (Figure 14).

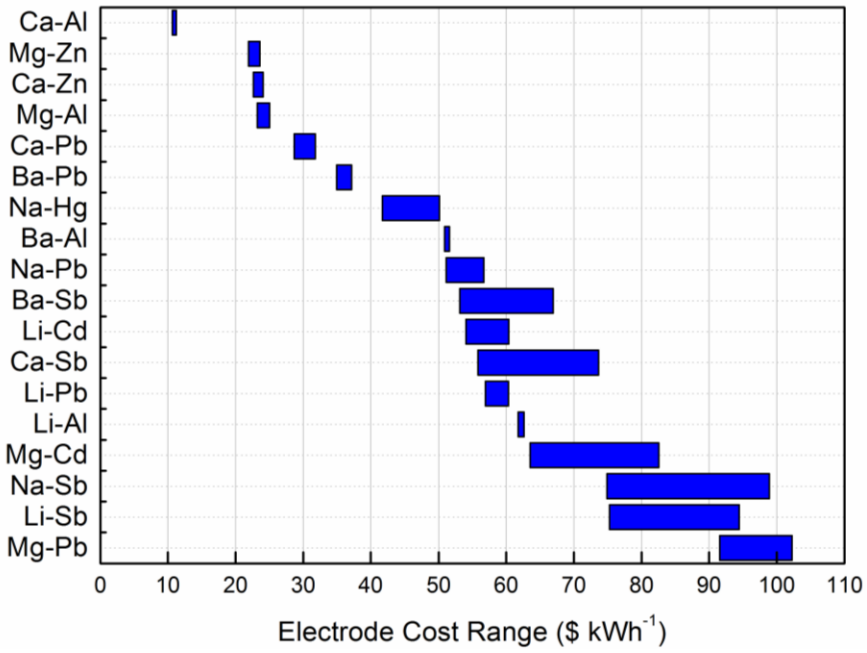

Figure 14 - Promising electrode couple costs (< $100/couple) with volatility-induced ranges

These ranges further sync with our predicted electrode cost of energy of $74.81. The fact that it is possible to dilute the more expensive antimony with less expensive lead means that the cost should sit somewhere between the theoretical range for Li||Pb and Li||Sb.

With regard to the operational loss contribution to active materials costs, the overpotentials due to charging and discharging far outweigh DC-DC inefficiencies. In addition, the $\eta_{DC\text{-}DC}$ inefficiency is set by readily available converter technologies in the industry and is unlikely to be a suitable target for innovation or improvement by a battery company. For this reason, driving down costs on the operational loss side is functional on mitigating overpotential loss mechanisms. As shown in Figure 7, the main loss mechanism during operation comes from IR-loss across the electrolyte. This loss, $\eta_{ohm,}$ is linearly dependent on current density and can be predicted via a simple Ohm's law relationship (Equation 17).

$$\eta_{ohm} = i \sum R_i \qquad \text{Equation 17}$$

$$\eta_{ohm} = iR_{ionic} = iG\rho = \frac{iG}{\sigma} \qquad \text{Equation 18}$$

Where i is the current, R_i are the various sources of resistance in the cell, G is the geometric cell constant, ρ is the resistivity of the electrolyte, and σ is the conductivity of the electrolyte. Generally speaking, the ionic resistance of the electrolyte is at least an order of magnitude larger than electrical resistances found in the wires or current collectors and as a result this equation is commonly simplified to only include electrolyte ionic resistance (Equation 18). It is clear from this relationship that, given a selected current and cell geometry, the key material parameter to consider is the conductivity of the electrolyte. By illustration, an electrolyte with a high ionic conductivity ($1x10^{-1}$ S/cm) like a molten salt will result in ten times less voltage drop than an

electrolyte of $1x10^{-2}$ S/cm as would be found in a common solid ion conductor. For this reason, electrolyte choice is another key decision in designing low-cost devices.

3.2.2 Inactive Cell Material Cost Contributors

The second largest contributor to unit cost, cell inactive materials, contains components that are required for the construction of the basic level cell but are not involved in the actual electrochemical mechanism. Table 12 presents these costs per unit cell.

Table 12 - Cell inactive materials costs. Bolded dollar values represent per cell costs.

Inactive Materials Costs			
Container			
	container area (in^2)	35.65	
	container height (in)	1.94	
	Container length/width (in)	5.98	
	container thickness (in)	0.13	
	container circumference (in)	18.77	
	Total Area of one container (in^2)	117.61	
	Total Number containers needed/year	60099.00	
	Total area for all containers (in^2)	7068321.58	
	Discount price Steel ($/in)	0.01	
	cost of container ($)		**$1.01**
Negative Current Collector			
	Copper disc or lead		**$0.52**
Insulating Seals			
	Cost of Hi-T Seal (>280°C)		**$5.00**
	Cost of Teflon O-ring seal (<280°C)		**$0.10**
Sheath			
	Graphite Sheath		**$2.00**
Argon			
	Argon Gas Flow rate (ft^3/hr)	20.00	
	Argon Gas per part (liters/unit)	1.50	
	Argon Gas per tank (liters, 1 atm)	8000	
	Cost of Argon per unit		**$0.02**
INACTIVE MATERIALS COST PER UNIT			**$8.55**

From this breakout it is clear that the two largest costs of inactive materials come from the device sealing and containment (sheaths and steel container). Because the steel and graphite

production industries are quite mature it is not expected that these prices will not change much in the foreseeable future. As a result, the most interesting price contribution comes from the cost of sealing the device.

Sealing of high-temperature electrochemical devices like LMBs requires not only hermetic protection from the environment for keeping atmospheric contaminants like O_2 and H_2O out but electrical isolation of the positive and negative leads. In selecting a seal for LMBs, there are two general categories to choose from: compressive and adhesive seals. Compressive seals are commonly found between metal parts in the form of metal fittings or compressed elastomeric gaskets and O-rings. Unfortunately, because of the need for electrical insulation, metal-based seals are not possible. Similarly, due to the high temperatures of operation of modern LMB's, elastomeric materials are generally not stable for usage either. As a result, most high temperature electrochemical devices, like the NaS and ZEBRA battery, use complex dielectric graded seals to bond metallic substances of differing thermal expansion.

A major challenge with these adhesive seal options is their cost and energy intensiveness. A study[95] on the cost breakdowns of 100 Ah NaS batteries used by the British Rail found that diffusion bond seals are the second most expensive part of the device and compose approximately 17% of the total manufacturing cost of the device. The same company, using glass-adhesive seals, achieved per unit costs of around 4% - 10% per device. These two cases define a range of between $2.00 to $12.00 per seal. Another study looking at hermetic seals for aluminum housings found that common dielectic seal options will range from $7.00 to $10.00 per unit cost[96]. These high costs are driven by high processing temperatures, surface grinding and metallizing, and slow multi-step seal grading procedures. From these numbers it is estimated that brazed seals for the LMB will optimistically come in at $5.00/seal with further development.

For a 300 Ah LMB cell with a 6’’ diameter, the ability to seal with a simpler Teflon O-ring would cost around $0.10 after bulk savings. This would represent a 50x decrease in cost from the glass- or ceramic-type seals. Enabling this type of seal, however, is dependent on the maximum operating temperature of the device. Most polymeric O-rings fail at temperatures around 200°C with the most stable fluoro-polymers surviving in sustained operation at maximum temperatures of 280°C. For this reason, the cost model chooses between $5.00 seals for LMBs operating in excess of 280°C and $0.10 polymeric seals for those below. The conclusion from this is that inactive material costs are strongly tied to the type of sealing used and therefore the temperature of operation of the device.

3.2.3 Electrical System Component Cost Contributors

Because LMB systems (cores and packs) must operate at voltages and currents greater than those achievable by an individual cell, there is a need to wire together cells and packs in series and in parallel to create a commercially valuable product. In order to do this, a great deal of electrical wiring and bussing is required to safely and efficiently facilitate these cell architectures. Because of the high C-rates (C/5) and resulting cell currents (60 A) the electrical component gauging required for the device are quite heavy-duty as compared to what would be seen in most residential or commercial applications. Specifically, 4 AWG wire or thicker would be required for cell-to-cell connections. This wire sizing becomes particularly costly because of the amount of conductor material required.

Perhaps more significantly, the fact that each cell, pack, and core will operate at elevated temperatures (>200°C) creates further demands upon the electrical equipment in terms of stable wire materials and insulation. In addition to scaling up further the AWG sizing, high temperatures also make pure copper wiring susceptible to oxidation over time. Though this is

more relevant for AC-type systems due to well-known skin effect, DC wiring at high temperatures is also susceptible to corrosion reactions, particularly if the device is meant to perform with lifetimes in excess of ten years. Table 13 summarizes the types of wiring and insulator wrapping material required for sustained operation at different temperatures.

Table 13 - Conductor and Insulator requirements for wires at elevated temperatures

Temperature (°C)	Wiring Material	Insulator (UL Style)
< 100	Native copper	Plastic/rubber
100 – 150	Sn-plated copper or native	Silicone rubber
150 – 250	Ag-plated copper	PTFE or PFA and fiberglass (TGGT)
250 – 450	Ni-plated copper	Mica Composite (MG)
450 – 550	Ni-plated copper (27%)	Specialty woven glass (fiberglass)

Because LMBs will likely all operate at temperatures above 200°C, we will assume Ni-plated copper conductors and investigate only the insulated materials TGGT, mica composite, and specialty woven glass. These different types of nickel-plated wire have quite different cost structures as the TGGT process can be completed at lower temperatures and with higher tolerances than the MG coating or glass ensconcing process. As a result, MG-type and fiberglass wires tend to be more expensive due to the processing required for reliability.

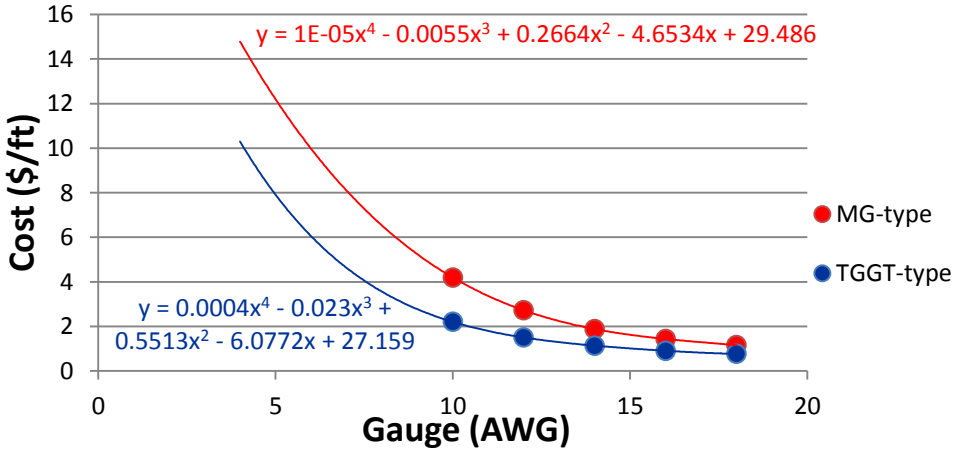

Figure 15 - Functionality of high-temperature wire cost on gauge

By plotting the costs of TGGT-type and MG-type wires vs AWG it is found that the cost per foot increases non-linearly with gauge. With this functionality it is predicted that wire costs can range from $10/ft at lower temperatures to $15/ft at high temperatures due to dielectric and insulation materials. These materials are also used in the bus construction and therefore create a similar 50% increase in cost at temperatures over 250°C.

3.2.4 Other Cost Contributors

It is important to acknowledge that there are numerous other areas where cost reduction could be achieved. For instance, the optimization of cell sizing, capacity, and active material cost could reveal a global minimum in that three-fold parametric space. Similarly, reductions in steel container thickness, electrical wiring architecture, or even vertical integration of raw material processing steps could further reduce the TCOE values per unit. That said, these important challenges more generally rely upon engineering optimization rather than materials innovation. It is therefore assumed that companies like Ambri or others will devote the necessary time to these topics regardless of the fundamental properties of the active materials in the battery. For this reason, this thesis work will not explore these optimization and business model decisions but rather focus upon the most promising cost levers which require experimental advancement to unlock.

3.2.5 Conclusions - Key Variables

Thus far we have investigated total system costs in terms of relative contributions in order to identify those processes and sub-processes that have the greatest bearing upon the TCOE. These processes were then unpacked in greater detail in an attempt to highlight the most important variables that can be meaningfully approached through lab-based research. Table 14 shows the most impactful cost levers, their associated material variable, and a potential method of dialing the variable in the correct direction to achieve savings.

Table 14 - Scientifically-approachable cost-reducing variables

Cost Lever	Variables	Pathway
Raw materials	Estimated couple price (C_{est})	Cost/Voltage screening
Operational losses	Electrolyte conductivity (σ)	High conductivity electrolyte
Inactive cell materials	Seal price (P_{seals})	Lower $T_{operation}$
Electrical components	Insulation type (MG or TGGT)	Lower $T_{operation}$

Whereas it may have been obvious before the cost modeling that developing a low-cost LMB would be directly related to the cost of the components that go in, the finding that lowering temperature can also have a large impact on the TCOE is, for the first time, identified and quantified here. Before finalizing those variables that should be targeted by an experimental plan, the last step is to get a comparative sense of the impact each of these levers has upon the TCOE.

3.2.6 Sensitivities

Before investigating the key variables further, it is first useful to get a sense of how much difference exists between the model input production capacity and that of a fully scaled plant. Figure 16 shows clearly the economies of scale accrued by moving to larger annual capacities. The larger scale allows for a better amortization of equipment, cheaper bulk prices, and improved operating procedures that allow for a reduction of the worker to machine ratio. An important takeaway from the above plot is that at our model input value of 10,000 kWh (10 MWh) the TCOE is only around 5% off of the fully-scaled value at maximum production (1 TWh). In addition, it is noteworthy that the 10 MWh production value does not occur immediately after a discontinuity in production line numbers. In these results, two production lines are not required until the production value reaches above 11,960 kWh (71 cores/year).

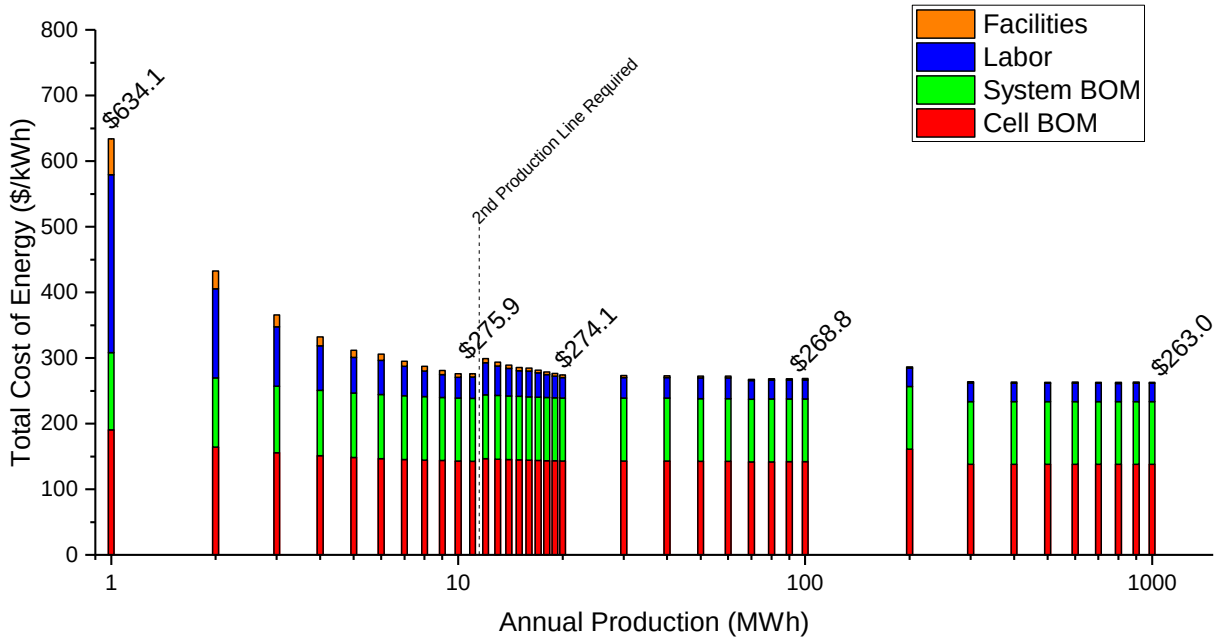

Figure 16 - Economies of Scale Curve for LMB production

This is important for our sensitivity analysis as minor perturbations to variable inputs leads to corresponding changes in production values. Were the model inputs too close to a required production line increase the differentials between the optimistic and pessimistic case could be obscured by the very large CAPEX cost incurred by having to grow factory capacity. Having noted this, it is possible to proceed to a simple sensitivity study though should remain vigilant for production line shifts.

One simple method of comparing the relative impact of the various cost levers is to investigate how sensitive the objective function, TCOE, is to variations in each of the critical variables. Variations have been chosen to represent ranges that offer a 10% estimated chance of occurring. These ranges are therefore not necessarily symmetric on input or output. For instance, it is much more likely that a company will be able to acquire pricing far preferential to that used as expected values in this cost model. Further, because certain part choices (e.g. seals) change at

specific inputs many fluctuations in prices may occur suddenly or as step functions and may not be equally distributed around the expected value model input value.

Table 15 shows the key 10% better/worse cases and shows the adjusted TCOE resulting from this modification. The variables are ranked according to the difference between their larger and smaller TCOE values, referred to here as swing. DC-DC efficiency has been included with the four aforementioned variables in order to provide a comparison point with a variable that is not well suited to an academic research effort.

Table 15 - Sensitivity results for 4 previously listed variables as well as DC-DC efficiency for comparison

	better case	Model Input	worse case	Swing
Temperature	250°C	450°C	500°C	
TCOE	$239.33	$276.00	$284.90	**$45.57**
Active Material Costs	0.7x	x	1.1x	
TCOE	$246.27	$276.00	$285.91	**$39.64**
Voltage	0.84 V	0.79	0.74 V	
TCOE	$262.22	$276.00	$295.97	**$40.64**
DC-DC Efficiency	95%	93%	90%	
TCOE	$271.13	$276.00	$288.03	**$16.91**
Conductivity	1.25x	x	0.75x	
TCOE	$270.40	$276.00	$286.20	**$15.80**

The most salient finding is that, of the four identified variables, temperature appears to have the strongest influence upon the final cost of the system. Upon careful consideration, this is not surprising considering the fact that, unlike other variables, simply suppressing the temperature of the device has the ability to create cascading savings in a number of areas. By comparison, improving something like electrolyte conductivity has only a single impact upon the total cost of the system. In this example, because electrolyte height is generally fixed due to safety considerations, increasing the conductivity of the electrolyte impacts only the overpotentials

experienced by the battery and thereby raises the discharge voltage. The impact of temperature here is likely an underestimate as a number of other ancillary costs such as corrosion mediated lifetimes, required joule heating, and thermal management unit sizing are not functionalized in this cost model. The other key insight provided here is that active materials and voltage, both variables that are coupled in practice, also have a very strong impact on the final device cost. For this reason, it is important to conduct a screening of the estimated couple price (Equation 15) during a down-selected process.

To further emphasize the relative differences between these key variables, a tornado plot is shown in Figure 17.

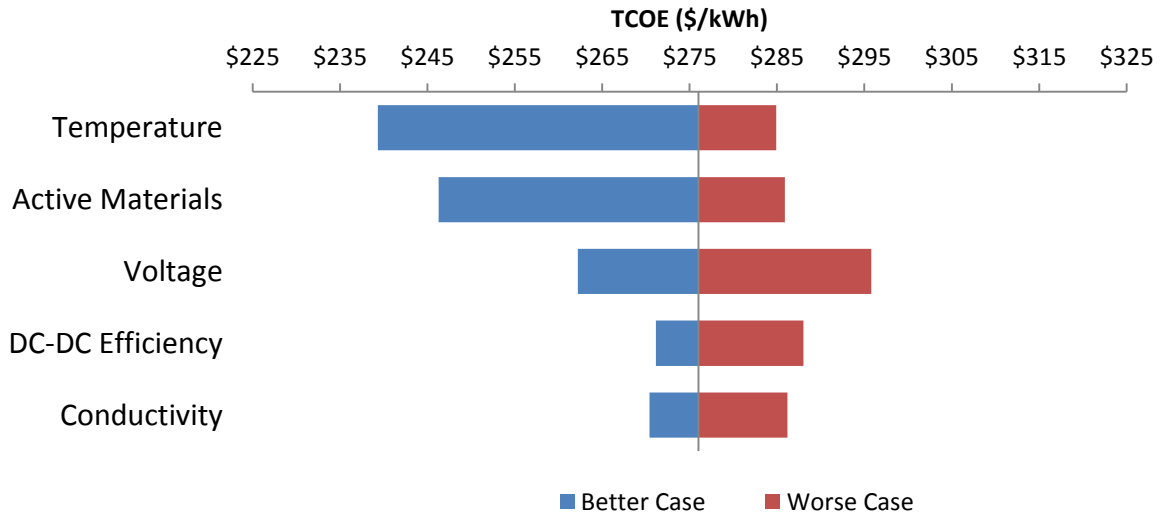

Figure 17 - Tornado plot of sensitivity of key variables

Not only does suppressing temperature create the largest reductions in TCOE, it also has the smallest down-side. This result proposes that system temperature should be one of the most actively explored system properties as the payoffs appear to outweigh the potential downsides. The asymmetric impact of DC-DC efficiency and conductivity also draws attention to the fact

that variables that might be thoughts to create direct linear impact on cost can sometimes be complicated by multiple or nonlinear dependencies.

The finding that temperature is predicted to have the largest impact on total cost of the system merits a final investigation into the functionality of TCOE on system operating temperature. Figure 18 shows the step-wise nature of this variable's dependency.

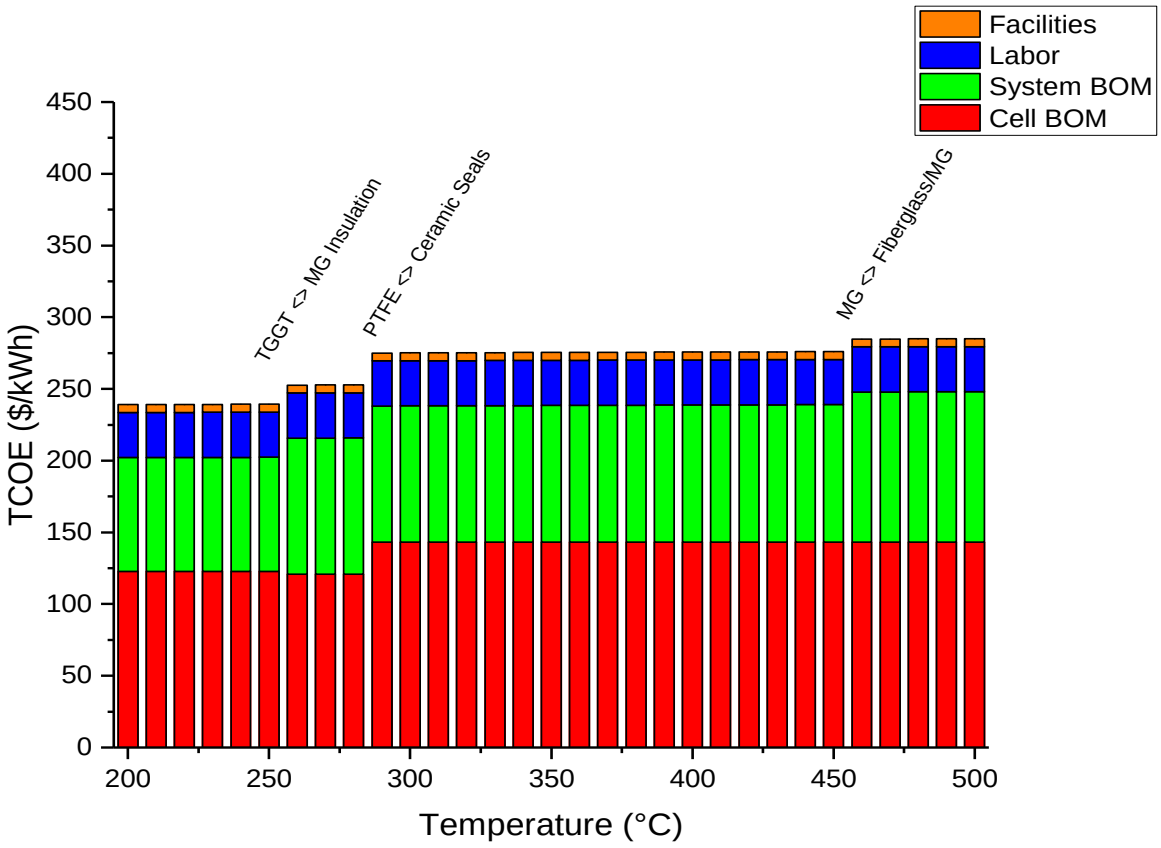

Figure 18 - TCOE as a function of system temperature

In this case, all discontinuities are relatable back to a fundamental change in either sealing options or electronic wiring insulation. Between these important transition points the TCOE remains relatively flat, though there are second and third order effects such as thermal management unit pricing that have not been captured in this model. The clear take-away from this analysis is that further temperature-driven suppression of TCOE can only be achieved if the

device is able to operate below 280°C. This temperature should therefore be considered as an important minimum target for research.

3.3 Down-Selection

Though there are a wide variety of potential LMB chemistries, developing a research plan to explore the entire space of all chemistries is far beyond the scope of a single thesis. As a result, one must deploy a systematic down-selection methodology to assist in identifying the most promising itinerant chemistry for LMB development. In order to do this, a screening on the basis of the previously identified critical variables of estimated couple price, operating temperature, and a newly introduced third metric of scalability will be performed.

3.3.1 Cost/Voltage Screening

The estimated couple price relation presented in the previous section (Equation 15) has been provided as a tool to simultaneously account for the coupled variables of cost and voltage. Because metals generally have a single prevailing market price and there exists only one thermodynamically stable EMF between one metal and another, it is not possible to select for one property without setting the other. For this reason, both must be accounted for in the same metric, C_{est}. Though this variable is not completely accurate as it utilizes the theoretical rather than operational voltage between two metals it is the most sensible representation of the maximum performance of the electrochemical couple. By revisiting the values provided in Table 11 and leveraging our new insights into LMB battery cost structure it is now possible to begin narrowing the field of research topics.

From our study of competitor systems as well as knowledge of the existing price of grid energy, bounds can be placed on material prices to help in the down-selection. First, it was shown that active materials will make up between 30-36% of the total price of the device. For

this calculation it is assumed that the prices in the above table are one third of the total cost of a full system. This multiplier moves several couples out of contention for future study. Assuming 7,300 cycles for a ten year lifetime battery with diurnal cycling, Equation 19 proposes that the estimated couple cost should come in under $304.

$$\frac{3 * (C_{est})}{Lifetime\ Cycles} \leq \$0.125 \qquad \text{Equation 19}$$

$$C_{est} \leq \$304 \qquad \text{Equation 20}$$

Couples much above this price have accordingly been removed from consideration and are denoted with orange shading in their respective box. In addition, couples with no thermodynamic information or immiscibility gaps in their phase diagrams have also been removed and are shaded with a light gray.

Table 16 - Estimated couple costs with couples significantly over $300 (orange) removed on the basis of $/kWh

	A (T^{MP}/°C)	**Li (181)**	**Na (98)**	**K (64)**	**Mg (650)**	**Ca (842)**	**Ba (727)**
B (T^{MP}/°C)	**$/mole**	**$0.444**	**$0.064**	**$5.080**	**$0.069**	**$0.140**	**$0.822**
Al (660)	**$0.056**	$62	N/A	N/A	$24	$11	$51
Si (1414)	**$0.067**	$32	N/A	N/A	$18	$11	N/A
Zn (419)	**$0.127**	$104	N/A	N/A	$23	$23	N/A
Ga (30)	**$30.875**	$2,015	$10,994	N/A	$5,766	N/A	N/A
Ge (938)	**$101.372**	$6,607	N/A	N/A	$11,128	N/A	N/A
Cd (321)	**$0.269**	$57	$103	N/A	$73	N/A	N/A
In (157)	**$66.390**	$4,750	$13,775	$20,513	$14,162	$4,959	N/A
Sn (232)	**$2.496**	$173	$285	N/A	$343	$147	$118
Sb (631)	**$1.648**	$85	$87	$324	$139	$65	$60
Hg (-39)	**$0.422**	N/A	$46	$520	N/A	N/A	N/A
Pb (327)	**$0.420**	$59	$54	$622	$97	$30	$36
Bi (271)	**$4.974**	$248	$311	$556	$575	$223	$176
Te (450)	**$27.886**	$611	$654	$689	N/A	N/A	$2,223

3.3.2 Temperature Screening

Our cost model has provided us a clear imperative for selecting electrode couples that can operate in a liquid state at or below around 280°C. This criterion will be applied strictly for negative electrode materials because this work will not consider the possibility of a co-itinerant devices. For this reason, all couples that utilize a negative electrode material that melts above 280°C are to be removed. This corresponds to the removal of Mg, Ca, and Ba. It should be noted that Mg and Ca, though attractive due to their low costs, create severe challenges when considering their vapor pressures and corrosivity at melt temperatures.

Table 17 – Estimated couple costs with couples in orange removed due to price, red due to temperature, and gray due to lack of thermodynamic data or phase separation.

	A (T^{MP}/°C)	**Li (181)**	**Na (98)**	**K (64)**	**Mg (650)**	**Ca (842)**	**Ba (727)**
B (T^{MP}/°C)	**$/mole**	**$0.444**	**$0.064**	**$5.080**	**$0.069**	**$0.140**	**$0.822**
Al (660)	**$0.056**	$62	N/A	N/A	$24	$11	$51
Si (1414)	**$0.067**	$32	N/A	N/A	$18	$11	N/A
Zn (419)	**$0.127**	$104	N/A	N/A	$23	$23	N/A
Ga (30)	**$30.875**	$2,015	$10,994	N/A	$5,766	N/A	N/A
Ge (938)	**$101.372**	$6,607	N/A	N/A	$11,128	N/A	N/A
Cd (321)	**$0.269**	$57	$103	N/A	$73	N/A	N/A
In (157)	**$66.390**	$4,750	$13,775	$20,513	$14,162	$4,959	N/A
Sn (232)	**$2.496**	$173	$285	N/A	$343	$147	$118
Sb (631)	**$1.648**	$85	$87	$324	$139	$65	$60
Hg (-39)	**$0.422**	N/A	$46	$520	N/A	N/A	N/A
Pb (327)	**$0.420**	$59	$54	$622	$97	$30	$36
Bi (271)	**$4.974**	$248	$311	$556	$575	$223	$176
Te (450)	**$27.886**	$611	$654	$689	N/A	N/A	$2,223

Though there are several positive electrode materials with temperatures above the 280°C limit, there exists a pathway for alloying such metals to form low temperature eutectics with minimal penalty to the voltage of the system[23]. As a result, with the exception of silicon, removing elements from the positive electrode rows on the basis of temperature would be premature. The result leaves us with only couples in the sodium and lithium columns remaining.

This is a sensible outcome and mirrors much of the research that has gone on historically as well as more recent developments in the Sadoway Group at MIT.

Choosing between lithium and sodium is particularly challenging given that they both demonstrate similar estimated couple prices. In order to select which itinerant metal to design a grid-storage system around, a final down-selective criteria which appears not from our cost modeling of an individual device but rather by asking important questions about how well certain chemistries might scale in global penetration scenarios will be used.

3.3.3 Scalability

For the global scenario, depending on the penetration of renewables into the electricity market and evolution of micro-grid modular infrastructures, the demand for grid storage may significantly tax both resource production as well as the energy inputs required to manufacture such storage devices. Barnhart et al.[13] project that for a conservative penetration scenario (4 to 12 hours of annual world energy demand) one could expect grid demand to range from 8.4 to 25.3 TWh. Such demands, were they to be met by modern storage technologies, could significantly perturb existing resource production to the point of needing to expand into further reserve sites in some cases (Figure 19[13]).

Figure 19 is divided into three sections: (left) ESP based on global production, (center) linear growth in ESP as a function of time, (right) ESP based on economically viable reserves and estimates for CAES and PHS appropriate geologies. A key conclusion to draw is that there are some materials, like cobalt and vanadium, that simply do not exist in large enough viable reserve quantities to supply a global grid-scale energy storage solution.

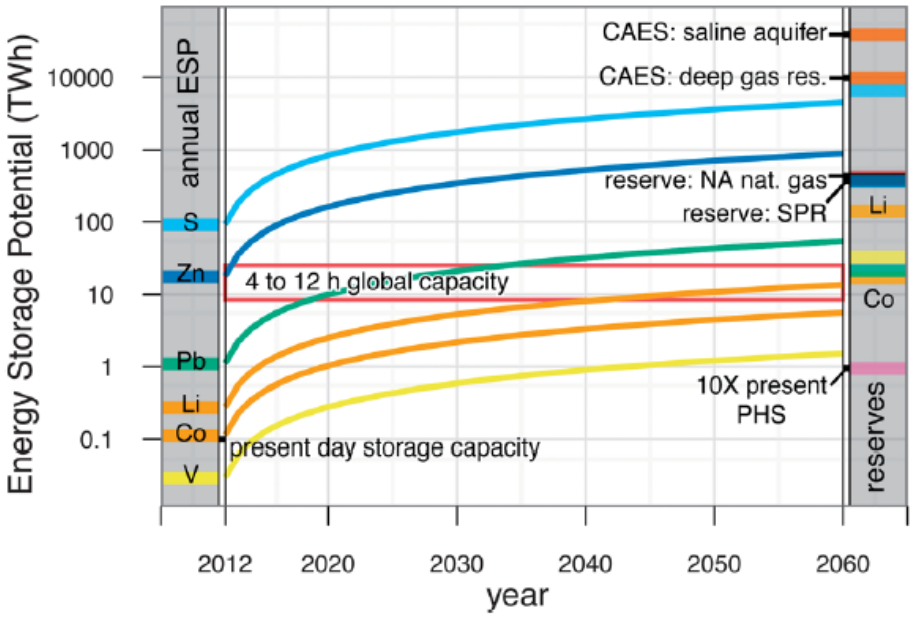

Figure 19 - The energy storage potential (ESP) for storage technologies based on material resources and appropriate geologic formations.

To give an example, Figure 19 proposes that even if all of the vanadium currently produced in the world were directed into providing storage via vanadium redox batteries (VRB), the devices built would fall short of the 4 hour global capacity mark by over two orders of magnitude. In addition, in order to produce this much vanadium-based storage, Barnhart et al. estimate that one would require a 3% increase in global primary energy production annually for the next 30 years. The take-away message is that solving global problems like grid storage necessitates a system that is material-constraint conscious, sensitive to embodied energy inputs, and flexible to changes in supply and pricing of various lithospheric resources.

A similar analytical framework has been proposed by Wadia et al[17] in which they calculated the annual ESP in TWh per year. For liquid metal batteries, the global energy storage potential is perhaps even more relevant as the energy provided by a mole of lithium or sodium is less than intercalation-type devices due to the 3 to 4 times lower voltage. By adapting this framework to the specific properties of LMB-type devices it is possible to arrive at ESPs for

various negative electrode candidates. By using the 2015 annual production of raw negative electrode materials[97], an efficiency of 95%, and a voltage value averaged over all known candidate positive electrode materials[19], one is able to develop order of magnitude estimates for how much total energy storage could be built each year if the entire production were diverted towards making LMB batteries. This extreme upper boundary defines the absolute maximum amount of storage available for a given negative electrode chemistry deployed in a LMB battery.

Table 18 - Energy storage production estimates based on annual production of elements

Element (ore source)	Approximate Ore Mass (g)	Theoretical Capacity (Ah/g_{ore})	Annual Ore Production (g/yr)	Couple Voltage (averaged)	ESP (TWh)
Ba (Barite)	233	0.230	$9.26*10^{12}$	1.28	2.59
Ca (Lime)	56.0	0.957	$3.50*10^{14}$	0.99	315
Mg (brine hydrate)	203	0.264	$7.88*10^{12}$	0.45	0.89
K (Potash)	94.2	0.285	$3.50*10^{13}$	0.78	7.33
Na (NaCl)	58.4	0.459	$2.69*10^{14}$	0.74	86.1
Li (LiCO3)	73.9	0.363	$3.60*10^{10}$	0.92	0.01

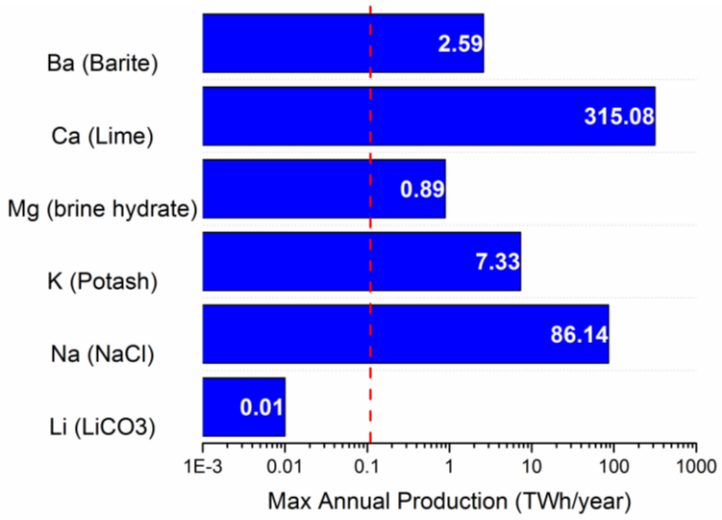

Figure 20 - Energy storage production estimates shown vs. 1% of the daily US electricity consumption

From Figure 20 one finds that even in the impossible scenario that all globally mined ore is refined to metal and dedicated to LMB production not all metals meet the short term goal of 1%

of the United States' 2009 daily electricity usage (109 MWh)[i]. Using this metric, one is able to identify a clear difference between sodium- and lithium-based chemistries. Sodium is at least two orders of magnitude above the minimum threshold with current production values while lithium falls critically short. In addition, though the lithium market is growing rapidly, so is the competition for lithium resources. In comparison, the sodium market has shown only modest year-on-year growth over the last decade[98].

Following our cost modeling and subsequent down-selection, we arrive at the conclusion that the most promising negative electrode chemistries to pursue, and therefore the best low-temperature systems for investigating candidate electrolyte systems, are sodium-based. Though this result is corroborated sodium's low cost ($0.06/mole), low melting temperature (97.8 °C), lithospheric abundance (1,150x more abundant than lithium), and strongly electropositive properties is has now been quantitatively unpacked how and why these influences make it such a good choice.

Though sodium melts far below our target temperature and it was shown that alloyed positive electrodes can achieve melting temperatures below 300°C, thus far nothing has been said regarding the availability of low-temperature sodium-itinerant electrolytes. Because an electrolyte with high conductivity and stability with metallic sodium is required, our principal set of options rests with molten salt type systems. This requirement drives forward the second half of this thesis as the identification and characterization of a low-temperature sodium electrolyte is the singular technical challenge between our current generation of liquid metal batteries and lower temperature, lower cost alternatives.

[i] This amount serves as an annual production rate target that should simultaneously allow the US to pursue its RPS goals in the short term (10-15 years) without incurring significant penalties from concurrent penetration of intermittency

Chapter 4 - A Review of Sodium-based Molten Salts

4.1 Basic Properties

A molten salt is simply a salt, or ionic compound, that exists in a liquid state either due to elevated temperature or because it has been synthesized in such a way as to allow for liquidity at standard temperatures and pressures. Molten salts are unique in that they are composed entirely of oppositely charged ions in a liquid state and interacting principally through coulombic interactions (Equation 21[99]).

$$E(r) = -\frac{NM_{AX}e^2}{r} + G(r) - \frac{C}{r^6} - \frac{D}{r^8} + \frac{Nhv_0}{2} \qquad \text{Equation 21}$$

Where M_{AX} is the Madelung constant, N is the Avogadro number, e is the charge of an electron, r is the distance between the two ions of interest, *h* is Planck's constant, and v_o is the frequency. The first term captures the electrostatic energy, the second the repulsive energy, the third and fourth multipole energy, and the last accounts for the quantum mechanical zero point energy. This form of coulombic interaction is characterized by attractions much stronger than those seen in most everyday polar and non-polar liquids (e.g. Lennard-Jones "6-12" potential) and therefore drive order over much larger ranges (Figure 21).

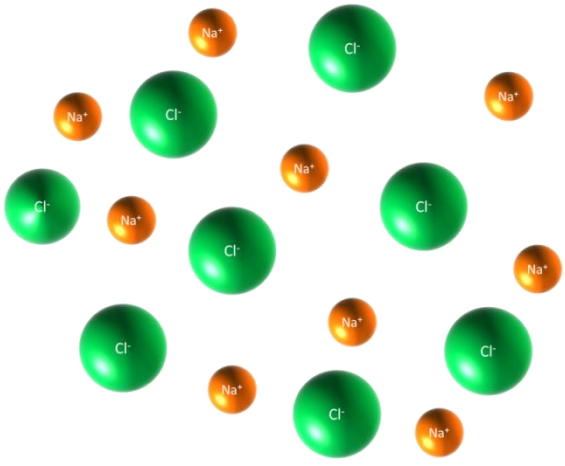

Figure 21 - Representation of a molten NaCl system showing short range ordering (SRO)

The graphic representation (Figure 21) of a simple molten NaCl system is meant to highlight the fact that, even in the molten state, the melt's structure demonstrates significant ordering beyond the nearest neighbor. In particular, cations and anions intersperse and commonly do so with coordination numbers that predominate throughout the solution. For this reason, most solution model theories of molten salts leverage lattice models to hang cations and anions from. These anion and cation "sublattices" are most often assumed to undergo random mixing of the respective cations and anions and to retain a constant number of lattice sites. As a result, molten salt solution theory and the resulting thermodynamic properties that evolve, is often validated by understanding the short- and medium-range ordering that exists in these materials in the liquid state. Such measurements are commonly carried out via x-ray and neutron diffraction.

Though a discussion of molten salt solution theory is beyond the scope of this work, numerous excellent texts exist to provide rigorous background on the field[100,101]. Important for this work is the understanding of which properties of molten salts make them particularly well suited to serve as electrolytes in electrochemical devices.

- **Electrical**
    - **High Conductivity**: Because molten salts are composed entirely of ions and exist in the liquid state they are particularly well-suited for ionic conduction due to an abundance of high mobility carriers.
    - **Low Dielectric Constant**: Molten salts also generally demonstrate low electronic conductivity which allows for electrochemical processes that require a spatial separation between the location of reduction and oxidation.

    - **Electrochemical Stability**: The simple nature of the liquid and absence of components like water that exhibit redox reactions at low voltages results in a material that can withstand high electrical potential differences

- **Thermal**
    - **Thermochemical Stability**: Due to strong coulombic forces mentioned above, molten salts have high melting and boiling points. This property allows them to be used in high-temperature processes.
    - **Low Vapor Pressure**: Strong and long-range coulombic forces between molten salts endows them with vapor pressures below those of ordinary room temperature liquids when scaled for melting temperature.
    - **Thermal Conductivity**: The semi-ordered liquid state of molten salts results in their ability to conduct heat easily. This allows for electrochemical processes that benefit from isothermal conditions.

Though these strengths are supplied as general trends, they do roughly capture the advantages of molten salts over aqueous or organic type systems accrued due to their unique structures and bonding. These properties have been observed and categorized for some time, though our focus will be on research pertaining to sodium-based systems as an exhaustive review of molten salt electrochemistry adds no value to our pursuit of a low-temperature Na-itinerant system.

Sodium-based molten salts were among some of the first to be explored and studied by chemists. This is likely due to their ubiquity as well as their importance to a number of industrial production processes. In addition to the more generalized molten salt investigations of the early 20^{th} century, historical work specifically targeting sodium-based non-aqueous electrolytes can be grouped into three rough categories: sodium metal electrowinning, nuclear energy heat transfer

media development, and electrochemical regenerative battery research. Though each of the aforementioned research areas provided significant insight into molten salt properties and characterization, they each coveted different characteristics of the sodium-based fused salts and as a result none can serve to provide a complete portrait of electrolyte possibilities for our purposes. Nevertheless, all three fields will be reviewed with transferrable knowledge for LMB systems being highlighted. In addition, attention will be paid to understanding why or how research in each of the three aforementioned areas diminished so as to address relevant concerns regarding the degree to which sodium-based molten salt systems have been explored.

4.2 Molten Salts in Sodium Electrodeposition

Since its discovery in 1807 by Sir Humphrey Davy[102], sodium metal has grown in importance and usefulness as chemists and engineers have found its unique physical, thermal, and electrochemical properties quite useful. Though initially a curiosity, following the discovery in 1825 by Hans-Christian Oersted that sodium metal could be used to reduce aluminum chloride to pure aluminum, interest in the metal rapidly grew. Initial sodium production methods utilized a thermochemical deposition similar to the initial technique deployed by Davy. Such approaches most commonly involved the reaction of a fused sodium salt with a variety of heated reducing agents including materials like carbon[103,104,105,106] , calcium carbide[104,105,107,108], iron carbide[109], iron[110], and magnesium[104]. The sodium salts most commonly reduced were those most readily available at the time: sodium carbonate[104], sodium hydroxide[111], and sodium chloride[112].

Though bulk thermochemical reductive processes like the Deville process[113] (1854) rapidly grew the demand for sodium to support early aluminum production, the process's inefficiencies and impurities drove Charles Martin Hall and Paul Héroult to simultaneously develop an alternative electrolytic processing route in 1886. This new method of aluminum

production, coupled with the yield inefficiencies and product impurities implicit in sodium-based thermochemical pathways reduced demand and price for metallic sodium and drove researchers to devise a similarly efficient and cheap electrolytic manner of producing sodium. In 1888, the Castner process[114] was born and the molten salts that were once treated as gross chemical reactants became the key electroactive component for sodium production. As an aside, it is quite interesting to note that the substantial time delay between the discovery and thermochemical extraction of sodium and aluminum (early 1800s) and the highly efficient electrolytic processes that followed (1880s) was related to the unavailability of reliable long-term current sources. It wasn't until after the invention and development of the electric dynamo by Charles Wheatstone and Werner von Siemens in the mid to late 1860s that electrolytic processes became viable means of bulk electrowinning.

The electrochemical Castner process involves the electrolysis of sodium hydroxide (NaOH) to form pure sodium on the cathode while oxygen and water is generated on the anode. The primary reactions are shown below:

Cathode: $Na^+ + e^- \rightarrow Na_{(l)}$ Equation 22

Anode: $4OH^- \rightarrow 2H_2O + O_{2(g)} + 4e^-$ Equation 23

Due to the hygroscopicity of NaOH and the solubility of metallic sodium at high temperatures (>300°C), the Castner process experiences a number of detrimental side reactions that act to reduce the efficiency of the process and lower the yield. Two are shown below.

Water at Cathode: $2Na + 2H_2O \rightarrow 2NaOH + H_2$ Equation 24

Sodium at Anode: $4Na + O_2 \rightarrow 2Na_2O$ Equation 25

In the first process, sodium metal produced at the cathode is oxidized back to its ionic state through a reaction with dissolved water. In the second process sodium metal that has dissolved and migrated across the melt reacts with produced oxygen to form a relatively insoluble sodium oxide product. These two inefficiencies resulted in an electrolytic processing route that rarely attained greater than 40% current efficiency or 20% energy efficiency[115]. Though seemingly unique to the NaOH system, these two loss mechanisms, the solubility of sodium in its molten salt electrolytes and the challenges imposed by contaminant water, are in fact principal challenges of modern sodium-based molten salts.

From 1891 until around 1920, Castner's process was responsible for a vast majority of the sodium metal produced in the United States and Europe[116]. It operated at between 4.5 to 5.0 volts, a current density of 1.5-2.0 A/cm^2, and resulted in approximately 15,000 tons kg/year (~10 kg/day per cell) for nearly 30 years. In addition to the noted inefficiencies, sodium hydroxide was still a relatively energy intensive component to produce as Chloralkali Hooker diaphragm cells had not yet been invented[117]. As a result, the Castner process fell out of favor (Figure 22)[116]

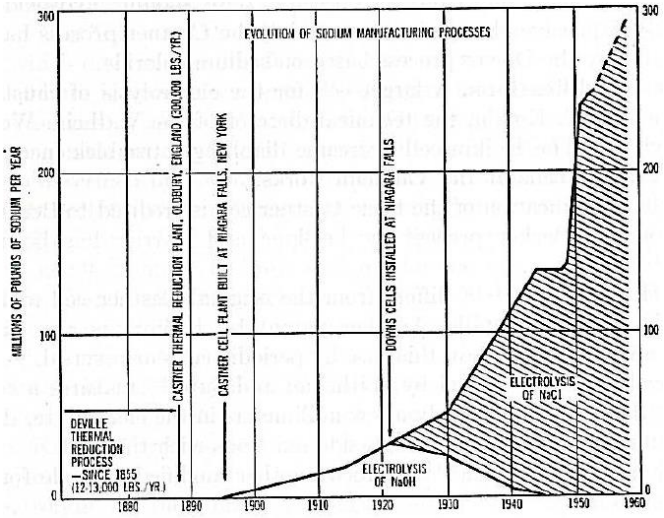

Figure 22 - Historical trends in sodium manufacturing

when compared to a newer process that utilized relatively plentiful NaCl stock as a reactant component. This new device, the Downs Cell[118], is still in use today with only minor modifications and remains the industry standard for sodium production.

It would be incorrect to say that the Downs cell was the first to use NaCl as a feed electrolyte. Rather, various configurations, including the Acker cell[119], the Ashcroft cell[120], the McNitt cell[121], the Seward Cell[122], and the Ciba cell[123], were developed based on adaptations or permutations from earlier Castner concepts. Compared to this prior art, the Downs cell leveraged two distinct advantages in its design as well as its chemistry. First, it deploys a cylindrically symmetric carbon anode and steel cathode separated by an iron screen to prevent cross-contamination of electrolysis products (Figure 23[124]).

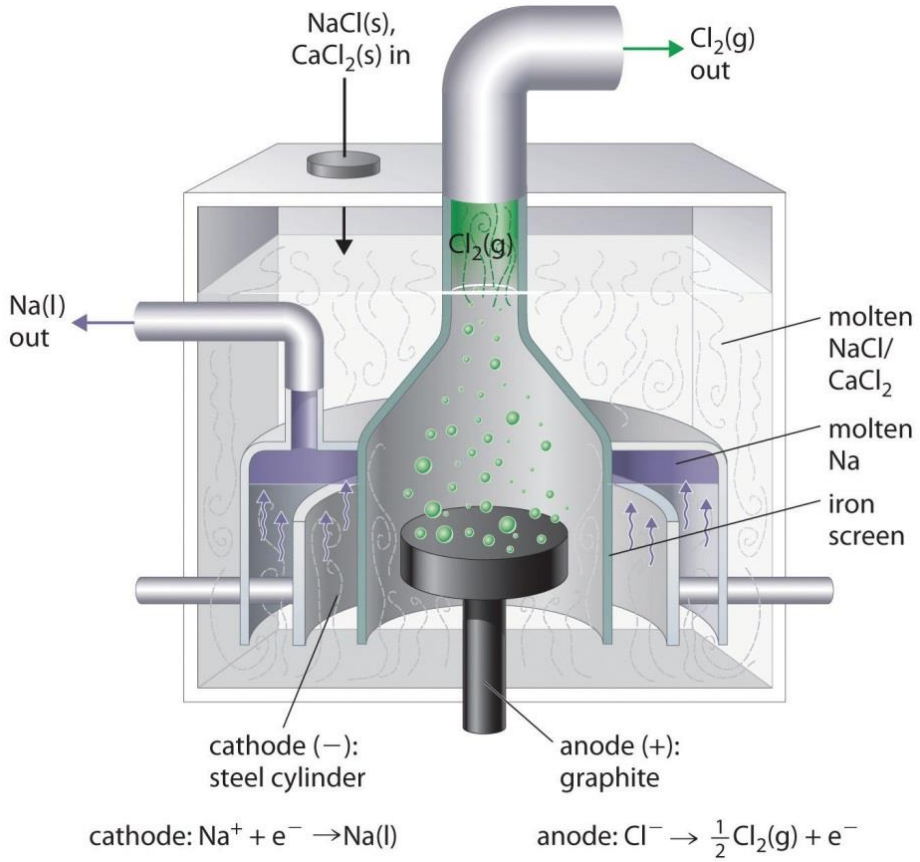

Figure 23 - Schematic representation of a Downs Cell for producing sodium metal and chlorine gas

Secondly, it obviates the traditional challenge of high NaCl melting temperatures (MP = 801°C) by using a second $CaCl_2$ (58% by weight) component to lower the overall operating temperature of the melt. Such a suppression of temperature not only reduces chlorine-based corrosion but also retards metallic sodium vaporization as well as solubility in the melt. In addition to producing higher purity sodium (>98%) the Downs cell also provides an additional benefit of generating pure chlorine gas on the anode. With these enhancements, the device operates between 590-610°C, at approximately 7 V, with current densities ranging between 0.6 to 0.9 A/cm^2 [125]. The overall current efficiency of the cell is around 80-90% with the losses coming mostly from solubility of sodium metal in the melt and its passage through the iron screen to recombine with anodic Cl_2 product[125].

Though the NaCl-$CaCl_2$ baths were used to great effect in the first half of the 20th century, as applications requiring sodium metal became more advanced, their tolerances for calcium contamination as well as product cost became more stringent and drove researchers to investigate new sodium-based electrolyte chemistries. In 1958, Wilson Cathcart investigated and patented[126] the replacement of calcium-based chlorides with more electropositive strontium and barium chlorides to reduce sodium metal impurities from 1% to 25 ppm. He also experimented with further additives like sodium fluoride to increase the conductivity of the melt and improve the energy efficiency. Four years later, William Loftus, also working for du Pont, patented[127] work on a process utilizing barium-heavy salts that operated at 610°C with an efficiency of 89%.

In addition to the development of the Downs process development, electrometallurgists occasionally resurrected older technologies with new approaches in hopes of finding a pathway towards cheaper and lower temperature sodium production. A 1939 patent by Gilbert[128] that improved the one-pot sodium hydroxide Castner cell by decoupling the reaction into two vessels

in order to enable the usage of aqueous electrolytes rather than molten salts was built upon by two major patented works by Yoshizawa[129] in 1966 and Heredy[130] in 1969. The former author's work explored options with several novel ternary systems employing NaOH, NaCN, NaBr, and NaI. Such electrolytes (Figure 24[129]), previously unattainable in the dehydrated state, expanded the number of sodium salt permutations available for electrolytes to work with. Similarly, Heredy's work introduced $NaNH_2$ as a polyanionic chemistry with the ability to substantially reduce molten salt melting points.

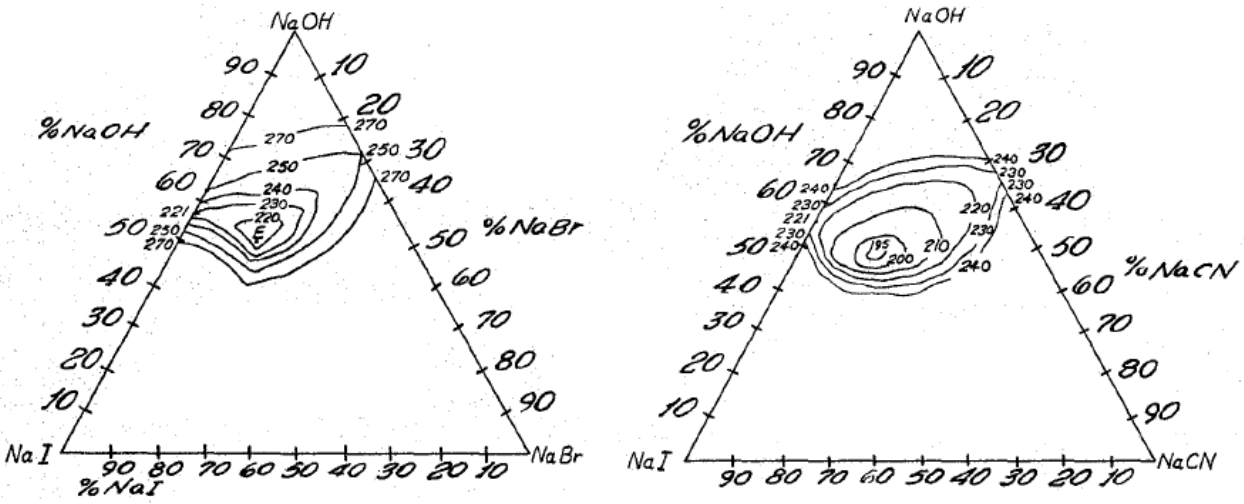

Figure 24 - Experimental phase diagrams of NaI-NaOH-NaBr and NaI-NaOH-NaCN ternary phase diagrams

The development of cheaper and lower temperature sodium production accommodated significant growth over the next several decades. The two principal research paths that benefitted from the ample supply of sodium and advanced our understanding of sodium-based salts were the post-war molten salt reactor industry in the 1950s and the early molten-salt based energy storage devices that were developed in the 1960s to harvest waste heat from the rapidly growing portfolio of nuclear power plants. These two research paths produced vast physical, thermal, chemical, and electrochemical foundational knowledge that aid our understanding today.

4.3 Molten Salts during Nuclearization

4.3.1 Properties

Though it had long been recognized that sodium had many suitable properties to serve as a heat transfer media, it wasn't until the growth and subsequent demand of the nuclear age with its molten salt and molten metal breeder reactors (Figure 25[131]) that production and research into sodium and sodium salts achieved international preeminence and support.

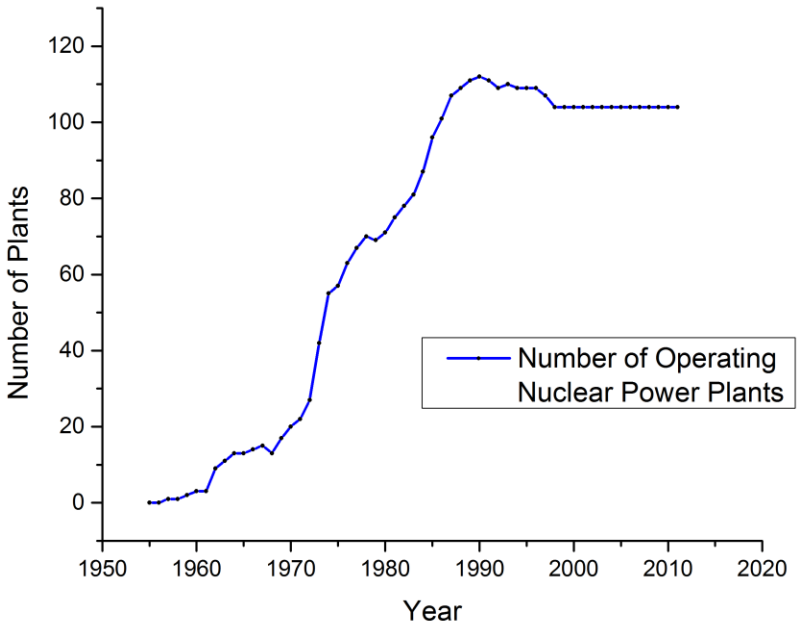

Figure 25 - Number of operable nuclear power plants in the United States since 1950

Whereas much of the earlier sodium electrolysis research was conducted by private companies like DuPont and patented to secure intellectual property rights, the molten salt and sodium research of the 1950s and 1960s was funded by tax-payer dollars and can therefore be found more prominently in the peer-reviewed literature. Various government agencies and labs, including the Atomic Energy Commission, National Bureau of Standards, Argonne National Lab, and Oak Ridge National Lab collaborated closely with private companies such as General

Electric, Atomics International, and North American Rockwell to produce a sizable collection of literature covering thermodynamic properties, kinetic models, and corrosion measurements. Working concurrently, and driven by cold war competition, Soviet chemists developed a sizable tomb of molten salt research, much of which is still inaccessible and untranslated.

The reader is directed to a number of excellent works on molten salt properties[101, 125], the structure and modeling of molten salts[132, 133], corrosion in molten salt systems[134, 135], and transport properties[136]. Of interest here are those works that present either physical property data for sodium-based systems or address solubility/corrosion phenomena with sodium salts. Fortunately, beginning in 1968 the U.S. National Bureau of Standards, under the Secretary of Commerce, contracted an aggregation of all known molten salt work up to that point. Much of what is presented below[137](Table 19, Figure 26) has been aggregated by Janz and colleagues in their comprehensive publications (Table 20) with only minor supplements from work scattered throughout the subsequent years.

Table 19 - Melting Temperatures, Conductivities, and Viscosities of common sodium-based salts.

Salt[ref]	T_{MP} (K)	Conductivity, k (S/cm)	Density (g/cm^3)	Viscosity (cp)
NaF[138, 139]	1253	$1.46 + 2.73x10^{-3}$ T	$2.65 - .54x10^{-3}$ T	
NaCl[140,141]	1073	$-2.49 + (8.04x10^{-3}$ T – $2.22E^{-6}$ T^2	$2.13 - .54x10^{-3}$ T	$81.90 - .18$ T + $1.42 x10^{-3}$ T^2
NaBr[142]	1023	$9.09 e^{-2324/RT}$	$3.17 - .81x10^{-3}$ T	$64.32 - .15$ T $+1.23 x10^{-4}$ T^2
NaI[143]	935	$-2.89 + 7.58x10^{-3}$ T - $2.23x10^{-3}$ T^2	$3.62 - .94x10^{-3}$ T	$7.17x10^{-2}$ $e^{5673/RT}$
Na_2CO_3[144, 145]	1127	$13.75 e^{-1327/RT}$	$2.47 - .44x10^{-3}$ T	$3.8x10^{-5}$ $e^{26260/RT}$
$NaNO_2$[146, 147]	558	$13.2 e^{-2600/RT}$	$2.22 - .74x10^{-3}$ T	$187.11 - .87$ T + $1.41x10^{-3}$ T^2
$NaNO_3$[148, 149]	583	$-1.57 + 4.38 x10^{-3}$ T	$2.32 - .71x10^{-3}$ T	$10.41x10^{-2}$ $e^{3886/RT}$
Na_2SO_4[150, 151]	1157	$11.89 e^{-3819.9/RT}$	$2.62 - 4.83x10^{-3}$ T	
Na_2MoO_4[152]	960	$-3.17 + 5.24 x10^{-3}$ T	$3.40 - .62x10^{-3}$ T	
Na_2WO_4[152]	971	$7.45 e^{-3931/RT}$	$4.62 - .79x10^{-3}$ T	
NaSCN[153]	583	$43 e^{-4740/RT}$	$526.39 - 2.49$ T + $3.96 x10^{-3}$ T	
NaOH[154]	591	$-3.23 + 9x10^{-3}$	$2.06 - .47x10^{-3}$ T	$164.77 - .61$ T + $7.80x10^{-4}$ T^2

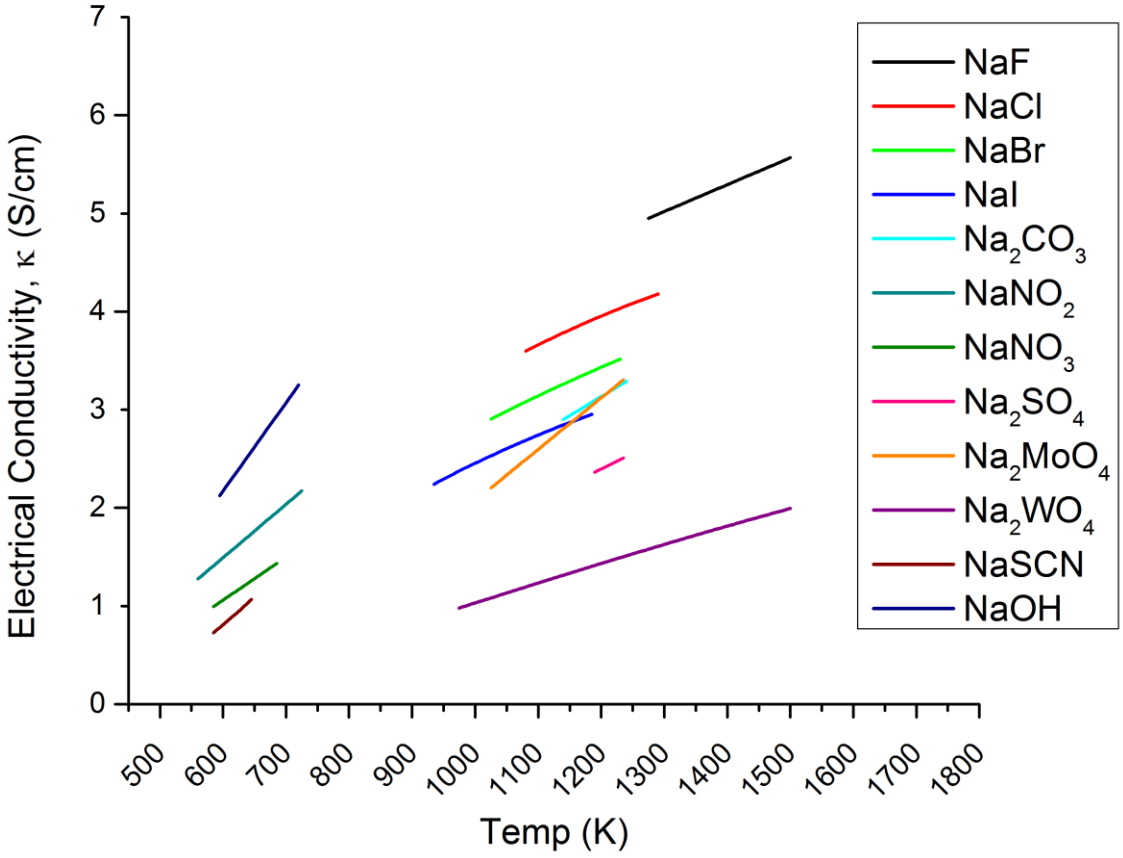

Figure 26 - Plot of conductivity vs. temperature for various pure molten salts

Table 20 - Listing of all U.S. Bureau of Standards Molten Salt Studies conducted under Janz.

Volume (Part)	Year	Description
1	1968	Single Salts - conductivity, viscosity, density
2	1969	Single Salts - surface tension
3	1972	Binary Mixtures - nitrates and nitrites
4 (1)	1974	Binary Mixtures - fluorides
4 (2)	1976	Binary Mixtures - Chlorides
4 (3)	1977	Binary Mixtures - bromides and iodides
4 (4)	1979	Binary Mixtures - mixed halides
5 (1)	1980	Binary mixtures - mixed anions other than nitrates, nitrites, and halides
5 (2)	1983	Additional Systems

Considering the ten basic sodium salts (excluding Na_2MoO_4 and Na_2WO_4 due to rarity), there are 45 possible binary combinations and 120 possible ternary combinations. Within each combination there exists an infinite gradiency of compositional variation though there will generally be one, or a continuous range centered on one, composition that corresponds to a lowest eutectic temperature and therefore optimal performance for a battery electrolyte. Although sodium unary systems have been deeply studied, many binary and ternary systems have been nearly entirely uncharacterized. This is in contrast to lithium binary and ternary systems that have been exhaustively researched[155] due to their potential application in metal sulfide thermal batteries[156] to be discussed later.

4.3.2 Corrosion

In addition to molten salt unary and binary mixture properties being studied and collated over the 1950s and 1960s, the use of molten salts at elevated temperatures as a heat transfer media instigated work in sodium and sodium-salt based corrosion processes[100]. For the purposes of LMBs, corrosion can occur through two different processes: either through a chemical reaction between two components or a solubility of one component in the other. More explicitly, in an LMB, the following processes are worth considering when mitigating the effects of corrosion:

I. Corrosion of the metal container by the liquid molten salt via chemical reaction
II. Corrosion of the metal container by the liquid metal anode or cathode via solubility
III. Corrosion of the electrodes by the liquid molten salt via chemical reaction
IV. Corrosion of the positive or negative electrode by the liquid molten salt via solubility

Processes I and II have been variously explored in the literature as they most closely mirror those issues faced by nuclear breeder reactors and thus were the topic inquiry for many years[157].

Though the selection of appropriate container materials for a given system is by no means a trivial task, the exploration and identification of such materials should only be considered following an initial investigation into sodium-based chemistries. In addition, several common candidate container materials like nickel and stainless steel have shown preliminary signs of compatibility with liquid sodium[158, 159] and molten sodium salts[160]. Thus, the investigation of corrosion processes I and II will not be addressed in this work.

In contrast to corrosion of the structural components in processes I and II, processes III and IV are less studied and have more to do with the selection of active components in the battery. Process III can be subdivided into corrosion of the positive and negative electrodes, with the negative (sodium) electrode frequently being trivial as the simplest molten salts provide no potential chemical pathways for corrosion outside of those afforded by impurities such as water. Some of the salts with larger anionic species do have the tendency to react with pure or high activity alkali metals such as the sodium nitrate in contact with sodium metal (Figure 27[161]).

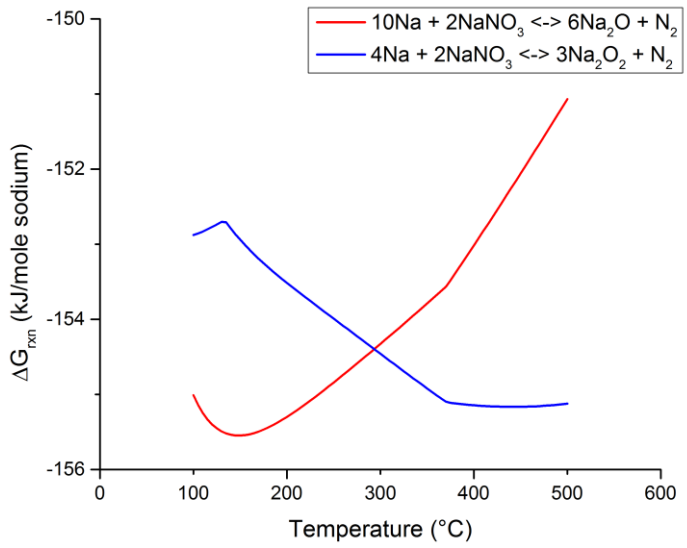

Figure 27 - Theoretical thermodynamic free energies of reaction for two potential nitrate reaction pathways vs. temperature

As a result, developing a molten salt that is chemically stable with sodium metal requires purification and drying processes for simpler salts and thermodynamic calculations coupled with experimental data for more complex salts. On the other side of the battery, the reaction of sodium-based molten salts with the positive electrode is, with a few notable exceptions including NaCl, $NaNO_3$, and NaOH, underexplored. The development of suitable sodium molten salts therefore impacts the set of possible cathode materials (or vice versa).

Corrosion process IV, the solubility of molten metallic species into molten salts, is of unique concern for sodium-based chemistries. Though it is uncommon for a metal to dissolve in its metallic state into a melt of ionic species, it has been numerously documented that sodium is highly soluble in sodium-based melts, particularly at higher temperatures in halide solutions. Bredig first measured and described[162] this phenomena through careful mixing, separation, and titration of sodium-sodium halide melts and found that the halide salt and metal species were mutually soluble in each other and demonstrated increased solubility at higher temperatures. Bredig and his associates later went on to use a modified thermal analysis technique[163], similar to modern DSC, to detect minor inflections in heat absorption/emission resulting from phase separation at the edge of the miscibility gap. This technique was able to make measurements at higher temperatures with greater accuracy and was applied[164] to sodium-based melts to determine a compositionally complete phase diagram (Figure 28[164]) for sodium in equilibrium with its various halide salts.

Far from being a scientific curiosity, metal solubilization results in a variety drawbacks for electrochemical processes. Early electrochemical winning of sodium using NaCl was principally held back by the efficiency losses resulting from the sodium “fogs” that indicated product loss and parasitic back-reactions. Similarly, in LMB setups, the dissolution of sodium

metal not only causes capacity fade due to loss of the negative electrode but it also results in reduced round-trip efficiency as the solubilized sodium can transport to the cathode and alloy without creating usable energy. In addition, sodium solubility also worsens fade rate as the solubilized sodium increases the electronic component of conductivity[165] and enhances electronic conduction at non-faradaic voltages.

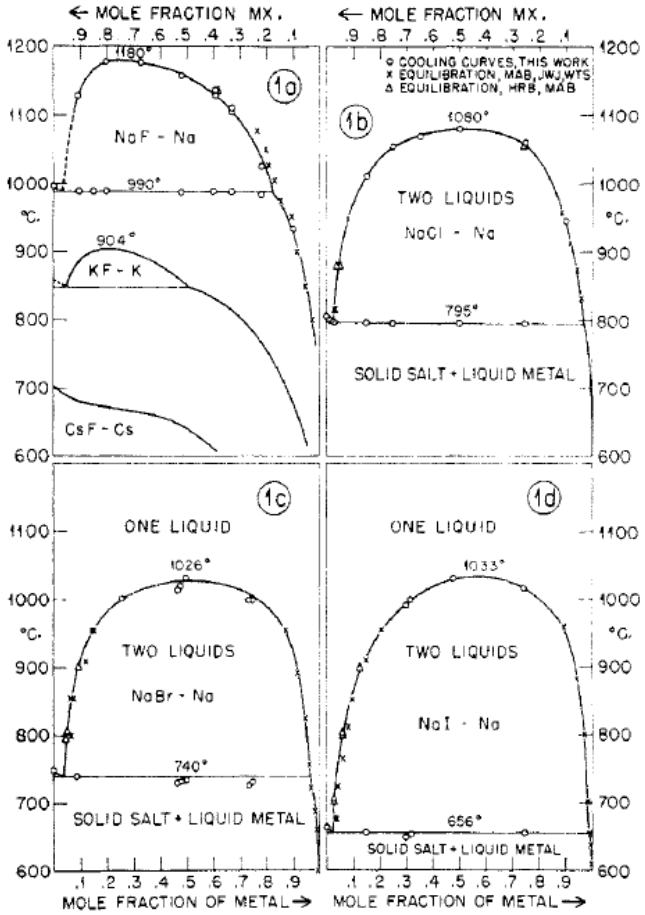

Figure 28 - Sodium metal solubility in NaF, NaCl, NaBr, and NaI, clockwise from top left, as demonstrated with liquid coexistence curves.

Although most work on sodium solubility in molten salts has been conducted on halide systems, literature investigating the deposition of sodium metal from non-halide melts often shows signs of sodium solubility. In a 2003 work investigating hydroxide melts as electrolytes[166], sodium deposition peaks are repeatedly shown without corresponding stripping peaks in a CV

scan (Figure 29[166]). Nevertheless, explicit studies of sodium solubility in non-halide sodium salts or binary halide melts have not yet been conducted. New investigations of alternative sodium itinerant electrolytes must not only be aware of this detrimental tendency but will also need to consider means of mitigating this phenomenon.

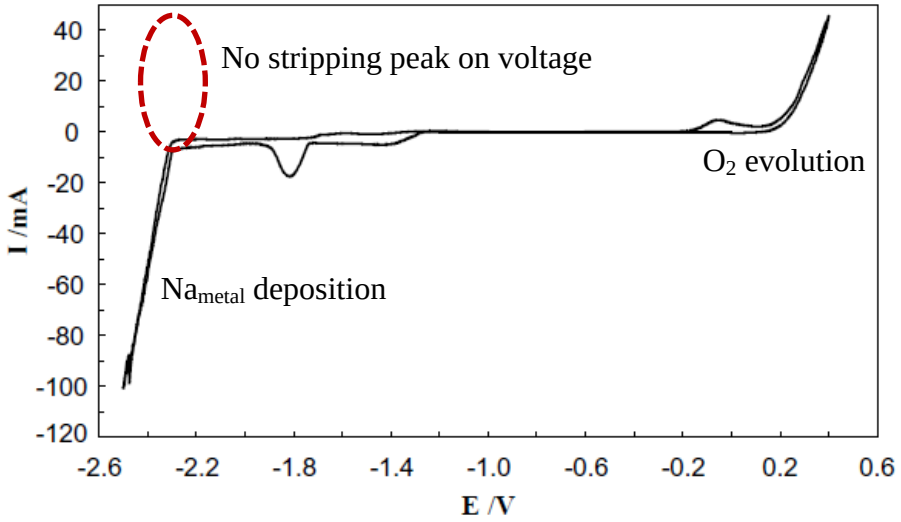

Figure 29 - Cyclic voltammetric study at 100 mV/s with a platinum electrode in molten LiOH-NaOH at 270°C

Current miscibility mitigation strategies[167] include (i) the use of mixtures of molten salts to decrease sodium metal activity and therefore solubility, (ii) the operation of the device at lower temperatures; and (iii) further separation of the anode and cathode compartments to reduce the concentration of sodium metal at the cathode. Determining the effect of polyanionic salt components as well as the suppression of temperatures below 300°C on solubility would be a novel contribution to the literature.

4.4 Molten Salts in Energy Storage Devices

Following the rapid growth of nuclear power and concurrent advances in the synthesis and characterization of molten salts, researchers began to turn their acquired skills towards a new problem; namely, that power plants and reactors generated significant quantities of waste heat

and there existed opportunity to harvest this thermal energy for useful purposes. In 1958 Yeager[168] proposed the concept of a "thermally regenerative closed cycle battery" that would convert waste heat into chemically stored energy by selectively separating a binary alloy, AB, into its two constituent metals by exploiting large differentials in vapor pressure between liquid metal A and B. Through this process it would vaporize metal A to recharge a three layer galvanic cell (Figure 30[169])

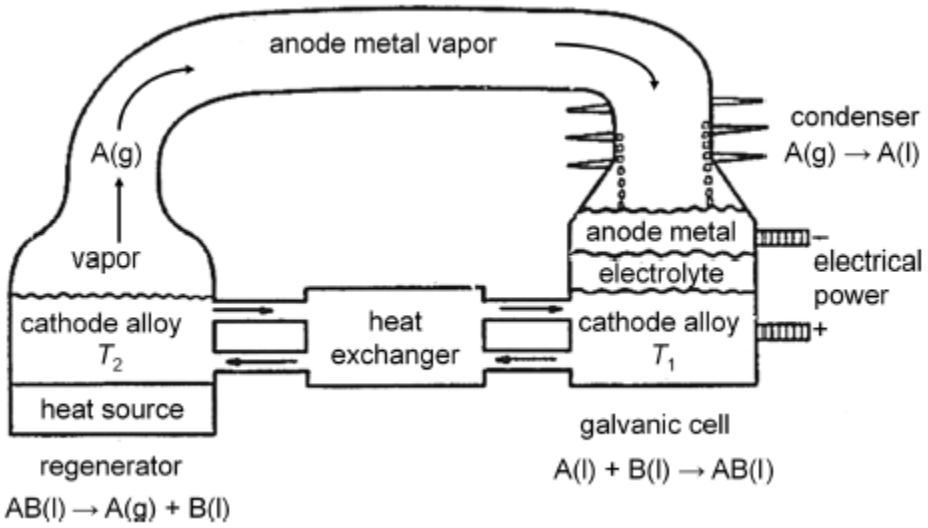

Figure 30 - Diagram of a thermally-regenerative type battery.

Though this device acts similarly to the LMB upon discharge, it is important to note that it is ultimately limited by the Carnot efficiency during discharging and that its temperature is set by the harvesting of waste heat from reactors at predetermined operating temperatures. Despite these constraints, research into thermal-type batteries exploded in the 1960s with Agruss filing for the first patent on thermally regenerative cells[170] and shortly thereafter publishing work[169] on Na-Sn systems that operated around 700°C with NaCl-NaI electrolytes. Work on similar systems (Table 21[171]) grew under Atomics International, General Motors, and Argonne National Labs (ANL) until such a point as systems that were fully electrically rechargeable were developed. These secondary bimetallic cells operated similarly to modern LMBs with minor geometric

exceptions. Of particular note was the achievement of over 12,240 hours of continuous cycling of a Na|NaF-NaCl-NaI|Bi cell discharged at massive current densities (> 5.0 A/cm^2) with no noticeable degradation in performance[172].

Over the next decade, secondary bimetallic battery work split into two major thrusts. The first, the Li-Te[173] cell, marked a shift in the research direction of the secondary bimetallic cells towards high voltage liquid metal cells for demanding vehicular applications. Though tellurium showed promise, its cost drove researchers towards more abundant selenium[174]. After difficulty was encountered with selenium's solubility and conductivity, work continued up the chalcogenide family until focus landed on Li-S systems[175]. These systems eventually evolved into the Li-Al||Fe_xS that eventually found commercial production and Li||air-type systems[176].

Table 21 – Historic thermal battery studies for thermally regenerative as well as secondary bimetallic devices.

	THERMALLY REGENERATIVE			
	Na-Sn[177]	**K-Hg[177]**	**Na-Hg[178-180]**	**Na-Pb[172]**
Temperature (°C)	625-650	325	490	575
Electrolyte	NaCl-NaI	KOH-KBr-KI	Na Halides	NaF-NaCl-NaI
OCV (V)	0.33-0.43	0.70-0.84	0.30-0.80	0.30-0.50
Current Density (A/cm^2)	N/A	N/A	N/A	0.11
Duration (hrs)	0.3	430	1200	45
	SECONDARY BIMETALLIC			
	Na-Sn[177]	**K-Hg[177]**	**Na-Bi[172]**	**Li-Te[82, 172]**
Temperature (°C)	700	325	580	480
Electrolyte	NaCl-NaI	KOH-KBr-KI	NaF-NaCl-NaI	LiF-LiCl-LiI
OCV (V)	0.33-0.43	0.70-0.84	0.55-0.75	1.7-1.8
Current Density (A/cm^2)	N/A	0.087	0.667	2.0
Duration (hrs)	744	N/A	12240	> 300

The other resultant research path from the early bimetallic work focused on the long-lifetime Na-Bi systems. In spite of their unprecedented performance, a major drawback of these devices related to their inability to be used in motive applications due to their fully liquid interiors. This need inspired further work and development of new solid electrolytes, nearly

simultaneously at Ford Motor Company (β-Al_2O_3) and at Dow Chemical Company (glass electrolyte). Both of these advancements unlocked the usage of Na-based systems for usage in non-stationary applications though necessitated that the devices operate above 300°C. By the 1980s β”-Al_2O_3 work came to dominate the field of Na-based batteries (Figure 31[181]).

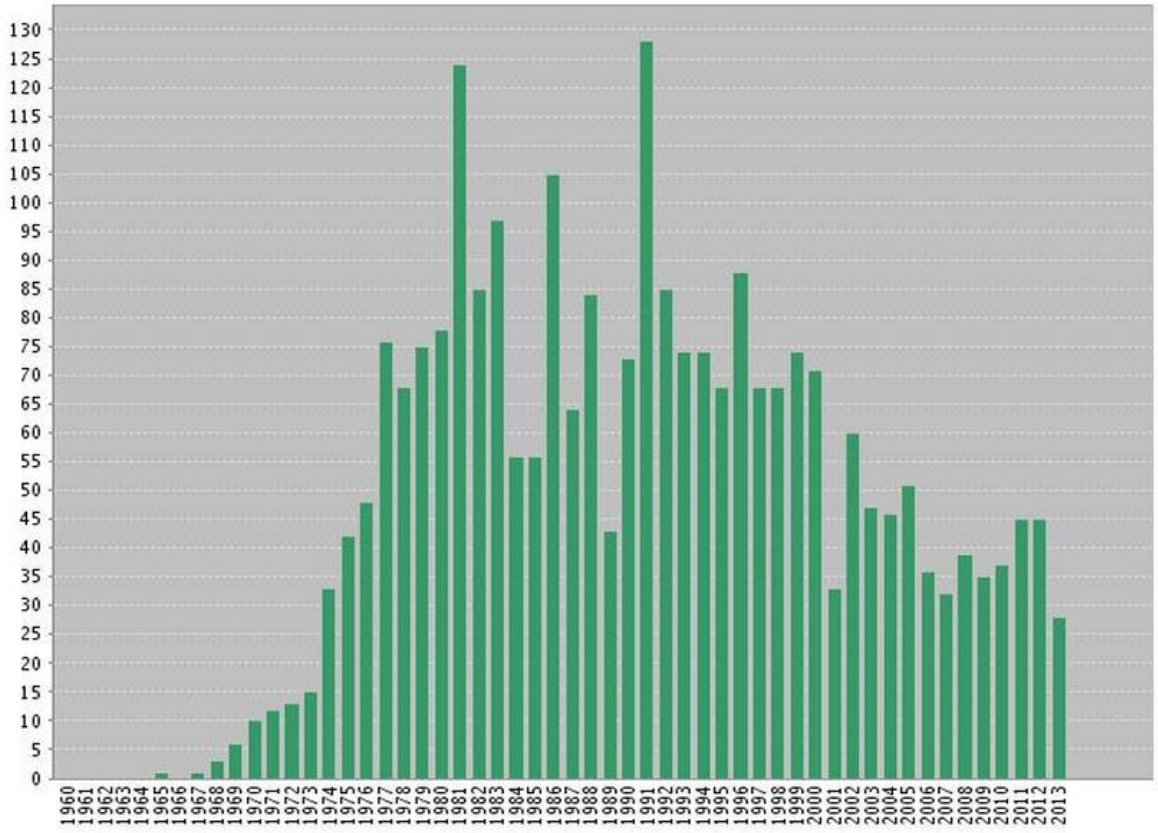

Figure 31 - Research papers published that focused on application of Beta-alumina electrolytes for energy uses.

This preoccupation with batteries for vehicles is unsurprising considering the incredibly cheap cost of grid power from coal and the volatile motions of the petroleum industry throughout the 1970s. As figure 31 clearly shows, research into β”-Al_2O_3 electrolytes exploded in the mid-1970s and was a product of a rapidly changing set of national energy and security priorities that manifest in declining support for the early stationary storage work of ANL in the 1960s and rechanneled federal funding for the development of traction batteries and petroleum alternatives.

Both of the above research thrusts did produce relevant molten salt work. In addition to a wealth of material preparation and device engineering enshrined in one of the dozens of now-declassified ANL reports, researchers also dabbled with new electrolytes. In one case, immediately preceding the development of β"-Al_2O_3, researchers working on the Na-Hg and Na-Sn thermally regenerative system explored the low-temperature electrolytes NaI-NaOH-NaCN and NaI-NaOH-$NaNH_2$[182] initially discovered and disclosed by the Okada and Yoshizawa teams. These chemistries, though particularly promising given their melt temperatures (160°C and 126°C, respectively) were only briefly investigated as the introduction of the Na^+ solid ion conductor rapidly shifted attention and money away from these formulations.

Only relatively recently has work refocused on the use of molten salts as electrolytes. β"-Al_2O_3 solid electrolytes (BASE) have proven hard to scale economically and the higher temperatures challenging to manage from a stability perspective[183, 184]. In addition, the low conductivity of β"-Al_2O_3 incentivizes a membrane as thin as possible. The resulting tradeoff between performance and cost, temperature and conductivity, and production scale and reliability has resulted in recent high-profile catastrophic failures[185]. As a result, Na||S and ZEBRA research has begun exploring "intermediate-temperature" electrolytes by using ionic liquids[186] and low-temperature molten salts mixed with aluminum chlorides[187] to achieve safety improvements without performance compromise.

Large companies have also moved towards lower temperature research following NGK's NAS battery explosion in 2011[188]. Sumitomo, in partnership with Kyoto University, has announced the development of a proprietary sodium-itinerant ionic liquid[186, 189, 190] with melting temperature of 57°C. Though this is an interesting pathway for large-scale storage, such ionic liquid-based systems are unsuitable for use in LMBs due to their high viscosities and

subsequently low conductivities limiting the maximum currents made possible by the molten metal electrodes.

4.5 The Window of Opportunity

Before embarking on a research program targeting low-temperature sodium-based liquid metal batteries it is important to address two important questions whose answers could indicate a null solution set to the search.

1. If low-temperature sodium-based salts exist and were researched by sodium producers, why haven't they been deployed over the higher temperature NaCl-$CaCl_2$ salts in modern Downs Cells?
2. If LMB-like batteries have been on the radar since the 1960s and sodium has been investigated as a negative electrode material, why hasn't there already been an exhaustive search of sodium-based molten salt electrolytes?

With regard to the first question, the answer mostly likely has to do with cost. Although the energy storage market is highly constrained by cost, the costs of the components of an electrochemical battery can be amortized over many cycles and years and thus the sum of each input only needs to be less than the value of energy saved over the lifetime of the device. In sodium production, by contrast, the electrolyte is the reactant and as a result is consumed on a 1-to-1 basis to create the product, pure sodium. In this scenario, the cost of the electrolyte must come in below that of the product on a per unit basis. Because of this, salts that are more expensive than NaCl, although researched in the patent literature, are likely not economically realistic solutions for sodium production. Another driving force for staying with the standard NaCl-$CaCl_2$ based process likely has to do with the additional economic value created in the

production of pure chlorine gas[98]. Though this is not as valuable on a per mole basis, the ability to produce two products diversifies income as well as potential customers.

On the second question, during the period of molten salt battery development in the 1960s the main down-selective criteria for materials selection were voltage, stability at high temperatures, and an ability to be integrated into a vehicular application. In all of these criteria, lithium beats sodium due to its greater electropositive nature, and lower metallic solubility in melts, and ability to be used with chalcogenide cathodes. As a result, the first answer to this question is that sodium was not a principal focus of research in the large government-funded programs. The second, perhaps more interesting answer to this question, has to do with the fact that the success of the Na-Bi cell (Table 21) came at a time when grid storage was not a concern or a priority for the United States. In other words, the value proposition created by a long-life, low voltage, battery was not competitive with the current pricing and trends in grid power. This is perhaps the reason why the invention of BASE and other solid ion conductors created so much interest amongst the research community. These technologies unlocked sodium's ability to be used in vehicular and other mobile applications and therefore resurrected a battery chemistry that had been second-place to lithium as a potential cost competitor for traction batteries.

With this history of sodium-based molten salts established it now becomes clear that a distinct window of opportunity exists. Specifically, though the development of low T_{melt} complex anion sodium salts (e.g. NaOH-NaX) was explored and dismissed by the electrowinning industry due to costs, this avenue was never properly explored by subsequent thermal battery research and development programs. Low-temperature NaOH-NaX type systems not only fulfill our requirements of temperature and cost, they are also accompanied by a base-level of electrowinning literature. This literature provides a starting place though by no means answers

all the questions that arise for an LMB use case. This work aims to build upon the knowledge accumulated but not put into practice from sodium production for use in an LMB-type grid-scaled storage device; A solution from decades ago that has only now begun to find itself one of the answers to society's greatest sustainable energy challenges.

Chapter 5 – An in-depth study of the NaOH-NaI System

5.1 Choosing a NaOH-NaX system

The selection of sodium hydroxide, NaOH, is a natural choice considering its very low cost ($0.02/mole[191]), high conductivity (>2.0 S/cm^2), and its strong tendency to suppress melting temperatures when mixed with sodium halide salts. Figure 32 shows ideal solution predictions for NaOH with the four most abundant sodium halides.

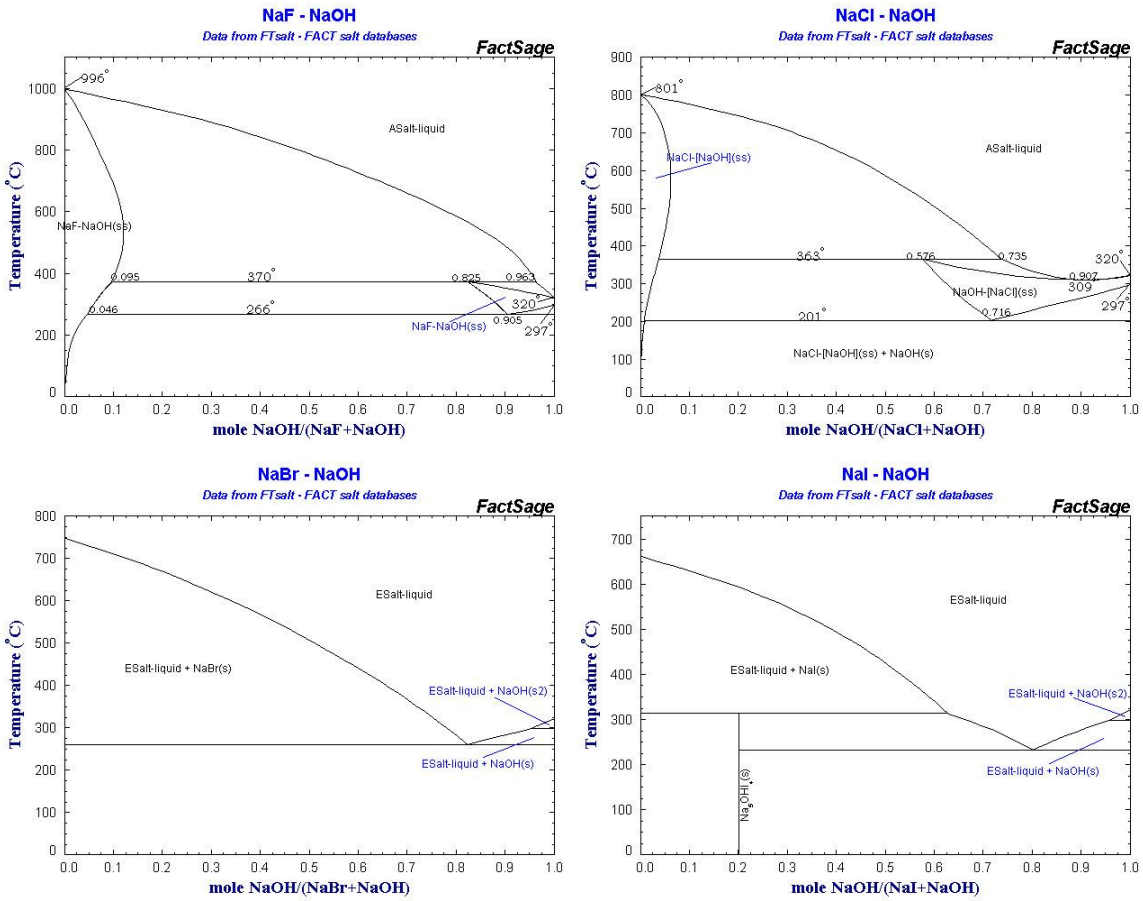

Figure 32 - NaOH-NaX predicted binary phase diagrams

These diagrams have been generated in FactSage 6.3 thermochemical software package using thermodynamic data for the pure end members, ideal mixing for the liquid solution, and solid solution models where such behavior is known[192-196]. Though they are only predictions, they do give a rough indication of the minimum temperature required to achieve a fully liquid state. The

goal is to select a binary salt system that simultaneously enables low-temperature operation without dramatically increasing cost.

Recalling the outputs from the cost model, the two key temperatures to target for cost reductions are 250°C and 280°C (Figure 18). These two temperatures correspond to the transition from TGGT-type insulated wire to MG-type and the transition from glass-ceramic seals to PTFE-based O-rings. Given these two threshold temperatures, it clear that the NaOH-NaF and NaOH-NaCl binary systems are not good binary systems to initially investigate as both of these appear to have minimum molten temperatures of at least 300°C. This, plus the fact that operating temperatures normally need to be 20-30°C in excess of the minimum melting component of the LMB mean that these binary systems would not allow us to achieve the considerable cost savings identified earlier.

Looking now at the NaOH-NaBr and NaOH-NaI systems, the latter is found to be preferable if viewed on the basis of temperature. Whereas the NaOH-NaBr has a eutectic temperature of around 255°C, the NaOH-NaI is proposed to melt closer to 225°C. This 30°C difference may potentially mean a very large difference if the latter system enables the use of TGGT-type insulation. Looking now at the cost of these two salts, industry-grade NaBr is found to be significantly cheaper ($3/kg[197]) as it is currently produced in large bulk quantities (tons) whereas NaI is far more expensive ($80/kg[198]) due to its smaller scale production. This difference in production amount is due principally to NaBr's common usage as a catalyst for the pharmaceutical industry and a dense fluid additive for oil well drilling. NaI, on the other hand, finds far smaller and boutique usages and is therefore not in high demand.

Since the commercial prices of NaBr and NaI do not reveal their intrinsic cost structures two further questions to ask are 1) how is each produced and 2) how much do their higher purity forms compare in costs as these may provide for a more fair comparison that controls for NaBr's scaling advantage. To the first question, both salts are produced in nearly identical manners via the reaction of NaOH with acidic iodides (Equation 26[199]) or bromides (Equation 27):

Sodium Iodide: $NaOH + HI \leftrightarrow NaI + H_2O$ Equation 26

Sodium Bromide: $NaOH + HBr \leftrightarrow NaBr + H_2O$ Equation 27

Because both of these acids are approximately the same price to acquire[200], it is believed that the synthesis itself drives the cost of production equally. The next major cost to NaI and NaBr salt synthesis are the purification and drying steps. Though the cost contributions from each of these steps is not yet clear, quotes for high purity and anhydrous NaI and NaBr from Alfa Aesar are available. These quotes indicate that ultradry 99.99% purity NaI is $5.00/g whereas NaI comes in at $3.90/gram. In the context of an LMB, these prices are quite high. Though such high purity salts will unlikely be used in the electrolyte these prices are meant to highlight the fact that the inclusion of a purification and drying step brings the actual cost of the NaBr and NaI salt quite close together. For this reason, and in the absence of other NaI-scaling projections, it is not possible discriminate the two salts on the basis of cost.

For the purposes of this study, we will here choose the NaOH-NaI system as the target "base" binary system for further study. By "base" it is implied that future ternary additions are expected and so the characterization and study of this mixture should create knowledge that can be used either for comparison or to theoretically extend into ternary salt space.

5.2 NaOH-NaI prior art

A vast majority of the NaOH-NaI specific literature comes from the research and development conducted jointly by the Engineering Research Institute of Kyoto University and Tekkosha Co., Ltd, a Japanese metallurgical and electrometallurgical company. This work targeted improvements to the aforementioned Castner- and amalgam-type sodium production processes. A simple diagram from an early chemistry textbook[201] visually depicts the process.

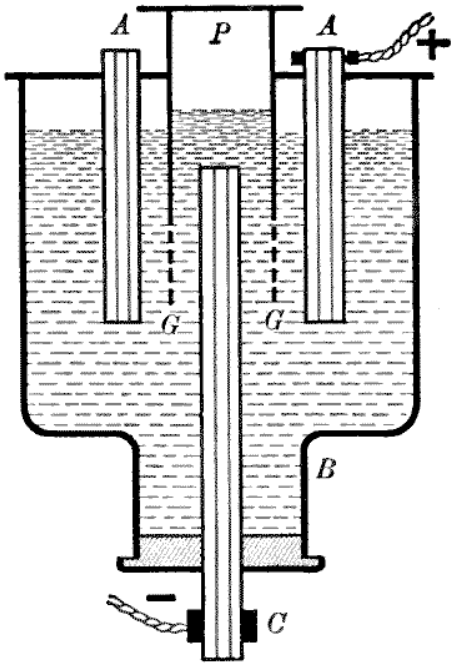

Figure 33 - Basic Castner cell for the production of Na metal from NaOH feedstock

In this embodiment, the cathode, A, reduces sodium from the NaOH fused melt while oxygen is produced on the anode, C. Both products are piped out of the device and the process is continually fed new electrolyte for separation.

This device encountered several challenges. First, at elevated temperatures the caustic melt would readily absorb moisture form the surroundings and this water contamination would reduce the sodium output via Equation 24. Another major challenge of this system was the

reactivity of pure sodium metal with the hydroxide. Not only would it slowly chemically react with the melt as below

$$Na_m + NaOH \leftrightarrow Na_2O + \tfrac{1}{2}H_{2(g)} \qquad \text{Equation 28}$$

but it would also metallically dissolve back into the electrolyte. This basic Castner process was therefore variously modified into an amalgam process whereby sodium metal would not be deposited in its pure form but rather into mercury to form a low-activity amalgam. This lowered concentration of sodium suppressed the reactivity and solubility of produced sodium and thereby increased the production efficiency. Following the amalgam formation, a second electrolysis step would be undertaken to purify the sodium metal of the mercury.

Yoshizawa and Okada both recognized that the Castner- and amalgam-type processes lagged behind Downs cells for these reasons and made great efforts to improve the process from the actual device design to the materials used. One of their main focuses was on identifying lower temperature electrolytes that would further suppress sodium solubility and reactivity as well as lower the vapor pressure of mercury to prevent cross-contamination from evaporation. This work began in the early 1950s with the publication of a phase diagram study of the ternary NaOH-NaI-NaBr system[202]. Because this study used capillary-based melting point determination they were only able to pinpoint the onset of melting and the appearance of a fully liquid state. Because of this, only eutectic and liquidus measurements were made (Figure 34). In this binary system, a eutectic was fond at 80/20 NaOH/NaI at 225°C. Similar measurements were made for all three binary systems and combined with a selected number of ternary compositions to form a ternary diagram. Isotherms were estimated and a ternary eutectic of 206°C was proposed

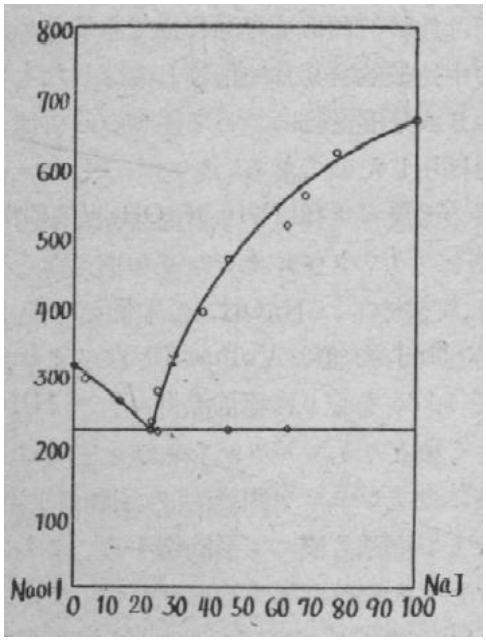

Figure 34 - The first binary phase diagram of NaOH-NaI

This work was later followed-up by a compatibility study to find suitable materials for use in the construction of future amalgam-type cells[203].

Table 22 - Materials surviving corrosion tests in NaOH-NaBr- NaI systems[203]

Material	Observation	Dissolution Rate ($mg/cm^2/hr$)	Corrosion Rate (mm/year)
Low-carbon steel	little corrosion	2.921	32.56
Ni	no change	0.004	0.04
Low-carbon steel with electropolishing in phosphoric acid solution	almost no change	0.011	0.12
Low-carbon steel with Phosphate conversion coating	almost no change	0.003	0.03
SS 18-8	almost no change	0.003	0.03
soda-lime glass	corroded and embrittled	-	-
Quartz	fragment into small pieces	-	-
PYREX glass	crack	-	-
Terex glass	fragment into small pieces	-	-
Porcelain	to peel off	3.541	129.20
Alumina	little corrosion	0.062	1.38
Magnesia	swollen	1.631	39.91

Though many materials were tested, the corrosive nature of the melt found that only a few materials were candidates for use in the device construction. Table 22 shows that several common materials including 18-8 steels, nickel, and alumina are all potential assembly components with a NaOH-based electrolyte. Importantly, for device lifetimes exceeding ten years, it is ideal to limit the corrosion of sidewalls to less than a millimeter and therefore only materials with corrosion rates of less than 0.1 mm/year would be suitable.

With construction materials identified, Okada and Yoshizawa embarked on one of their most comprehensive studies of the NaOH-NaX system electrolytes for use in sodium electrowinning. Specifically, because the voltage of operation is directly related to the energy input required it is desirable to understand the conductivity properties of the electrolyte. In practice, electrowinning processes often operate at very high current densities to increase the yield per unit time. This, in turn, requires that voltages far above the theoretical deposition voltage due to heavy overpotential losses (Equation 11). The degree to which an operator must input excess energy to create certain yield rates is therefore very functional on the conductivity of the electrolyte used. For this reason, Okada and his team explored the functionality of conductivity on temperature and composition[204]. For our purposes, only results from the NaOH-NaI system will be shown though studies for the NaBr-based systems are also available. Figure 35 includes data replotted from Okada[204] as well as data from an earlier study by Demidov[205]. Because Demidov's work only reported a linear functional form for conductivity the data from this source likely contains a greater degree of error. From these studies, the NaOH-NaI system demonstrates conductivities ranging from 0.35 S/cm to over 1 S/cm depending on the composition and temperature selected. It should also be pointed out that the 82.2% NaOH system

has measurements at the lowest temperatures, likely indicating that this composition is quite close to the actual eutectic temperature of the system.

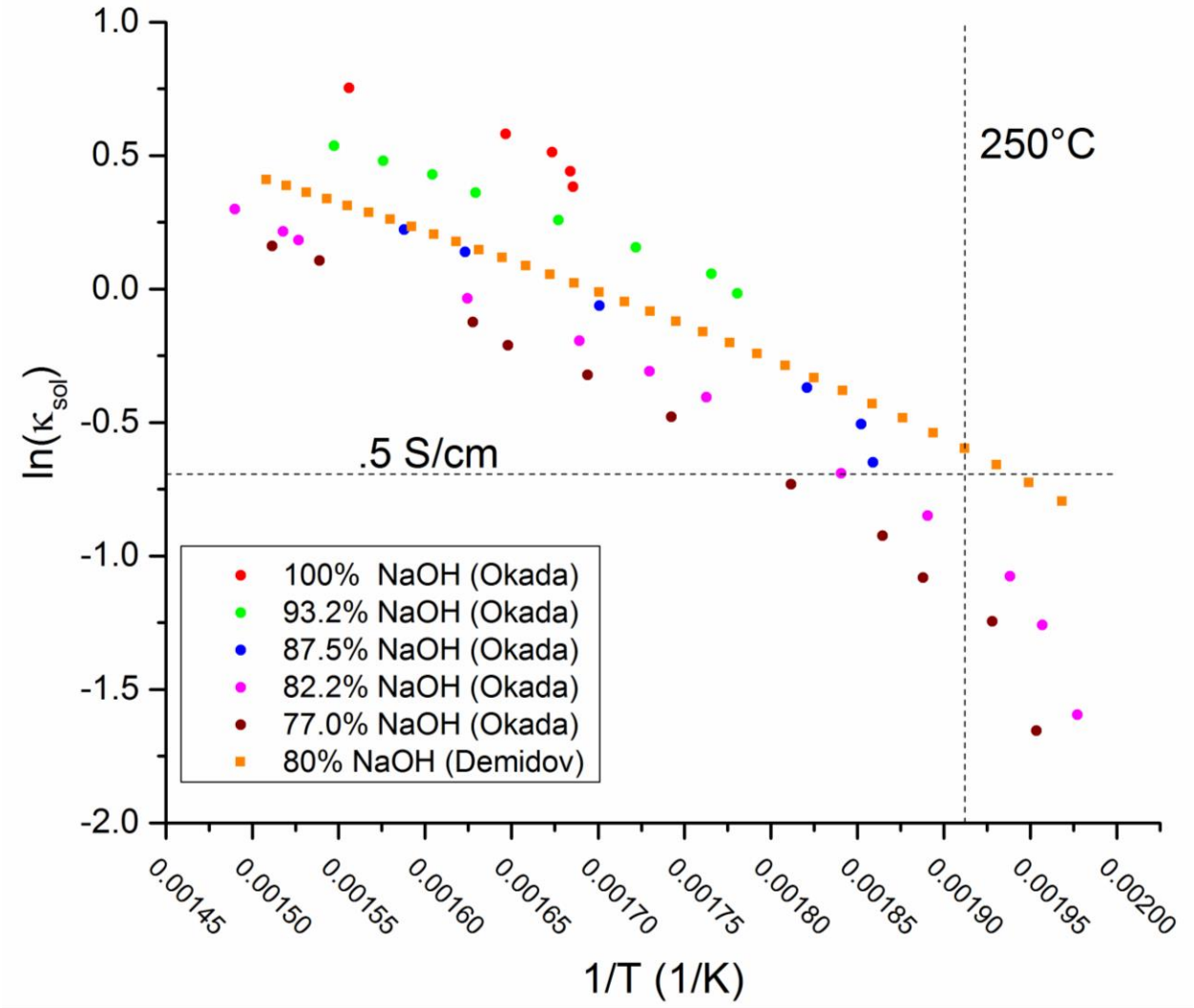

Figure 35 - Conductivity of various compositions of NaOH-NaI compositions as a function of temperature. Earlier data by Demidov is also overlaid to show general reproducibility of conductivity values.

A final point on these measurements is that they are likely systematically underestimates due to the fact that NaOH during these periods often contained 1-3% $NaCO_3$ impurity due to reaction with CO_2 during synthesis. These impurities lowered the ionic conductivity of melts slightly due to their larger size anions and tendency to increase the viscosity of the system. This disclaimer,

also provided by Okada et al., explains why their pure NaOH conductivity measurement (red circle) is slightly below that of today's commonly accepted value (Table 19) by 100 mS/cm.

With this information, Okada and Yoshizawa began to assembly new sodium production devices and examine the impact of their lower temperature electrolyte. Patents[129] detail new designs for amalgam-type electrowinning and studies in the English literature mark a departure from their early-stage research and development. One very important study[206] investigated and quantified the degree of sodium loss via two distinct mechanisms: the reactivity of molten sodium with the melt and the dissolution of metallic sodium into the melt. These two mechanisms were generally discussed earlier in section 4.3.2 Corrosion and were classified as Type III and Type IV mechanisms, respectively.

In the case of Type III corrosion the reader is referred back to the reaction outlined by Equation 28. Though this reaction is thermodynamically expected and observed to occur for pure molten sodium in contact with pure molten sodium hydroxide (> 318°C), the introduction of a lower temperature system complicates a prediction of reaction spontaneity. The reason for this is because the reaction is driven entropically by the creation of a gaseous product and is therefore very susceptible to changes in temperature and pressure. As a result, creating a binary system that allows for lower temperatures via eutectics should impact the degree of reactivity via this Type III corrosion process. In addition, the creation of a binary system also reduces the activity of NaOH from unity. This process, modelled in Equation 29, is inversely related to a_{NaOH} and is therefore driven towards the reactants as this value decreases.

$$\Delta G_{rxn} = \Delta G^0 + RTln\left(\frac{(a_{Na2O})(p_{H_2})^{1/2}}{(a_{NaOH})(a_{Na})}\right) \qquad \text{Equation 29}$$

In order to measure the degree of chemical reactivity of sodium in contact with the ternary (NaOH-NaI-NaBr) molten electrolyte, known quantities of molten salt and metal were exposed to each other at various temperatures and the production of H_2 gas was measured. This H_2 gas was then related back to an amount of sodium reacted via a simple 2:1 molar ratio and reported as a consumed sodium value (Table 23[206]).

Table 23 - Chemical Reactivity of Na metal with ternary NaOH-NaBr-NaI salt at different temperatures

Temperature (°C)	Consumed Sodium (g_{Na} / 100 g_{salt} / hour)	
	Experiment 1	Experiment 2
231	0.000	0.000
239	0.000	0.000
249	0.000	0.000
259	0.000	0.000
270	0.000	0.000
278	0.000	0.000
285	0.010	0.011
285	0.011	0.012
295	0.034	0.039
300	0.047	0.054

This experiment established the positive result that below a threshold temperature (~280°C) the reactivity of hydroxide based melts with pure sodium metal is significantly suppressed. From their paper,

> "the relation between bath temperature and amount of reactive sodium (g/100g/hr), shows that violent reaction occurs at ca. 280°C and then beyond 300°C it becomes more violent with spouting foam from molten salt. Though Na_2O is produced at a temperature below 280°C, the reaction is very slow and cannot be measured by this apparatus."

This is a positive result not only for the electrowinning of sodium but also for application in a long-life battery as a slow or absent chemical corrosive process means minimal coulombic efficiency loss during the cycling of the device.

The second experiment aimed to identify the degree to which sodium metal dissolves into the melt. This experiment exposed the molten salt bath to pure sodium at set temperatures and allowed them to equilibrate. The salt samples were then removed and analyzed for sodium metal content. The results are provided in Figure 36[206].

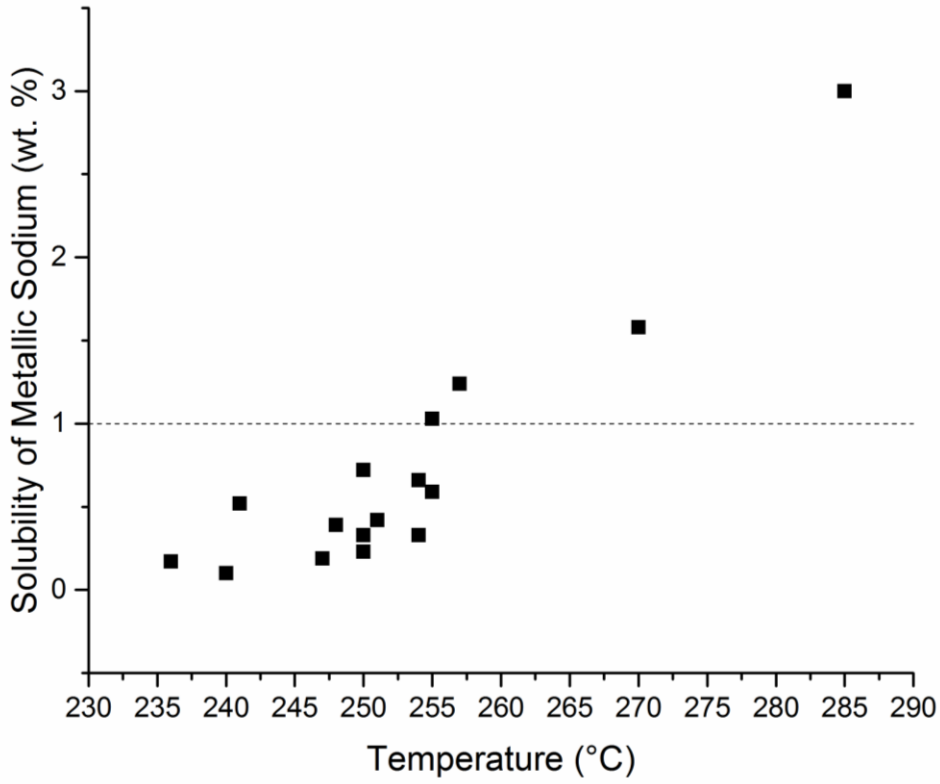

Figure 36 – Replotting of the solubility of sodium metal in ternary salt as a function of temperature.

As can be seen, for temperatures below 255°C the solubility of sodium metal in the salt was found to be less than 1.0 weight percent and often an order of magnitude lower in several studies. This experiment was then accompanied by a measurement of how mobile these metallic species

were. This diffusion experiment set up a three liquid layer cell in which sodium metal, the molten salt, and pure mercury sat as three layers in a sintered alumina tube. Sodium metal was given time to solubilize and equilibrate in the melt and then mercury was periodically piped out from the bottom at set times to measure the sodium content. Because there was no closed circuit for electrons to pass through, any sodium found in the mercury must have arrived in the metallic form in order to for the amalgam. From these measurements, rough metallic sodium diffusion in the melt could be estimated at different temperatures (Table 24[203]).

Table 24 - Sodium metal solubilization and diffusion experiment

Temperature (°C)	Diffusion Velocity of Sodium ($g/cm^2/hr$)
239	0.0003
249	0.0006
251	0.0012
260	0.0009
263	0.0013
270	0.0015
278	0.0023
285	0.0028
285	0.0028
292	0.0051
300	0.0086

This experiment also provides useful information for those wishing to develop an LMB-type system as the diffusion values can be translated directly into leakage currents (Figure 37[203]). These leakage currents are in fact quite similar in magnitude to those found in analogous Li-based systems[23] and are an order of magnitude below those found in the Na||Bi cells constructed at Argonne National Labs[76]. When scaled differently, these results demonstrate a very strong Arrhenius-style temperature dependence (Figure 38). Considering the uncharged nature of the

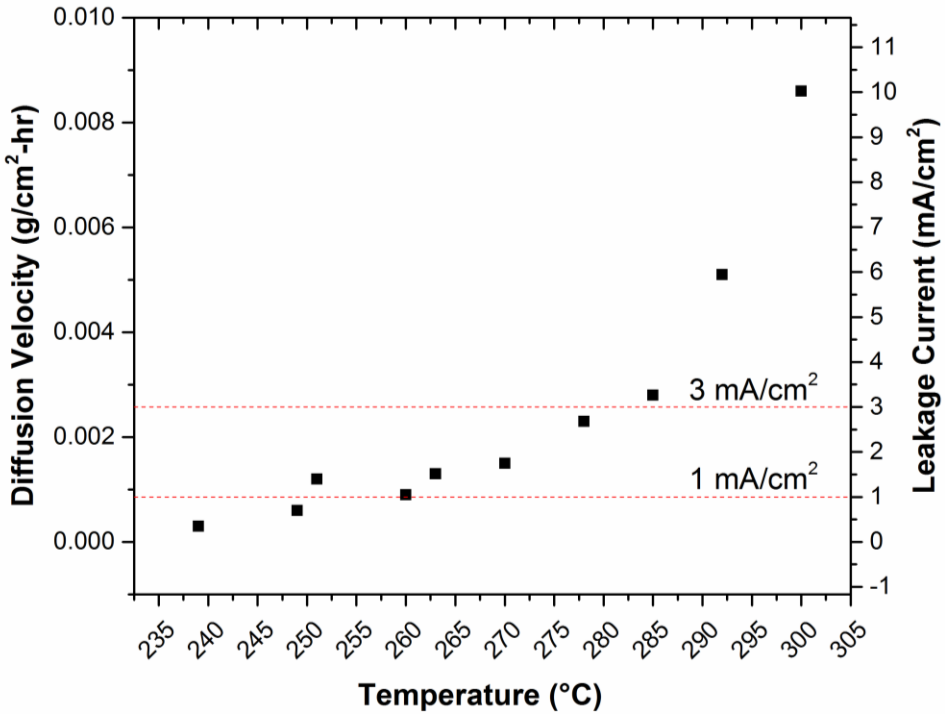

Figure 37 - Replotting of the Na metal diffusion experiment results mapped to corresponding leakage currents.

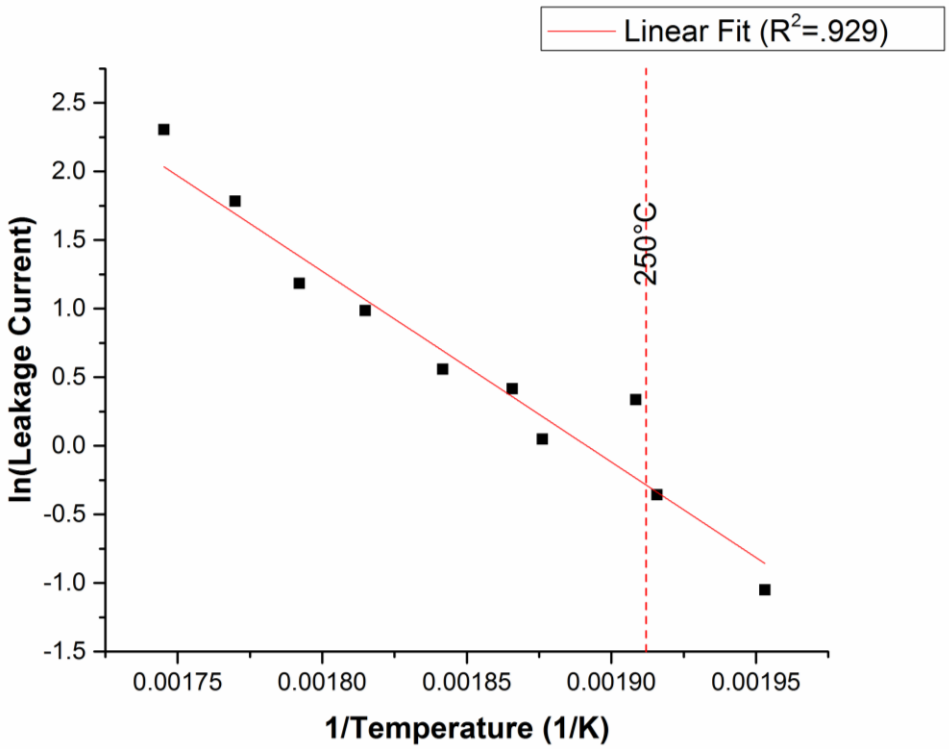

Figure 38 - Leakage current activation plot replotted from Okada's data

species, this is an interesting result and may relate to the diffusivity constant's relationship with viscosity and therefore temperature.

The final piece of prior art that exists on the NaOH-NaI system relates to the further development of the phase diagram for the system. Because differential scanning calorimetry (DSC) technology was not introduced until 1962[207] and made commercially available in 1963, Yoshizawa and his colleagues were not able to improve upon the initial Okada diagram from 1953 until 11 years later[208].

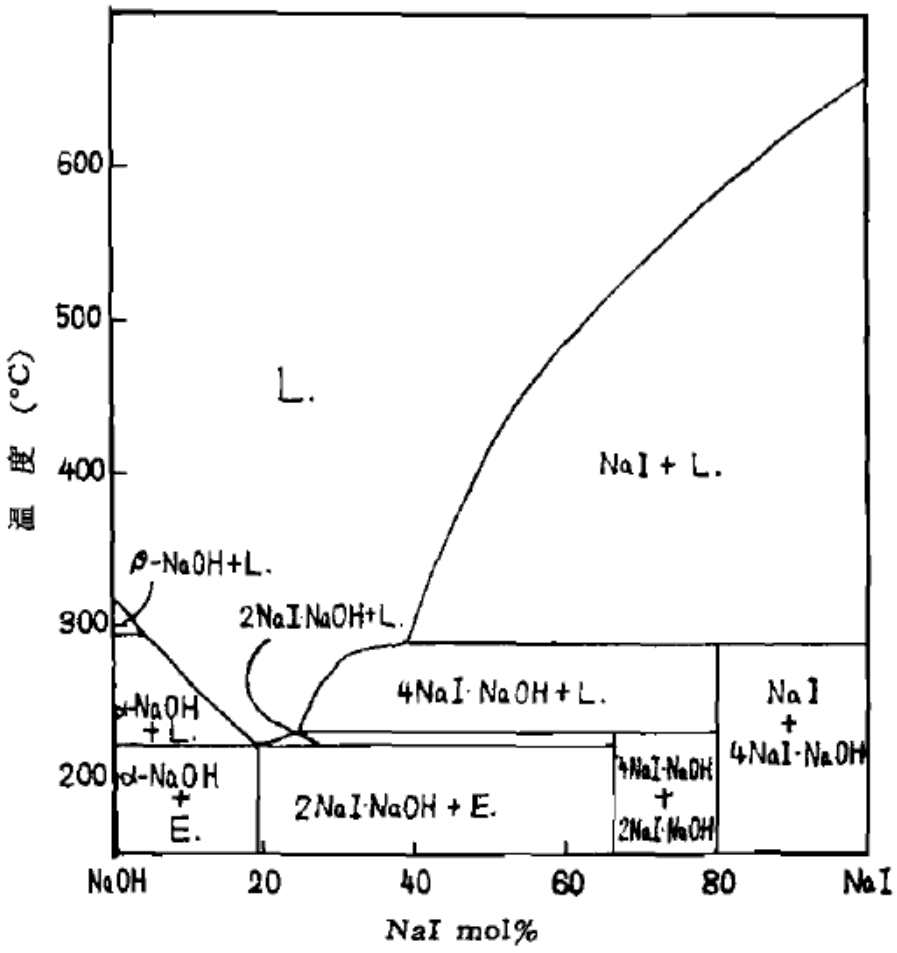

Figure 39 - NaOH-NaI phase diagram following the invention of DSC.

This work identified a number of new phase transformations and greatly expanded knowledge of the NaOH-NaI binary diagram. In addition to confirming the eutectic at around 224°C the phase diagram in Figure 39 identifies two new peritectic transitions occurring at 234°C and 290°C. The transitions were proposed to come from incongruently melting compounds and the compositions of those compounds were selected to occur according to the existence or absence of DSC signals. For example, the $Na_3(OH)I_2$ compound was proposed because there were no eutectic signals detected between 66-100% NaI. Unfortunately, the original data from Yoshizawa's experiments is not provided in the paper so it is hard to know how or if they tested for metastable phase signals or the reproducibility of those signals. That said, the temperatures at which signals occur are likely to correspond to real transitions though the precise location of those compounds is likely not accurate.

This phase study was the last piece of work on the NaOH-NaI system until 1999 when Sangster et al.[209] applied their FactSage software and methods to model the binary system using end-member (NaOH and NaI) thermodynamic data coupled with the work conducted by Yoshizawa and previous authors[210]. Their method of calculation used a least-squares approach to minimizing the free energies of mixtures while respecting experimental invariant points as inputs. As a result, the accuracy of their method is quite dependent on the quality of the experimental data. Sangster's calculated phase diagram (Figure 40) was able to fit a 231°C eutectic point at 80/20 as well as the liquidus data from Yoshizawa's[208] and an earlier author, Scarpa's work[i], though encountered difficulty with the proposed compounds. Specifically, the 290°C peritectic transition reported by Yoshizawa and ascribed to a $Na_5(OH)I_4$ compound could only be fit at 310°C. Further, the lower melting $Na_3(OH)I_2$ compound could not be fit at all and as a result

[i] The work by Scarpa, published in 1915, is no longer available and is therefore not commented on in this survey of the literature.

likely influenced the elevated eutectic temperature arrived at in their model. Sangster made specific mention of the fact that they were unable to arrive at simultaneous excess free energy solutions for equilibrium between the liquid and a compound at $Na_3(OH)I_2$. This fact, combined with the knowledge that neither Scarpa or Okada had found evidence for the low-temperature peritectic transition but that two authors had found the high-temperature (290°C) transition led Sangster to optimize his diagram with only one compound.

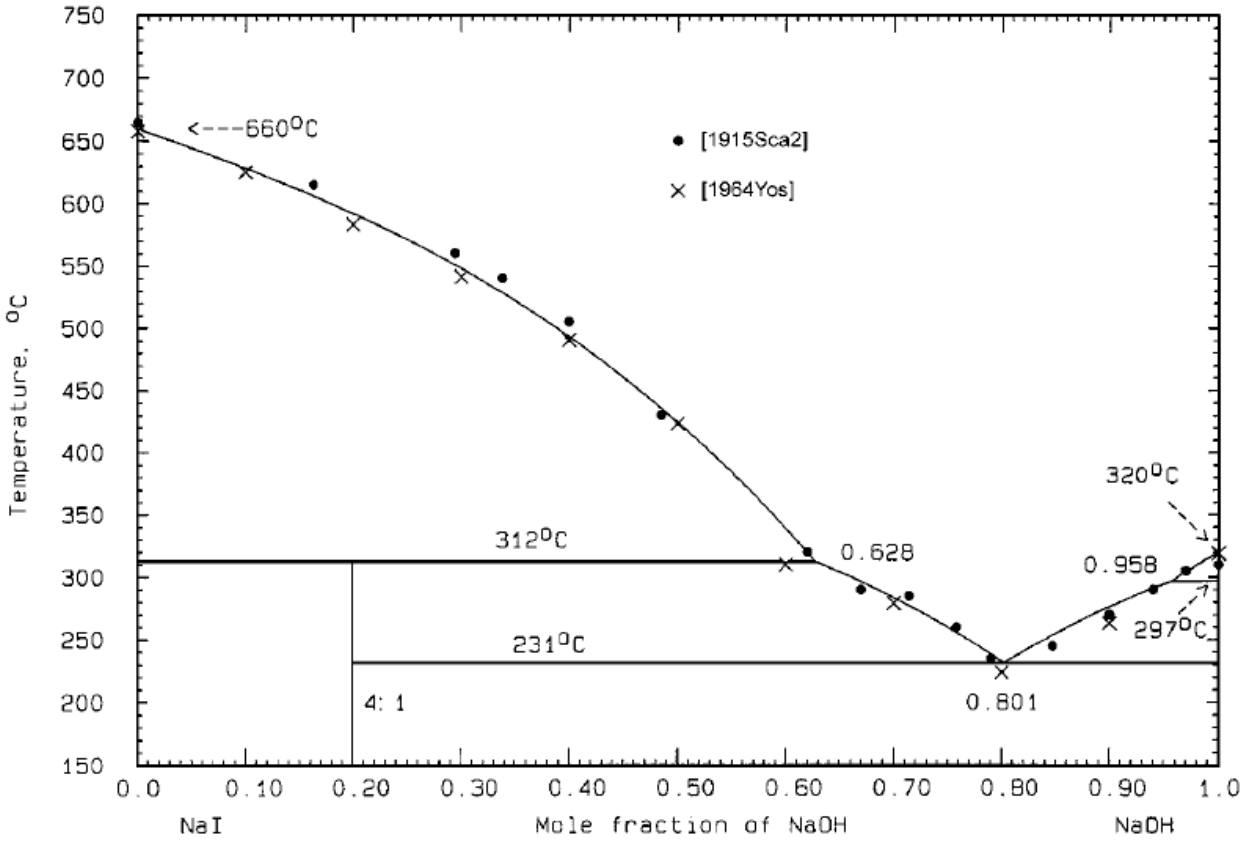

Figure 40 - Sangster's calculated phase diagram using Fact methods and experimental data from Yoshizawa and Scarpa.

Overall, the existing NaOH-NaI literature developed for sodium electrowinning provides exciting initial validation of the potential of this binary system. Work has demonstrated a low eutectic (225°C), potential stability with sodium metal, and a conductivity that is satisfactory for high current density operation. Existing studies therefore support the idea that NaOH-NaI could

be an excellent electrolyte for an LMB yet there is general disagreement on a correct phase diagram, there is little work done on thermodynamically modeling the solution or intermediate compounds, we've found no work studying the electrochemical stability of the electrolyte, and no attempt has been made to demonstrate a reversible cell in which sodium can by oxidized and redeposited as occurs in an LMB. The experimental portion of this thesis will investigate these areas while also spending time to reexamine those findings from Yoshizawa and Sangster that are still speculative in nature.

5.3 Experimental Techniques

5.3.1 Materials Preparation and Containment

The preparation of molten salts for electrochemical study is not a well-standardized process. Though many references[211-213] discuss suitable methods for drying and homogenizing, literature rarely defers to a single process for preparation and often keeps particular details of the operating procedure internal. The main reason for this is that the purity and dryness required for different experimental setups varies. For our work, it is important to acquire salts that are both chemically homogenous and contain as little moisture as possible. Chemical homogeneity ensures the accurate and reproducible thermal measurements while the removal of moisture is critical for accurate electrochemical and cycling measurements.

In order to accommodate these two needs, a stainless steel test chamber was constructed such that it allowed for the alternating flow of inert gas (high purity Argon) and pulling of a vacuum (10 mTorr). A titanium getter was also used in order to further reduce the presence of oxygen in the inert processing gas. Because this chamber, shown in Figure 41, was also constructed with the intention of providing a controlled experimental environment for numerous long-term electrochemical studies it was additionally fit with numerous ultra-torr ports to allow

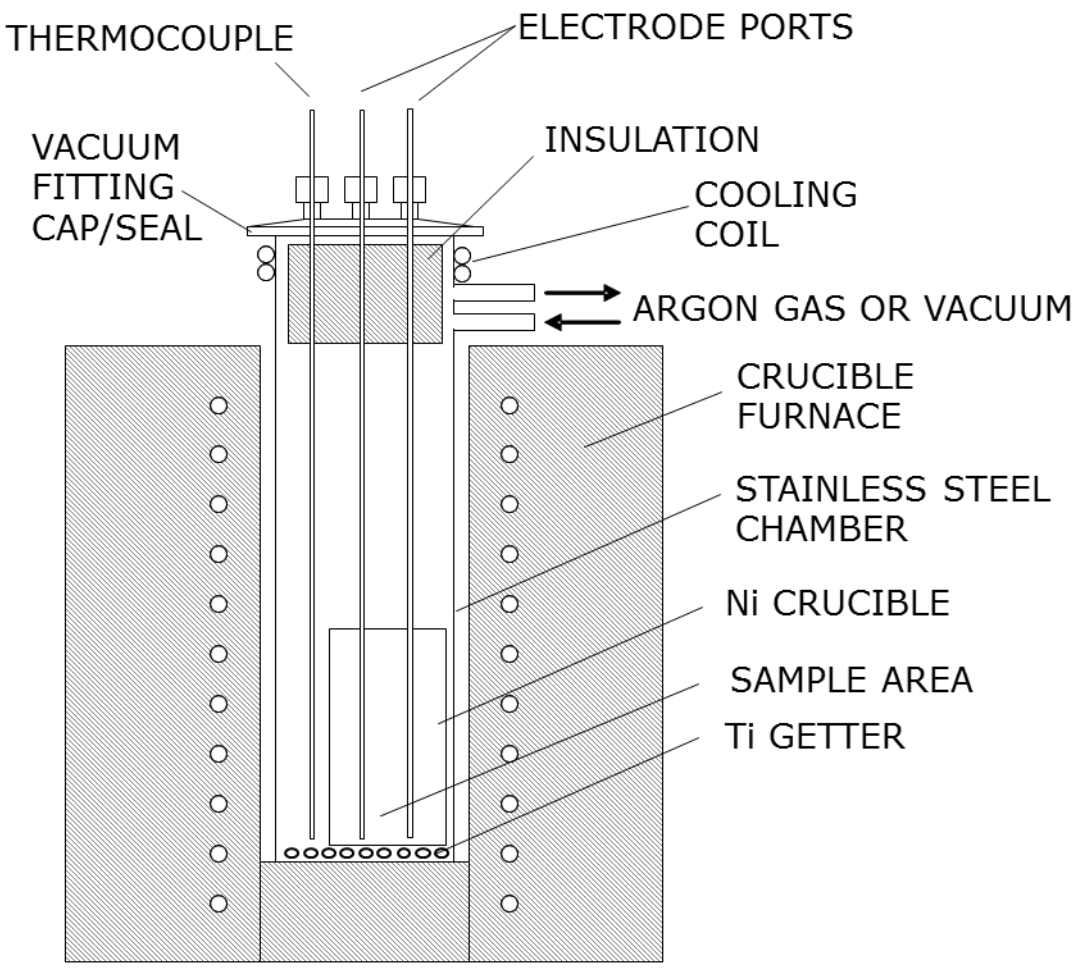

Figure 41 - Experimental chamber used for drying and electrochemical experiments.

for electrode and thermocouple insertion. The chamber supported an isothermal 6" experimental area by utilizing metal baffles to slow thermal conduction away from the sample and reduce convective motion. Finally, because the crucible is expected to sit at elevated temperatures for sustained periods of time, it was sized and shaped such that the sample area (bottom) sat deep within a PID-controlled Thermo Scientific furnace hot zone while the top sealing area was cooled by a constant flow of chilled water through copper coils. This allowed for a simple PTFE O-ring hermetic seal at the top of the crucible.

For the NaI-NaOH system, a procedure that is simultaneously able to remove remnant moisture from commercially packaged anhydrous NaOH (<0.5% H_2O by weight) while respecting the relatively high vapor pressure (Figure 42) of sodium iodide[214] is required.

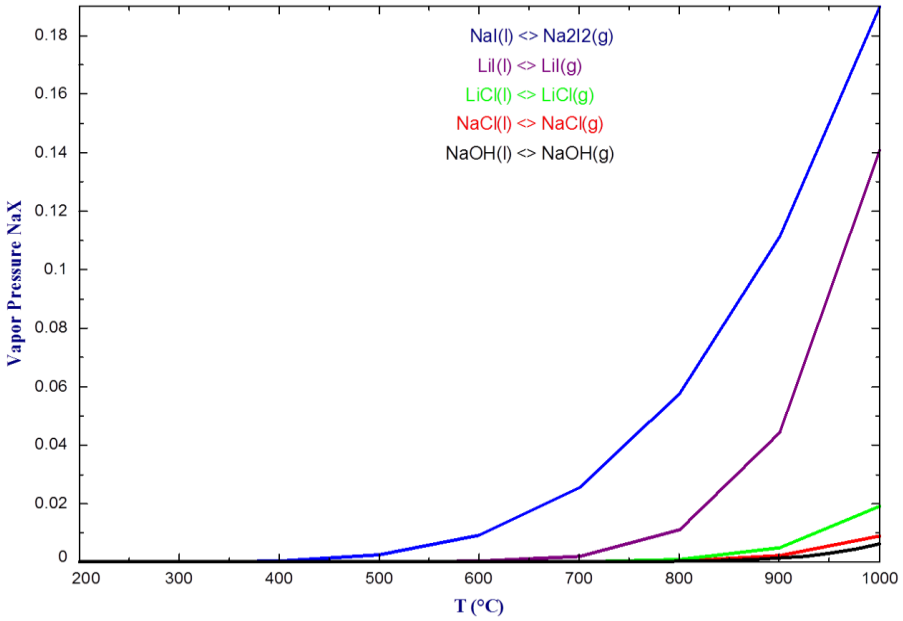

Figure 42 - Calculated vapor pressure of pure NaI, NaCl, NaOH, LiI, and LiCl

In order to do this, 99.9% purity anhydrous NaOH from American Elements was first dried separately from the NaI. The NaOH granules were contained in Ni-201 crucibles and held at 500°C and approximately 100 mTorr for 4 to 5 hours. This procedure was recommended by Yurkinskii[215] as it maximized the amount of dehydration while avoiding the formation of putative Na_2O byproducts. These two competing reactions are shown below:

$$NaOH \cdot H_2O \rightarrow NaOH + H_2O_{(g)} \qquad \text{Equation 30}$$

$$2NaOH \rightarrow Na_2O + H_2O_{(g)} \qquad \text{Equation 31}$$

Omission of this drying process resulted in strong water reduction signals during voltammetric studies (Figure 58).

Once dried, the NaOH pellets were returned to an inert Argon-filled glovebox environment and combined with 99.99% purity ultradry NaI from American Elements to form the required molar compositions. The NaI powder was placed on the bottom of the crucible while NaOH was placed on top. This was done as a means of circumventing high binary melting temperatures. Because NaOH melts 300°C below NaI, the hydroxide salt melts first and then slowly solubilizes the NaI below. By holding at temperatures slightly below the theoretical NaI melting temperature (661°C) it is possible to create homogenous salt mixtures without incurring an unknown degree of preferential vaporization from the NaI. In the absence of this procedure, vaporizing NaI decreases the compositional accuracy and contaminates the crucible.

Table 25 - Binary salt melting and homogenization procedure.

Temp (°C)	Time (hrs)	Atmosphere	Description
150	2	Vacuum	Surface moisture removal
250	2	Vacuum	Organic material removal
350	4	Vacuum	NaOH melting and moisture removal
550	6	Argon	NaOH dissolution of NaI powder
200	4	Repeat Purging	Slow temperature drop from 550 to 200 to promote equilibrium structure
25	-	Argon	Melt completion

Following this melting procedure, the salt samples are returned to the argon-filled glovebox, removed from the crucible, and pulverized using a mortar and pestle to increase the homogeneity.

Figure 43 - 80/20 NaOH/NaI salt in a Ni-201 crucible after melting and before pulverization

During this process the color and hardness were noted and samples lacking consistency throughout their depth were remelted in the furnace to improve homogeneity.

The correct selection of container materials for the salt preparation above as well as the electrochemical experiments to follow is very important. Building upon Yoshizawa's and Okada's work on compatible materials, several materials were tested for use as electrode and crucible materials. First, a wide variety of metals and ceramics were tested in 80/20 NaOH/NaI at 300°C. The materials showing no visible corrosion were then used in a variety of long-term static-corrosion tests as well as dynamic electrochemical experiments. Following each of the tests, salts were investigated using direct current plasma atomic emission spectroscopy (DCP-AES) according to ASTM E 1097-12 standards. This test was conducted in order to search for corrosion products that may have resulted from the molten salt's contact with various container or electrode materials. The results from the DCP-AES study are provided in Table 26.

Table 26 - Corrosion study of the subset of materials that showed no visual corrosion (<.0005 is below detection).

Sample Description	Test Environment	Weight %				
		Ag	Pt	Al (Al_2O_3)	Ni	H_2O
Ag Probe Al_2O_3 crucible	Impedance Study 1 month	<0.0005	N/A	0.0005	N/A	0.30
No Probe Ni crucible	Static Corrosion 1 week	N/A	N/A	N/A	<0.0005	0.22
No Probe Al_2O_3 crucible	Static Corrosion 1 week	N/A	N/A	<0.0005	N/A	0.12
Ag Probe Ni crucible	CV Study 1 month	<0.0005	N/A	N/A	<0.0005	0.67
Ag, Ni, Pt, β-Al_2O_3 Ni crucible	CV Study 1 month	<0.0005	<0.0005	0.0053	<0.0005	N/A
Ag, Ni, Pt, β-Al_2O_3 Ni crucible	CV Study 1 month	<0.0005	<0.0005	0.0058	<0.0005	<0.01

All metals showed strong resistance to attack though silver did occasionally show embrittlement for the longer-term or repeat use tests. Alumina similarly showed general resistance to the molten

salt in spite of its being reported to have variable resistance to pure hydroxides[216] or NaOH-NaX melts[203]. For this reason, Al_2O_3 crucibles were used only for experiments lasting no longer than 1 month. Similarly, β"-Al_2O_3 ion conducting ceramics also showed early resistance to hydroxide melts though did begin to break down after approximately 100 days[217]. As a result, β"-Al_2O_3 was also employed though limited in its service life to 1 month or less.

Of the metals tested, nickel (high purity and Ni-201) is both the most economical and showed most consistent resistance to attack by NaI/NaOH molten salts.

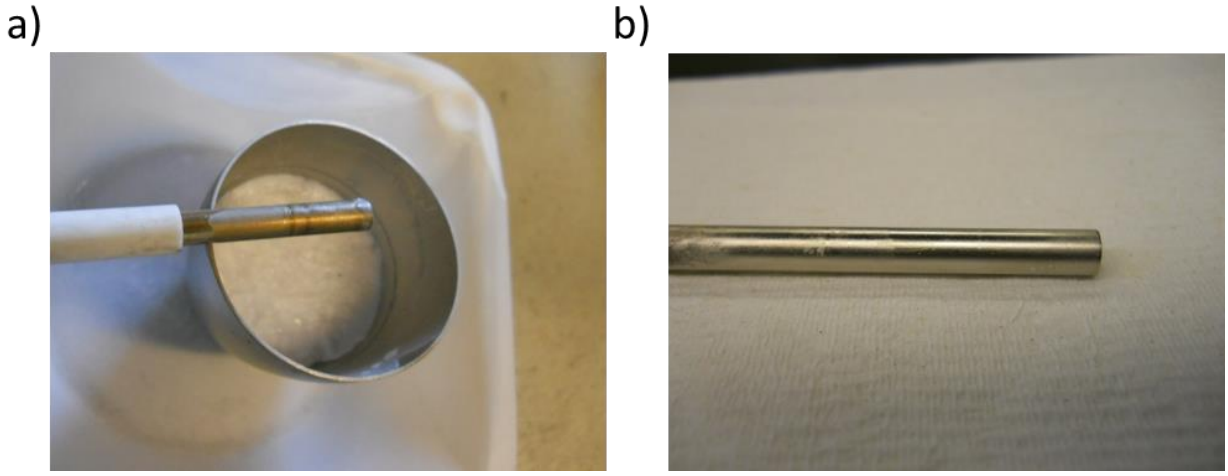

Figure 44 - Pure nickel probe after a 1-month experiment in 80/20 NaOH/NaI molten salt. a) shows the probe immediately after removal while b) shows the probe after washing and pickling.

Because nickel is such a resistant material, high purity (> 99.9%) wire was used for electrodes whereas easy-to-obtain Ni-201, a commercially pure form of nickel, was used for crucibles. Before use, all nickel materials were cleaned by washing with acetone, deionized water, pickling according to a common industry formulation (H_2SO_4, HNO_3, NaCl, and H_2O)[218], and then drying under vacuum at 150°C to remove all moisture. This process could also be used to remove occasional discoloration, the result being shown in Figure 44b.

A final important point to note is that the moisture content of the salt following prolonged periods of experimentation within the test chamber is quite low. This measurement confirms the

hermiticity of the test chamber as both NaOH and NaI are extremely hygroscopic salts and therefore act as getters for moisture within the experimental setup. For this reason, it is assumed that a majority of the water contamination that occurred throughout the life of the experiment is cumulatively captured in the salt and presented in the H_2O weight percent value in Table 26.

5.3.2 Differential Scanning Calorimetry (DSC) Measurements

Differential Scanning Calorimetry (DSC) is a thermoanalytical technique in which phase transitions and other thermodynamic properties are measured via a heat flow differential between a reference and a sample. A diagram of the device operation is provided in Figure 45.

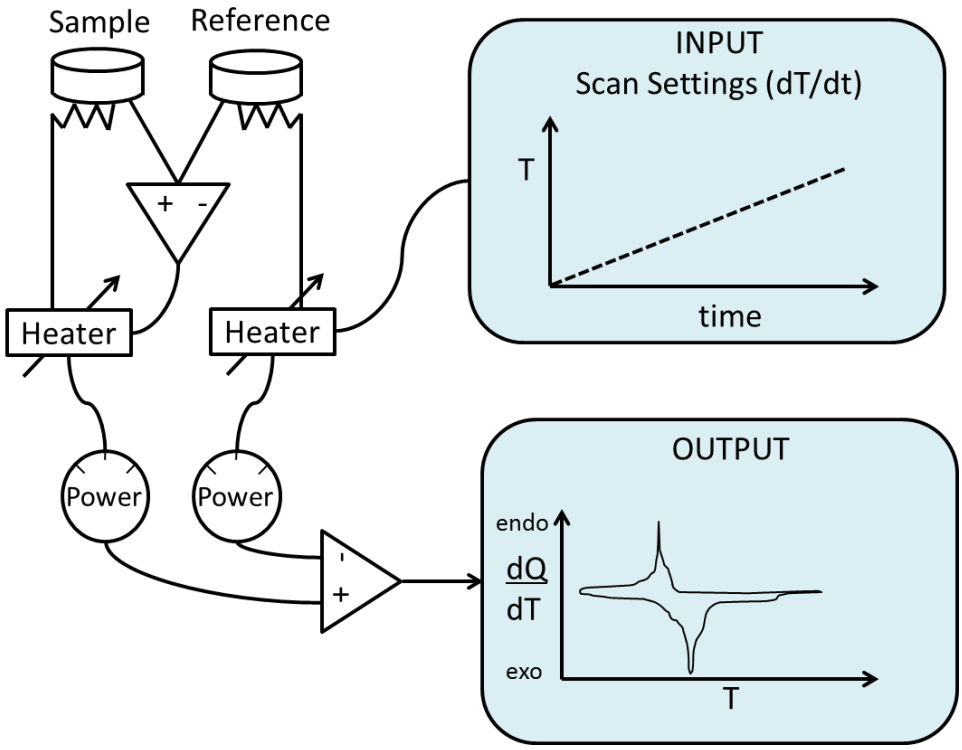

Figure 45 - Diagram of how a DSC extracts thermodynamic information from a sample.

In standard operation, the sample crucible (Al_2O_3 with salt) and reference crucible (empty Al_2O_3) are heated with the goal of keeping both crucibles at equivalent temperatures. Because the sample crucible contains material with an additional specific heat and which may also undergo unknown phase transformations, this crucible will require a different amount of heat flow to

achieve this isothermal goal. As a result, the device increases or decreases, in situ, the heat flow to the sample crucible in order to equilibrate these two systems. The difference in heat flow between the sample and reference crucible is then registered and shown as a heat flux. Because the system is maintained in an inert environment at constant pressure, the heat flow is thermodynamically equivalent to enthalpic changes. This method provides a means of very accurately identifying the temperature at which phase transformations commence and, with the correct software, other properties such as latent heats of transformation and specific heats.

For this study, the interest lies in reproducibly measuring the temperatures at which transformations occur as this will allow for a more accurate NaOH-NaI phase diagram. For this task, the system must first have a baseline signal run to account for the standard heat absorption of the Al_2O_3 crucibles as well as the flowing inert shield gas, argon. This is accomplished by running both the sample and reference crucibles empty. The signal is then attached as a baseline to all subsequent runs. Following this, a calibration must be conducted for both the heat flow (y-axis) as well as the temperature (x-axis) derived from the sample crucible thermocouple and amplifier. To do this, five ultra-high purity calibration metals (In, Sn, Bi, Zn, and Al) that melted around the expected range of the salt's transformations were studied. Figure 46 shows one of the three runs conducted on the indium. Figure 46 is also provided in order to demonstrate how melting (endothermic) and freezing (exothermic) signatures look. The choice of y-axis direction is arbitrary but the nomenclature of exo/endo refers to the evolution or input of energy from/to a sample, respectively. In the case of melting (blue curve), energy is input into the system and the curve therefore traces an endothermic (positive energy) process.

Upon lowering the temperature (purple) the sample freezes and emits energy and this is therefore shown as an exothermic (negative energy) process. An entire temperature

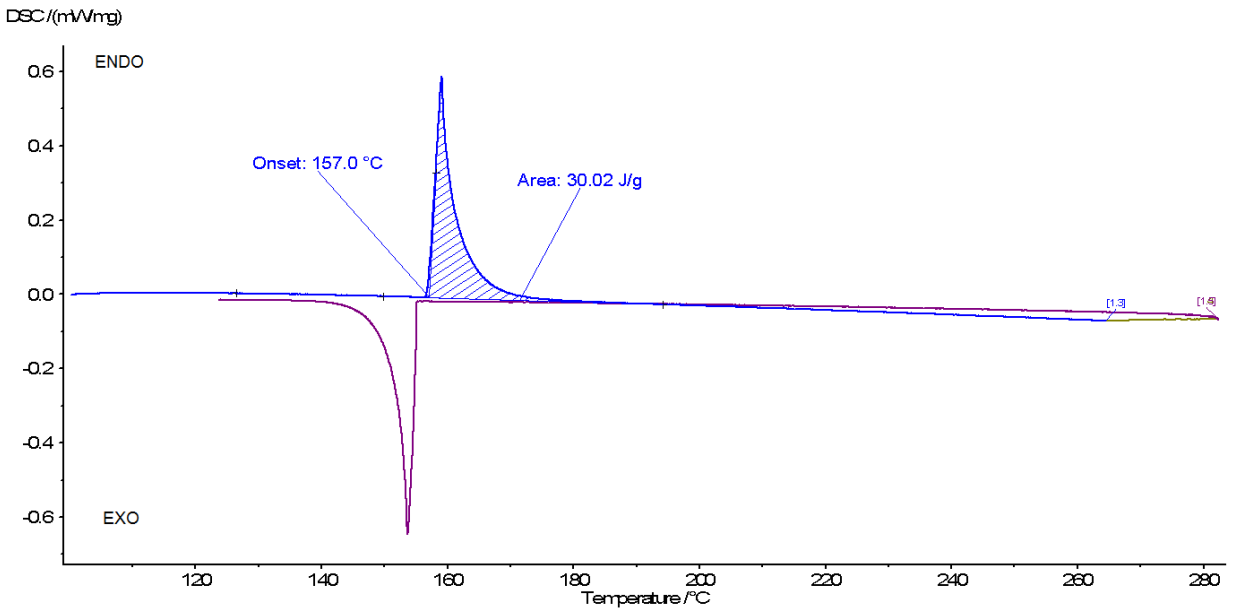

Figure 46 - DSC scan of an indium calibration material. Blue curve shows melting upon temperature increase and purple curve tracks the freezing process upon temperature decrease.

process that passes through this transition point exo- and endothermically is hereafter referred to as a cycle. Each of the five calibration materials was cycled three times and the transition temperature (peak onset) and heat evolution (peak area) were averaged. These ten values (5 temperatures and 5 energies) were then compared with known thermodynamic data and fitted using a proprietary equation that accounts for the configuration of the machine. This curve is then used as the calibration curve for all subsequent salt sample measurements. This ensures that all measurements made on the salt fall near anchored points on a calibration curve (Figure 47).

With calibration in hand, salt samples of various compositions were synthesized as per the process in 5.2.1. Table 27 shows the common molar percentages synthesized for DSC study. Because each DSC run only required 10-20 mg of binary salt per experiment, multiple experiments could be run with each synthesized sample in order to ensure against compositional heterogeneity.

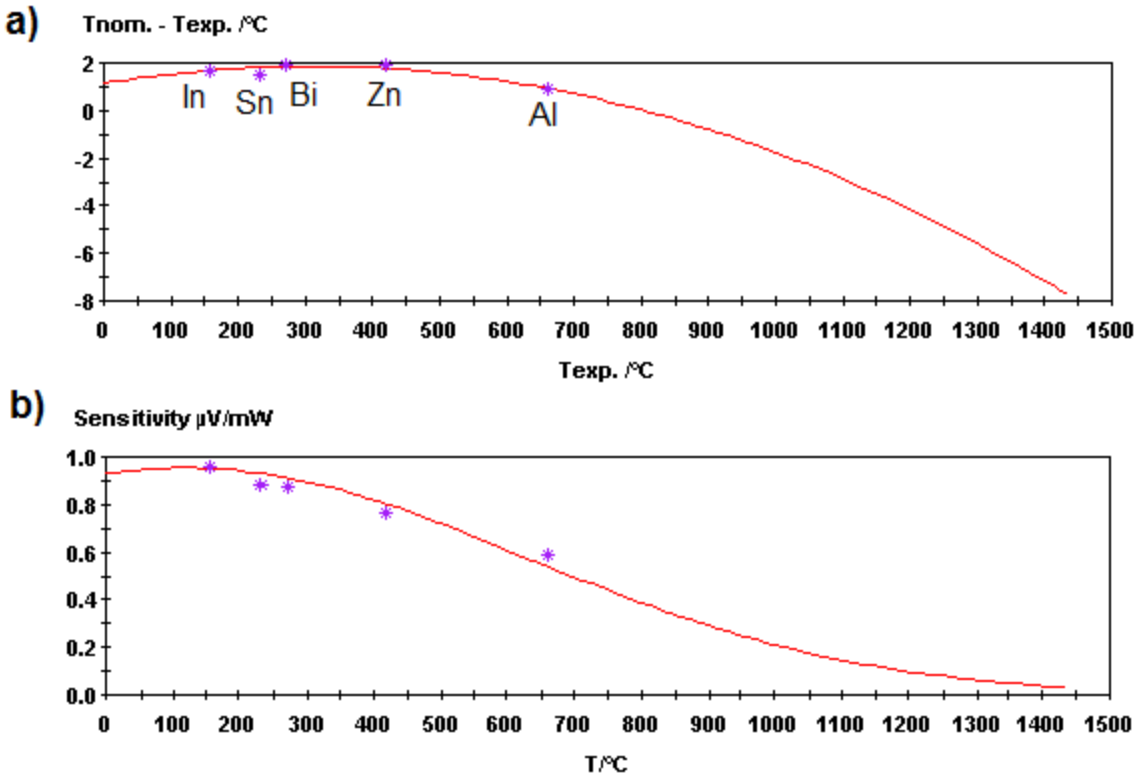

Figure 47 – DSC calibration curves for a) x-axis temperature calibration and b) y-axis heat flow calibration.

When variations in collected signals were found, the salt was further pulverized and additional experiments were run to identify the prevailing signals for the bulk salt.

Table 27 - Binary NaOH/NaI samples synthesized for DSC study

ID	Mole % NaI +/- 0.3%	Mole % NaOH +/- 0.3%	Number of unique samples	Number of Experiments Run
NaI	100%	0%	1	1
NaOH	0%	100%	2	3
1	10%	90%	2	2
2	20%	80%	3	7
3	30%	70%	3	5
4	50%	50%	3	5
5	70%	30%	1	3
6	90%	10%	1	1
7	40%	60%	1	1
8	60%	40%	1	1

In addition, most samples were newly synthesized several months later and rerun with an updated calibration to ensure against impacts from salt moisture levels, device drift, and differences between NaOH and NaI source material. Figure 48 shows the hierarchy of measurements.

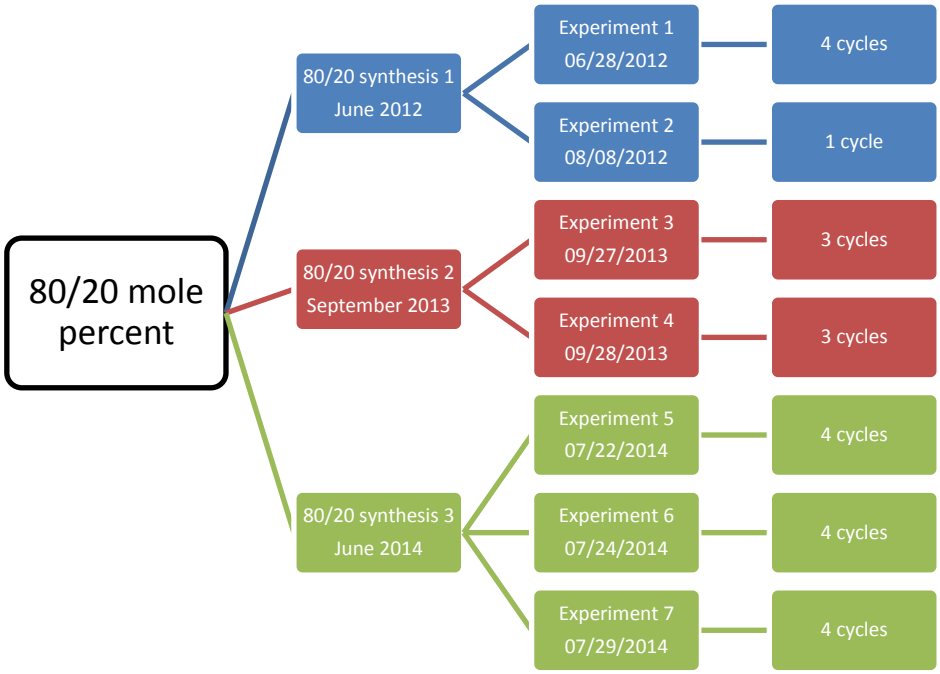

Figure 48 - Hierarchy of DSC measurements for the 80/20 sample. Each piece of transition data comes from a single cycle.

All thermal measurements were carried out on a Netzsch STA 409 CD in differential scanning calorimetry mode. Crucibles were composed of Al_2O_3 and were not sealed to allow for constant pressure measurements in the argon environment. Because of this, salt samples were briefly (<10 s) exposed to dry atmospheric conditions. Each experiment began with a wide-range temperature scan at 20 °C/min to initially identify all phase transformations followed by multiple cycles through each targeted phase transition. Transition temperatures were only extracted from temperature increases in order to avoid error from super-cooling effects. At the end of each temperature cycle, the sample was left to anneal at sub-transition temperatures to minimize the presence of non-equilibrium transitions involving metastable phases (Figure 49).

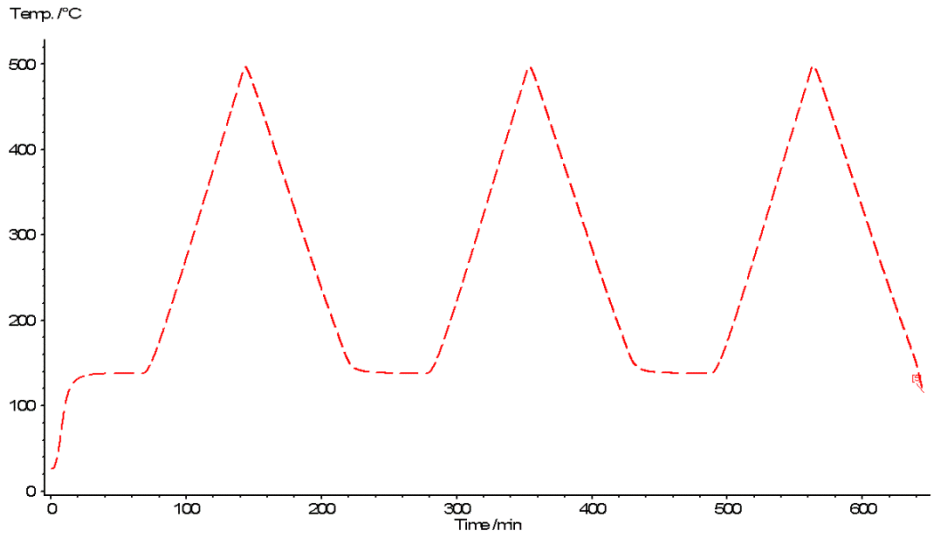

Figure 49 - Example of an experiment with 3 temperature cycles.

For transitions that were separated by temperature intervals exceeding 100°C, each individual signal was characterized by a discrete set of temperature cycles. Only phase signals that appeared in all temperature cycles for all samples have been proposed as points on the phase diagram and used in subsequent modeling.

5.3.3 X-Ray Diffraction (XRD) Studies

In concert with thermal analysis from the previous section, X-Ray Diffraction (XRD) was employed to elucidate or confirm the presence of compound phases. Prior to XRD, samples were pulverized and annealed for at least one week at sub-transition[i] temperatures to ensure homogeneity and the removal of metastable phases. In addition, XRD compound study samples were synthesized with slight excess such that compositions were ensured to fall between the proposed compound and the closest unary end component (Table 28). For example, $Na_5(OH)I_4$ had a 0.1 molar percent excess towards NaI to minimize the appearance of signals from more NaOH-rich compounds in the signal.

[i] In the case of incongruently melting compounds, the temperatures used were those slightly below the proposed peritectic temperatures.

Table 28 - Proposed compounds investigated by XRD

Compound	mass NaI	mass NaOH	mole % NaI	mole % NaOH
$Na_5(OH)I_4$	14.167	0.939	80.10%	19.90%
$Na_7(OH)_5I_2$	8.992	6.107	28.20%	71.80%

XRD was performed on a PANalytical X'Pert Pro Multipurpose Diffractometer with a rotating sample stage (1 Hz) and Bragg-Brentano divergent beam optics for 12 hours per scan at 1,000 s/step scan rate. The setup used a 1.8 kW sealed X-ray tube with Cu source, nickel filter, and programmable fixed slit of ¼. Due to the hygroscopicity of salt samples, a special air-sensitive sample holder was prepared in an argon-filled glovebox to prevent atmospheric contamination. The polymer dome creates known low-angle scattering that can be accounted for during data processing (Figure 50).

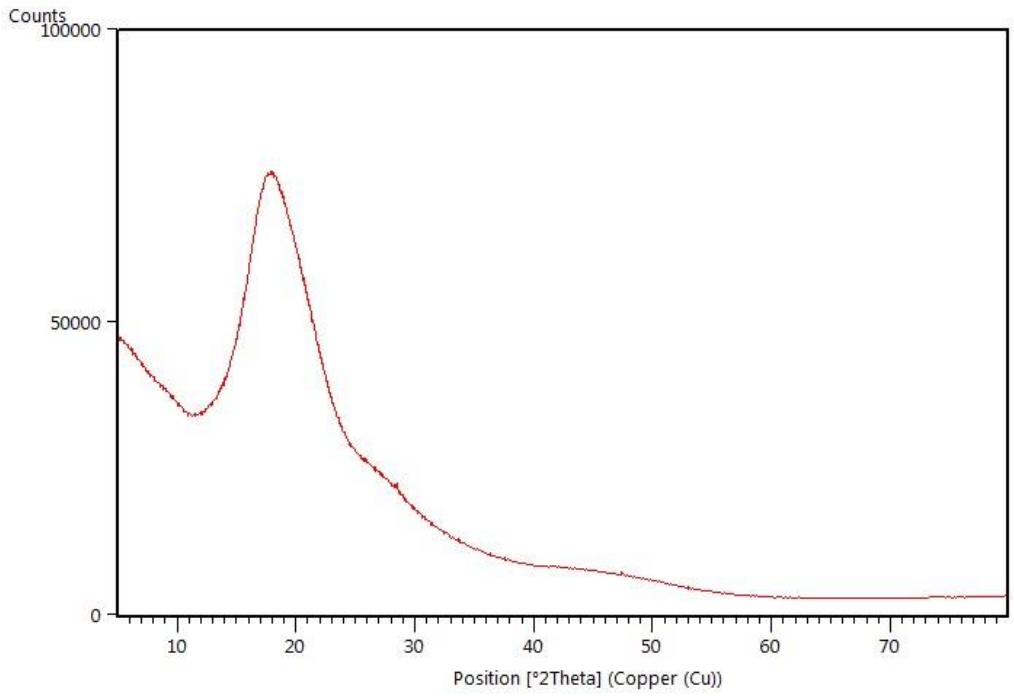

Figure 50 - Predictable low-angle background from air-sensitive sample holder. Spectrum collected with 1000s/step from 2 theta ranging from 5° to 90°.

Analysis took place using PANalytical HighScore Plus software that allowed for amorphous polymer dome scatter fitting as well as crystallographic indexing methods. Powder diffraction files were obtained from ICDD PDF-4+ database and used for compound identification.

5.3.4 Thermodynamic Modeling

The computational thermodynamic modeling performed to optimize the parameters of the theoretical model necessary to reproduce the phase diagram data of the binary system NaI-NaOH has been carried out according to the CALPHAD method within the FACTSage Thermochemical Software package[219]. Values of the model parameters were optimized with the Optisage module of FactSage leveraging the NOMADS algorithm[220, 221]. The method proposes the simultaneous optimization[i] of all Gibbs free energy functions of existing components within the phase diagram including the binary liquid phase (solution model), all intermediate compounds and pure end members (Equation 32-Equation 37), and solid solutions (if applicable).

$$G(T)_{pure\ substance} = H(T) - T \cdot S(T) \quad \text{Equation 32}$$

$$where\ H(T) = H_{298} + \int_{298}^{T} c_p \cdot dT \quad \text{Equation 33}$$

$$where\ S(T) = S_{298} + \int_{298}^{T} {c_p}/{T} \cdot dT \quad \text{Equation 34}$$

$$\therefore\ G(T)_{pure\ substance} = H_{298} + \int_{298}^{T} c_p \cdot dT + S_{298} + T \cdot \int_{298}^{T} {c_p}/{T} \cdot dT \quad \text{Equation 35}$$

$$where\ c_p(T) \sim a + b \cdot T + c \cdot T^{-2} \quad \text{Equation 36}$$

$$\therefore\ G(T)_{pure\ substance} = A + B \cdot T + C \cdot Tln(T) + D \cdot T^2 + E \cdot T^3 + F/T^2 \quad \text{Equation 37}$$

[i] By optimization it is meant that a global minima must be searched for amongst the various Gibbs free energy functions in such a way as they generate phase boundaries that closely follow those found via experimental interrogation.

In this case, the thermodynamic properties for the liquid phase and intermediate compounds have not been measured and as a result a thermodynamic solution model for the liquid phase must be proposed and a Kopp-Neumann linear approximation for the enthalpy of formation, absolute entropy, and temperature dependent heat capacity must be used as a first approximation for the intermediate compounds.

In lieu of reliable thermodynamic data (ΔH_f, $H_{298,}$ C_p) for these compounds it is possible to leverage the phase transformation data identified from our DSC study as well as phase equilibria data collected in previous literature. In particular, points in the temperature-composition (T-X_i) space corresponding to the liquidus, peritectic transitions, and eutectic transitions are valuable because these points represent conditions in which two or more phases are in equilibrium with each other. These locations allow us to create equivalences and therefore constraints upon the Gibbs free energy relations for the relevant compounds.

Figure 51 shows the most up-to-date optimized phase diagram for the NaOH-NaI prior to the work in this dissertation. It is provided to give a visual example of the step-wise optimization method used to improve the thermodynamic modeling of the binary system with new experimental data. The method consists of modeling the thermodynamic properties of a system by first considering the unary end-members, i.e. NaOH and NaI, for which the thermodynamic properties have been well characterized. For most common compounds these properties are available in thermodynamic compilations[222] as well as in databases used by thermodynamic calculations software. For the present work, data for NaOH and NaI have been taken from the *Pure Substances* database (FactPS) of FactSage 6.3[223]. The established Gibbs free energy functions for these unary end members are used to optimize the parameters of the solution model for the binary liquid along all liquidus points in which the end members are in equilibrium with

the liquid. This process creates an initial estimation for the liquid's Redlich-Kister parameters. Optimization "1" is shown in the blue circle.

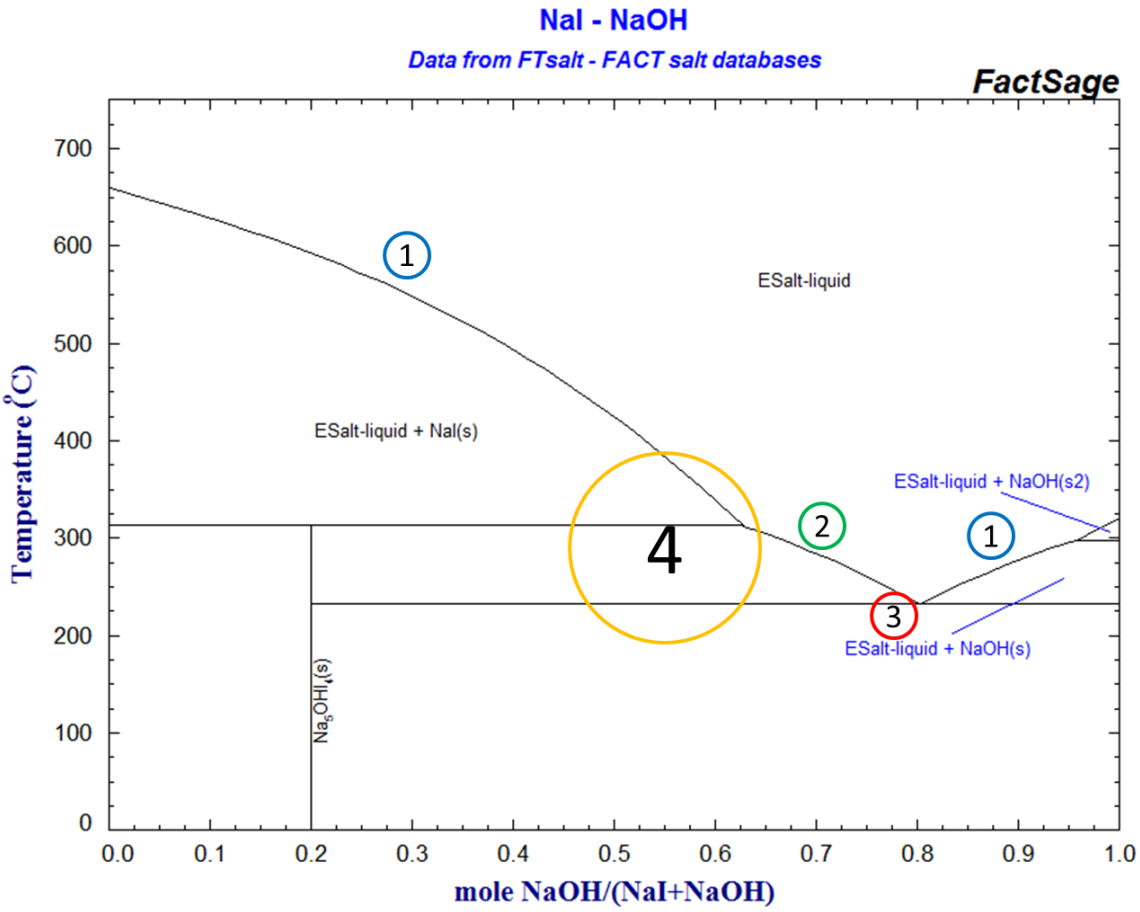

Figure 51 - Sangster's optimized phase diagram as generated using the FactSage thermochemical software suite. This phase diagram is provided to demonstrate the optimization steps followed during the CALPHAD method.

From there, the initial solution model for the liquid is then used to optimize proposed intermediate compound(s). Because the compounds began with linear approximations of the coefficients of their thermodynamic free energy function finding a set of coefficients that reproduce the experimental data requires multiple iterations. In the case of Figure 51this corresponds to the optimization step "2" using the single compound $Na_5(OH)I_4$. The new values for the compound(s) are then further optimized with the proposed eutectic point as this invariant point creates thermodynamic relationships between the solution, the unary end member NaOH,

and $Na_5(OH)I_4$ (step "3" in red). Finally, having found the Gibbs free energy coefficients that locally minimize the free energy of the system, the entire phase diagram with all phases is run with the hope of identifying a global minima with consideration all constraints (step "4" in orange).

5.3.5 Electrochemical Measurements

All electrochemical measurements were performed using an AutoLab PGSTAT 302N potentiostat/galvanostat. Experiments were conducted within a sealed, argon-filled, stainless steel chamber that was placed inside of a PID-controlled Thermo Scientific furnace. The stainless steel chamber is designed (Figure 41) with ultratorr ports to allow multiple air-tight and insulated electrodes and thermocouples access to the electrochemical system. The eutectic salt was held in a Ni-201 crucible surrounded by an Al_2O_3 crucible to shield the melt crucible from electrical contact to the stainless steel chamber and the chamber was electrically grounded to minimize induction from the furnace coils.

Cyclic voltammetry requires, at minimum, a three-electrode setup (Figure 52) in order to accurately probe the analyte (electrolyte) redox behavior.

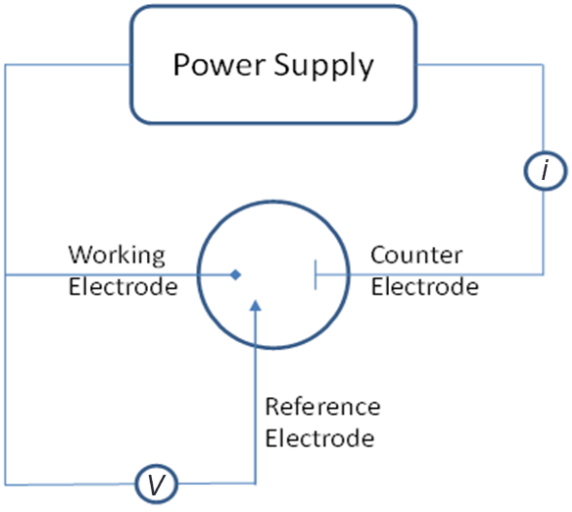

Figure 52 - Schematic of a 3-electrode setup.

By providing a counter electrode to supply current, it is possible to avoid polarization of the reference electrode which makes the critical voltage measurement of the working electrode. The goal of a cyclic voltammetry experiment is to scan for oxidation or reduction reactions via a current signal generated during a linear ramp the voltage between the reference and working potential. This current may occur either a) due to the electrolyte being driven to react due to the potential difference between the working and reference or b) because the working electrode itself is driven to undergo a reaction due to the driving force of the potential. As a result, the stability of electrode materials is critical to be able to make valid measurements of an electrolyte's electrochemical window or oxidation/reduction species.

As has been shown in section 5.2.1, nickel, silver, and platinum are all stable when placed within the binary melt. It is now important to consider the possibility of what happens when these metals are polarized with respect to each other and have access to the melt as a means for electrical communication. Figure 53 shows a theoretical voltage window of the binary melt that is bounded by the cathodic limiting reaction (Na reduction, red) on the left side and the

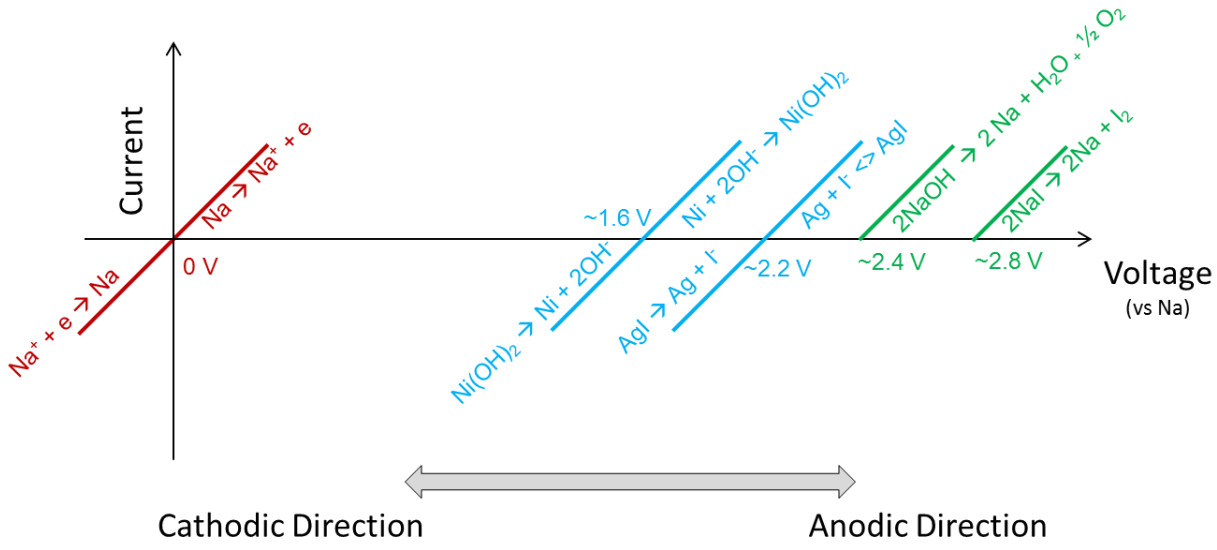

Figure 53 - Theoretical electrochemical window with potential side reactions of metals found to be stable in corrosion tests.

anodic limiting reactions (oxygen and iodine gas evolution, green) on the right side. This range, known as the electrochemical window (ECW) of the electrolyte, is set at 0V for sodium deposition and defines the range of voltages that the electrolyte can withstand before breakdown. Reactions that produce only condensed phase products are shown with the reaction line occurring above and below the abscissa to indicate potential reversibility. Reactions that entail the creation of a gaseous phase are shown only with the reaction line occurring in the anodic direction to indicate the unlikelihood of reversibility due to gas evolution. It is also important to note that the voltages shown in Figure 53 are only approximate and correspond to calculations of pure, activity equals one, components. As a result, though sodium deposition will still be set as zero as the reference point, the voltages at which other reactions occur with respect Na/Na^+ will vary the as the constituents are moved further away from ideal conditions.

Thermodynamic calculations with FactSage, coupled with experimental studies of each metal, have identified key reactions that prohibit the use of certain metals at certain polarizations along the voltage window. The blue lines show the reaction of nickel and silver with hydroxide and iodide, respectively. As a nickel wire is polarized to around 1.6V anodic of a pure sodium reference electrode, it undergoes an oxidation to form $Ni(OH)_2$. This reaction has been observed via the formation of a water-insoluble green product on nickel wires following cyclic voltammetry experiments. Similarly, by polarizing silver 2.2 V anodic of sodium metal it is possible to generate AgI. An Ag probe is shown in Figure 54 in a post-mortem SEM of a Ni working electrode wire as well as its dissolution in H_2SO_4 and formation of yellow iodine species. As a result, neither Ni or Ag would make good anodic sweep working electrodes as they would tend to react before reaching the major electrolyte oxidation events of interest (O_2 and I_2).

Unlike the other two materials platinum showed no anodic reactivity with the melt over the experimental range though suffers from solubility with deposited sodium metal in a similar fashion to Ag. Both platinum[224] and silver[225] form intermetallic compounds with sodium (NaPt, $NaPt_2$, and $NaAg_2$) and result in unpredictable mixed potentials on the working electrode where sodium is deposited upon cathodic sweeps. As a result, neither of these metals is satisfactory to serve as a cathodic working electrode. Nickel, by contrast, forms no intermetallics or alloys[226] and is therefore an ideal electrode material for cathodic (depositive) sweeps.

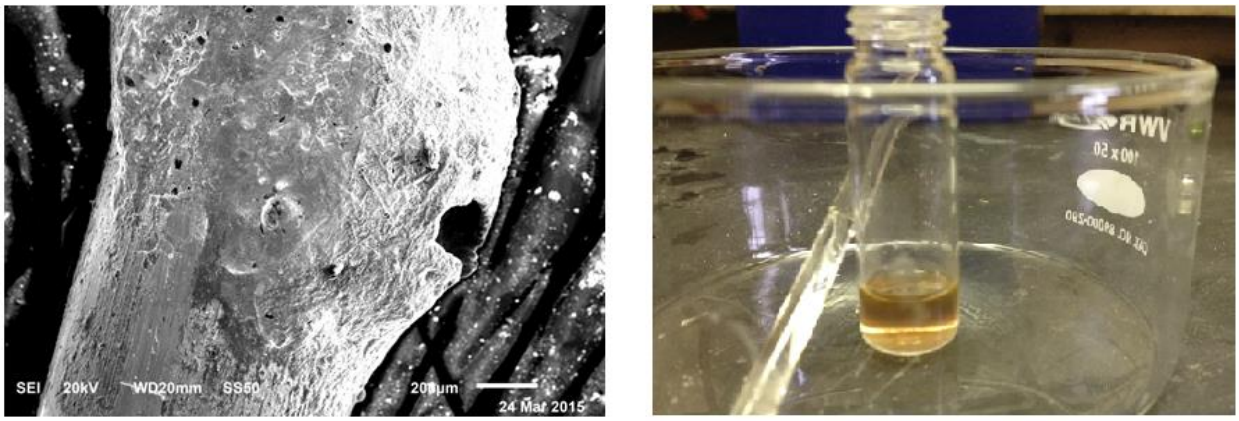

Figure 54 – On left, an SEM (scale bar 20um) image of the product accumulated on a silver wire after holding at 2.2 V for 1 minute. This material was found to have high iodine content from chemical mapping. On right, the same wire immersed in H_2SO_4 bath. The yellow is an indicator for iodine species.

From these electrode compatibility studies it is therefore proposed that cyclic voltammetry be broken into a separate cathodic and anodic sweeps in which the cathodic sweep deposits sodium metal on a nickel working electrode whereas on the anodic sweep oxygen and iodine may be generated on a platinum working electrode. By the same logic, the counter electrode is to be made of the opposite metal as this is where the opposite redox reaction occurs. In the case of sodium deposition on the nickel working electrode, the counter electrode facilitates an oxidation and is therefore to be made of platinum. Upon sweep reversal, the oxidation that occurs on a platinum working electrode will generate electrons that will be sent around the circuit to a nickel counter electrode where sodium is likely to be produced.

The final electrode required for cyclic voltammetry studies is the reference electrode. This is, in many cases, the most challenging electrode to design as it must maintain a stable, well-defined electrochemical potential throughout the lifetime of the experiment. In addition, the reference electrode should demonstrate a low impedance in order to minimize the impact of uncompensated resistance in voltage measurements. Finally, the fact that this stable reference electrode must operate without drift at temperatures over 100°C and must be in contact with a caustic melt rules out all forms of aqueous- or silica-based reference systems.

In order to fulfil these requirements, a reference electrode inspired by the negative electrode design of a Na-S battery was developed. In this new electrode design, high purity sodium metal (>99.98%) is stored inside of a β''-Al_2O_3 tube (6.5 mm Ø, Ionotec) that is submersed inside of the molten salt. The well-established ionic conductivity of the β''-Al_2O_3 acts as the communication channel for Na^+ while at the same time prevents direct contact between the sodium metal and the rest of the melt. This is critically important as the degree of reactivity and solubility of sodium metal are still not fully quantitatively established. Figure 55 shows the low DC impedance exhibited by the system. For a current of less than a microamp passing through the reference and working, this corresponds to less than a millivolt of DC error and is therefore considered negligible. Figure 56 shows the various types of electrodes used in a standard CV experiment. Working and counter electrodes utilized Ø 1 mm platinum and nickel wires (99.95% Sigma Aldrich and 99.98% Goodfellow, respectively). Of note are that all electrodes are sheathed in Al_2O_3 rods to protect them from shorts and that the counter electrode exposed area is at least 10 times larger than the working electrodes. Also, the electrical lead wire for the reference electrode was chosen to be tantalum (99.95% Ø 1 mm, Alfa Aesar) due to its complete immiscibility with liquid sodium metal.

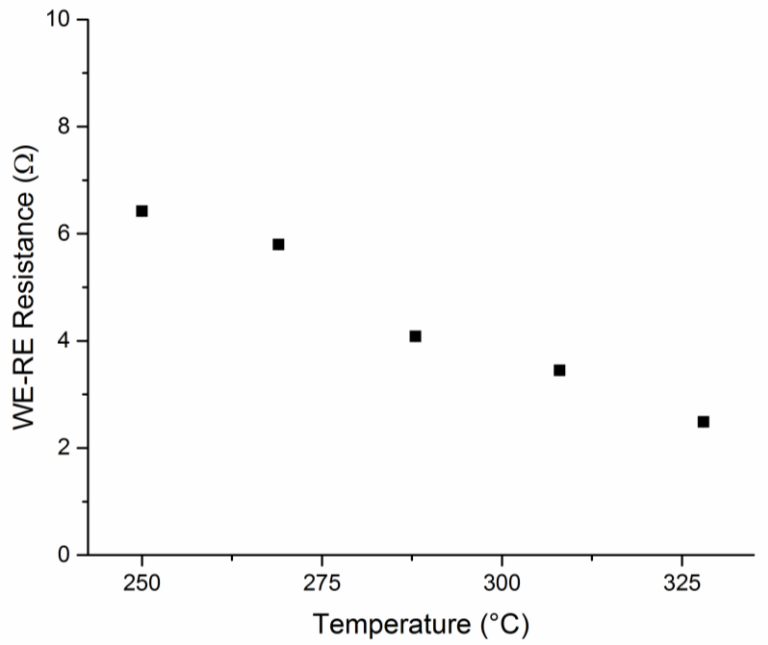

Figure 55 - Impedance between TaNaB reference electrode and platinum working electrode. Reference area is ~6 cm^2 and working electrode is ~0.3 cm^2

Because the reference electrode is constructed as Ta-Na-β''-Al_2O_3 it will hereafter refer to it as a TaNaB reference electrode.

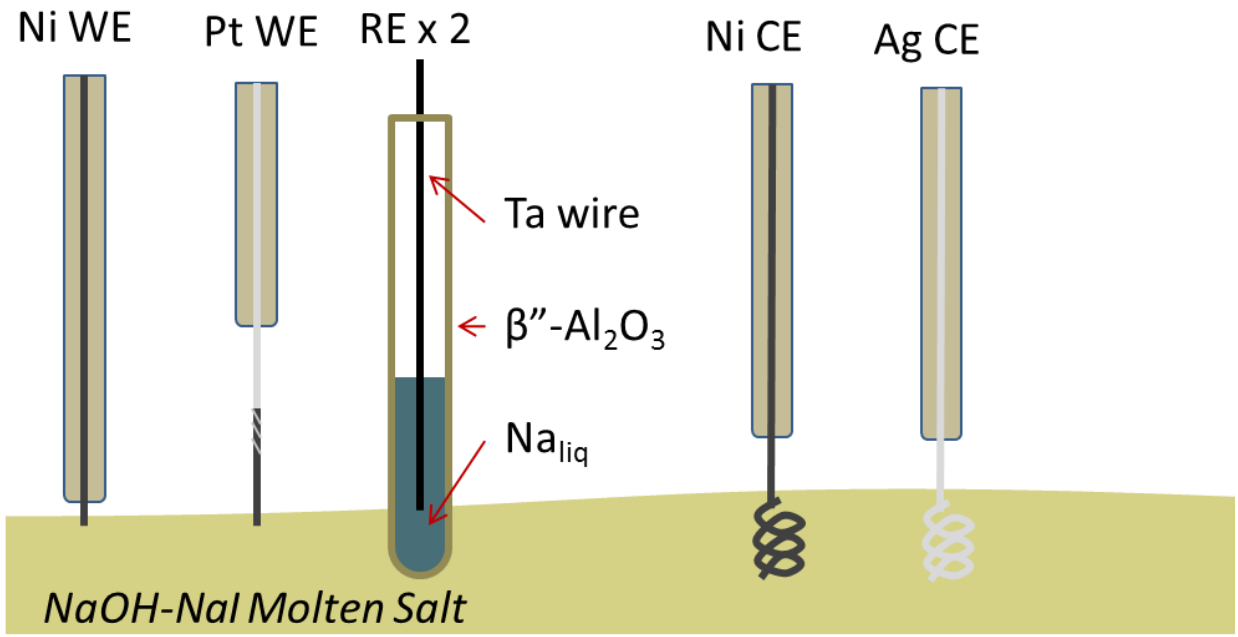

Figure 56 - A summary of the electrodes used in the various CV experiments.

It is also worth noting that all CV-type experiments used two reference electrodes in order to monitor if there was any drift throughout the experiment. Before each day of measurements the two references had their open circuit potentials measured against each other and against known sodium deposition in order to quantify their drift.

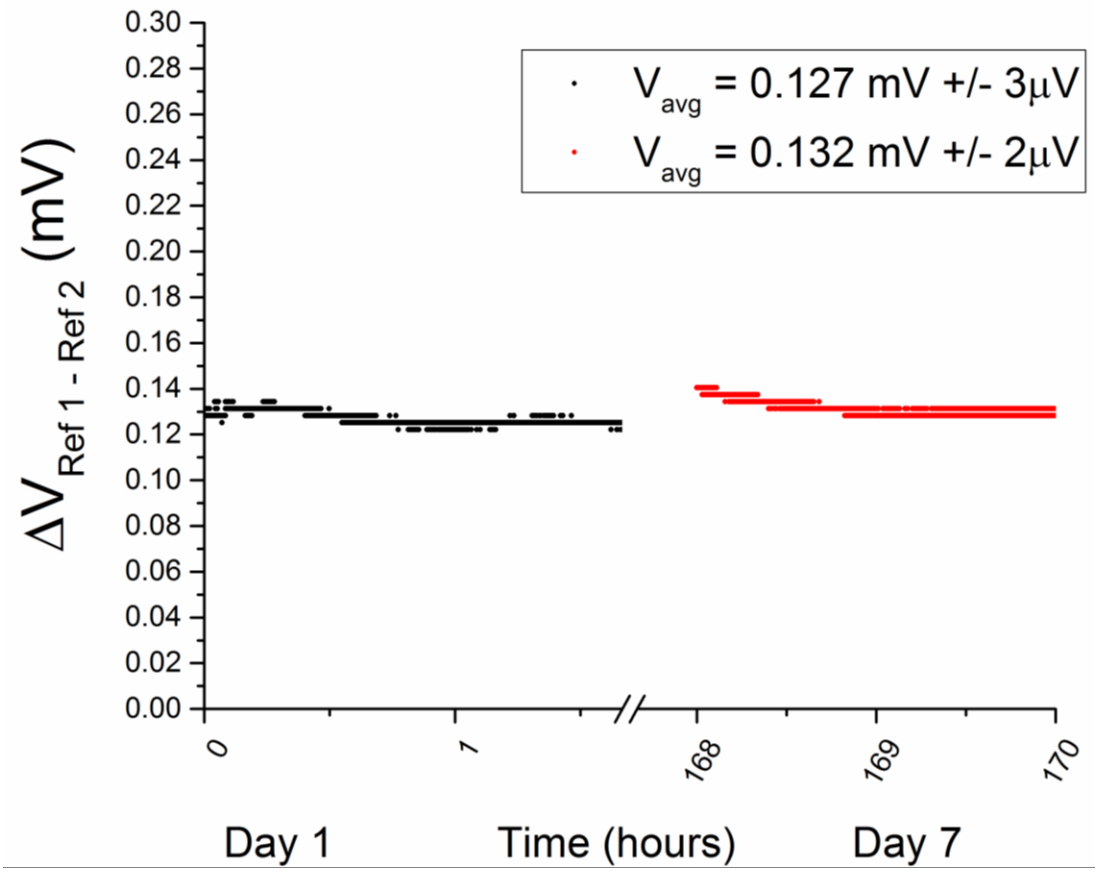

Figure 57 - Drift between TANAB reference electrodes after one week of experimentation.

As can be seen, measurements demonstrated excellent electrode stability with a voltage shift only 5 μV over a seven-day period. These measurements also showed no discernable drift away from sodium deposition at 0 V. For this reason, the TaNaB electrode is here presented as an excellent new type of high-temperature reference electrode for molten salt systems.

By way of example, Figure 58 depicts a cathodic voltammetry study in which a nickel and platinum working electrodes and a TaNaB reference electrode were deployed. This particular

scan was run at a fast rate of 25 mV/s whereas most scans to be described were run at between 1 to 10 mV/s.

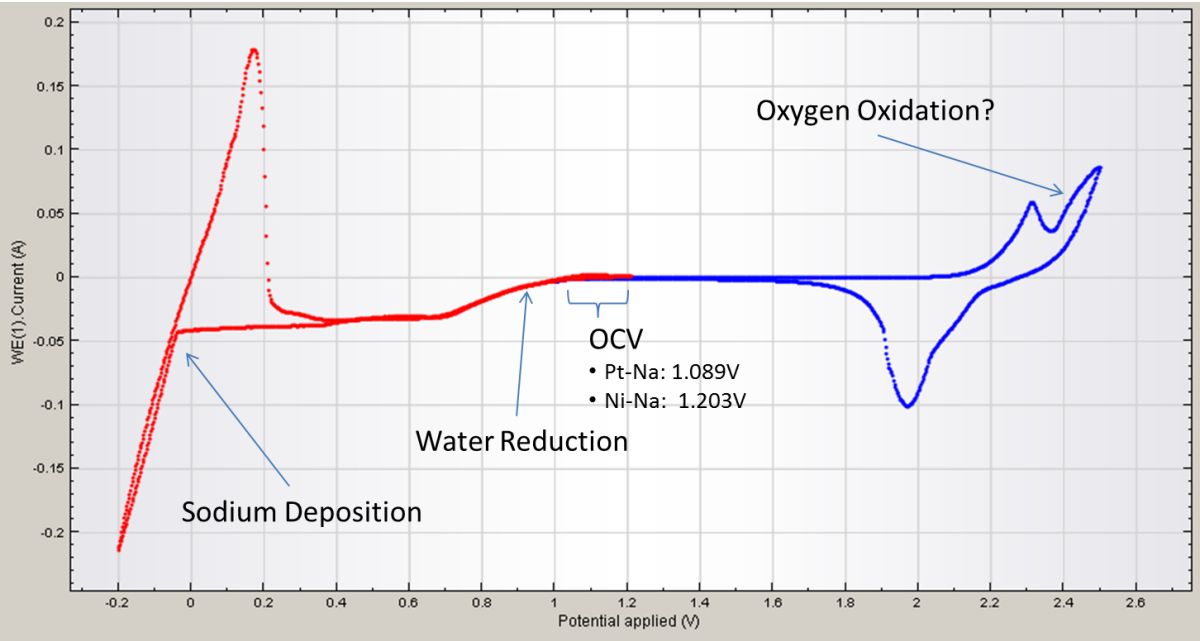

Figure 58 - Example CV of an undried NaOH/NaI (80/20) electrolyte at 25 mV/s.

In this study, because the TANAB reference electrode uses sodium metal as its reference point, 0 V on this figure corresponds to the deposition of sodium on the nickel working electrode (red scan) whereas the oxidation at high potentials occurs on platinum (blue scan). These two scans can be stitched together as the reference electrode used in both is the same. Other noteworthy features in this scan are the oxidation peaks occurring between 2.2 and 2.4 V and the steady reductive signal beginning at 1 V and remaining present at all increasingly cathodic potentials. The former features will later be revealed to be an oxidative signal corresponding to the oxidation of Na_xO_y species and the latter signal is related to the presence of moisture within the sample. Other studies and similarly found hydrogen reduction to occur at between 0.9 to 1.0 V positive of sodium metal. Because this experiment was an early study it was not fully dried before running the CV. This digression is therefore presented to highlight the importance of a robust salt drying procedure as discussed in Section 5.2.1.

5.3.6 Cell Cycling Study

In order to test the viability of the NaOH-NaI binary system, it was employed in a proof-of-concept liquid metal battery device to determine its actual operation during charge and discharge. An electrochemical cell consisting of a Na negative electrode, a eutectic Pb-Bi alloy (44-56 mole %) positive electrode, and the eutectic NaOH-NaI salt was assembled (Figure 59).

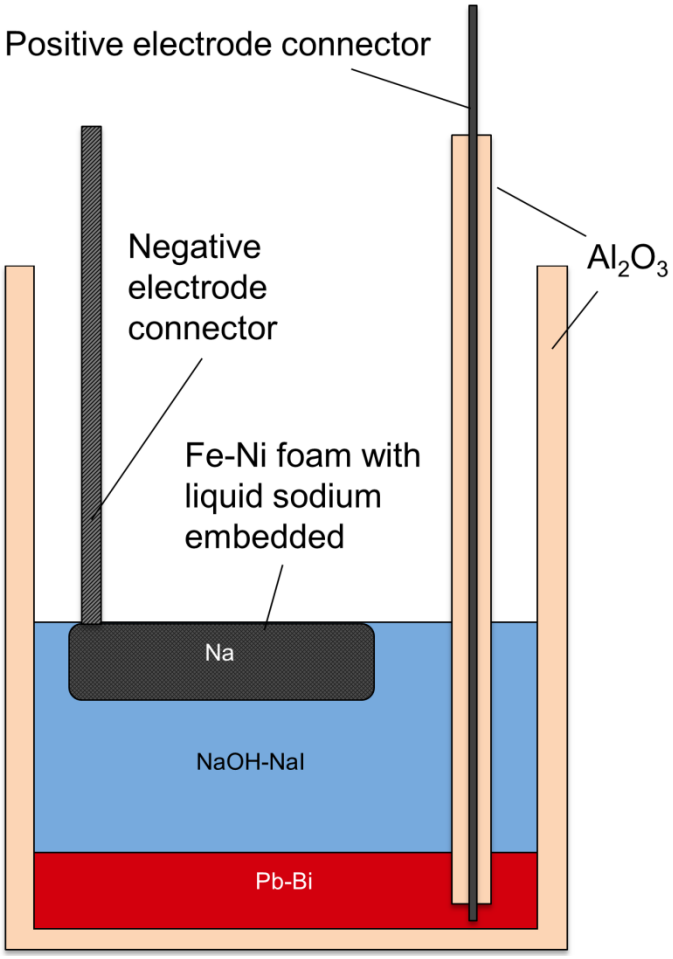

Figure 59 - Proof-of-concept cell utilizing the eutectic NaOH-NaI binary system.

In this device the decision was made to only use construction materials that are already in use in laboratory-scale LMBs. Because pure nickel is too expensive to use for the cell body or the larger negative current collector (NCC), the decision was made to instead use an industrially common Fe-Ni foam compression-attached to a steel rod. The body was constructed from an Al_2O_3 crucible to simulate the presence of a ceramic insulating sheath, and the positive current

collector (PCC) utilized Ni due to its proven resistance to the salt and minimal solubility with lead or bismuth.

Cycling tests were performed using a Maccor (Model 4300) battery tester and a cycling program that tested charge/discharge cycles, impedance, and leakage current was run over the course of several weeks. The following cycling schedule was used to probe cycling performance, energy and coulombic efficiencies, and leakage current.

Table 29 - Na||Pb-Bi prototype cell cycling schedule

Step	Purpose	Control Variable	Cutoff
Initialize	Charge	Voltage = 1.2 V	t = 3 hours
	Rest	Current = 0 A	t = 1 min
Cycling Loop	Discharge	Current = 0.05 A	Voltage ≤ 0.05 V
	Rest	Current = 0 A	t = 1 min
	Charge	Current = 0.05 A	Voltage ≥ 1.21 V
	Leakage Current	Voltage = 1.2 V	t = 1 hour
	Rest	Current = 0 A	t = 1 min
End	Charge	Current = 0.05 A	Voltage ≥ 1.21 V

Following cycling the cell was sectioned post-mortem in order to investigate the state of the device and composition of the electrodes.

5.4 Results and Discussion

5.4.1 Differential Scanning Calorimetry (DSC) Results

Differential Scanning Calorimetry was conducted on the compounds shown in Table 27. These compounds produced a number of key signal types that correspond to different types of transitions within the binary space. First, one of the most important properties for usage in a

liquid metal battery is the lowest temperature at which a composition of the salt can be molten. This temperature, known as the eutectic temperature, features a single transition from a fully solid state into a fully liquid state without passage through a 2-phase region. This invariant point occurs at unique compositions and temperatures in a binary diagram. In the case of the NaOH-NaI system it was found to occur at approximately 80% NaOH and 20% NaI (Sample ID #2). Figure 60 shows a typical DSC scan of this sample through the eutectic. Important features to note are the strong endothermic signal upon heating at 220.3°C and exothermic signal upon cooling at 214.7°C upon cooling.

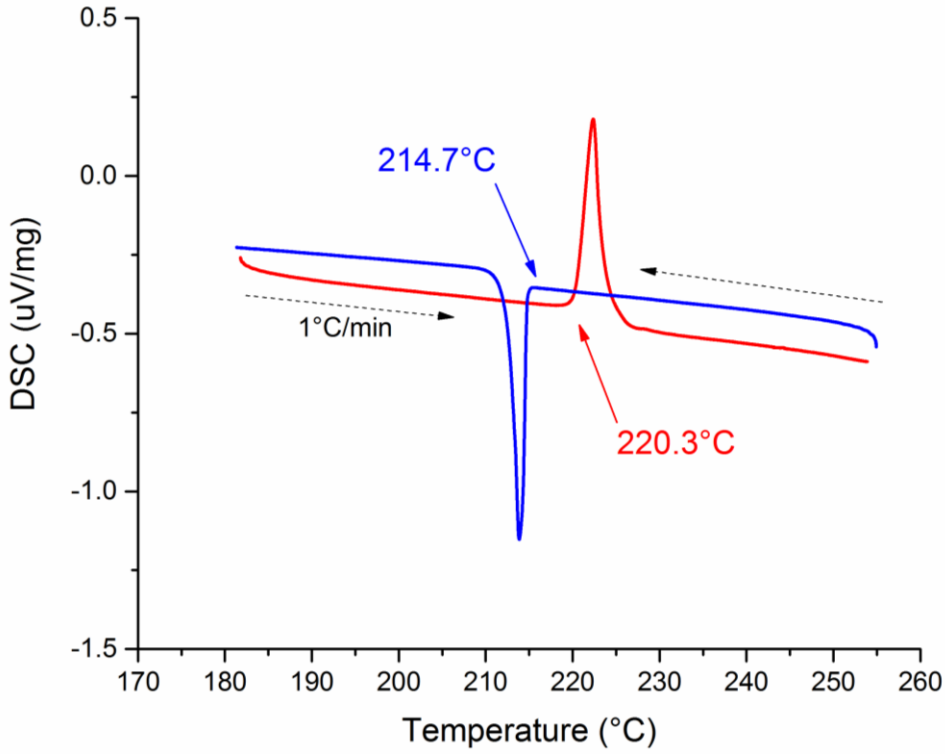

Figure 60 - 1 °C/min scan of an 80% NaOH - 20% NaI salt sample. Red signal corresponds to melting and blue corresponds to freezing.

These correspond to melting and freezing, respectively. Due to the tendency of molten salts to maintain their liquidity several degrees below freezing temperature (supercooling) the melting temperature is traditionally read only from the melting scan (red). For this reason, future DSC

spectra will principally only show the heating step of cycles. Another noteworthy point is that there is larger gap (5.6°C) between the melting and freezing signal beyond what is expected from super-cooling (usually 1-2°C). This hysteresis is due to the use of Al_2O_3 crucibles which limits heat transfer and responds sluggishly to heat removal. Such a lag will be seen in all future samples.

The final, key feature of the DSC graph is that the heat flow signal is very flat and stable following the melting event. This stability indicates no further endothermic processes are occurring following the initial melt signal at 220.3°C. Such stability leads to the conclusion that there is no passage through a 2-phase region prior to reaching a fully liquid state. For this reason it is proposed that the 80/20 mixture is quite close to the actual eutectic composition and that the eutectic melt temperature of the system is approximately 220°C.

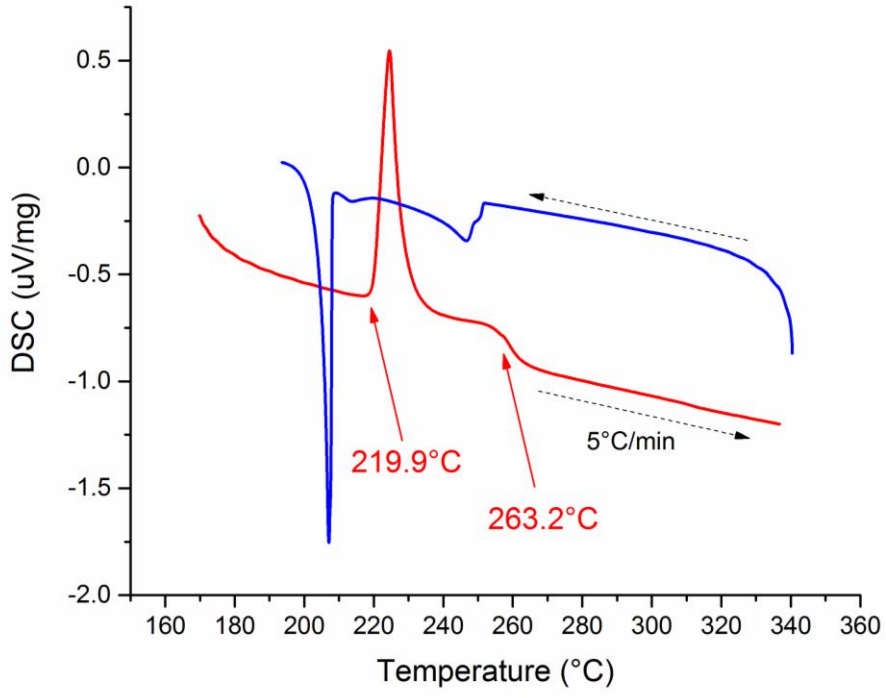

Figure 61 - 5 °C/min DSC scan of 90% NaOH and 10% NaI melt. The melting at 219.9°C is later followed by a slow exist from a 2-phase region.

Moving compositionally to the right of the eutectic shows clearly what happens as melting is accompanied by a two-phase transition region prior to full liquidity. Figure 61 shows clearly a composition in which the melting that first occurs at the eutectic temperature of 219.9°C is followed by a transition through a 2-phase region before exiting at 263.2°C. This behavior is best explained by exploring the process on a simplified phase diagram cartoon (Figure 62) in which the heating process follows the red dotted line.

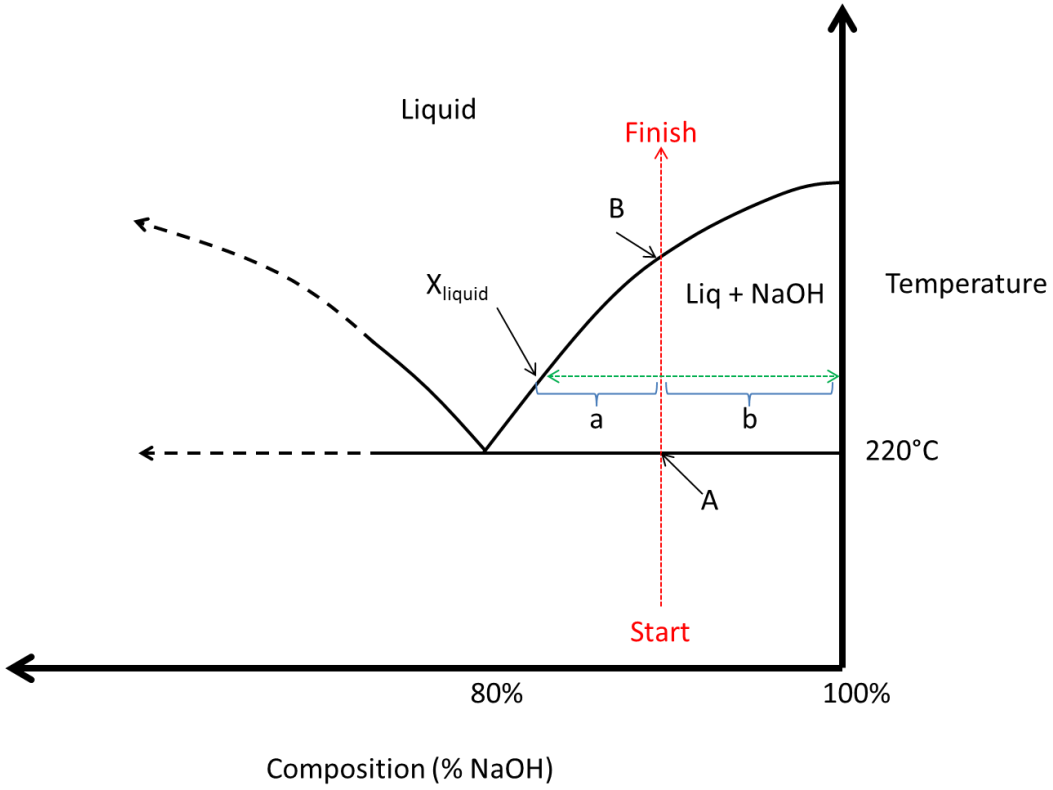

Figure 62 - Schematic depicting the passage through a 2-phase region and the compositional changes that occur.

In the figure above, as the 90% NaOH sample is heated it first passes through the eutectic temperature at point A and regsiters the signal at 219.9°C . Once through, the salt enters a two phase region in which the partial free energy of a liquid of composition X_{liquid}, is in equilibrium with that of the pure solid NaOH. At any point in the two-phase region the amount of liquid and solid can be determined by a lever rule according to Equation 38 and Equation 39.

$$amount\ liquid = {}^{b}/_{(b+a)} \qquad \text{Equation 38}$$

$$amount\ NaOH = {}^{a}/_{(b+a)} \qquad \text{Equation 39}$$

At each incrementally higher temperature, the liquid composition becomes further enriched in NaOH as it follows upwards along the liquidus line, each step entailing the incremental input of thermal energy to convert an infinitesimally small amount of solid NaOH into liquid NaOH and therefore enrich the liquid phase. Each of these energy inputs registers as an endothermic signal on the melting curve in Figure 61 and creates the hump following the eutectic transition. Upon reaching point B, the remaining solid NaOH is instantly converted to liquid and therefore the exit (and entrance) of the liquidus often corresponds to a peak. The width of the peak, as compared to that of the eutectic signal, is indicative of a process that does not happen instantly and rather lags behind the temperature slightly. It is for this reason that the strength of signal seen during the 2-phase region passage is highly correlated with the slope of the liquidus line. Larger slope lines create large signals as more material requires thermal input for transition per unit Celsius. More graduate liquidus curves create barely noticeable 2-phase signals and rarely present a clear exit as in Figure 61 due to the slower and less energy intense conversion process.

In the case of 90% NaOH and 10% NaI this slope is fortunately quite steep and provides us with the insight that the liquidus occurs at approximately 263°C for this composition. In addition to the single scan provided in Figure 61 it is important to run multiple studies on different days to check the reproducibility of the results as well as to test the impact of varying scan rates on phase transformation temperature. Figure 63 provides the results from DSC tests run on two different occasions with different 90/10 samples at varying scan rates. The results from these tests clearly show that the two transition points measured in Figure 61 are quite

reproducible. The eutectic measurement from Figure 60 is corroborated with a measurement averaging at 219.6°C and a tightly grouped set of data for the liquidus occurring at around 264°C with a standard deviation of around 2.5°C. Because these points have been found in all scans and appear with minimal scatter, these are considered good data and will be used for phase diagram construction.

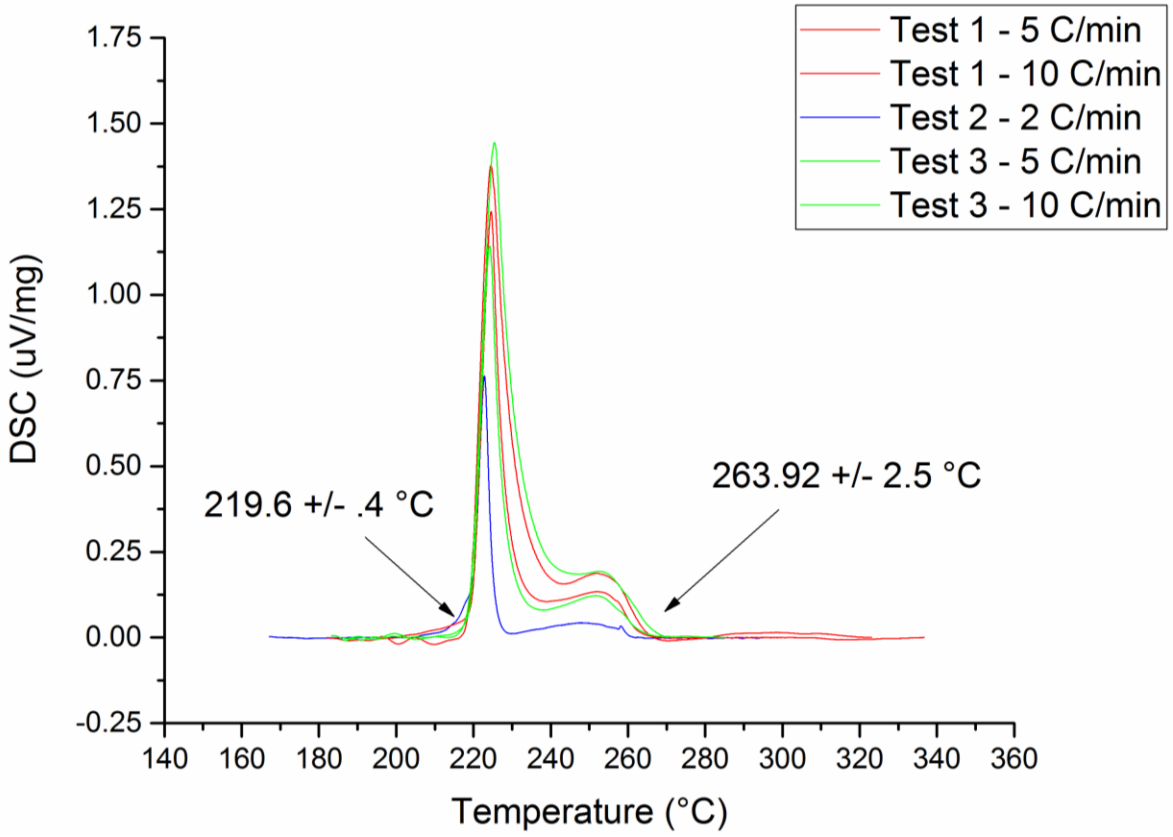

Figure 63 - DSC test run on 90% NaOH 10% NaI over two days with two different samples.

So far behaviors corresponding to a simple single-peak eutectic signal and a normal eutectic + liquidus measurement but have not yet found data for intermediate compounds. Specifically, for compounds that melt incongruently, it should be possible to identify clear signals within a scan that indicate the sudden appearance of an incongruent phase (from two phases) or disappearance (into two compositionally different phases). In fact, this is the case at

least twice in the NaOH-NaI binary system. Figure 64 shows scans of a 60/40 NaOH/NaI binary melt with two very clear peaks and what looks very similar to a two-phase passage with exist. The first, very small peak occurring around 218°C is again thought to be caused by the eutectic transformation from earlier. The latter, much larger peak at around 229°C is proposed to be from an as-yet unknown incongruently melting binary compound.

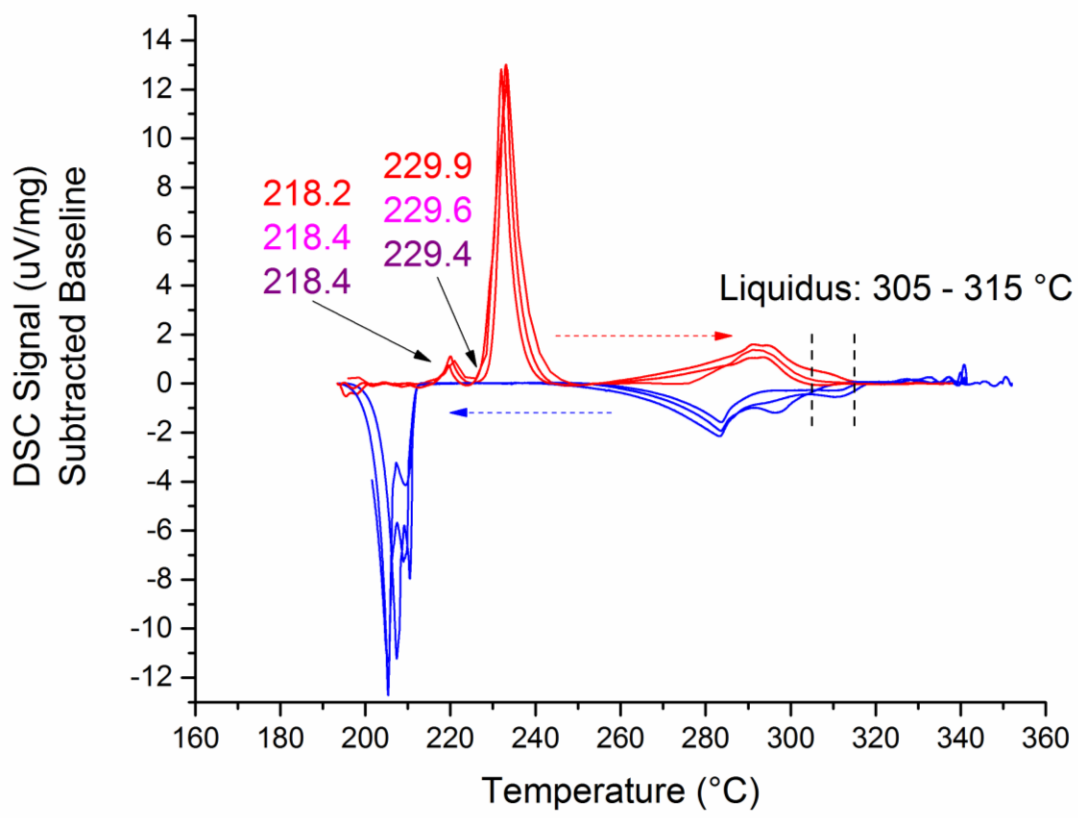

Figure 64 - Three successive 5°C/min DSC scans of a 60% NaOH / 40% NaI sample with baseline adjustment made to emphasize transitions.

This compound was not visible in the 90/10 composition scan as this material existed to the right of our proposed 80/20 eutectic and it was therefore thermodynamically not possible for this sample to reach the relatively NaI-rich compound phase transition.

One unique feature of this scan that is well-highlighted by the baseline fitting is the abnormally large 2-phase transition and exit signal that is seen starting at around 270°C and lasting until 320°. It is clear that there is a liquidus exit somewhere between 305°C and 315°C though the strong signal seen occurring around 290°C may indicate the trace formation of another phase that is compositionally much more NaI rich than the one we've just identified. Figure 64 has been provided to both show what the formation of a new compound looks like as well as to provide the reader a sense of the kind of ambiguity that can present itself in even the most controlled of experimental settings.

The last individual shared here is that of the 30% NaOH / 70% NaI system. In this investigation there are two unmistakable signals but their implications for the phase diagram are

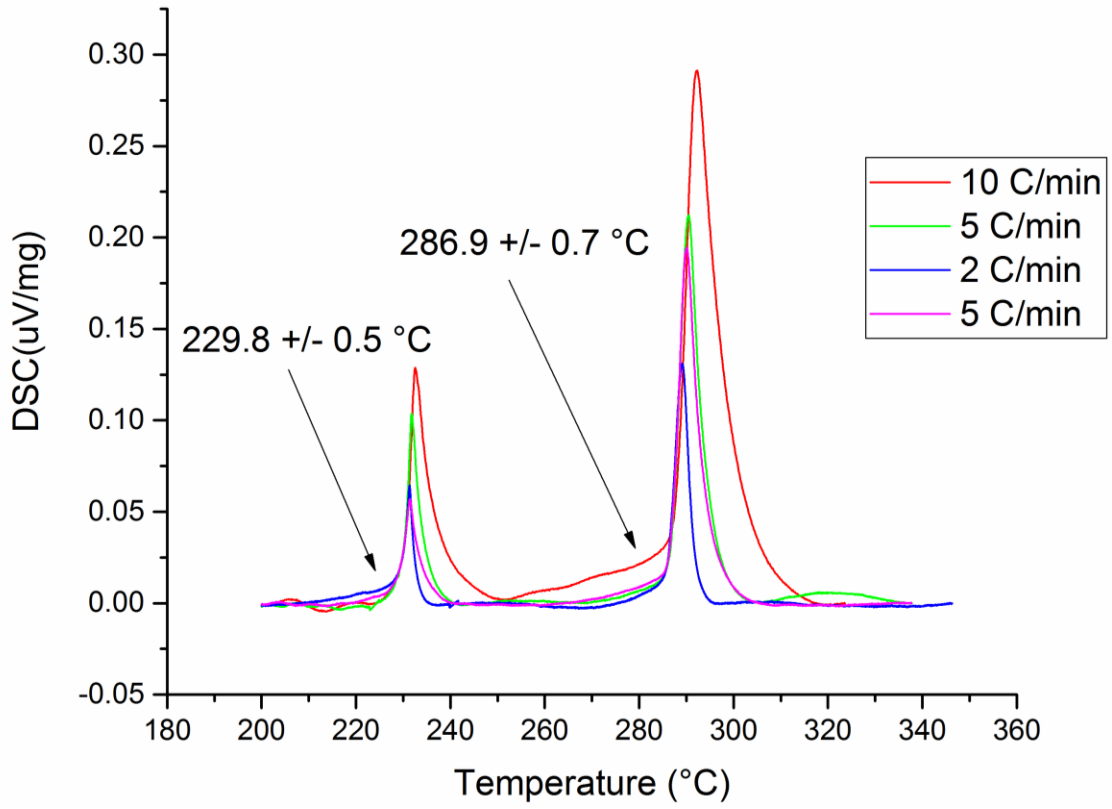

Figure 65 - DSC study of 30% NaOH / 70% NaI on two separate test days.

quite important. Figure 65 again corroborates a strong signal at 229°C however also shows an even stronger compound-like signal occurring at 287°C. Though this compound is likely the same observed by Yoshizawa[208] and modeled by Sangster[209] this single plot shows the simultaneous existence of both compounds. In addition, this 287°C melting compound likely contributes to the abnormally large liquidus signal seen in Figure 64.

Over 25 experiments and 100 unique scans were pursued in order to identify transition points within the NaOH-NaI binary system. Rather than go through all of these scans, the previous examples have been provided to single out different transition types as well as introduce phases that will be shortly proposed in the phase diagram. Table 30 provides a concise summary of the key transitions found for the prepared samples (Table 27).

Table 30 - DSC results with high confidence points in green, medium confidence points in orange, and low confidence points in red.

% NaOH	Transition 1		Transition 2		Transition 3		Transition 4	
	Temp (°C)	Error (°C)	Temp (°C)	Error (°C)	Temp (°C)	Error (°C)	Temp (°C)	Error (°C)
100	285.3	0.9	292.1	0.6	314.1	0.1		
90	219.4	0.3	264.3	2.4				
80	220.4	0.2						
70	219.8	1.0	230.1	0.7	276.4	5.15		
60	218.3	0.1	229.6	0.3	304.3	1.16		
50	219.1	0.6	229.2	1.1	285.7	0.7	404.9	2.26
40	228.8	0.8	287.9	1.1				
30	229.5	0.5	286.8	0.3				
10	287.1	0.3	597.0	3.23	647.7	3.91		
0	660.7	1.8						

Points noted in green as “High Confidence” are points that occurred in every scan for each experiment and/or sample and occurred with minimal error (< 2.5°C). Points in orange are here considered of “Medium Confidence” as they either did not occur in every scan or the error from

measurement to measurement showed deviation of over 2.5°C. Finally, scans that showed a clear peak but had very large error (>5°C) or appeared only occasionally are noted in red as "Low Confidence". Scans in red are not used for the construction of the binary phase diagram. Figure 66 shows only high and medium confidence data overlaid with historical literature.

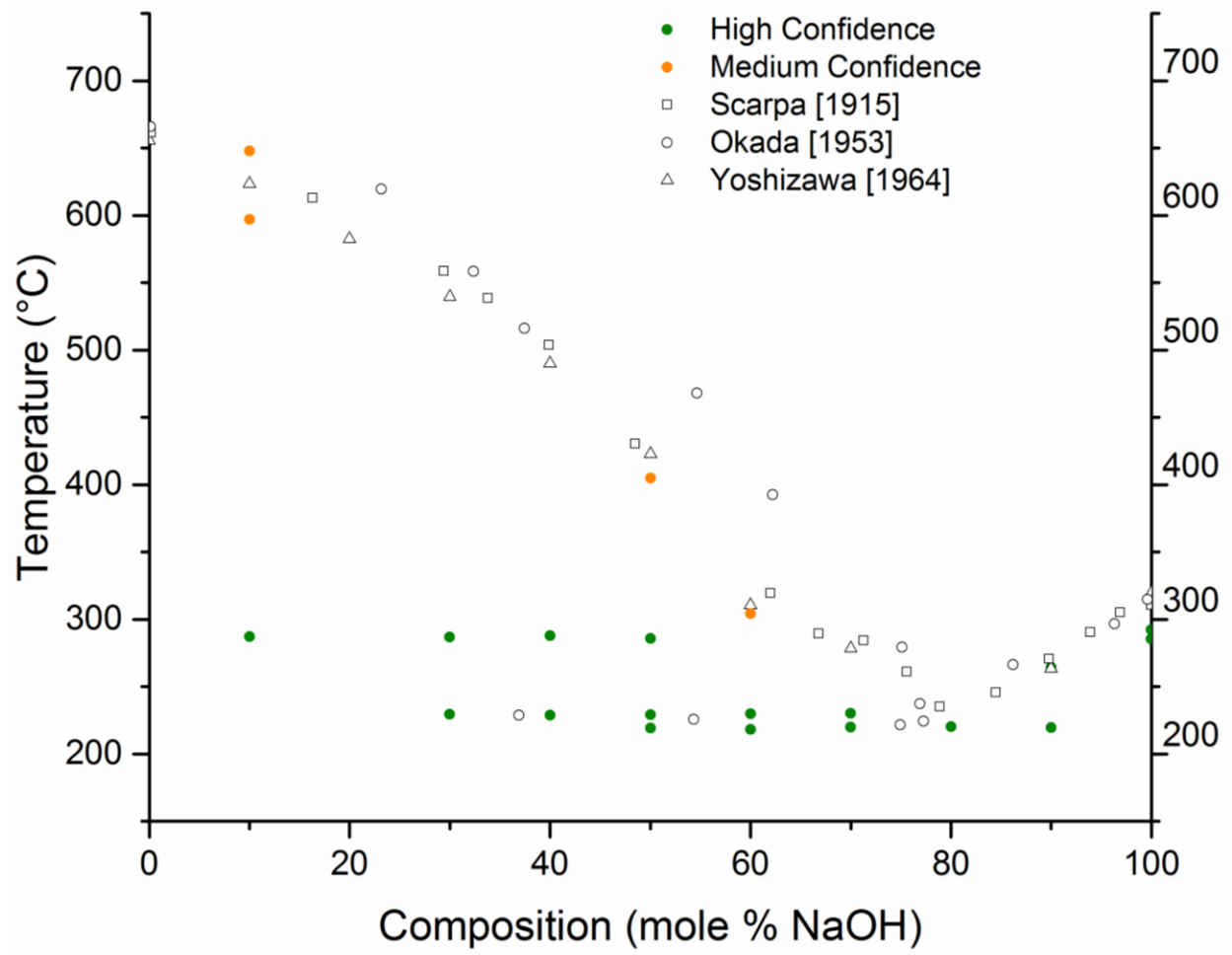

Figure 66 - NaOH-NaI binary phase diagram with experimental DSC points and data from literature.

The phase diagram above provides clear insight into particular characteristics of the phase diagram. First, it is clear that the establishment of the eutectic signal at around 220°C is clear and convincing as this signal is repeated with little error at numerous compositions. Further, when combined with the existing liquidus data from the historical literature, the 80/20 compositional

location of this eutectic is further supported as both NaI- and NaOH-rich liquidus curves converge at this location. The other clear outcome of this study is that there are at least two compounds that incongruently melt around 229°C and 287°C. The disappearance of the eutectic signal at around 50% NaOH would seem to indicate that this is the location for the low-melting compound. Further, the disappearance of the 287°C signal below 30% NaOH corroborates the historical literature's selection of $Na_5(OH)I_4$ as the composition of the NaI-rich compound.

The only oddity in the data collected are the two high-temperature signals recorded for the 10% NaOH / 90% NaI at 597°C and 648°C. It is hard to say whether these are both independent points referring to unique transitions or are instead the result of sample vaporization and condensation. In the former case of the signals being real, these may point to some amount of solid solubility range on the NaI-rich side of the binary system. This would result in the first signal at 597°C being related to the NaI-rich solidus and the 648°C being the actual liquidus melting event. In the latter case, a vaporization and condensation of the sample could not only explain the strong heat flux signals but also compromise them as the composition of the sample may change if the NaI is preferentially vaporizing over the NaOH. For this reason and in the absence of any other data that points to a solid solubility range[i] these points are discounted and not used in the modeling in spite of their reproducibility.

Rather than drawing lines directly on top of the points and proposing a phase diagram as is often done in the historic literature, this work will instead pursue a more rigorous process that attempts to identify the missing NaOH-rich compound and then uses the thermodynamic modelling described in 5.2.4 to establish curves by computationally minimizing free energy

[i] The analogous NaOH-NaBr system also does not show any sort of solid solubility on the NaBr-rich side.

functions. This process will yield a solution model for the binary liquid that will then provide useful context for understanding the electrochemical properties of the melt.

5.4.2 X-Ray Diffraction (XRD) Results

In order to determine the identity of the NaOH-rich compound, X-ray diffraction was performed on several eutectic composition (80/20) melts before and after various electrochemical experiments. Because the 229°C melting compound is expected to be the compound closest to pure NaOH, it should exist in solid state equilibrium with NaOH below the eutectic point. The use of multiple experiments was required as the sample presented strong amorphous character due to the rapid solidification that occurs upon passing through the eutectic and the potential for quenching. Figure 67 is provided below as it captures the general result obtained when amorphous content and preferred orientation were addressed.

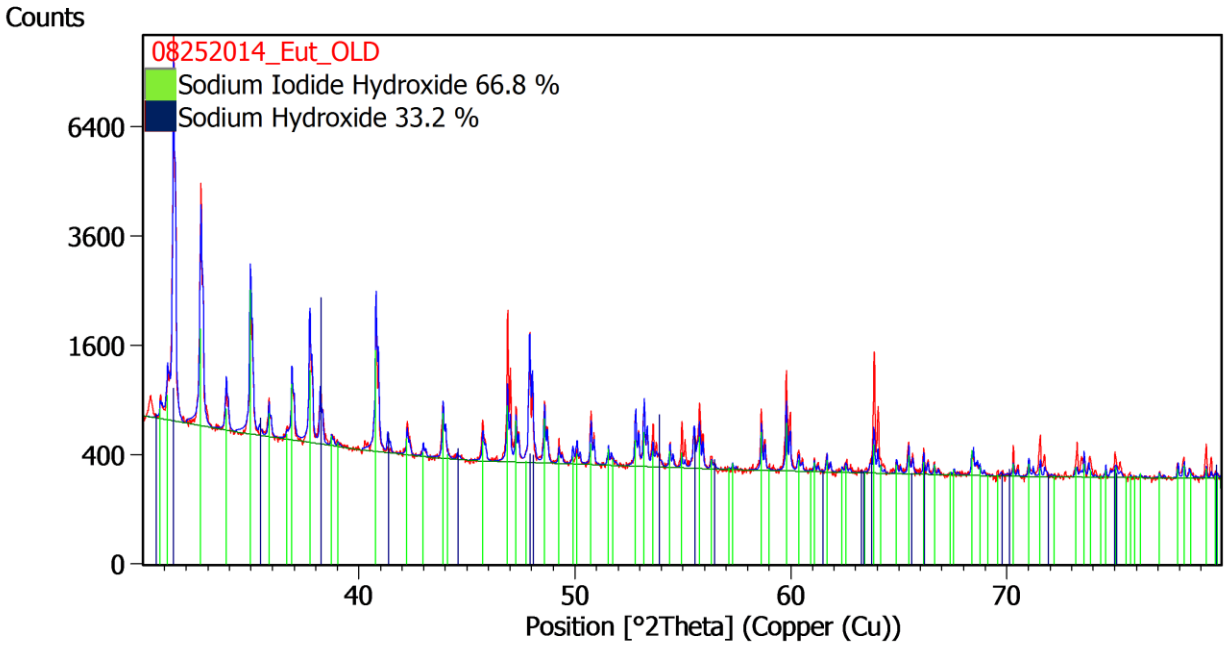

Figure 67 - XRD scan of an 80/20 eutectic melt post cyclic voltammetry. Only two phases presented themselves clearly with trace amounts of $Ni(OH)_2$ present but not quantifiable due to the background from the air-sensitive sample holder.

In the XRD spectra in Figure 67 only two phases presented themselves above the baseline of the air-sensitive dome. The presence of the pure phase, α-NaOH, confirms that the eutectic occurs to the right of any NaOH-rich compound. The second phase, unknown in the molten salt literature, can be found in a relatively recent paper[227] that was submitted to the German crystallographic literature but apparently was not found by the investigations of Sangster in his team's subsequent study of the binary system[209]. This new phase, $Na_7(OH)_5I_2$, was studied with single crystal XRD and theoretically modeled to corroborate the stoichiometry of the binary components. Their findings propose a P4/nmm crystal structure that forms a "new type of structure with puckered layers of $^2[Na_7(OH)_5^{2+}]$ connected via iodide ions". Figure 68 provides the proposed crystal structure of the compound for which crystal lattice parameters and powder diffraction file have been developed.

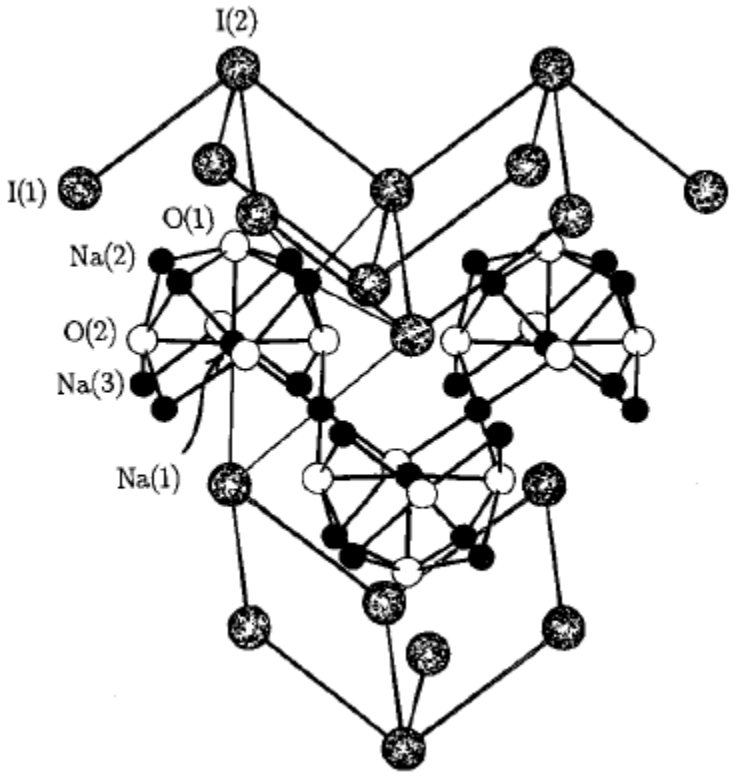

Figure 68 - Proposed crystal structure of $Na_7(OH)_5I_2$.

In a semi-quantitative study, it is found that the eutectic composition (80% NaOH 20% NaI) was composed of 66.8% $Na_7(OH)_5I_2$ and 33.2% α-NaOH. By using the lever rule to predict the amount of $Na_7(OH)_5I_2$ (71.4% NaOH) expected in the two phase region it is possible to arrive at the conclusion that for a fully equilibrated eutectic sample, there should be 70% $Na_7(OH)_5I_2$ and 30% α-NaOH. The fact that the XRD quantification matches the percentages expected for a eutectic sample with $Na_7(OH)_5I_2$ and α-NaOH in equilibrium (Figure 69) provides very strong validation that this new compound is, in fact, present.

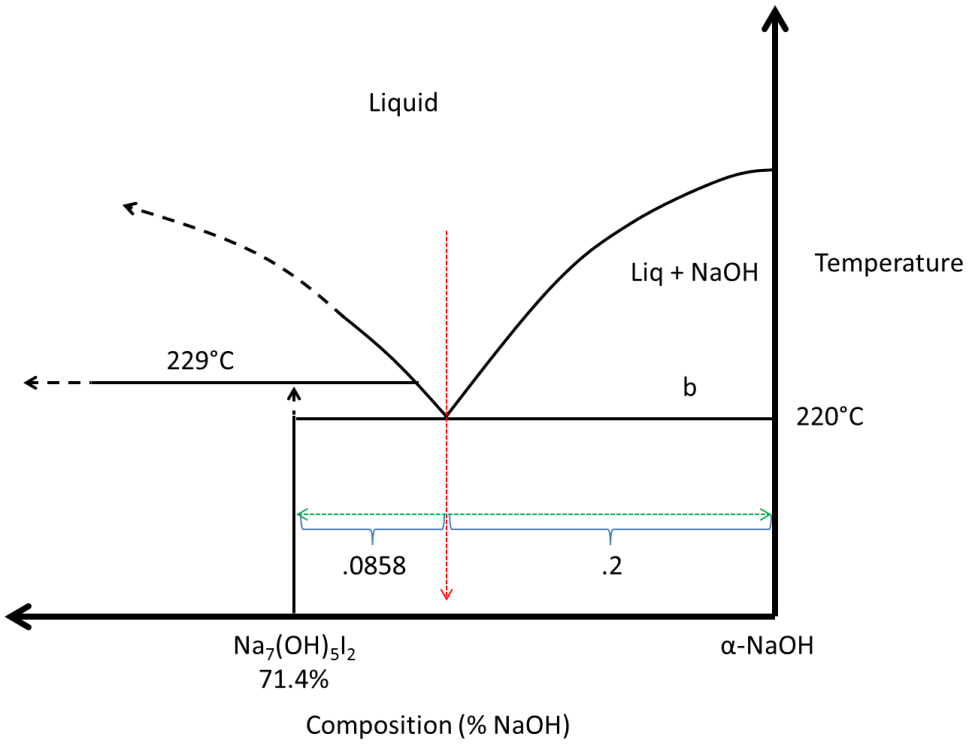

Figure 69 - The ratios of $Na_7(OH)_5I_2$ and α-NaOH expected for a frozen sample of eutectic composition

With this compound identified, it is important to explain how it is this compound could exist in light of the DSC data that found eutectic signals as far out as 50-50 in composition (Figure 66). Similar to Yoshizawa's logic[208] in placing a $Na_3(OH)I_2$ stoichiometry compound, the experimental data would indicate that the more NaOH-rich compound should be located to

the left of the 50/50 compositional location. The reason for this is because stoichiometries to the left of the most NaOH-rich compound should be shielded from the eutectic line transformation while those to the right would undergo this phase transition. The error in this approach and explanation for the anomalous high-NaI eutectic signals is here explained as the result of a Scheil-Gulliver[228, 229] non-equilibrium solidification process in which the composition of the liquid-phase follows closely the liquidus upon cooling. In this scenario, as a salt system with bulk composition to the left of the $Na_7(OH)_5I_2$ cools, the rejected liquid phase material is incrementally enriched in NaOH beyond the 5:2 (71.4%) stoichiometry. At the 229°C the solid phase that has been accumulated thus far begins to transform into $Na_7(OH)_5I_2$ and drive the $Na_7(OH)_5I_2$ peritectic signal. On the other side of the two phase region, the liquid has been substantially enriched so that it no longer must pass through the peritectic. Rather, the liquid enters a new two-phase region. This enriching process continues down towards the eutectic composition until the enriched liquid phase reaches the eutectic at approximately 220°C and freezes, creating a thermal signal in spite of the compound's overall composition indicating a different positioning on the phase diagram. If the diffusivity within the liquid is accepted to be much larger than that in the solid then the frozen eutectic composition has little time to equilibrate and is then re-melted upon heating. The result of this non-equilibrium cooling is that solid grains exist as compositionally graded or "shelled" regions and that, for the purposes of DSC measurement, it is possible to detect metastable phases that should not exist in equilibrium according to the phase diagram.

With this explanation validating the possibility of $Na_7(OH)_5I_2$ in spite of metastable eutectic signals, XRD study is now turned towards the compound with the goal of confirming its signal with minimal α-NaOH impurity signals. As per Table 28, a sample with 71.80% NaOH

was synthesized to try and minimize the presence of compounds from the left of the $Na_7(OH)_5I_2$ compound. This sample was then annealed below 220°C for two weeks in an attempt to remove any non-equilibrium phases. Figure 70 shows the result of a 1000 step/s slow scan with preferred orientation minimized via a rotating sample stage.

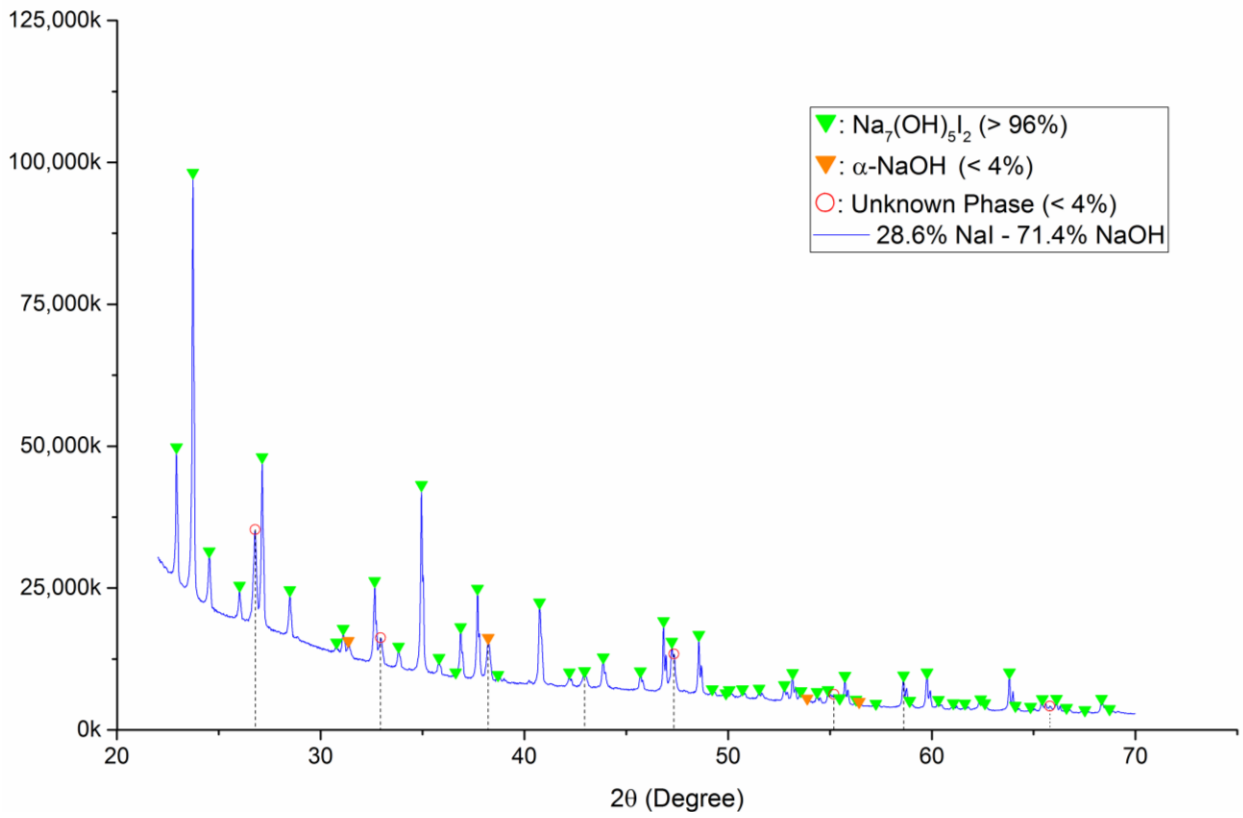

Figure 70 - XRD of well-annealed $Na_7(OH)_5I_2$ sample. The two expected phases, $Na_7(OH)_5I_2$ and α-NaOH are present alongside a third, unknown phase.

The $Na_7(OH)_5I_2$ is here confirmed to exist as the majority component (>95%) in the sample. The narrowness of the peaks and reproducibility of the experiment point to the stability of this new, highly crystalline phase[i]. The second phase that is clearly represented is that of α-NaOH. Though attempt was made to minimize the contribution of this compound, the complete

[i] This compound will later be assumed to exist as a line compound with no solid solubility in order to facilitate modeling of its thermodynamic properties. The highly crystalline nature of the XRD plot supports the notion that the compound is likely to exist with minimal solubility.

removal of this phase is generally not possible in powder diffraction and instead requires precise single crystal synthesis to ensure phase purity. The third, and perhaps most interesting, signal is that of a crystalline phase that is not explainable by any known compound[i] composed of the experimental or environmental elements[ii]. In some cases the peaks present themselves as unmatched, stand-alone signals as in Figure 71 at 26.7453° 2θ.

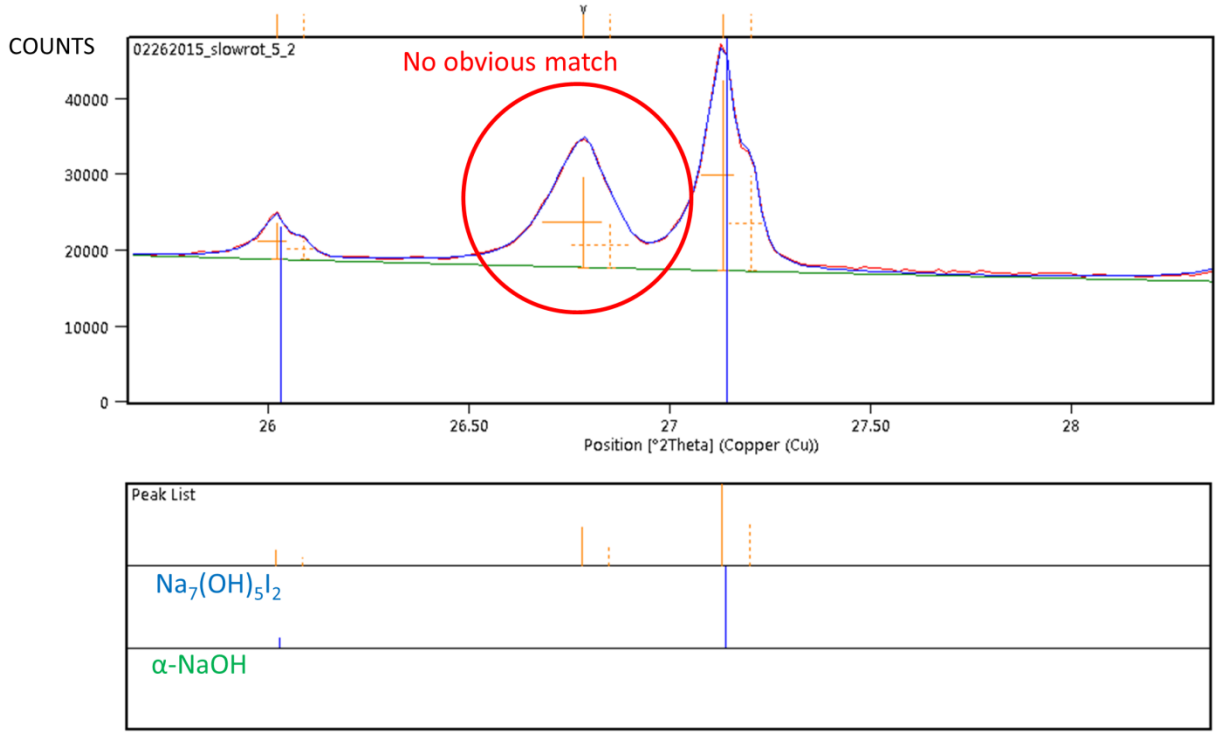

Figure 71 - Example of an unmatched peak at 26.7453°. There were no compounds in the ICDD PDF-4+ database that could account for this signal within reasonable error.

In other cases, signals for the two identified compounds were far out of proportion from what their PDF file suggests. An example of this occurs for the α-NaOH peak at 38.17° 2θ (Figure 70). Though this peak is predicted to be the largest in the α-NaOH spectra, it is more than twice as large as it should be when considered in scale (via RIR ratio) with the other peaks in the spectra.

[i] Within the ICDD PDF-4+ database
[ii] The pattern match scanned all compounds containing the following: Na, O, H, I, Ni, Al, Ar, Fe, Pt

Overall, there are eight features that are either unexplained or out of proportion and merit further examination.

In order to provide answers to the large number of unaccounted peaks in Figure 70, a similar experiment was conducted with the $Na_5(OH)I_4$ composition that has been variously reported to produce the 287°C peritectic signal though has never been studied or confirmed on a crystallographic basis.

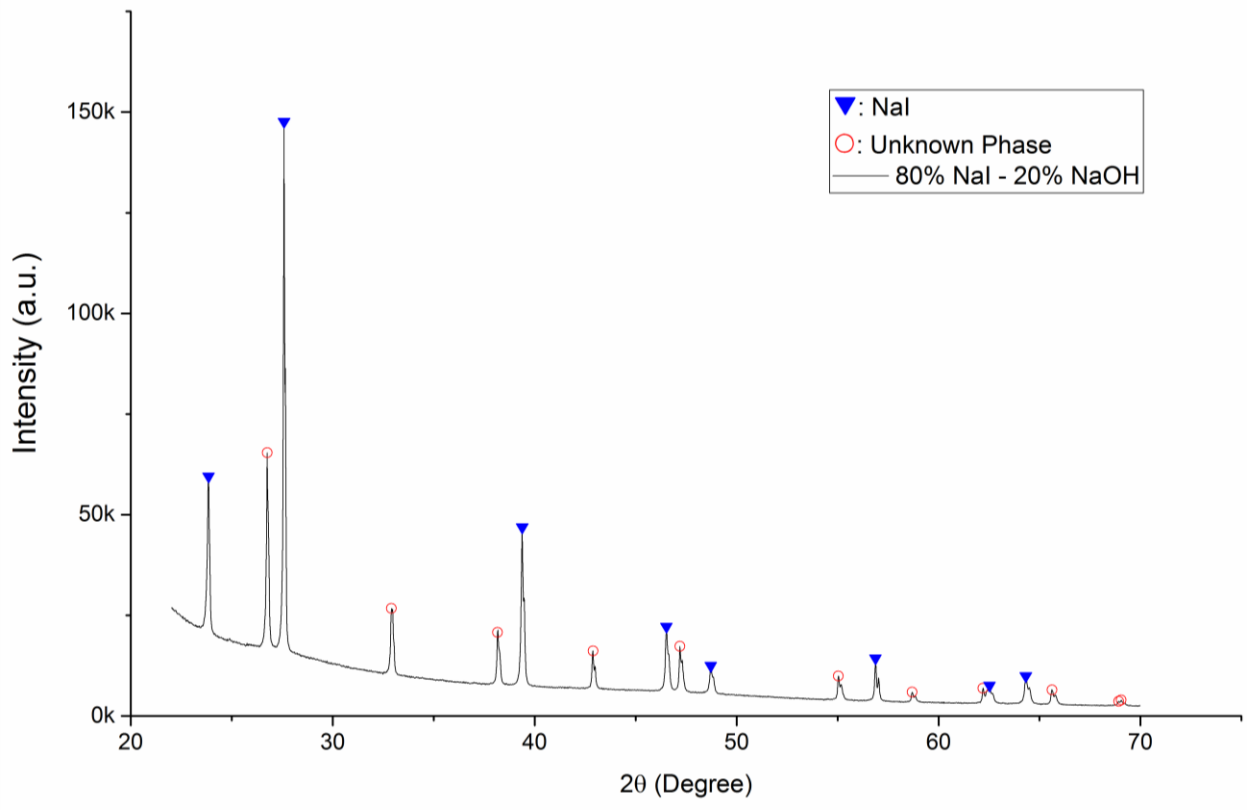

Figure 72 - XRD results of a well-annealed $Na_5(OH)I_4$ sample. Sample quantification is not possible due to the strong presence of an unknown phase for which there is no RIR reflectivity data.

Figure 72 shows the XRD results of a $Na_5(OH)I_4$ sample that has been synthesized with a slight excess of NaI in order to minimize the presence of the NaOH-rich $Na_7(OH)_5I_2$ phase. The high crystallinity and signal-to-noise ratio (1000:1) emphasize the presence of two distinct phases. The first, NaI, is expected to exist from the two-phase cooling above 287°C. Its high relative

intensity ratio (RIR = 10.28) further ensures that even small quantities of NaI create strong signals in the XRD spectra. The second phase, shown with red circles, is similarly not matchable to any known phases consisting of elements present in the sample or environment. Though the phase does appear fairly crystalline, the peaks at higher 2θ angle do present some degree of twinning and thus prevent an accurate indexing of the phase.

The most interesting outcome of these two XRD studies is readily apparently if they are compared one on top of the other (Figure 73)

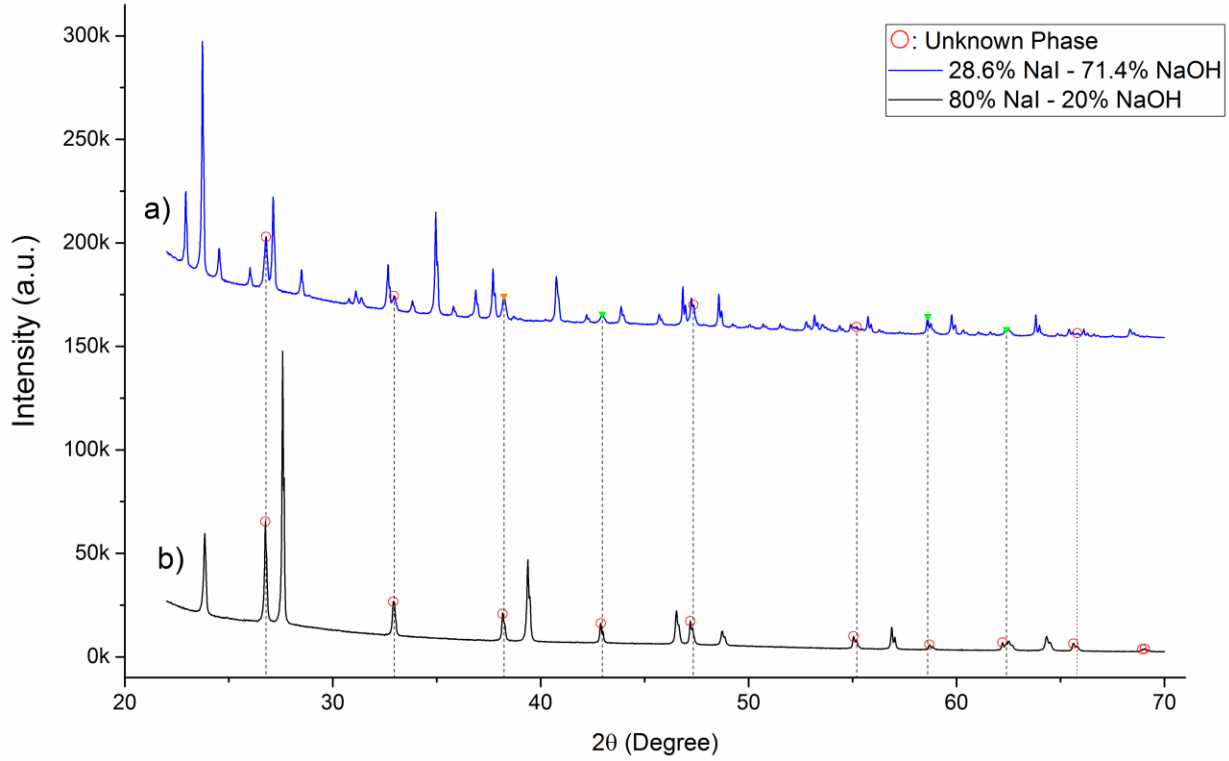

Figure 73 - Comparison of a) $Na_7(OH)_5I_2$ and b) $Na_5(OH)I_4$ spectra. The unknown points clearly identifiable in spectra "b" all coincide with unknowns or abnormally large peaks in spectra "a".

It is immediately clear that the unknown and disproportionate signals in the $Na_7(OH)_5I_2$ spectra line up directly with the clearly identified unknown phase in the spectra for the $Na_5(OH)I_4$ salt. The appearance of the $Na_5(OH)I_4$ in the $Na_7(OH)_5I_2$ can again be explained as the result of a

Scheil-Gulliver solidification process and, as a result, it appears in small quantities in the $Na_7(OH)_5I_2$ due to two-phase solidification that occurs above 287°C. With confirmation of the same unmatchable peaks in two separate XRD experiments, it is now possible to propose the unique 2θ positions of the $Na_5(OH)I_4$ phase (Table 31). This is a very important contribution as it will provide a basis for further single crystal studies of the system and also indicates an initial sense of the symmetry of the system.

Table 31 - Peak List for the unknown NaI-rich phased proposed to be $Na_5(OH)I_4$

Peak #	2θ (degree)	Intensity (%)	Comments
1	18.8479	47%	Background error from air-sensitive dome
2	26.7453	100%	
3	32.921	32%	
4	38.1703	29%	
5	42.8764	22%	
6	47.1846	25%	
7	55.0378	13%	
8	58.689	5%	
9	62.2	9%	
10	65.608	9%	
11	68.92	1%	Potentially twinned with peak #12
12	68.99	2%	Potentially twinned with peak #11
13	72.15	1%	
14	75.335	4%	

With these peaks, the pattern can be indexed and ideal pattern created to attempt a space group search. Unfortunately, because of the twinning and peak widening that occurs on higher angle peaks it is not yet possible to make any predictions on the correct stoichiometry for x and y coefficients in the generalized formula $Na_{x+y}(OH)_xI_y$.

Figure 74 shows the indexed phase (green) from the original pattern (black) along with an example of an isostructural compound of space group 221 (Pm-3m) in blue. Indexing yielded

greater than 70% hit for a cubic system with most recommendations returning Pm-3m. Several compounds of this type found great match agreement with our indexed pattern with $InPu_3$ showing the greatest resemblance. It is therefore used to support the proposal that the unknown NaI-rich compound, historically considered to be $Na_5(OH)I_4$, is likely of this or a very similar symmetry.

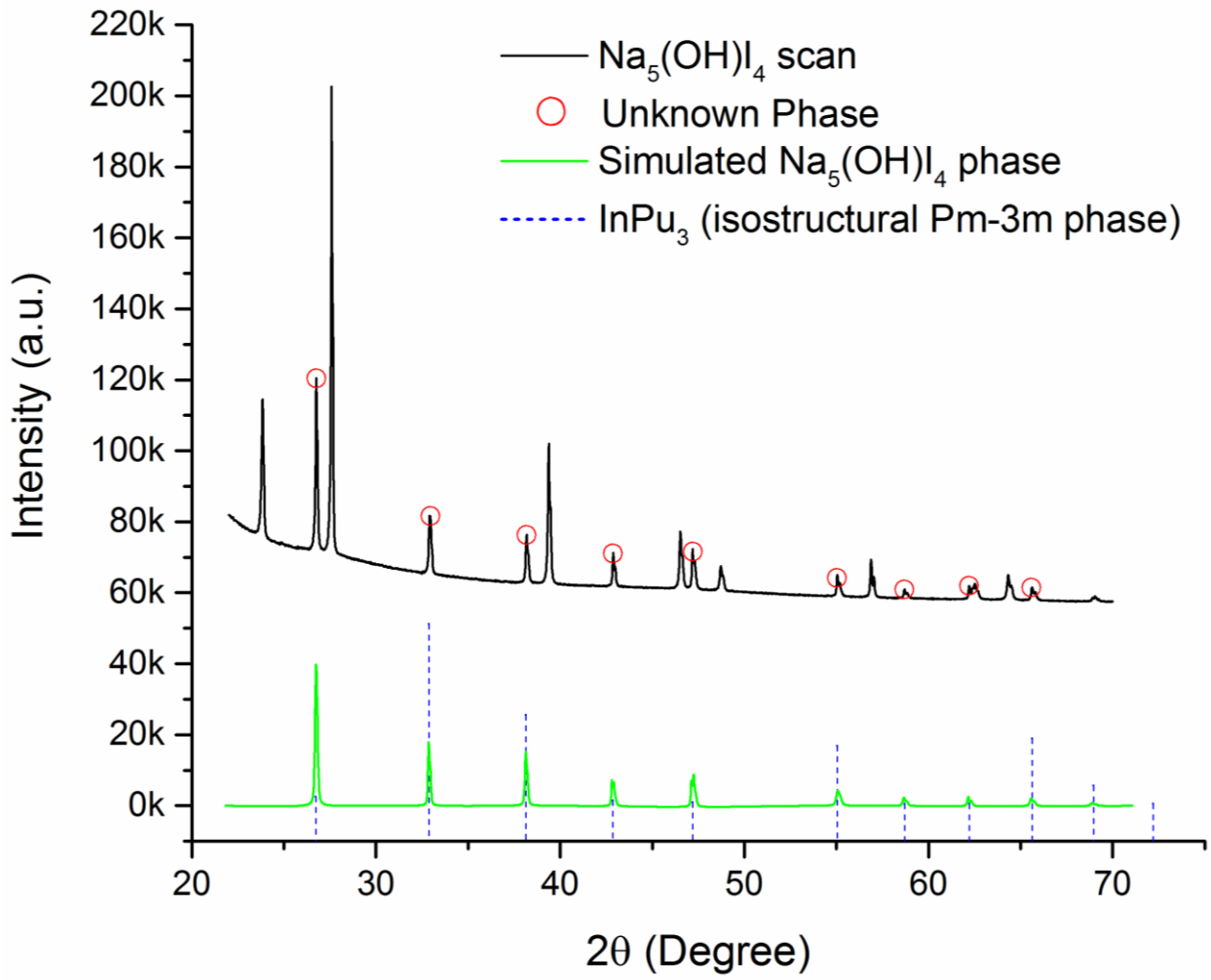

Figure 74 - Plot showing the original XRD of the $Na_5(OH)I_4$, the indexed phase in green, and an example Pm-3m isostructural compound in blue. Though the heights of the pattern line are irrelevant, the spacing between the various lines is indicative of the ratio of spacing between atomic sites.

Due to the lack of single crystal data, the indexed pattern cannot be converted to a stoichiometry as the errors implicit in the peak placement are too large to allow for confident fitting. For this

reason, this analysis will proceed under the assumption of a $Na_5(OH)I_4$ line compound stoichiometry though other NaI-rich stoichiometries[i] may be possible.

5.4.3 Thermodynamic Modeling Results

Having now collected DSC data, confirmed the $Na_7(OH)_5I_2$ compound, identified a NaI-rich compound via XRD, and settled on the $Na_5(OH)I_4$ stoichiometry we are now almost ready to begin a thermodynamic optimization of the binary system. First, it is worth noting that the identification and selection of compounds is very important because the optimization of the full phase diagram implies several two-phase regions in which the two members must be in thermodynamic equilibrium without each other. Thus, though it is possible to initialize the solution model values with liquidus values, it is critical for this solution model's composition and temperature functionalities that it be constrained by the additional requirements of equilibrium with the two identified compounds at these two-phase locations.

The second item that requires attention is the selection of a suitable solution model for our NaOH-NaI binary liquid. Though the simplest models, ideal solution and regular solution theory, do work for a subset of systems, their applicability is limited to those systems in which configurational entropy is ideal or nearly ideal. For solutions in which there are large energy differentials between bonds of different atoms, this energy asymmetry not only affects the enthalpy (via Margules or activity coefficients) but also the configurational entropy as the assumption of fully randomized mixing quickly fails. In these cases, excess energy terms must be developed to account for deviations from the ideal state. For our purposes, because the electrolyte has dissimilar and physically asymmetric anions (OH^- and I^-) it is unlikely that either

[i] For example, $Na_4(OH)I_3$ is a compound that mirrors several Pm-3m type crystal stoichiometries. The only condition on stoichiometry at this point is that the NaI must be at least 70% molar. This is because of the low-melting eutectic signal detected at this composition during DSC studies.

the ideal or regular solution models will work. Further, because there is a goal of developing a model of a binary system so that future work may incorporate ternary components, it is important to select a formalism that allows for the simple expansion into ternary space.

For these reasons, this study has chosen to work within the framework of the Compound Energy Formalism (CEF) with a two-sublattice solution[230, 231]. This approach not only allows for a sublattice approach to separate ion mixing with cations, Na^+, and anions, I^- and OH^-, confined to their separate model sublattices, but also allows for expansion to ternary and higher order systems in future work. The Gibbs free energy is given by:

$$G = \sum_i \sum_j \left(y_i^{cation} y_j^{anion} G_{ij}^0\right) - TS + G^{excess} \qquad \text{Equation 40}$$

Where y_i^{cation} and y_j^{anion} are site fractions of constituent i and j on the cationic and anionic sublattices, respectively, and G_{ij} corresponds to end member standard Gibbs free energy. The second term accounts for the ideal entropy of mixing (Temkin-like[232]). The excess term, G_{excess} captures the non-idealities of the solution via temperature dependent interaction parameters, L^k, expanded as Redlich-Kister polynomials. In the case of a single cation, this term reduces to

$$G^{excess} = y_{OH} y_I \sum_k L^k (y_{OH} - y_I)^k \qquad \text{Equation 41}$$

This is the form that will be optimized first with liquidus and end member data from the FactPS database (Table 32): NaOH corresponding to the data reported in the NIST-JANAF thermodynamic table[222] and NaI from Barin[233]. Further refinements of the parameters for the liquid have been conducted simultaneously with the optimization of the thermodynamic properties of the intermediate compounds in order to reproduce the thermal arrests for the eutectic and the peritectics. For our purposes, this corresponds to 220°C to 229°C for $Na_7(OH)_5I_2$ and 229°C to 287°C for the $Na_5(OH)I_4$ compound.

Table 32 - Thermodynamic data for pure end members.

Compound	$\Delta H^0_{298.15\ K}$ (kJ/mol)	$S^0_{298.15\ K}$ (J/mol/K)	C_p ($J.mol^{-1}.K^{-1}$]
α-NaOH	-425.931	64.445	**298.15 to 570.15 K**: 74.575 – 0.126 T + 2.56E^{-4} T^2 **570.15 to 593.15 K**: 86.023 **593.15 to 2500 K**: 167.644 – 0.029 T – 1824129.7 T^{-2} +4.219E^{-6} T^2 + 35363.805 T^{-1} - 2929.249 T$^{-0.5}$
β-NaOH	-419.571	75.600	**298.15 to 570.15 K**: 74.575 – 0.126 T + 2.56E^{-4} T^2 **570.15 to 593.15 K**: 86.023 **593.15 to 2500 K**: 167.644 – 0.029 T – 1824129.7 T^{-2} +4.219E^{-6} T^2 + 35363.805 T^{-1} - 2929.249 T$^{-0.5}$
$NaOH_{(liq)}$	-413.211	86.322	**298.15 to 570.15 K**: 74.575 – 0.126 T + 2.56E^{-4} T^2 **570.15 to 593.15 K**: 86.023 **593.15 to 2500 K**: 167.644 – 0.029 T – 1824129.7 T^{-2} +4.219E^{-6} T^2 + 35363.805 T^{-1} - 2929.249 T$^{-0.5}$
NaI	-287.859	98.324	**298.15 to 1577 K**: 48.877 + 0.0121 T
$NaI_{(liq)}$	-269.692	113.045	**298.15 to 1577 K**: 64.852

The best compromise corresponds to the phase diagram presented in Figure 75, and experimental data are reproduced within the experimental errors.

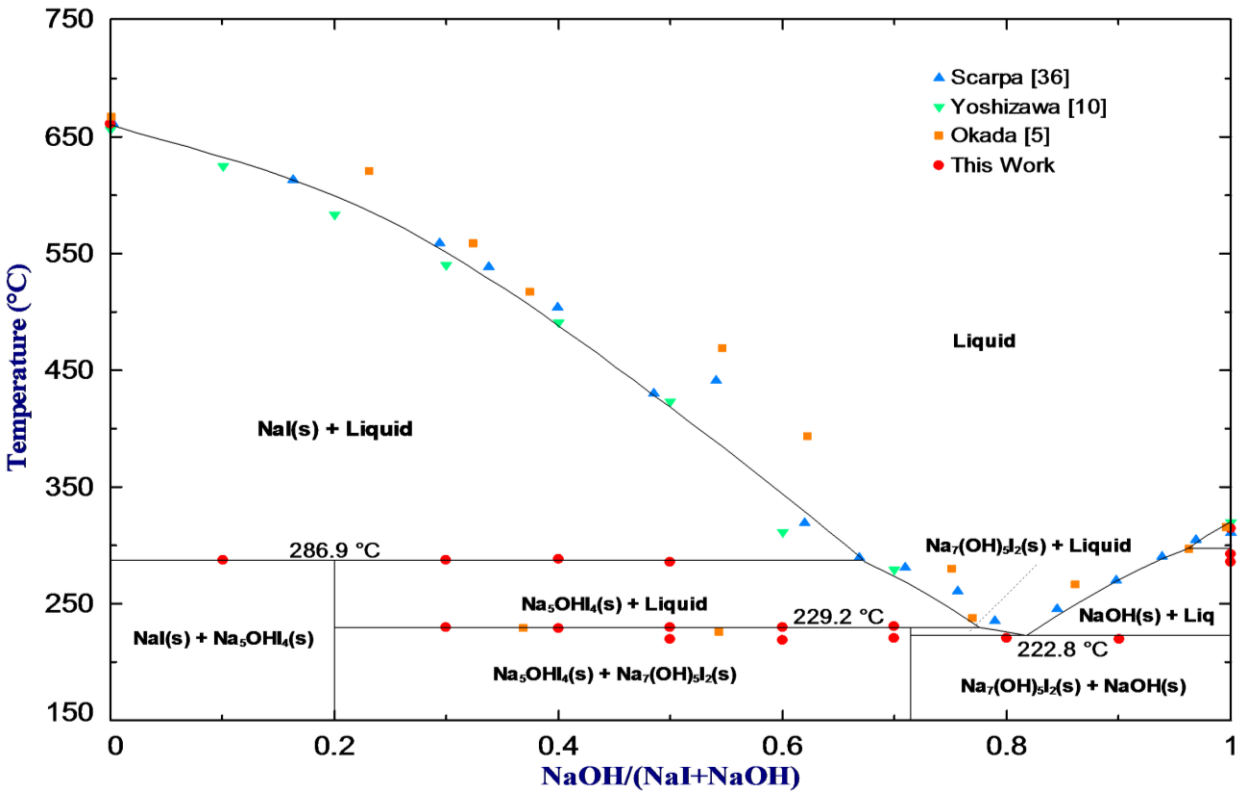

Figure 75 - Optimized phase diagram fit using CEF solution model and optimized data for $Na_7(OH)_5I_2$ and $Na_5(OH)I_4$

This optimized phase diagram shows a very close fit to all of the critical temperatures found during DSC measurement and when compared to existing literature (Table 33).

Table 33 - Comparison of experimental and modelled transition data to existing literature.

Source	Eutectic	Peritectic #1	Peritectic #2
Scarpa[210]	220	N/A	300
Okada[202, 234]	225	N/A	N/A
Yoshizawa[208]	225	234	290
Sangster[209]	231	N/A	312
This Work – DSC	219.9 +/- 0.4	228.9 +/- 1.4	286.4 +/- 0.7
This Work - Model	222.8	229.2	286.9

A major takeaway from this modeling exercise is to get a sense of the compositional window available at different LMB operating temperatures. At a temperature of 250°C, all liquid operation constrains electrolyte compositions to remain between 74.3% and 86.3% NaOH. Though our electrochemical studies will focus on the eutectic melt as this is the composition that provides the greatest flexibility and lowest temperatures in terms of the temperature of operation, exploration of the molten salt compositional space could be expanded to those locations bounded by the two liquidus curves.

The only feature that could benefit from improved data is the eutectic temperature at 222.8°C. The close proximity of the eutectic and peritectic #1 in composition and temperature creates challenges in fitting with low-order polynomials as it forces slope changes of thermodynamic functions in very close proximity. The three ways to resolve this are to identify the exact stoichiometry of the NaI-rich compound, add further parameters to the solution model, or conduct calorimetry experiments on the two compounds in order to determine their enthalpies of formation or temperature dependencies of specific heat. These final refinements are left for future work as they do not add substantively to the general shape or model of the binary system.

The optimized two-sublattice solution interaction parameters as well as the enthalpy of formation, absolute entropy at 298.15 K, and heat capacity functions for the two intermediate compounds are provided in Table 34. The values found for enthalpy and entropies are the correct order of magnitude for intermediate salt compounds of similar structural complexity. With these functionalities available, it is now possible to distill unique insights that would otherwise be impossible to extract from hand-drawn phase diagram construction methods.

Table 34 - Optimization Results from the thermodynamic optimization of the $Na_5(OH)I_4$ and $Na_7(OH)_5I_2$ compounds and binary solution.

Compound	**$\Delta H^0_{298.15\ K}$ (kJ.mol^{-1})**	**$S^0_{298.15K}$ (J.mol^{-1}.K^{-1})**	**C_p (J.mol^{-1}.K^{-1})**
$Na_5(OH)I_4$	-1,634	355.690	298.15 - 570.15 K: 333.98 - .126T+2.56E^{-4}T^2 570.15 - 593.15 K: 345.43
$Na_7(OH)_5I_2$	-2,758	422.513	298.15 - 570.15 K: 68.346 +1.586T-.0013T^2 570.15 - 593.15 K: 559.819
Solution	**RK Coef**	**Interaction Parameter (J)**	
NaOH-NaI	L^0 L^1 L^2	-6,189.49 - 8.028T -585.07 - 4.825T -15,989.2 + 20.717T	

In addition to being able to extract out free energy curves of all components the activities of both the components of the mixture can now be parsed. Figure 76 shows the three dimensional a_{NaOH} surface for different compositions of NaOH at different temperatures. Projected into 2-D it is possible to see how activity increases with temperature and composition and how the 80% NaOH eutectic composition shows activity values for temperatures lower than any other due to its suppressed melting point (Figure 77). A major take-away from this plot is that the activity of NaOH in the eutectic melt is substantially less (40%) than that of pure sodium hydroxide (a_{NaOH} = 1) at melt temperatures (318°C). The 2-sublattice CEF solution model also shows that the non-idealities of mixing are non-negligible as an ideal eutectic solution would show an activity of 0.8

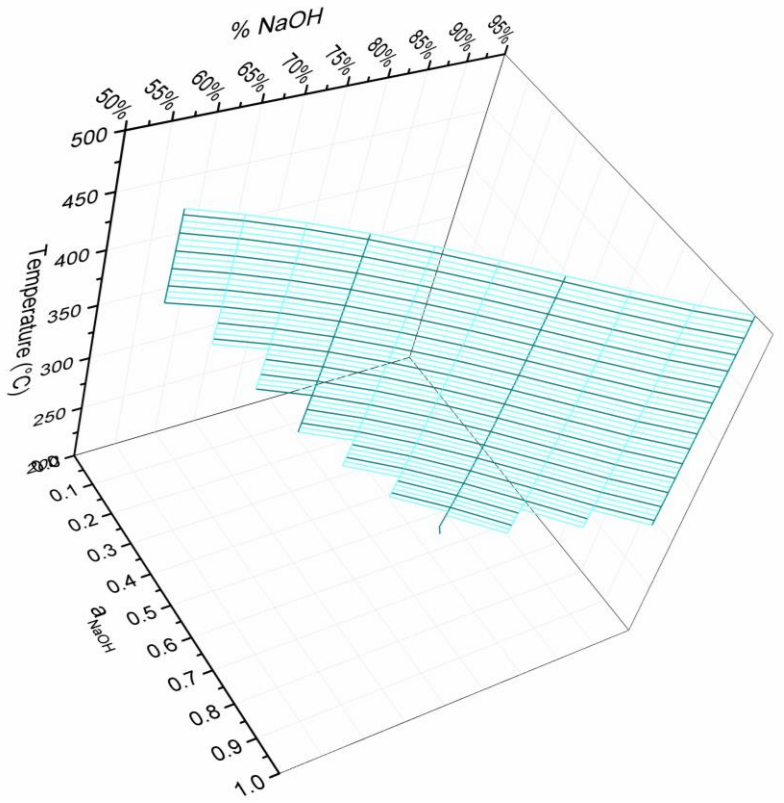

Figure 76 - Plot of NaOH activity from the CEP model as a function of temperature and composition.

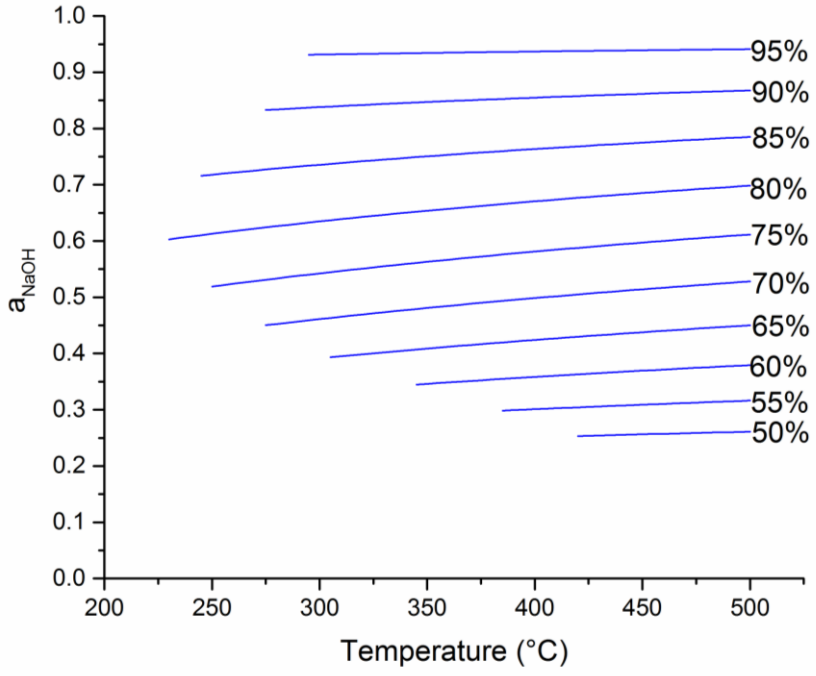

Figure 77 - 2D representation of the data from the Temperature-Activity-Composition study of mixed NaOH.

whereas the solution here shows approximately 0.6 activity. This is a promising result as it leads the way towards reduced reactivity of sodium metal with the molten salt. That said, these results also show that it is better to toggle concentration rather than temperature if the sole goal is to minimize the activity of NaOH.

Data like those above can add further insights when it comes to predicting theoretical properties of the salt. The Castner process has found repeatedly that the predominant electrolysis process occurs as the sum of Equation 22 and Equation 23:

$$2NaOH \leftrightarrow 2Na_m + H_2O + \frac{1}{2} O_{2\,(g)} \qquad \text{Equation 42}$$

This reaction occurs with a voltage modeled as

$$\Delta V_{win} = -\frac{1}{nF}\left(\Delta G^0 + RTln\left(\frac{(a_{Na})^2(p_{O_2})^{1/2}(p_{H_2O})}{(a_{NaOH})^2}\right)\right) \qquad \text{Equation 43}$$

This means that as the activity of NaOH is reduced, the voltage required for this nonspontaneous reaction is increased[i]. From this data, the predicted breakdown voltage for a binary system in which the activity of NaOH has been reduced (Figure 78) can be calculated. For this calculation an activity of unity for pure sodium is assumed and partial pressures of O_2 and H_2O approximated as the stoichiometric production values of 1/3 and 2/3, respectively.

From this plot it is clear that NaOH, even in its reduced concentration form, electrolyzes at far less positive voltages than NaI in its pure ($a_{NaI} = 1$) state. This means that any major oxidation experienced in this melt due to voltage breakdown is thermodynamically expected to be the oxygen species as opposed to iodine and that iodine cannot thermodynamically be present

[i] This is true for cases where $\Delta G^0 > 0$.

until at least around 2.8 V (vs. Na)[i]. The other thing this plot provides is an important comparison point between the thermodynamic properties our molten salt model predicts and those that can be found experimentally through cyclic voltammetry experimentation. For this reason, this investigation will not only the cathodic behavior of sodium deposition in the melt but will also probe the limiting anodic oxidation reactions as well.

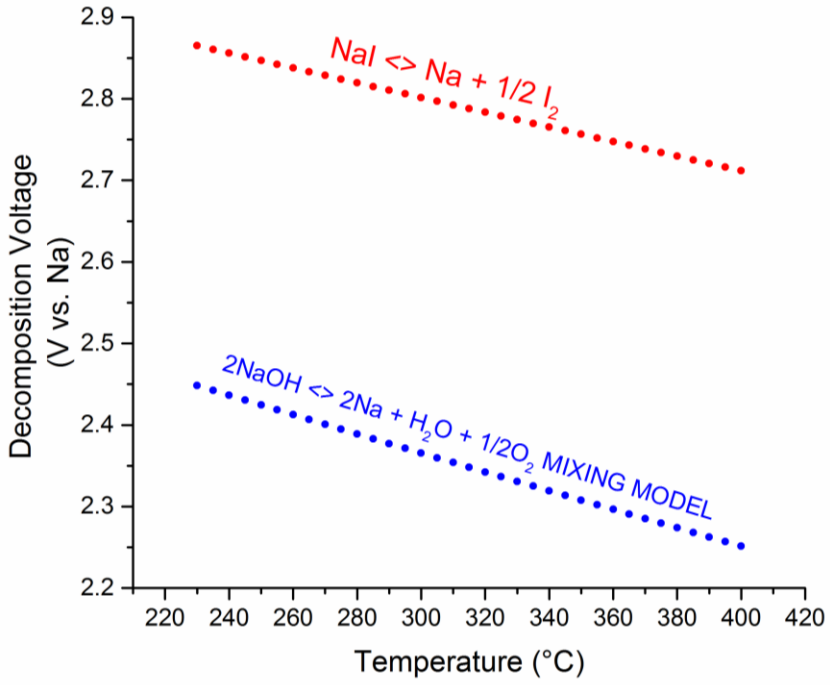

Figure 78 - Decomposition reaction for modelled NaOH liquid with non-unity activity. This value is compared to the voltage expected for pure NaI breakdown.

5.4.4 Electrochemical Measurements – Cathodic Study

The cathodic limit of the electrolyte is particularly important to the proper operation of a Na-based LMB. This is because the charging and discharging processes rely upon the deposition and stripping of metallic sodium and, as a result, operate at the extreme cathodic end of the electrolyte window. It is important to ensure that sodium can be both plated and stripped and also

[i] This value is actually larger in the case of a binary molten salt as the activity of NaI is reduced.

that there are no major reductive events that occur at less cathodic potentials that would serve to prevent sodium from being reduced and oxidized easily.

A series of cathodic scans was run down to -200 mV vs. Na. These scans were run to investigate the scan rate functionality of the deposition and stripping process. For many redox reactions, a reversible process on the working electrode will reveal the diffusion limitation of the analyte in providing reactive species to the reaction surface at a rate to match the reaction rate. In the case of liquid sodium deposition from a single cation molten salt, this rate of sodium ion transport is sufficiently fast and as a result no scan rate dependence was found in cathodic scans up to 200 mV/s.

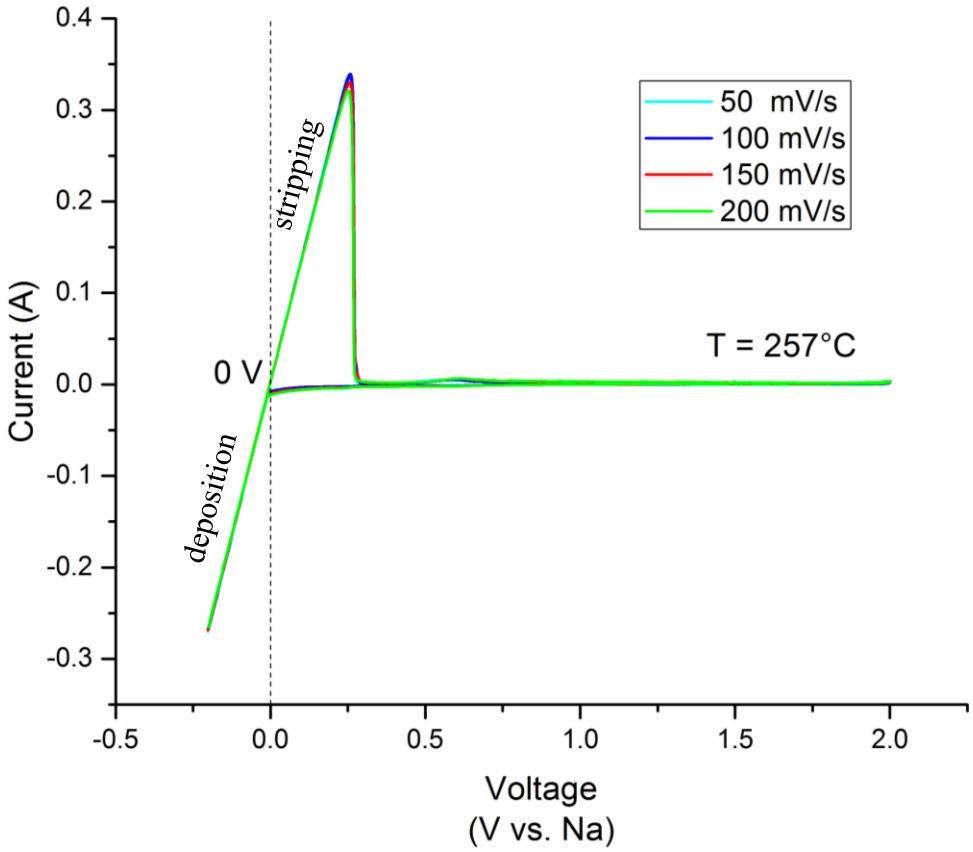

Figure 79 - A pure Ni 0.314 cm^2 working electrode is measured against a TaNaB reference electrode in a series of cathodic CV scans to -200 mV (vs. Na) at 257°C

The most important feature in this scan, sodium deposition at 0 V, is followed by subsequent stripping upon the anodic sweep to more positive voltages. The anodic process driven on the counter electrode is likely due to oxidation of the hydroxide species, similar to the ~2.3 V reaction carried out in pure molten hydroxide on the anode during the Castner electrodeposition process (Equation 23). It is also important to note that the scan region to the right of the deposition and stripping is particularly flat, indicating very little redox reactivity in the melt. There is one slight oxidative peak beginning at around 325 mV however this peak is not reproducibly found at temperatures below 280°C.

There are three major takeaways from this initial cathodic voltammagram. First, there are temperatures at which the electrolyte appears extremely stable at reductive potentials. This is important for an LMB because strong reductive signals occurring prior to sodium deposition would amount to parasitic reactions that would consume current without charging the battery via the reversible alloying process. The second important feature worth noting is that there is a clear stripping peak upon reversal. Though this is theoretically expected it has rarely been seen in sodium-based molten salt chemistries. Miles[166] was unable to produce any sort of stripping peak in a series of hydroxide-based molten salt experiments. Figure 29 highlighted this behavior which was attributed to the "deposited sodium reacting…to produce hydrogen gas". The fact that this work obtains a strong stripping peak is a very important finding and is an early indication of improved stability of the molten salt with metallic sodium. Finally, the lack of a water reduction signal between 0.9 V and 1.0 V, as seen in Figure 58, indicates a highly oxo-basic sample that has little water initially present in bulk. Continued cycling and reduction of sodium at the working electrode are predicted to create water byproduct at the counter electrode (Equation 23). As a result, a minor cathodic signal at around 900 mV vs sodium and similar to

those found in NaOH-KOH studies[166] occasionally appeared after several days of investigation. This water production reaction is not expected to occur in an LMB as the complementary anode and cathode cell reactions do not produce water as a product.

To further study the electrolyte, CVs were conducted at different temperatures. Figure 80 shows clearly the effects of increasing the temperature of the melt.

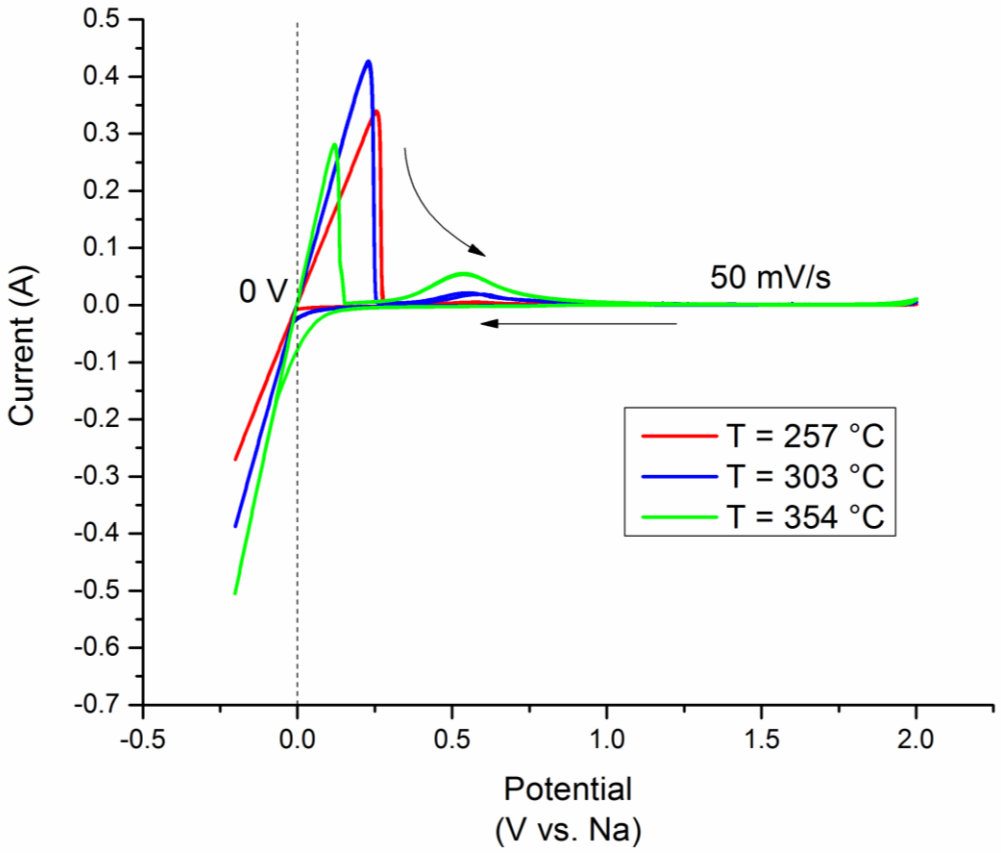

Figure 80 - 50 mV/s CVs conducted at different temperatures on 0.314 cm^2 Ni working electrode and TaNaB reference.

First, it is clear that as temperature increases the conductivity of the melt is increasing. The total electrolyte resistance of the melt can be gauged from the slopes (I/V) of the deposition and stripping process. Though the electrolyte conductivity has been exhaustively studied, this behavior prompted a simple EIS study of the electrolyte resistance as a function of temperature (Figure 81).

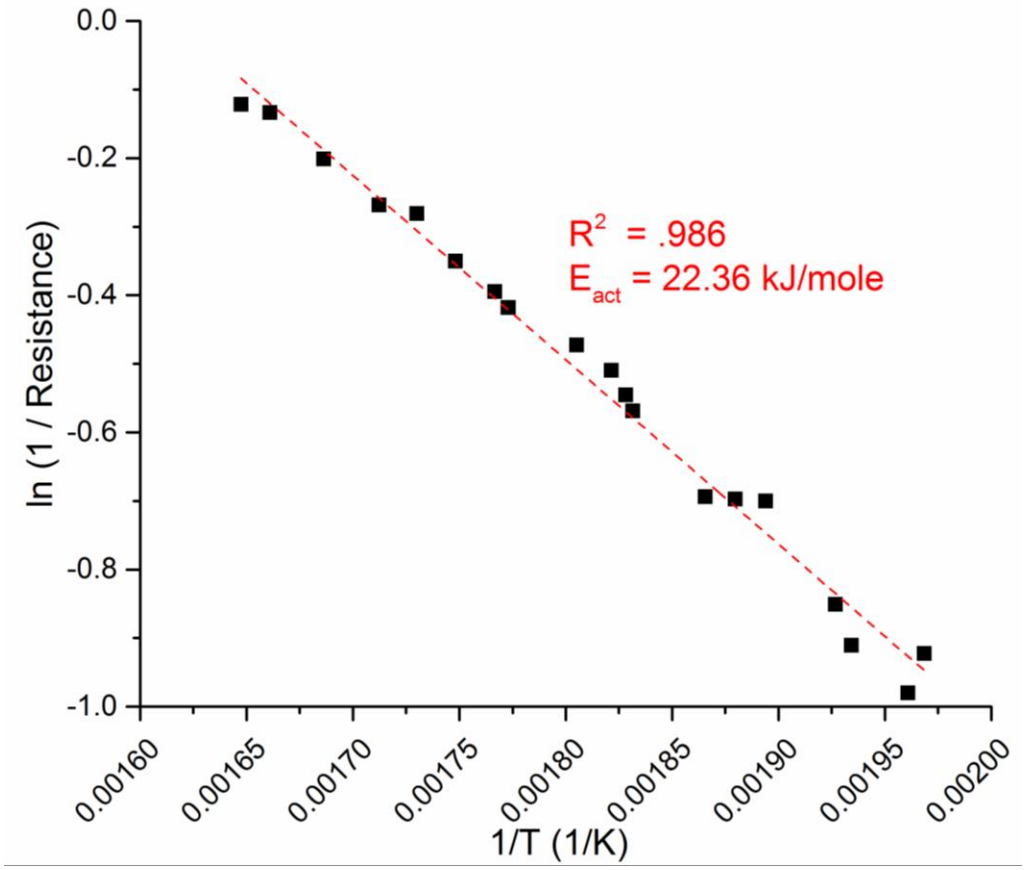

Figure 81 - Resistance measurement plotted to highlight Arrhenius temperature relationship. Though no cell constant was measured, the setup geometry was held constant at all temperatures.

The activation energy term, E_{act}, quantifies the thermal energy barrier that modulates the impact of temperature on conductivity. This value, extracted from the slope of the line and therefore agnostic to cell geometry, can be compared to the activation behavior seen in Okada's work in Figure 35. Okada's closest compositional comparison, the pink curve (82.2% NaOH), yields an activation energy of 22.0 kJ/mole, only 1.6% different from that found in these experiments. The important message here is that the transport through the electrolyte follows a simple thermally-activated behavior rather than a more complex VTF-type response as is sometimes seen with ionic liquids with more complex anions[235].

Another feature worth noting is that, as temperature is increased, the stripping signal starts to drop off relative to the deposition. In other words, it appears as though sodium metal stripping decreases as temperature increases. In order to investigate this more quantitatively, a stripping efficiency, η_{strip}, is here defined as:

$$\eta_{strip} = \frac{\int_{t_2}^{t_3} I_{cathodic} dt}{\int_{t_1}^{t_2} I_{anodic} dt} x100 \qquad \text{Equation 44}$$

Where t_1 is the time when voltage drops below 0 V (vs. Na), t_2 is the time when current first becomes positive upon anodic sweep, and t_3 is the time when the anodic sweep exits the major stripping process. These points are shown in Figure 82.

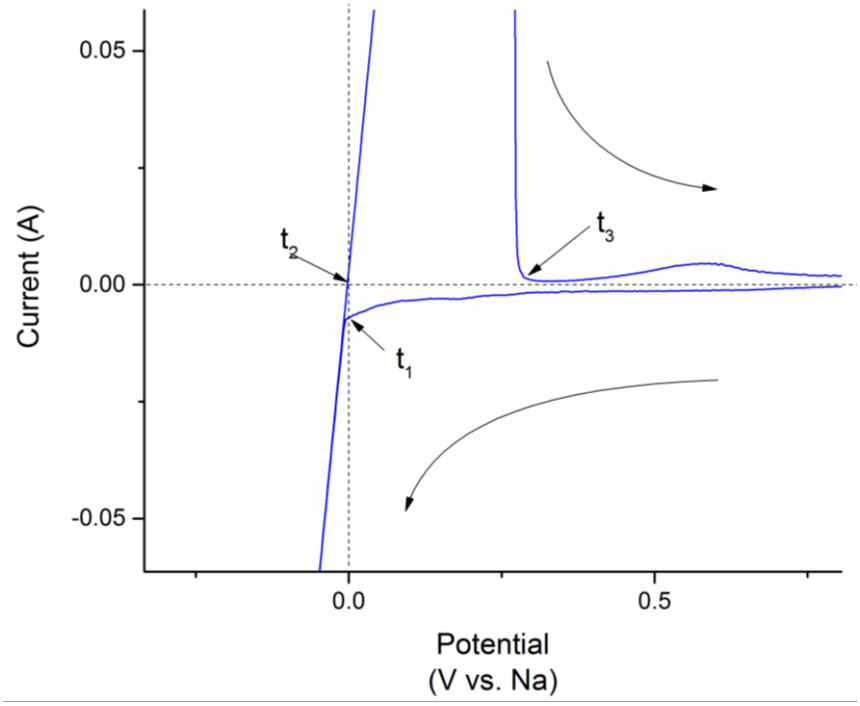

Figure 82 - Integration times used in the stripping efficiency calculation

The result from this integration is shown in Figure 83. Not shown are points for temperatures in excess of 325°C. This is because those points rarely showed any sort of anodic current within the

t_2 to t_3 range and therefore the efficiency was quite low. Rather, the plot below is selected to highlight the 280°C-300°C range in which stripping begins to precipitously drop off towards zero. This range is also coincidentally the same range in which Yoshizawa[206] observed a rapid onset of bubbling and reactivity between molten hydroxide and sodium metal. Thus, a suitable explanation for this loss of stripping is that deposited sodium chemically reacts with the melt.

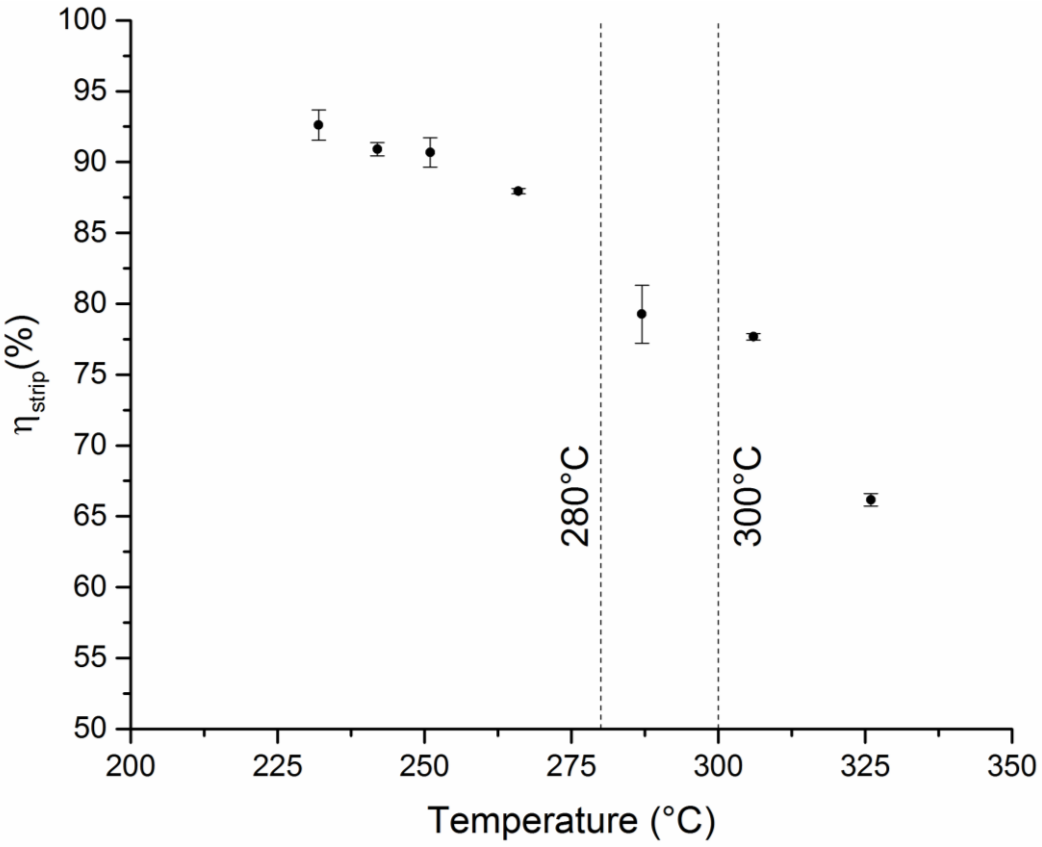

Figure 83 - Stripping efficiency of cathodic CVs conducted at varying temperatures.

These temperatures (280-300°C) therefore likely represent the range over which the reactivity between the NaOH in the binary and pure sodium metal (Equation 45) crosses over between spontaneous and non-spontaneous.

$$2NaOH_{x=0.8} + Na_{(l)} \rightarrow Na_2O + \tfrac{1}{2}H_{2\,(g)} \qquad \text{Equation 45}$$

For pure NaOH ($a_{NaOH} = 1$), this reaction is expected to occur spontaneously with a free energy of around 4.1 kJ/mole (42 mV) at temperatures immediately above the melting temperature of pure NaOH (318°C). In the case of our system, because the activity has been suppressed by 67% and the temperature is also lowered ($\Delta T_{melt} = 99°C$) the free energy of reaction is expected to become less negative. The functionality of this reaction on temperature and activity is shown in Equation 46.

$$\Delta G_{rxn} = \Delta G^0 + RTln\left(\frac{\left(p_{H_2}\right)^{1/2}\left(a_{Na_2O}\right)}{\left(a_{NaOH}\right)^2\left(a_{Na}\right)}\right) \qquad \text{Equation 46}$$

By substituting in the CEF modelled activity of NaOH ($a_{NaOH} = 0.671$ at 250°C) in the binary system, setting $a_{Na}$and a_{Na_2O} to unity, and assuming p_{H_2} is 1 atm at the counter electrode, it is found that for temperatures between 280°C and 300°C the G_{rxn} is made more positive by between 4.3 kJ/mole to 4.5 kJ/mole. This is almost exactly balanced with the spontaneous reaction with sodium metal at standard temperature and unit activities. Thus, it is possible to corroborate the decline in reactivity between sodium metal and the salt and have a thermodynamic explanation rooted in our solution mixing model to articulate this phenomenon.

Referring back one more time to Figure 80, two final features that are apparent are the increasing under-deposition of sodium at temperatures above 300°C and the growth of the oxidative signal at around 325 mV. By restricting the CV cathodic sweep to programmed pre-deposition voltages (Figure 84) a relationship between the reductive and oxidative signal can be shown. The reductive current achieved before sodium deposition (> 0V vs. Na) was not found to deposit any sort of sodium species and is proportionally linked to the return oxidative sweep. This finding implies that whatever species is deposited above sodium deposition is retained (70 – 80%) on the working electrode for re-oxidation.

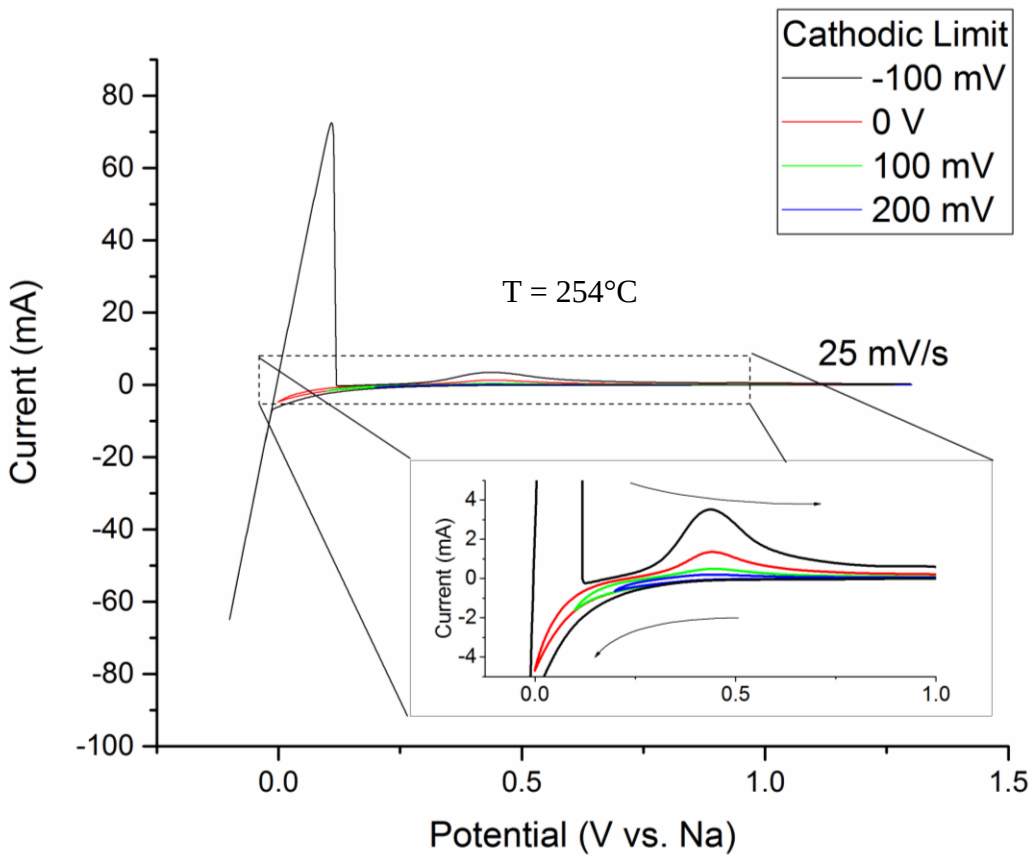

Figure 84 - Restricted CV demonstrating the linkage between the under-deposition signal and the oxidative signal

Furthermore, the coulombic efficiency of the CV measurements increases as scan rate is decreased (Figure 85). The contrary is expected to be true for sodium fog production and subsequent solubilization as has been alternatively proposed in other sodium halide systems[236]. This may also indicate that the products formed and re-oxidized are stable and perhaps self-inhibiting as they are more efficiently removed at slower rates. Though these findings do not fully clarify the mechanism, the most likely candidate is postulated to be related to H_2 reduction and potential storage within or formation of hydrides with nickel. The redox behavior of hydrogen on nickel electrodes is well studied[237] and shows similar irreversibility ($\Delta V \approx 200$ mV) between its anodic and cathodic peaks. In addition, the simultaneous production of Na_2O would explain the self-inhibiting behavior as well as describe this compounds presence in the melt as will be shown shortly.

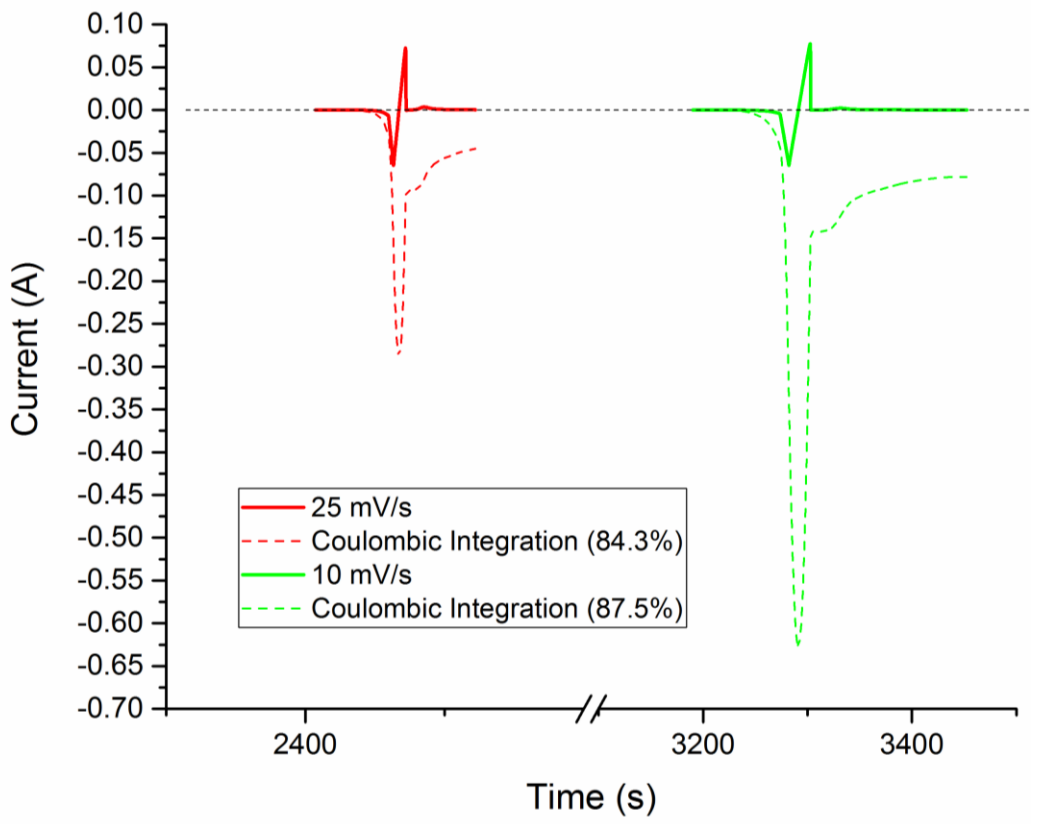

Figure 85 - Integration of two CV studies at different scan rates. The slower rate is found to more completely oxidize the reduced species, pointing to an insoluble surface species.

Overall, these anodic studies have found that, at low temperatures, the electrolyte is particularly stable with respect to pure sodium metal. A high η_{strip} efficiency was found at low temperatures and the sudden change in metallic reactivity and loss starting at 280°C was observed and explained via our binary solution model. Furthermore, though there is an as-yet unexplainable electroactive species anodic to the sodium deposition, this signal is only very slight at low temperatures and is likely related to a reaction mediated by the nickel electrode – an electrode that will not play a role in a realized LMB device.

5.4.5 Electrochemical Measurements – Anodic Study

With the cathodic side of the electrochemical window established, we now turn our attention to the oxidation limits placed upon the binary system. Figure 86 is provided below and

shows the location of four major oxidative events that were measureable during experiments with the eutectic (80/20) binary salt.

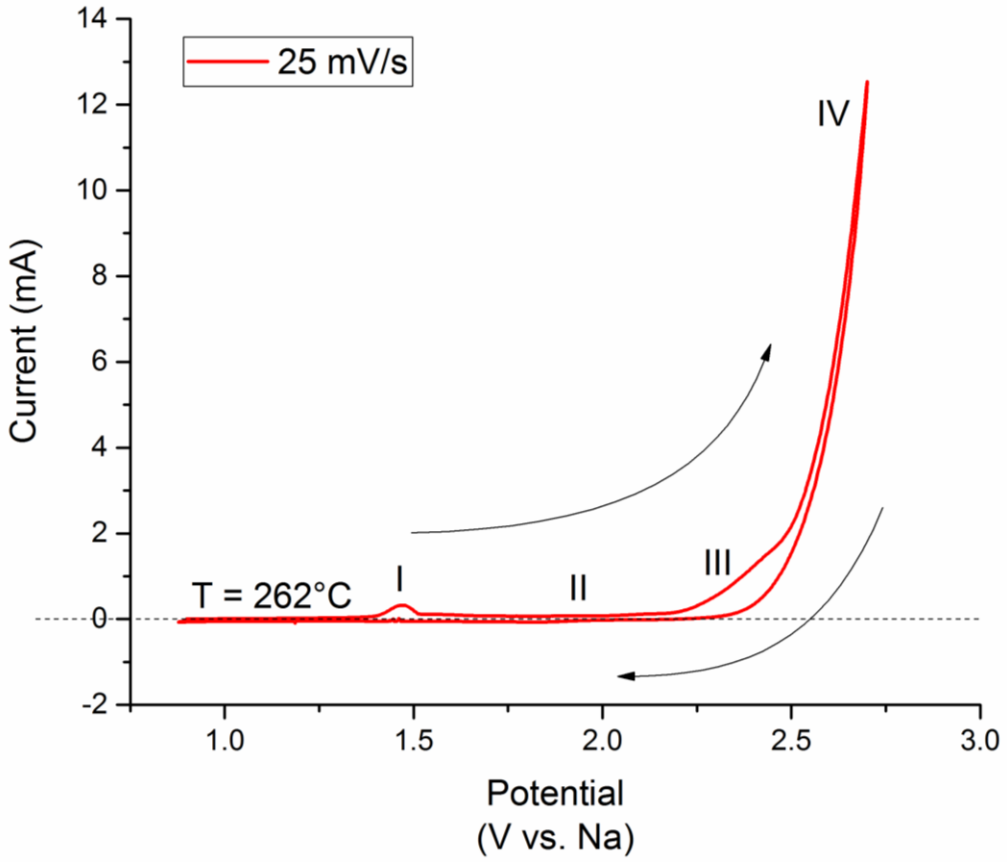

Figure 86 - An anodic CV on a 0.314 cm^2 platinum working electrode showing the location of all four anodic processes discovered in the melt.

The first two oxidative events, peak I at around 1.5V, and peak II at around 1.9V, are signals that were only rarely seen during anodic studies of the melt. In fact, the figure above was intentionally measured following a cathodic study because this was found to increase the height of the signal on peak I. Other experiments that did not include cathodic scans showed little sign of these reactions.

Looking now at peak I, from thermodynamic calculations using FACTSage 6.3 and the relevant JANAF databases the only available materials that give signals in this regime at 260°C

are the formation of $Ni(OH)_2$ (1.57 V vs. Na) or the oxidation of Na_2O to Na_2O_2 (1.52 V vs. Na). In order to determine which species is reacting, an experiment comparing the signal from a nickel working electrode to a platinum working electrode was designed. If nickel were the reactive species the experiment with the nickel electrode should show much greater oxidative activity and platinum should provide little signal due to the lack of pure nickel in the melt.

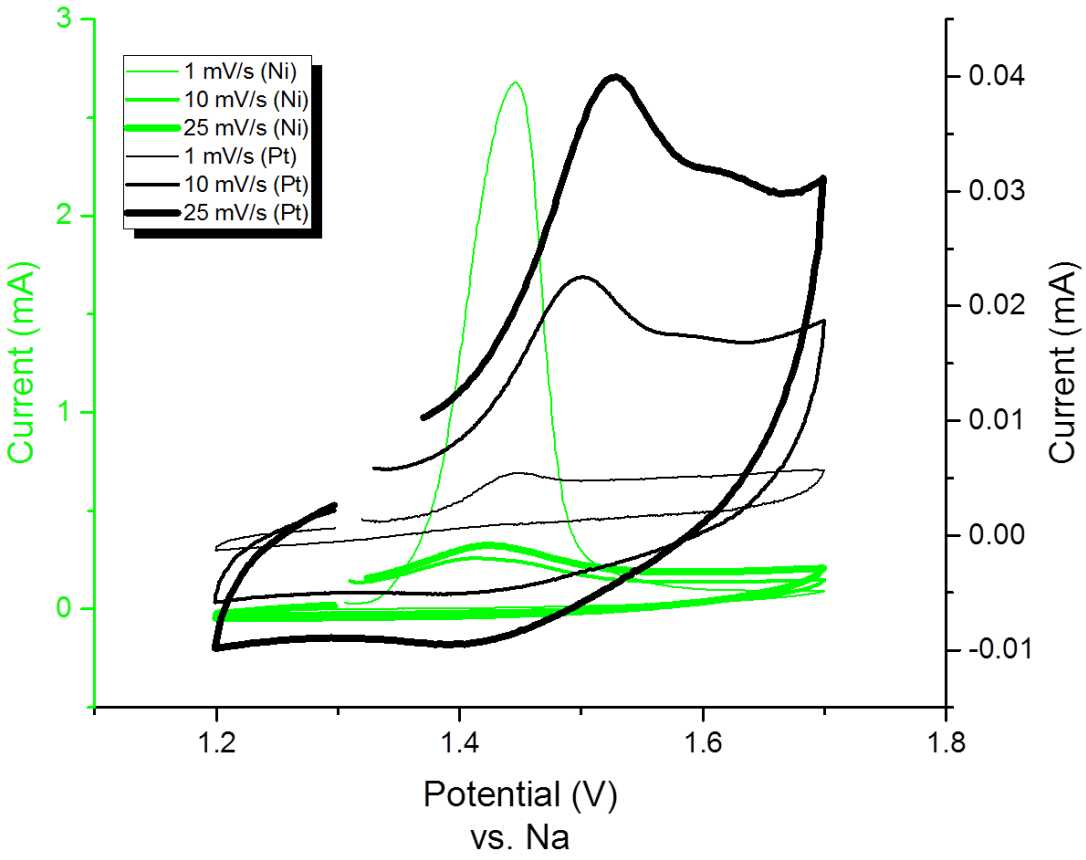

Figure 87 - Investigation of the 1.5 V oxidation signal via Ni and Pt working electrodes.

The results show that not only did platinum show greater oxidative behavior but that the behavior was diffusion limited and that the oxidation species was unavailable for reduction upon sweep reversal. This experiment proposes that, rather than being the result of a nickel impurity in the melt, peak I likely results from the oxidation of Na_2O species to Na_2O_2. This result makes sense as both Na_2O and Na_2O_2 are known to exist in highly oxo-basic (anhydrous) sodium

hydroxide melts. Further, Na_2O is a likely product of the unknown oxidation reaction discussed during the cathodic study. This would explain why peak I (1.5 V) is mostly present following reduction studies. The presence of a low concentration oxidizable Na_2O in solution would also explain the signal at peak II. The only reaction that can account for a signal at this voltage is the complete oxidation of Na_2O to pure sodium and oxygen (1.79 V)

Turning attention now to the two major and reproducible peaks in the anodic scan, peaks III and IV, Figure 88 shows the impact of repeated CV experiments on peaks III and IV. Peak III has been registered as starting around 2.1 V (vs. Na) and peak IV at around 2.5 V (vs. Na). Peak III drops with each cycle and as a result the responsible species is thought to be depleted as oxidation recurs. Peak IV, on the other hand, proceeds with little reduction or impediment on each cycle. Also noticeable is that there is no sign of any reduction signal for either peak upon the cathodic return sweep. This indicates that the oxidation products are likely to be a gaseous phase that leaves the melt. It is also noteworthy that both of these peaks quite temperature sensitive. This sensitivity further supports the proposal that the products are gas phases because non-condensed phases, responsible for large entropic changes in free energy, are far more susceptible to temperature and pressure changes.

Referring now to thermodynamic calculations, Peak III is here proposed to derive from the full oxidation of sodium peroxide (Na_2O_2) to sodium and oxygen. This reaction occurs at 2.06 V (vs. Na) at 260°C and would sensibly exist following the proposed production of Na_2O_2 at peak I. A final point before reviewing the final oxidation (peak IV) is that many studies have reported on the presence of sodium superoxide (NaO_2) in hydroxide melts. This species is commonly formed via the reaction of atmospheric O_2 with hydroxide ions in the melt.

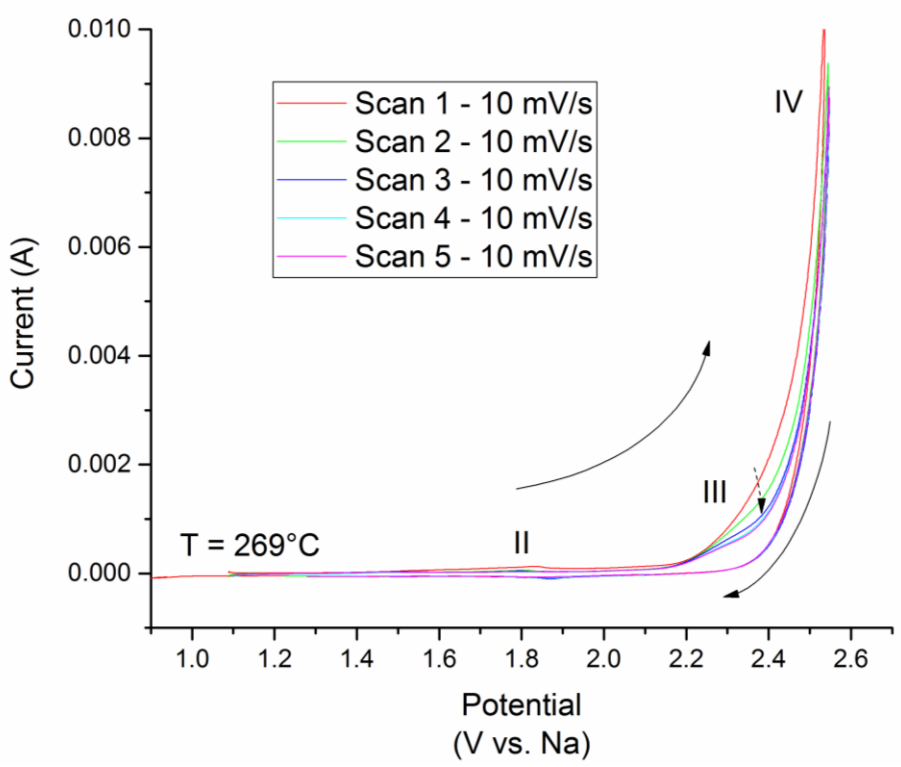

Figure 88 - Repeated anodic CVs run to show the depletion of the species that drives peak III.

Throughout our electrochemical studies no sign of this species was found. Most studies[166, 238] place the superoxide reduction at around 1.8 V vs. Na. This reduction is quite strong and requires the presence of water to proceed (Equation 47).

$$O_2^- + 2H_2O + 3e^- \rightarrow 4OH^- \qquad \text{Equation 47}$$

Because there have been no detectable reduction signals at this voltage during any of the sweeps, the reaction above is not active and as a result there is likely very little superoxide in the melt.

The final, and most important, anodic reaction is represented by mechanism IV. This reaction represents the "limiting" reaction in that it represents the electrolysis of a major component of the melt, NaOH. As has been shown already, the NaI species is not thermodynamically electroactive at voltages below 2.8 V. In addition, oxidation experiments conducted inside of an argon-filled glovebox created oxygen spikes in the oxygen sensor

following studies that scanned beyond 2.5 V. This reaction, shown in Equation 42 and reproduced below in the peak table, serves as the absolute upper boundary on the electrochemical window of the binary salt.

Table 35 - Proposed reactions at each of the peaks in the oxidation studies.

Peak	Reaction	Voltage (at 260°C)
1	$2Na_2O \rightarrow Na_2O_2 + Na$	1.52
2	$Na_2O \rightarrow 2Na + ½O_{2\,(g)}$	1.79
3	$Na_2O_2 \rightarrow 2Na + O_{2\,(g)}$	2.06
4	$2NaOH \rightarrow 2Na + H_2O + ½O_{2\,(g)}$	2.42

By plotting I vs V data on a log-normal scale (Tafel plot) it is possible to identify distinct reaction regions that correspond to these four mechanisms (Figure 89).

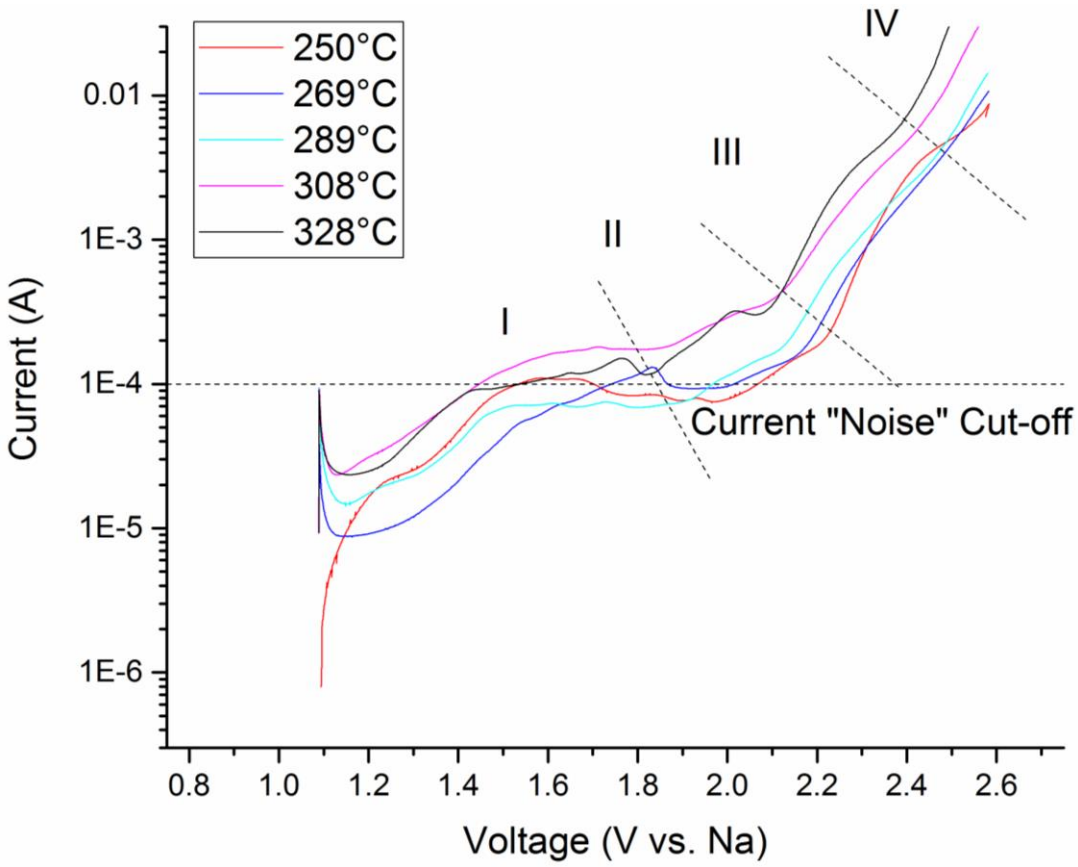

Figure 89 - A Tafel-type plot of the anodic scan of binary eutectic at various temperatures. Different reaction mechanisms are clearly visible and their onsets occur at the voltages shown in Table 35.

This is valuable because it highlights the voltage region over which process IV is dominant and provides the ability to locate the region over which one can reliably extrapolate back from to determine the zero current crossover point. This method of extrapolating the anodic reaction onset voltage has been used variously[187, 239] and is here used to find the change in the major oxidation event as a function of temperature.

In order to extrapolate the NaOH electrolysis anodic limit this analysis will use only the CV portion of the curve that occurs at voltages in the stage IV region. Because the theoretical electrochemical window (ECW) for this salt is officially defined as the voltage window bounded by the major reduction of sodium at zero volts on the cathodic end and the major oxidation of oxygen at more positive potentials, the voltage measured at zero current is also equal to the electrochemical window.

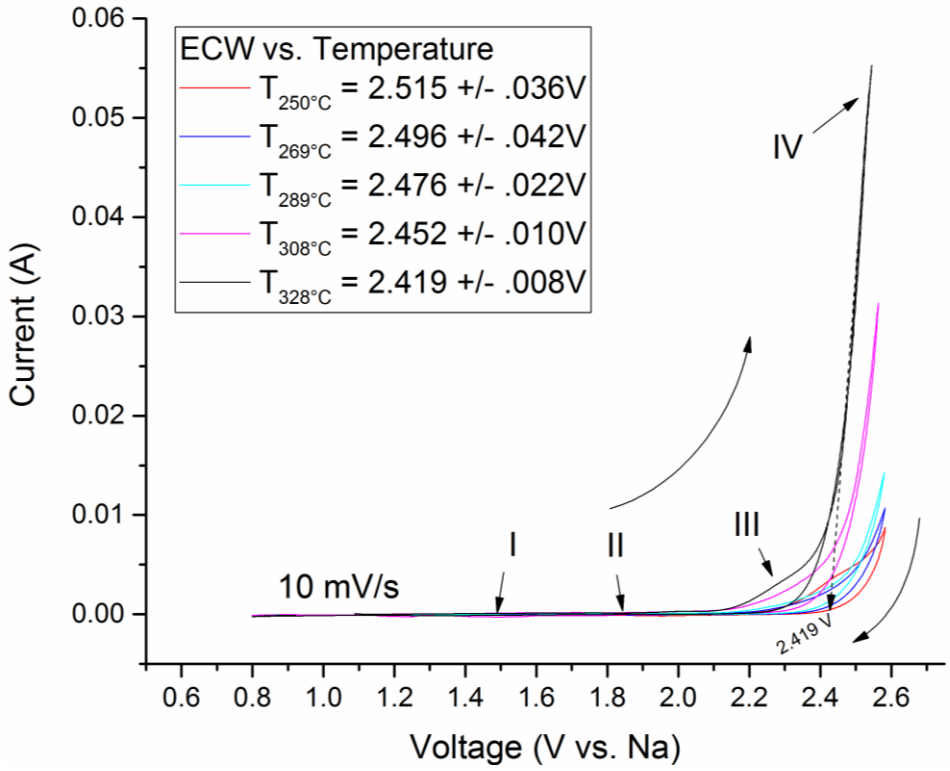

Figure 90 - Functionality of ECW on temperature study. ECW is extrapolated back from stage IV anodic process. Dotted arrow demonstrates this procedure for the T=328°C voltammagram.

For this reason, it will interchangeably be referred to as the anodic limit or ECW. Figure 90 shows five anodic sweeps conducted at different temperatures. Even after removal of the temperature-dependent uncompensated resistance these scans still show a strong relationship between the anodic limit and the temperature of the melt. As demonstrated for the 328°C scan, a line extrapolated back from the voltage range covering stage IV (from Figure 89) provides a voltage of 2.419 V vs. Na. This process is repeated for the other four curves and the collective ECW values show a very predictable linear relationship with temperature, as predicted in Equation 43.

These experimental ECW values can then be compared (Figure 91) to those predicted from the thermodynamic model (Figure 78) for the binary solution at the composition.

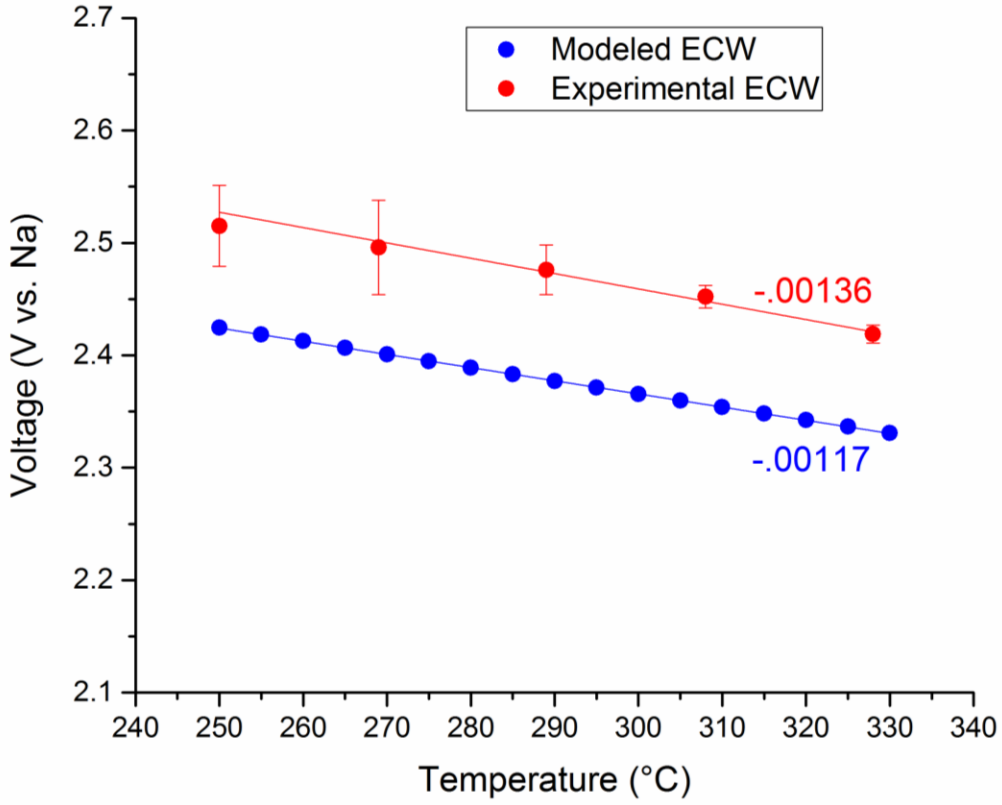

Figure 91 - Comparison of the experimentally measured oxygen production voltage with that predicted from the thermodynamic model. Slopes are provided next to curves.

Of greatest note is that the experimental and theoretical data show strong agreement in their trend as a function of temperature. The slopes, related to the entropy[i] of the reaction, are found to be within approximately 15% of each other. These minor differences in the slopes are related to error arising from the solution model and assumptions of gaseous product pressures. Because the activity values for NaOH would need to be an order of magnitude lower to match the experimental findings, we speculate that differences in the absolute voltages of the reaction are related to the oxygen production overpotential. In spite of this, the thermodynamic modeling of the liquid solution is here confirmed to produce results that are realized experimentally.

From this anodic study it is found that the molten salt has a theoretical electrochemical window of between 2.4 (330°C) and 2.5 V (250°C). Practically speaking, an electrochemical window free of any of the Na_xO_y impurity redox reactions exists up to around 2 volts as there were processing conditions that lead to binary salts that showed no redox behavior corresponding to peaks I or II. In other words, there are preparation methods that should allow a binary molten salt to obviate these reactions though the oxidation at 2.07 and 2.5 V cannot be avoided. Though this window might seem quite small for those experienced with Li-ion based systems, it is perfectly well-suited for our uses in an LMB system. As was clearly shown in Table 1, there are no Na-based LMB couples that operate over 1.7 V in their maximum charge state.

Having now explored the thermal and compositional window of operation (5.3.1), identified and confirmed two binary compounds (5.3.2), used DSC data and XRD studies to model the molten salt with a 2-sublattice sub-regular solution model (5.3.3) that creates real predictions with regards to sodium metal stability (5.3.4) and electrochemical window

[i] And therefore activities of the reactants and products

functionality (5.3.5) now is a good time to see if the molten salt we have down-selected and studied can perform in a proof-of-concept liquid metal battery.

5.4.6 Cell Cycling Study

A proof-of-concept cell was constructed using eutectic NaOH-NaI (80/20) as the Na^+ itinerant electrolyte and Na||Pb-Bi as the electrode couple. The Pb-Bi alloy was created at 44/56 mole percent Pb/Bi to take advantage of its low eutectic melting temperature (125°C). The cell was charged and discharged at 270°C according to the schedule in Table 29. Over one month the cell cycled 112 times with smooth charge and discharge profiles through most of the operation. Though no features can be clearly distinguished in Figure 92, this image is provided as proof of the longevity of this prototype cell.

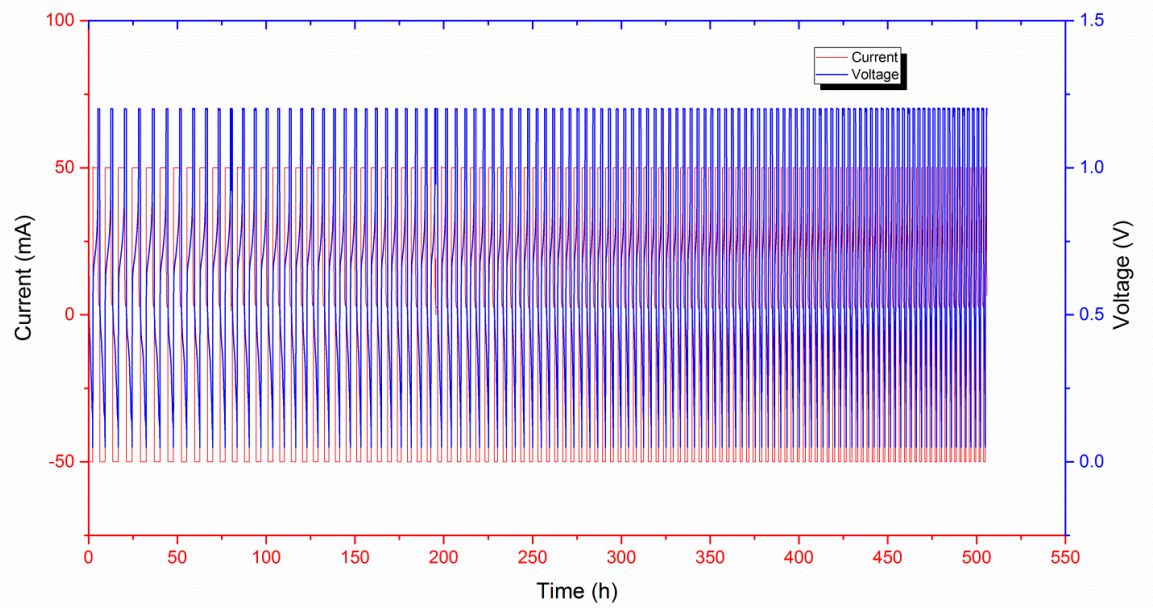

Figure 92 - 112 charge-discharge cycles

Zooming in on cycles 9 through 11, one can clearly see the smooth charge-discharge profiles of the battery (Figure 93). The most striking features of these cycles are the large overpotential, the bumpy profile at the end of discharge, and the extremely low leakage current.

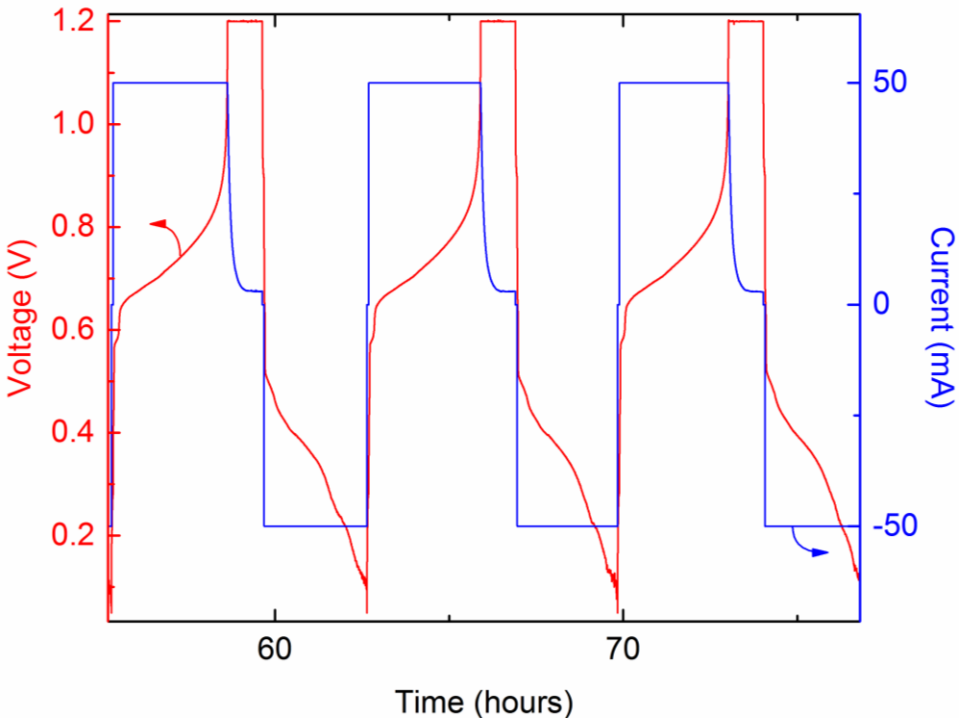

Figure 93 - Cycles 9 through 11 out of 112 of the charge-discharge experiment

The overpotential, here visualized on the charge/discharge capacity curves (Figure 94), starts at around 75 mV and slowly grows as discharge proceeds.

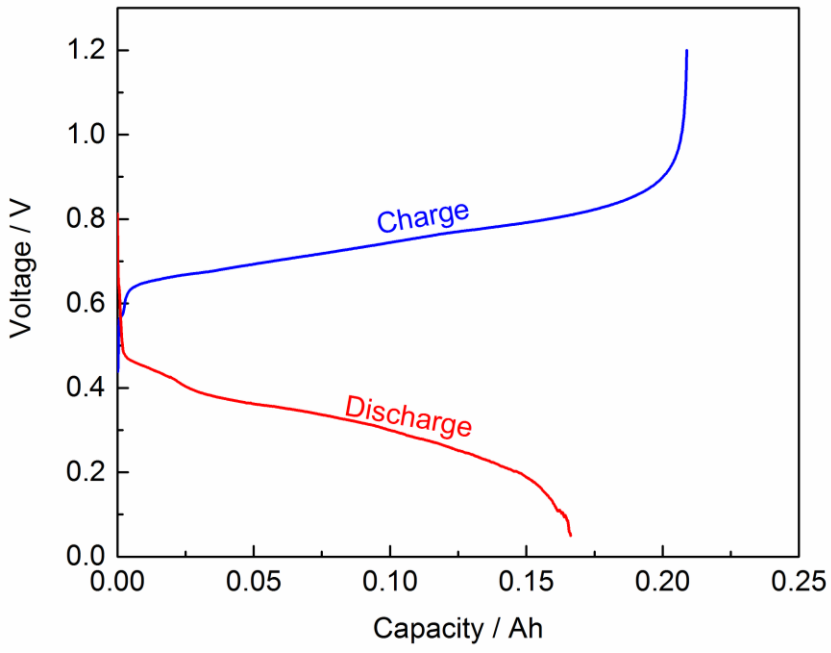

Figure 94 - Charge and discharge vs capacity curve for a single cycle.

This overpotential was interestingly found to be 3 to 4 times larger than the impedance measurement (or theoretical conductivity) would predict. This may be due to the formation of low-diffusivity, high-melting, intermetallic at the surface of the positive electrode[i]. The asymmetry of the overpotential, favoring the discharge curve over the charge curve, coupled with the bumpiness experienced at the end of discharge, both favor the idea that the positive electrode is driving up the overpotential at the surface.

Referring now to the test schedule in Table 29, the leakage current measurement, also known as self-discharge, was made by holding the cell at a charging voltage for one hour and measuring the resulting current through the electrolyte. This process ensures that leakage due to solubilized sodium or other parasitic reactions are measured via the potential gradient's ability to create currents in all non-ionic electronic pathways. A close-up of a typical leakage current measurement is shown in Figure 95.

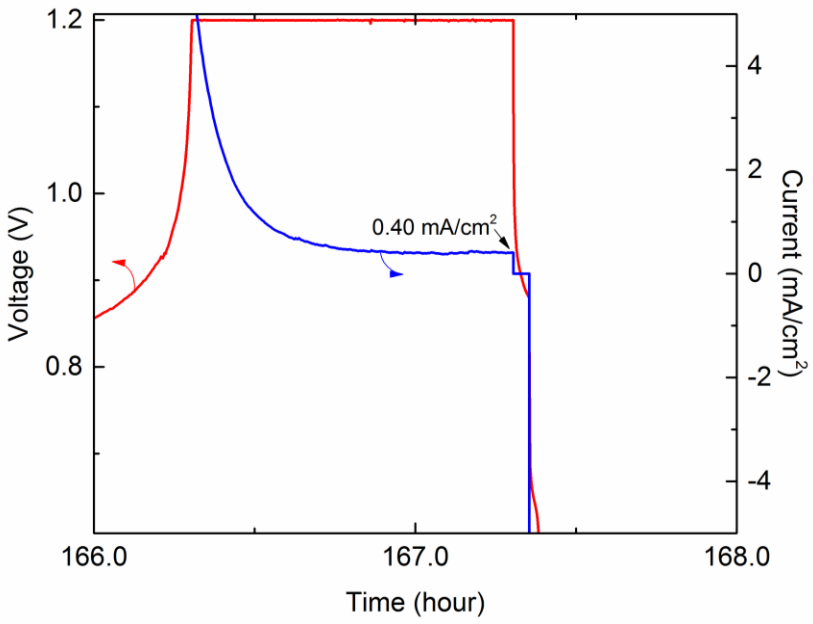

Figure 95 - Leakage current (self-discharge) measurement after a full charging step.

[i] Sodium forms several 300°C+ compounds with lead and an 845°C melting Na-rich compound with Bismuth. In the event that sodium preferentially reacts with one of these constituents, a solid compound may form on the surface.

By normalizing the total current by the area of the electrodes (8.548 cm^2) it is possible to calculate a current density of 0.40 mA/cm^2. Similarly, the average leakage current density over the entire cycling study was 0.34 mA/cm^2. This is an incredibly low value when viewed in the context of previous studies involving a sodium metal anode. In comparison to the cells developed by Argonne National Labs, our device shows a leakage current that is two orders of magnitude lower than their Na-Bi cell[172]. Even more impressive is this device's performance in the context of the current LMB under development at Ambri. Publicly available literature[23] reports the Li||Pb-Sb leakage current to be twice as large at 0.6 mA/cm^2. Therefore, the Na||Pb-Bi leakage current found here is not only impressive in the context of sodium-based batteries but also when compared to other Li-based systems that have not historically showed this as a failure mechanism.

Finally, the energy and coulombic efficiency of each cycle can be calculated. Figure 96 clearly shows a stable coulombic efficiency hovering at around 90%, matching those of earlier CV studies (5.3.4), and energy efficiency at 40%. Though the η_{energy} numbers are low, the cycled cell is also not optimized in terms of temperature, composition, or design. Rather, these data show, at minimum, what is possible with this new electrolyte chemistry. It is theorized that the energy inefficiency comes from a combination of the aforementioned solid intermetallic formation on the surface of the positive electrode, poor sodium metal wetting at the anode, and the reaction of hydroxide with bismuth and lead to form small percentages of dielectric bismuth and lead oxides. These species were corroborated from sectioning of the cell as the color of the salt had changed to a yellowish orange and SEM EDX studies revealed low percentages (1-2%) of lead and bismuth present in the salt (Figure 97).

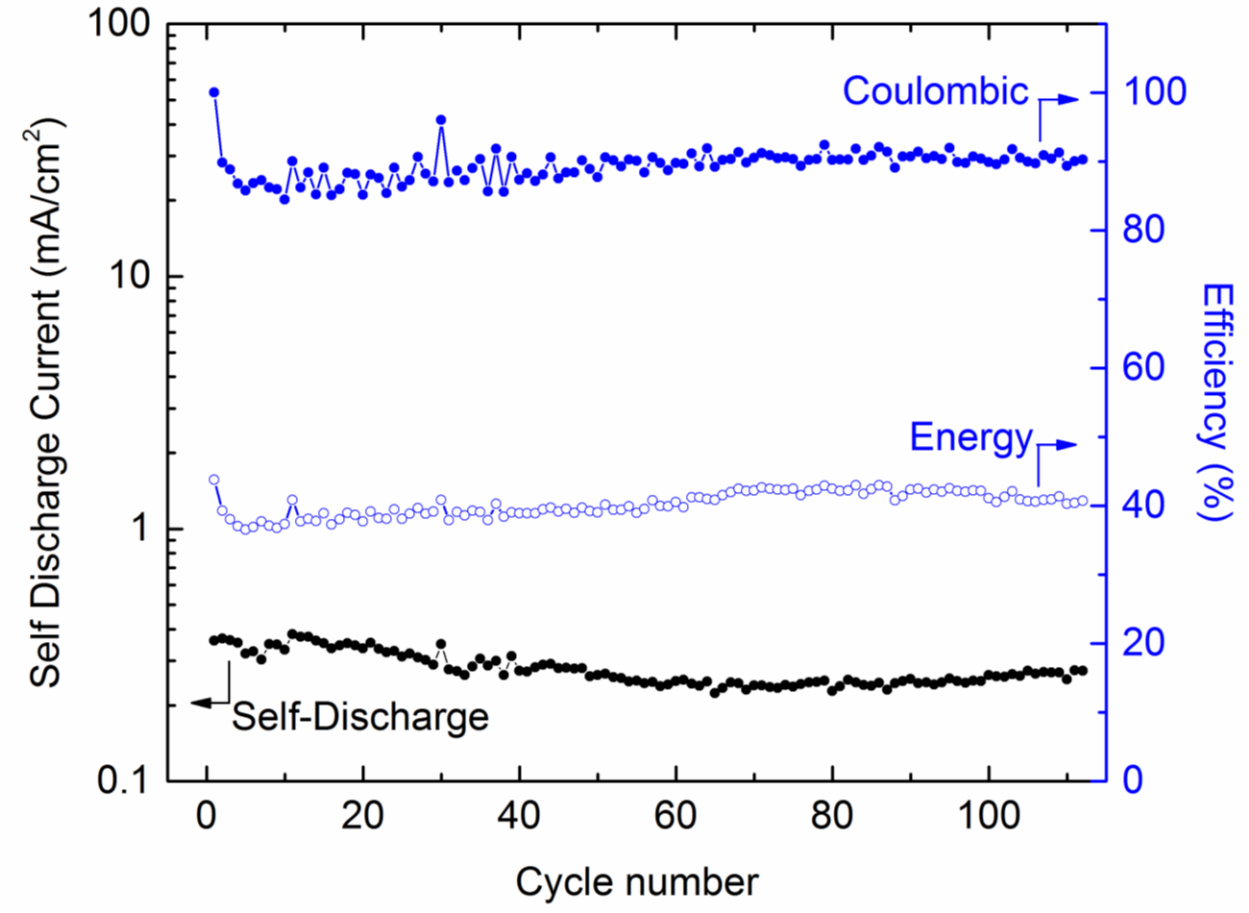

Figure 96 - Energy and coulombic efficiency data calculated for each cycle alongside each leakage current measurement.

The SEM micrograph shows iodine and oxygen in approximately atomic percentages that yield fairly accurate predictions of the eutectic salt composition. Because SEM cannot identify hydrogen, the atomic percentages shown do not include this value and therefore the totals are skewed. Correcting for this undetectable hydrogen one finds expected ratios of Na-O-I for the ideal eutectic salt to be 50.0-36.5-13.4. These numbers are within the experimental accuracy of the EDX equipment and the sample is therefore confirmed to be of eutectic composition. Any differences in atomic percentages are therefore proposed to result from the minor inclusion of dissolved/oxidized lead and bismuth species.

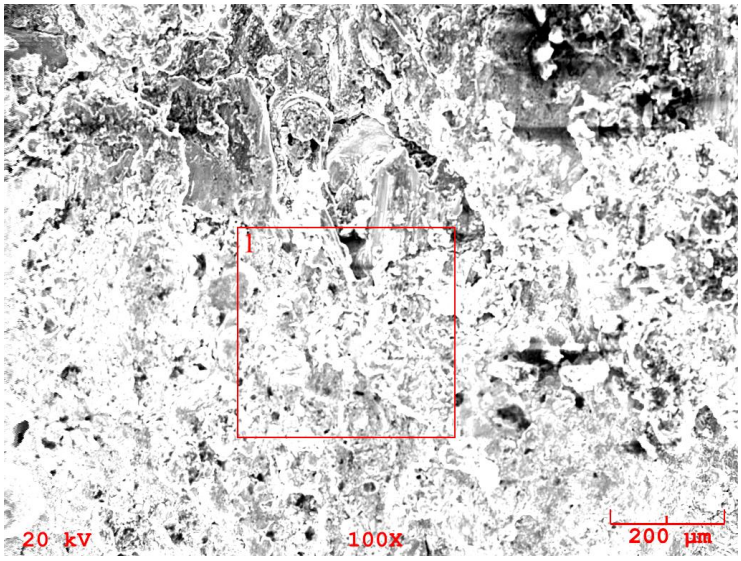

Element	Intensity (c/s)	Atomic %	Conc.	Units	Error 2σ
O	655.63	37.2	15.0	wt.%	0.38
Na	1,527.59	46.3	26.9	wt.%	0.44
I	769.87	14.0	44.8	wt.%	1.09
Pb	16.39	1.4	7.3	wt.%	2.41
Bi	11.63	1.1	6.0	wt.%	2.62

Figure 97 – SEM (on previous page) of the NaOH-NaI salt after 1 month of cycling (112 cycles).

SEM was similarly employed to confirm the presence of metallic sodium in the positive electrode (Figure 98). Because the batteries were not fully charged prior to decommissioning, the atomic percent of sodium is expected to be quite low. From the figure above it is clear that there exists sodium metal at various portions of the electrode. The point scans at #2 and #3 are both relatively free of salt and still show a signal for sodium[i]. Another finding worth noting is that there do appear to be portions of the metal that have been oxidized ($O_{point\ 3}$ = 7.7%). This may contribute to some of the overpotential upon discharge at the positive electrode.

A final point worth noting is that the cell displayed a very high capacity fade rate (1%/cycle). This was the principal failure mechanism of the device and limited its operation to

[i] Data from Box Scan #1 are excluded here as there was later shown to be a great deal of salt present (dark regions) in the scan region. These portions of salt, resulting from the polishing procedure, compromise measurements of sodium in the positive electrode.

only slightly over 100 cycles. The steady capacity fade is here proposed to be due to the slow evaporative loss of sodium metal from the negative electrode.

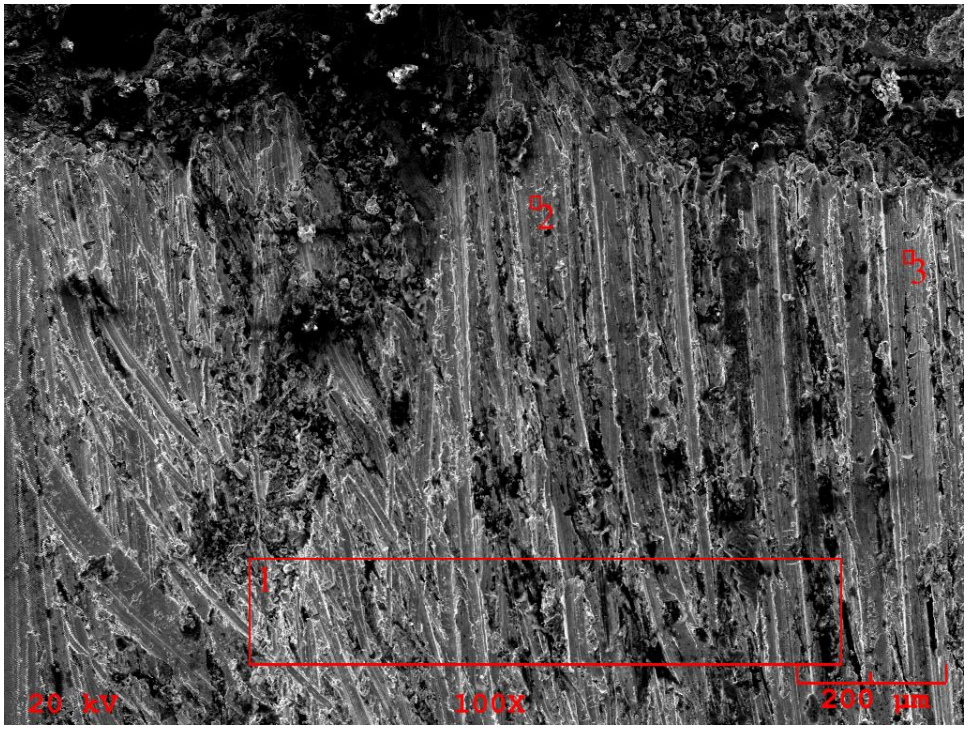

Element	Point 2 Atomic %	Point 3 Atomic %
O	0.0	7.7
Na	3.0	6.3
I	1.0	0.8
Pb	44.6	41.6
Bi	51.4	43.6

Figure 98 - SEM of the electrode-electrolyte interface with sample points being taken at the surface of the electrode. The darker region represents salt due to its lower atomic electron count resulting in lower backscattering.

Because the cell was constructed in an open crucible (Figure 59) and the top of the experimental chamber was at room temperature, we believe the small amount of sodium composing the negative electrode steadily evaporated and collected at the top of the crucible similar to a cold finger effect. This capacity fade is therefore an important failure mechanism to study though should be addressable via a closed cell design in future experiments.

Overall, the findings from the cell prototype study are extremely promising. Not only did the cell cycle over 100 times with the first system developed, it did so while addressing the

principal failure mechanism found in Na_m-type batteries, leakage current. Though there is a great deal of room for further work, this study has successfully highlighted the promise held by the NaOH-NaI binary salt system to serve as a low-temperature molten salt electrolyte.

Chapter 6 – Conclusions and Next Steps

6.1 Work Summary

This body of work has set upon the task of improving the liquid metal battery's (LMB's) ability to store and deliver energy in a manner that best positions it to address the application space of grid-scaled storage. To this end, this work has aimed to set a methodological standard for how LMB research should be targeted and has subsequently employed this methodology to explore an exciting new system that is projected to lower costs. For this reason, the high level goal of this thesis has been to prove how a rigorous understanding of the LMB and existing literature can lay the foundation for improved research outcomes that translate more quickly into actual device improvements.

In order to accomplish this goal, the logic flow proceeded systematically along the steps described in Figure 99. The steps also mirror the construction of the chapters in this thesis

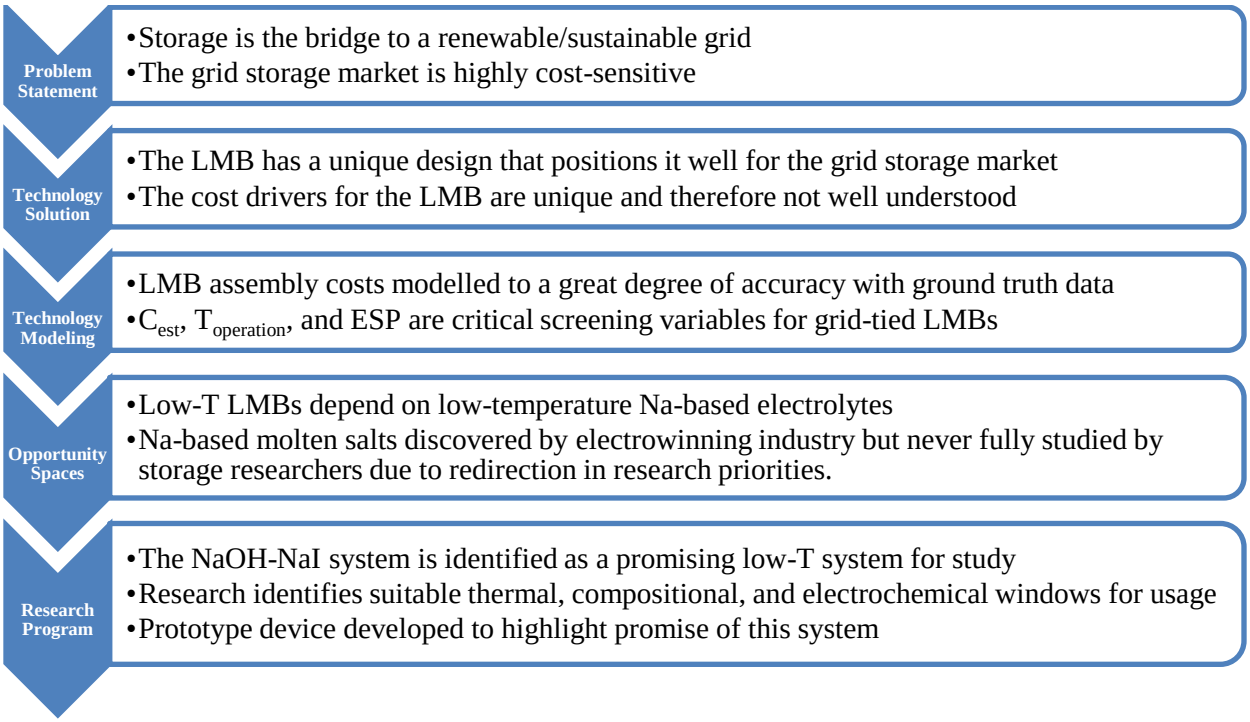

Figure 99 – Description of the logical flow used during this thesis work

and the reader is therefore directed back to the relevant section for further review of the logic. In addition to setting a standard for how LMB research programs should be designed, the two major results sections, Chapter 3 and Chapter 5, have additionally provided some specific insights into the LMB that are novel and worth final summary.

6.1.1 Cost Modeling and Down-Selection

One of the key assumptions in selecting the LMB as a potential solution for the severely cost-sensitive space of grid storage is that, because it is built and operates in a manner unique from other batteries, it must also have a very unique cost structure that advantages it in achieving particularly low levelized total costs of energy (TCOE). This assumption, though based on reasonable knowledge of the inputs and construction processes has never been quantitatively modeled or shown to be true. This work has, for the first time, shed light on the cost structure of the LMB and additionally provides insights into those areas that create substantial impact on TCOE versus those that do not.

From Figure 12, it is clear that active cell materials make up one of the largest single portions of an LMB's cost at between 30-36% of the total BOM. Though a large contribution is expected, when compared to commercialized technologies like Li-ion where active cell materials make up between 50-70% of a pack's total cost[240], the LMB is unique in being far less functional on its active cell materials. This result makes sense given what is known regarding the more complicated and expensive processing steps required for nanostructured intercalation-type electrodes and also when considering the fact that the active materials used in the LMB are not far down the processing line from their raw sources. This finding also proposes that the extreme focus placed on anode and cathode materials by the Li-ion research community is probably not appropriate for alloying-type LMBs as the TCOE savings from such efforts are negligible.

An additional conclusion that can be drawn regarding the relatively smaller role played by active materials is that the effect on TCOE from changing the negative electrode material is quite small. In the very optimistic case where an optimal Na||X couple has the same performance metrics as the Li||Pb-Sb system, substituting sodium metal for lithium has only marginal impacts upon the total cost of the system. Holding everything else constant, the cost model predicts that a move to sodium creates only a 5-6% reduction in the TCOE ($260/kWh) which could later be offset by lower discharge voltages. For this reason, a major conclusion from the LMB cost model is that a move to sodium for the sake of its lower cost has only marginal returns. This is quite contrary to the common logic amongst most battery researchers working on Na-S, Zebra, or Na-ion devices where it is proposed that a move to sodium will significantly suppress $/kWh values in comparison to their lithium analogues. The LMB's cost structure and operation is unique in that the smaller role played by anode materials and the greater weight placed upon the positive electrode, electrolyte, and systems-level controls results in weak anode price sensitivity.

Perhaps the most interesting find from the cost modeling exercise is to identify the large contribution to cost from the systems-level electrical and thermal control components. Specifically, between 26-32% of total system cost comes from wiring, battery management systems (BMS), and thermal systems that help to safely and reliably cycle the cell. Unlike most other battery systems that also require BMS support when aggregated into stacks, the LMB faces unique challenges deriving from its high temperatures of operation. In addition to requiring additional insulation, cooling, and heat management it also creates substantial burdens on the electrical wiring of the system. A standard LMB pack operating at over 50 amps per device can see currents ranging between 0.5 to 1.0 kA. Such currents require large diameter wire gauging and advanced thermal insulation. Further, these requirements are only made more expensive by

the elevated operating temperature. As has been shown, reductions to temperatures below 300°C enable simplifications in these systems via smaller gauge wiring, simpler wire insulation, and the opportunity to use PTFE for containment and sealing in the device.

The LMB cost model provided here has therefore achieved several goals. First, it has accurately modeled the BOM costs of a standard LMB device. This represents the first known public model of a high-temperature grid-storage battery. Secondly, it has provided insights into cost structure that are corroborated by a deep understanding of LMB raw materials and device assembly. Finally, it has highlighted those areas where savings can be accrued through further study. As with most highly engineered systems there are of course improvements that can be made by optimizing engineering decisions like device geometry, cycling parameters, steel grade, or even electrolyte thickness. There are also those material properties like temperature that can act as a multifaceted cost lever in that they are able to create cascading impacts on system cost by unlocking simpler material containment, thermal controls, wiring, and sealing. Specifically, temperatures below 280°C experience 8-10% savings in TCOE while those able to dip below 250°C may enjoy 10-15% reductions. It is because of this unique impact on cost and because of the scientific challenge in identifying and testing such a system that low-temperature LMBs have been selected and novel molten salt systems have been studied in depth.

6.1.2 The NaOH-NaI System

Because the operating temperature is set by the highest melting component in the LMB, it is most often the case that the molten salt electrolyte, with its stronger ionic bonding, sets this operational parameter. For this reason, moving to a low temperature system LMB system is fundamentally dependent on identifying a suitable low temperature electrolyte that is stable with liquid metals and allows for high transport properties. As was elaborated in Chapter 4, the key window of opportunity that exists for our work is the ability to build upon the knowledge

accumulated but not put into practice from sodium production for use in an electrochemical storage device. Of the electrolytes explored by this industry, NaOH-NaX type systems are found to have significantly suppressed melting temperatures while also providing substantial conductivities in excess of 0.5 S/cm. The selection of NaOH-NaI (5.1.1) has been made on the basis of its low eutectic temperature, high conductivity, and existing literature studies by Okada and associates (5.1.2). In order to completely de-risk this system for use in an LMB, the remaining challenges to be addressed involve developing a full understanding of the compositional, thermodynamic, and electrochemical windows of the electrolyte. These pieces of knowledge, in conjunction with existing data on density and conductivity, provide the scientific justification for testing and studying this binary system in cell trials.

Differential scanning calorimetry has been used to reproducibly identify the solid-solid and solid-liquid transitions in the binary space. Studies confirm the existence of a eutectic temperature at 219°C and 80% NaOH/20% NaI. This eutectic temperature, 99°C below the melting point of pure sodium hydroxide, allows for the practical operation of an LMB cell between 240°C and 260°C. These phase data, in conjunction with existing liquidus studies of the binary system allow for the construction of an experimental phase diagram (Figure 66) that can give indications of binary compounds in the system. It has further been shown that previous conclusions regarding the locations of binary compounds has been incorrect via high-resolution x-ray diffraction scans of various annealed melt compositions. These scans point to the existence of two highly crystalline compounds, $Na_5(OH)I_4$ and $Na_7(OH)_5I_2$. The first compound, $Na_5(OH)I_4$, has been previously predicted but never before studied crystallographically. This work provides the first diffraction study and proposes both a peak list and potential symmetry for this material. The second compound, $Na_7(OH)_5I_2$, has been described in the crystallographic

literature but was never before considered by molten salt researchers. It is here confirmed to exist and has further been used to experimentally confirm the 80/20 location of the eutectic composition.

The DSC phase transition points, in addition with the location of the two binary compounds, has allowed for a computational modeling of the thermodynamic functions of the various phases in the phase diagram. Whereas historic work has only interpolated the phase boundaries free-hand, this work has sought to quantitatively model and create a fully self-consistent thermodynamic picture of the entire space in order to allow for further calculations of the melt and predictive ternary expansion in the future. Given these goals, and considering the asymmetric nature of the anions in the melt, a two-sublattice compound energy formalism (CEF) was used to model the liquid phase while functions like those shown in Equation 37 provided a framework for optimization within the FactSage software. The highly iterative process (Figure 51) yields fully consistent thermodynamic function coefficients for all of the new phases (Table 34) and most importantly provides insights into the activities of liquid phase constituents (Figure 77). This data allowed for a theoretical prediction of salt properties like electrochemical window and reactivity against sodium metal, both things that can be tested experimentally.

In order to understand the electrochemical window of the melt and validate the thermodynamic model from earlier, 3-electrode cyclic voltammetry (CV) has been performed. This experimental pathway required the long-term study of crucible and electrode material stability (Table 26) as well as the development of a new stable TaNaB reference system (Figure 57) for use in high-temperature caustic melts. Once complete, CV studies focused separately on the anodic and cathodic limits in order to understand the limiting reactions on both sides. At the cathodic limit, sodium metal deposition and stripping were both found at temperatures below

300°C. A deposition-to-stripping ratio was developed in order to quantify the retention of sodium metal following deposition. This study showed that the sodium metal is remarkably stable against the melt when compared to previous work. The thermodynamic model of the melt similar predicts reactivity suppression between sodium and the melt due to the lowered temperatures and suppression of NaOH activity.

The anodic study fully characterized four different signals that were seen during the sweep. The first three signals correspond to trace Na_xO_y-type impurities in the melt while the final, limiting, oxidation represents the evolution of oxygen gas. This limiting anodic reaction was studied as a function of temperature in order to provide a point of comparison with the predicted electrochemical window. Though the absolute values between the experimental and model ECW values are shifted due to oxygen production overpotential, the model is shown to successfully reproduce the slope of the reaction. This is indicative of a model that correctly predicts reactant activities as these directly affect the slope of the curve.

Finally, having explored the thermal and compositional window of operation (5.3.1), identified and confirmed two binary compounds (5.3.2), used DSC data and XRD studies to model the molten salt with a 2-sublattice sub-regular solution model (5.3.3) that creates real predictions with regards to sodium metal stability (5.3.4) and electrochemical window functionality (5.3.5), this study finally turns to developing a prototype liquid metal battery in order to test the outcome of the rigorous molten salt screening process employed.

A proof-of-concept cell was constructed using the NaOH-NaI eutectic (80/20) as the Na^+ itinerant electrolyte and Na||Pb-Bi as the electrode couple. The Pb-Bi alloy was created at 44/56 mole percent Pb/Bi to take advantage of its low eutectic melting temperature (125°C). The cell

was successfully charged and discharged at 270°C with a notably low leakage current of 0.34 mA/cm^2 (Figure 95). This is two orders of magnitude less than those found in early Na-Bi cells and half that demonstrated for promising Li-based LMB chemistries. The cell was cycled over 100 times (Figure 92) and was ultimately limited by the evaporative loss of sodium metal into the much larger testing crucible environment. This failure mechanism likely accounts for a vast majority of the 1%/cycle capacity fade rate experienced as the experiment progressed. Throughout the lifetime of the device, coulombic efficiencies of around 92% and energy efficiencies around 41% were measured (Figure 96). The low energy efficiency was found to derive principally from suboptimal cell design and the positive electrode reaction, specifically the overpotential associated with the formation of a solid Na-Bi phase in the positive electrode. These results present the first known LMB-type rechargeable storage device that can operate below 300°C.

In summary, the cost modeling and down-selection provided clear criteria for the selection of a low-temperature Na^+-itinerant molten salt system. This system has been shown to possess the required compositional, thermal, and electrochemical windows to allow its service as an LMB electrolyte. It has further been shown through experiment and modeling that many of the detrimental reactions and loss mechanisms historically experienced in sodium systems can be mitigated or circumvented entirely via reduction of system temperature and activity of the NaOH species. Finally, a low-temperature Na-based LMB was developed and cycled for the first time. By substituting in the prices of sodium and cost projections for the eutectic electrolyte ($0.01/g), an operating temperature of 250°C, a discharge voltage of 700 mV, and energy efficiency of 80% we find for a future optimized prototype Na||Bi-X cell that the cost model predicts a total system cost of around $241/kWh, approximately 12.7% less than that of the modeled Li||Pb-Sb system

and precisely in line with earlier projects of 10-15% reductions. Though there are still several areas in which cell improvements are required, these findings point not only to the possibility that low-temperature molten salts do in fact provide a pathway towards cheaper grid storage but also that following a methodological thought process for system selection can and does yield exciting results.

6.2 Next Steps

Though this work has attempted to lay the foundation for a new rigorous approach to LMB research and made the case for temperature as a critical variable, there is still quite a bit of further work that can be done to improve each step along the way. First, the cost model can and should have more material prices functionalized by volume to account for the changing economies of scale in prices. At this time, the model only uses online bulk pricing available to MIT as a compromise between small scale orders and those achievable through preferred partnerships. Functionalizing material prices, though perhaps not impacting any particular price a great deal, may have an overall large impact considering the percentage of TCOE that comes from active and inactive materials. It will also change the TCOE as a function of annual storage production volumes as larger volumes would necessitate larger bulk orders.

Another point of further resolution needed for the cost model is to better model the thermal management and BMS support systems for the packs and cores. Though the electrical wiring is fairly accurate, the actual modules that regulate charging and temperature lack high quality projections due to their custom-built nature. Correctly modeling these, and understanding how their capacities or functionalities may change with temperature or core size, would be a valuable addition to the model.

A final point of worthwhile inquiry would be to further break out the pack and core assembly process to both understand the correct ratio of human labor to automation but also to add much-needed resolution to the costs and times it takes to wire up a multi-cell module. In this model, core and pack assembly is estimated on the basis of the number of cells (in packs) or packs (in cores) and the amount of wire that would need to be run. This approximation ignores important things like connections, alignments, and final testing. These steps all need to be captured as they may impact the rate limiting step during manufacturing.

With regards to the experimental work presented in this thesis, there are several areas that would benefit from further study. First, the cyclic voltammetry work would be aided by a further understanding of the unknown signals that occur several hundred millivolts positive of sodium deposition. Further, controlled studies of sodium dissolution in eutectic melts, as well as lower concentration NaOH binaries, would help to further pin down the crossover point at which the melt is fully stable against the pure sodium metal. It would also be valuable to run XRD experiments on samples of high NaI-purity (e.g. 90% NaI) in an attempt to semi-quantitively extract the stoichiometry of the NaI-rich compound. This information could then be fed back into the solution model and re-optimized to achieve coefficients that more closely represent the behavior of the binary liquid.

Another interesting area for improvement is in the refinement of the solution model used to model the binary liquid. High temperature X-ray or NMR studies could be used to probe the short range order of the binary molten salt in order to acquire insights into solution models that best accommodate the structure of the solution. For instance, the asymmetric OH^- anions may not be well modeled as sitting on a single anion lattice site and as a result a modified sublattice model would need to be incorporated. Similarly, aggregates or clusters of complexed ions may

exist in solution. If this were the case modifications to the Redlich-Kister coefficients would be needed to simulate this. In either case, the ability to more accurately model the solution is valuable as this would allow for what is perhaps the most exciting future research opportunity: a predictive expansion into molten salt ternary space.

Most of the industrial practices utilizing molten salts have arrived at their specific recipes and procedures via substantial trial-and-error. This Edisonian-style process, though capable of producing good results, becomes quite intimidating when considering the huge combinatorial space occupied by ternary or higher-order mixtures of salts. The ability to use the NaOH-NaI binary solution model as a jumping off point for intelligent expansion into ternary space presents an exciting line of inquiry that is akin to the philosophy presented here. Specifically, it is possible to add more rigor and structure to the otherwise ad hoc study of a highly-dimensional space. The results of the model presented here are now readily integrable into a ternary modeling approach on FactSage or similar software packages. With experimental work complementing promising theoretical findings, it may become possible to computationally develop, to a high degree of accuracy, the exact cocktail of molten salts components needed to satisfy certain thermodynamic requirements.

A final area for future work involves the development of a larger flight of Na|NaOH-NaI|X cells. For these trials there are both meaningful design improvements that can be tested as well as new chemistries. On the design side, the testing of closed cells with PTFE seals would represent a significant step towards cheaper and simpler LMB devices. PTFE seals and simple Fe-based container materials would be both particularly easy to manufacture as well as scale cheaply. On the chemistry side, there is great opportunity in identifying new positive electrode materials and alloys that simultaneously provide high voltages against sodium while being stable

with a hydroxide-based electrolyte. In addition to alloys with bismuth, another potential material of study would be to deploy mercury as a positive electrode material or alloying component. This metal has been shown to be stable against hydroxide and would likely provide smooth discharge voltages from approximately 700 mV. In addition, the ability to put all of the stockpiled mercury to use in a technology that is both highly controlled and maintained away from the residential consumer could decrease society's exposure to this harmful material while simultaneously providing value through improved renewables integration for the grid.

In summary, the work presented in this thesis is meant to serve as the first and foundational step towards low-temperature and therefore low-cost LMBs. As with any research project, there are still strategic areas that could use further de-risking, however, the outputs from this work are meant to be directly integrable into future low-temperature work. At the time of publication, a great deal of research within the Sadoway Group is shifting towards low-temperature or high-voltage systems. This speaks to both the predictive power of the cost model and the terrific promise presented by lower-temperature devices.

Works Cited

1. Diebel, J.; Norda, J. WeatherSpark Beta.
2. Spliid, I. B., Data on operating and decommisioned wind turbines. Agency, D. E., Ed. www.ens.dk, 2013.
3. Thostrup, K., Wholesale electricity market data. Energinet, Ed. Energinet.dk, 2013.
4. Sharman, H.; Meyer, H.; Agerup, M., Wind Energy: The Case of Denmark. *Center for Politiske Studier (CEPOS)* **2009**.
5. Lund, H.; Hvelplund, F.; Ostergaard, P. A.; Moller, B.; Mathiesen, B. V.; Andersen, A.; Morthorst, P. E.; Karlsson, K.; Meibom, P.; Munster, M.; Munksgaard, J.; Karnoe, P.; Wenzel, H.; Lindboe, H. H. *Danish Wind Power: Export and Cost*; Aalborg University: Department of Development and Planning, 2010.
6. Rastler, D. *Electricity Energy Storage Technology Options: A White Paper Primer on Applications, Costs and Benefits*; Electric Power Research Institute (EPRI): Palo Alto, California, 2010.
7. Eyer, J.; Corey, G. *Energy Storage for the Electricity Grid: Benefits and Market Potential Assessment Guide: A Study for the DOE Eenrgy Storage Systems Program*; Sandia National Labs: Albuquerque, New Mexico, 2010.
8. *Annual Energy Review 2011*; Department of Energy: Washington DC, 2011.
9. EIA, U., Electric Power Monthly. In *Net Generation by Energy Source*, Energy, U. S. D. o., Ed. Washington, D.C., 2014.
10. Electricity: Renewable Energy Generating Capacity and Generation. Administration, U. S. E. I., Ed. Washington, DC, 2011.
11. Kintner-Meyer, M.; Balducci, P.; Colella, W.; Elizondo, M.; Jin, C.; Nguyen, T.; Viswanathan, V.; Zhang, Y., National Assessment of Energy Storage for Grid Balancing and Arbitrage: Phase 1, WECC. Energy, D. o., Ed. Pacific Northwest National Laboratory: Richland, Washington, 2012.
12. *Energy Storage Activities in the United States Electricity Grid*; Electricity Advisory Committee - Energy Storage Technologies Subcommittee: 2011.
13. Barnhart, C. J.; Benson, S. M., On the importance of reducing the energetic and material demands of electrical energy storage. *Energy & Environmental Science* **2013,** *6* (4), 1083-1092.
14. Nelson, P. A.; Gallagher, K. G.; Bloom, I.; Dees, D. W. *Modeling the Performance and Cost of Lithium-Ion Batteries for Electric-Drive Vehicles*; Argonne National Laboratory: 2012.
15. *Electric Power Industry Needs for Grid-Scale Storage Applications*; Sandia National Laboratories: 2010.
16. Yang, Z. G.; Zhang, J. L.; Kintner-Meyer, M. C. W.; Lu, X. C.; Choi, D. W.; Lemmon, J. P.; Liu, J., Electrochemical Energy Storage for Green Grid. *Chemical Reviews* **2011,** *111* (5), 3577-3613.
17. Wadia, C.; Albertus, P.; Srinivasan, V., Resource constraints on the battery energy storage potential for grid and transportation applications. *J. Power Sources* **2011,** *196* (3), 1593-1598.
18. Oskvig, D.; Chevrette, J. *2013 Strategic Directions in the US Electric Industry*; Black and Veach: 2013.
19. Kim, H.; Boysen, D. A.; Newhouse, J. M.; Spatocco, B. L.; Chung, B.; Burke, P. J.; Bradwell, D. J.; Jiang, K.; Tomaszowska, A. A.; Wang, K.; Wei, W.; Ortiz, L. A.; Barriga, S. A.; Poizeau, S. M.; Sadoway, D. R., Liquid Metal Batteries: Past, Present, and Future. *Chemical Reviews* **2012**.
20. Newhouse, J. M.; Poizeau, S.; Kim, H.; Spatocco, B. L.; Sadoway, D. R., Thermodynamic properties of calcium–magnesium alloys determined by emf measurements. *Electrochimica Acta* **2013,** *91* (0), 293-301.
21. Kim, H.; Boysen, D. A.; Bradwell, D. J.; Chung, B. C.; Jiang, K.; Tomaszowska, A. A.; Wang, K. L.; Wei, W. F.; Sadoway, D. R., Thermodynamic properties of calcium-bismuth alloys determined by emf measurements. *Electrochimica Acta* **2012,** *60*, 154-162.

22. Poizeau, S.; Kim, H.; Newhouse, J. M.; Spatocco, B. L.; Sadoway, D. R., Determination and modeling of the thermodynamic properties of liquid calcium–antimony alloys. *Electrochimica Acta* **2012,** *76* (0), 8-15.
23. Wang, K.; Jiang, K.; Chung, B.; Ouchi, T.; Burke, P. J.; Boysen, D. A.; Bradwell, D. J.; Kim, H.; Muecke, U.; Sadoway, D. R., Lithium-antimony-lead liquid metal battery for grid-level energy storage. *Nature* **2014,** *514* (7522), 348-350.
24. Gasior, W.; Moser, Z., THERMODYNAMIC PROPERTIES OF BINARY LITHIUM-ZINC SYSTEM. *Journal de Chimie Physique et de Physico-Chimie Biologique* **1993,** *90* (2), 387.
25. Chiotti, P.; Stevens, E. R., THERMODYNAMIC PROPERTIES OF MAGNESIUM-ZINC ALLOYS. *Trans. Metall. Soc. AIME* **1965,** *233* (1), 198.
26. Pogodaev, A. M.; Lukashenko, E. E., THERMODYNAMIC INVESTIGATION OF MOLTEN MAGNESIUM-ZINC ALLOYS. *Russ. J. Phys. Chem.* **1972,** *46* (2), 197.
27. Chiotti, P.; Hecht, R. J., THERMODYNAMIC PROPERTIES OF CALCIUM-ZINC SYSTEM. *Trans. Metall. Soc. AIME* **1967,** *239* (4), 536.
28. Delcet, J.; Egan, J. J., THERMODYNAMICS OF LIQUID CA-ZN ALLOYS. *Metallurgical Transactions B* **1978,** *9* (4), 728.
29. Huggins, R. A., *Energy storage*. Springer: New York ; London, 2010; p 1 online resource (xxviii, 406 p.) :.
30. Lantratov, M. F.; Mikhailova, A. G., THERMODYNAMICS OF LIQUID METAL SOLUTIONS OF SODIUM WITH CADMIUM. *Zhurnal Prikladnoi Khimii* **1971,** *44* (8), 1778.
31. Iwase, M.; Sugino, S.; Ichise, E.; Waseda, Y., APPLICATION OF NA+-ION-CONDUCTING BETA-AL2O3 TO THERMODYNAMIC STUDIES OF LIQUID SODIUM-BASED ALLOYS - (XNA+(1-X)CD), (XNA+(1-X)IN), AND (XNA+(1-X)SN). *Journal of Chemical Thermodynamics* **1985,** *17* (7), 601.
32. Terpilow, J.; Barycka, I., THERMODYNAMICAL PROPERTIES OF LIQUID CADMIUM-MAGNESIUM SOLUTIONS. *Bull. Acad. Pol. Sci., Ser. Sci. Chim.* **1961,** *9* (4), 175.
33. Iverson, M. L.; Recht, H. L., ACTIVITY OF SODIUM IN SODIUM AMALGAMS FROM EMF MEASUREMENTS. *Journal of Chemical and Engineering Data* **1967,** *12* (2), 262.
34. Hsueh, L.; Bennion, D. N., EMF MEASUREMENTS OF SODIUM ACTIVITY IN SODIUM AMALGAM WITH BETA-ALUMINA. *Journal of the Electrochemical Society* **1971,** *118* (7), 1128.
35. Bykova, M. A.; Morachev, A. G., THERMODYNAMICS OF LIQUID ALLOYS IN SODIUM-MERCURY SYSTEM. *Zhurnal Prikladnoi Khimii* **1973,** *46* (2), 312.
36. Ishiguro, T.; Takeda, S.; Tamaki, S., EMF-MEASUREMENTS ON LIQUID NA-HG ALLOYS AND THEIR THERMODYNAMIC PROPERTIES. *J. Phys. F: Met. Phys.* **1982,** *12* (5), 845.
37. Armbruster, M. H.; Crenshaw, J. L., A thermodynamic study of liquid potassium amalgams. *Journal of the American Chemical Society* **1934,** *56* (7), 2525.
38. Agruss, B.; Karas, H. R., The Thermally Regenerative Liquid Metal Concentration Cell. In *Regenerative EMF cells*, Gould, R. F., Ed. American Chemical Society: Washington, DC, 1967; pp 62-81.
39. Wen, C. J.; Boukamp, B. A.; Huggins, R. A.; Weppner, W., THERMODYNAMIC AND MASS-TRANSPORT PROPERTIES OF LIAL. *Journal of the Electrochemical Society* **1979,** *126* (12), 2258.
40. Belton, G. R.; Rao, Y. K., A GALVANIC CELL STUDY OF ACTIVITIES IN MG-AL LIQUID ALLOYS. *Trans. Metall. Soc. AIME* **1969,** *245* (10), 2189.
41. Notin, M.; Gachon, J. C.; Hertz, J., THE GIBBS ENERGY AND ENTROPY OF FORMATION OF INTERMETALLIC AL-CA COMPOUNDS - SOLID ELECTROLYTE GALVANIC CELL STUDIES. *J. Less-Common Met.* **1982,** *85* (2), 205.
42. Srikanth, S.; Jacob, K. T., THERMODYNAMICS OF ALUMINUM-BARIUM ALLOYS. *Metallurgical Transactions B* **1991,** *22* (5), 607.
43. Wen, C. J.; Huggins, R. A., ELECTROCHEMICAL INVESTIGATION OF THE LITHIUM-GALLIUM SYSTEM. *Journal of the Electrochemical Society* **1981,** *128* (8), 1636.

44. Tamaki, S.; Cusack, N. E., THERMODYNAMIC PROPERTIES OF LIQUID NA-GA ALLOYS. *J. Phys. F: Met. Phys.* **1979,** *9* (3), 403.
45. Morachevskii, A. G., Thermodynamic analysis of interaction between components in liquid sodium-gallium alloys. *Russ J Appl Chem* **2000,** *73* (12), 2017.
46. Slaby, H.; Terpilow.J, THERMODYNAMIC PROPEFTIES OF LIQUID MAGNESIUM-GALLIUM SOLUTIONS. *Bull. Acad. Pol. Sci., Ser. Sci. Chim.* **1964,** *12* (9), 581.
47. Nebell, H., THERMODYNAMIC PROPERTIES OF LIQUID MAGNESIUM-LEAD, MAGNESIUM-INDIUM AND MAGNESIUM-GALLIUM ALLOYS. *Revue Roumaine de Chimie* **1970,** *15* (1), 59.
48. Predel, B.; Hulse, K., THERMODYNAMIC PROPERTIES OF SOLID MAGNESIUM-GALLIUM SYSTEM. *J. Less-Common Met.* **1979,** *63* (2), 159.
49. Wen, C. J.; Huggins, R. A., THERMODYNAMIC AND MASS-TRANSPORT PROPERTIES OF LIIN. *Materials Research Bulletin* **1980,** *15* (9), 1225.
50. Rais, A.; Cusack, N. E.; Neale, F. E., SIMULTANEOUS MEASUREMENT OF RESISTIVITY AND THERMODYNAMIC PROPERTIES OF LIQUID BINARY-ALLOYS - APPLICATION TO NA-IN, NA-SN. *J. Phys. F: Met. Phys.* **1982,** *12* (6), 1091.
51. Takenaka, T.; Petric, A.; Saboungi, M. L., THERMODYNAMIC PROPERTIES AND PHASE-EQUILIBRIA OF THE POTASSIUM INDIUM SYSTEM BY ELECTROMOTIVE-FORCE MEASUREMENTS. *Journal of Physics: Condensed Matter* **1991,** *3* (11), 1603.
52. Morachevskii, A. G.; Bykova, M. A., Thermodynamic analysis of component interaction in liquid alloys of the potassium-indium system. *Russ J Appl Chem* **2001,** *74* (11), 1793.
53. Delcet, J.; Egan, J. J., THERMODYNAMICS OF LIQUID CA-AG AND CA-IN ALLOYS. *J. Less-Common Met.* **1978,** *59* (2), 229.
54. Gray, P.; Cusack, N. E.; Tamaki, S.; Tsuchiya, Y., THERMODYNAMIC PROPERTIES OF LIQUID NA-TL. *Physics and Chemistry of Liquids* **1980,** *9* (4), 307.
55. Lantratov, M. F.; Tsarenko, E. V., STUDIES ON THE THERMODYNAMIC PROPERTIES OF LIQUID METALLIC SOLUTIONS - THE SYSTEM POTASSIUM-THALLIUM. *Zhurnal Fizicheskoi Khimii* **1959,** *33* (8), 1792.
56. Terpilowski, J.; Slaby, H., THERMODYNAMIC PROPERTIES OF LIQUID MAGNESIUM - THALLIUM SOLUTIONS. *Bull. Acad. Pol. Sci., Ser. Sci. Chim.* **1963,** *11* (6), 317.
57. Wen, C. J.; Huggins, R. A., CHEMICAL DIFFUSION IN INTERMEDIATE PHASES IN THE LITHIUM-TIN SYSTEM. *Journal of Solid State Chemistry* **1980,** *35* (3), 376.
58. Wen, C. J.; Huggins, R. A., THERMODYNAMIC STUDY OF THE LITHIUM-TIN SYSTEM. *Journal of the Electrochemical Society* **1981,** *128* (6), 1181.
59. Yuan, D.; Kroger, F. A., SOLDIUM ACTIVITY IN LIQUID SODIUM-TIN ALLOYS. *J. Phys. Chem.* **1969,** *73* (7), 2390.
60. Rivier, M.; Pelton, A. D., THERMODYNAMIC PROPERTIES OF LIQUID NA-SN ALLOYS BY EMF-MEASUREMENTS WITH BETA-ALUMINA ELECTROLYTES. *Journal of the Electrochemical Society* **1978,** *125* (9), 1377.
61. Tamaki, S.; Ishiguro, T.; Takeda, S., THERMODYNAMIC PROPERTIES OF LIQUID NA-SN ALLOYS. *J. Phys. F: Met. Phys.* **1982,** *12* (8), 1613.
62. Egan, J. J., Thermodynamics of liquid magnesium alloys using CaF2 solid electrolytes. *Journal of Nuclear Materials* **1974,** *51* (1), 30.
63. Eckert, C. A.; Irwin, R. B.; Smith, J. S., THERMODYNAMIC ACTIVITY OF MAGNESIUM IN SEVERAL HIGHLY-SOLVATING LIQUID ALLOYS. *Metallurgical Transactions B* **1983,** *14* (3), 451.
64. Delcet, J.; Delgado-Brune, A.; Egan, J. J. In *Coulometric Titrations Using CaF2 and BaF2 Solid Electrolytes to Study Alloy Phases*, Symposium on Calculation of Phase Diagrams and Thermochemistry of Alloy Phases, Milwaukee, Wisconsin, Chang, Y. A.; Smith, J. F., Eds. Metallurgical Society of AIME: Milwaukee, Wisconsin, 1979; p 275.

65. Gasior, W.; Moser, Z., Thermodynamic study of liquid lithium-lead alloys using the EMF method. *Journal of Nuclear Materials* **2001,** *294* (1-2), 77.
66. Fray, D. J.; Savory, B., MEASUREMENT OF ACTIVITY OF SODIUM IN SODIUM + LEAD ALLOYS BY USE OF BETA-ALUMINA. *Journal of Chemical Thermodynamics* **1975,** *7* (5), 485.
67. Matsunaga, S.; Ishiguro, T.; Tamaki, S., THERMODYNAMIC PROPERTIES OF LIQUID NA-PB ALLOYS. *J. Phys. F: Met. Phys.* **1983,** *13* (3), 587.
68. Lantratov, M. F., STUDIES OF THE THERMODYNAMIC PROPERTIES OF LIQUID METAL SOLUTIONS - THE SYSTEM POTASSIUM-LEAD. *Zhurnal Fizicheskoi Khimii* **1960,** *34* (4), 782.
69. Saboungi, M. L.; Leonard, S. R.; Ellefson, J., ANOMALOUS BEHAVIOR OF LIQUID K-PB ALLOYS - EXCESS STABILITY, ENTROPY, AND HEAT-CAPACITY. *Journal of Chemical Physics* **1986,** *85* (10), 6072.
70. Weppner, W.; Huggins, R. A., THERMODYNAMIC PROPERTIES OF INTERMETALLIC SYSTEMS LITHIUM-ANTIMONY AND LITHIUM-BISMUTH. *Journal of the Electrochemical Society* **1978,** *125* (1), 7.
71. Egan, J. J., COULOMETRIC TITRATIONS USING CALCIUM-FLUORIDE SOLID ELECTROLYTES TO STUDY SOME IONIC ALLOYS. *High Temp. Sci.* **1985,** *19* (2), 111.
72. Morachevskii, A. G.; Bochagina, E. B.; Bykova, M. A., Thermodynamic properties of liquid alloys in the system bismuth-sodium-antimony. *Russ J Appl Chem* **2000,** *73* (10), 1699.
73. Morachevskii, A. G.; Bykova, M. A.; Rozova, T. T., THERMODYNAMIC PROPERTIES OF LIQUID ALLOYS IN SODIUM-ANTIMONY SYSTEMS. *Zhurnal Prikladnoi Khimii* **1970,** *43* (7), 1611.
74. Saboungi, M. L.; Ellefson, J.; Johnson, G. K., LIQUID POTASSIUM-ANTIMONY ALLOYS - INVESTIGATION OF SOME THERMODYNAMIC PROPERTIES. *Journal of Chemical Physics* **1988,** *88* (9), 5812.
75. Morachevskii, A. G.; Bochagina, E. V., Thermodynamic analysis of alloy formation in the system potassium-antimony. *Russ J Appl Chem* **2000,** *73* (11), 1875.
76. Cairns, E. J.; Crouthamel, C. E.; Fischer, A. K.; Foster, M. S.; Hesson, J. C., Galvanic cells with fused salts. Argonne National Laboratory: Chicago, 1967.
77. Iwase, M.; Sugino, S.; Ichise, E., Determination of the Thermodynamic Properties of Liquid Na-Tl, Na-Pb and Na-Bi Alloys by EMF. *High Temperature Materials and Processes* **1984,** *6* (3&4), 143.
78. Morachevskii, A. C.; Bochagina, E. V., Thermodynamic properties of sodium bismuthide Na3Bi. *Russ J Appl Chem* **2000,** *73* (6), 952.
79. Petric, A.; Pelton, A. D.; Saboungi, M. L., THERMODYNAMIC PROPERTIES OF LIQUID K-BI ALLOYS BY ELECTROMOTIVE-FORCE MEASUREMENTS. *J. Phys. F: Met. Phys.* **1988,** *18* (7), 1473.
80. Delcet, J.; Heus, R. J.; Egan, J. J., ELECTRONIC CONDUCTIVITY IN SOLID CAF2 AT HIGH-TEMPERATURE. *Journal of the Electrochemical Society* **1978,** *125* (5), 755.
81. Delcet, J.; Brune, A.; Egan, J. J., EMF METHOD USING CAF2 AND BAF2 SOLID ELECTROLYTES TO STUDY ALLOY PHASES. *J. Met.* **1979,** *31* (8), F37.
82. Cairns, E. J.; Shimotake, H., High-Temperature Batteries. *Science* **1969,** *164* (3886), 1347-1355.
83. Morachevskii, A. G., Thermodynamic analysis of alloying in the system lithium-tellurium. *Russ J Appl Chem* **2001,** *74* (4), 564.
84. Morachesvkii, A. G.; Maiorova, E. A.; Romanchenko, N. M.; Kozlova, M. V., THERMODYNAMIC PROPERTIES OF THE SODIUM-TELLURIUM SYSTEM. *Russ. J. Appl. Chem.* **1982,** *55* (3), 481.
85. Petric, A.; Pelton, A. D.; Saboungi, M. L., ELECTROMOTIVE-FORCE MEASUREMENTS IN LIQUID K-TE SOLUTIONS WITH A POTASSIUM BETA-ALUMINA ELECTROLYTE. *Journal of Chemical Physics* **1988,** *89* (8), 5070.
86. Newhouse, J. M. Modeling the Operating Voltage of Liquid Metal Battery Cells. MIT, Cambridge, Ma, 2014.
87. Newhouse, J. Modeling the operating voltage of liquid metal battery cells. Massachusetts Institute of Technology., Cambridge, Ma, 2014.
88. Sudworth, J.; Tiley, A. R., *Sodium Sulphur Battery*. Springer: 1985.

89. Bandhauer, T. M.; Garimella, S.; Fuller, T. F., A Critical Review of Thermal Issues in Lithium-Ion Batteries. *Journal of The Electrochemical Society* **2011,** *158* (3), R1-R25.
90. Schoenung, S. *Energy Storage Systems Cost Update: A Study for the DOE Energy Storage Systems Program*; Sandia National Laboratories: 2011.
91. *A Review of Battery Life-Cycle Analysis: State of Knowledge and Critical Needs*; DOE: Argonne National Laboratories, 2010.
92. Hueso, K. B.; Armand, M.; Rojo, T., High temperature sodium batteries: status, challenges and future trends. *Energy & Environmental Science* **2013,** *6* (3), 734-749.
93. Eyer, J.; Corey, G., Energy Storage for the Electricity Grid: Benefits and Market Potential Assessment Guide - A Study for the DOE Energy Storage Systems Program. Sandia National Laboratories: Livermore, CA, 2010.
94. Rempel, J.; Barnett, B.; Hyung, Y. *PHEV Battery Cost Assessment*; TIAX LLC: Lexington, MA, 2013.
95. Sudworth, J. L.; Tilley, A. R., *The Sodium Sulfur Battery*. Chapman and Hall: London, 1985.
96. Pollock, J., The True Cost of Hermetic Seals for Aluminum Housings. *Microwave Journal* 1997.
97. Mineral Commodity Summaries. U.S. Geological Survey: p 2013.
98. Clarke, D. M., Conversation about modern sodium production via the Down's Cell. Spatocco, B., Ed. Cambridge, MA, 2015.
99. Shimoji, M., Interaction in molten salt mixtures. *Discussions of the Faraday Society* **1961,** *32* (0), 128-137.
100. Lovering, D. G., *Molten Salt Technology*. 1 ed.; Springer: 1982.
101. Mamontov, G., *Molten Salt Chemistry: An Introduction and Selected Applications*. kluwer: Camerino, Italy, 1986.
102. Davy, H. In *Bakerian Lecture before the Royal Society*, London, Society, R., Ed. London, 1807.
103. Regelsberger, F., *Chemische Technologie der Leichtmetalle*. Leipzig, 1926.
104. Meyer, R., Gmelin's Handbuch der anorganischen Chemie. *Verlag Chemie* **1924,** *21*.
105. Batsford, H., *Chem. Met. Eng* **1922,** *26*, 932-935.
106. Friend, J., *A Textbook of Inorganic Chemistry*. J.B. Lippincott & Co.: Philadelphia, 1924; Vol. II.
107. Wolfram, G., *Abs. J. Soc. Chem. Ind.* **1898,** *18*, 832.
108. Specketer, H. Manufacture of Alkali Metals. 1903.
109. Castner, H. Manufacture of Sodium and Potassium. 1886.
110. Hackspill, L.; Grandadam, R., *Compt. Red.* **1925,** *180*, 68-70.
111. Netto, C. Process of Making Sodium or Potassium. 1891.
112. Mellor, J., *A Comprehensive Treatise on Inorganic and Theoretical Chemistry II*. Longmans, Green & Co: London, 1946.
113. Deville, H. S. C., *Compt. Rend.* **1854,** *38* (279).
114. Castner, H. Process of Manufacturing Sodium and Potassium. 1891.
115. Roeber, E. F.; Parmelee, H. C., *Electrochemical and Metallurgical Industry*. Electrochemical Publishing Company: 1906; Vol. 4.
116. Sittig, M., *Sodium: It's Manufacture, Properties, and Uses*. Chapman & Hall, Ltd.: London, 1956.
117. History of the Chlor-Alkali Industry. In *Handbook of Chlor-Alkali Technology*, Springer US: 2005; pp 17-36.
118. Downs, J. C. Electrolytic Process and Cell. 1924.
119. Acker, C. E., *Trans. Am. Electrochem. Soc.* **1902,** *1*, 165.
120. Ashcroft, E. A., *Trans. Am. Electrochem. Soc.* **1906,** *9* (124-126).
121. McNitt, R. J., *Chem. Met. Eng* **1917,** *16*, 401.
122. Seward, G. O.; Kugelgen, F. v.; Bidder, F. v. Electrolytic Production of Light Metals. 1912.
123. Ind., G. f. C. 1910.

124. Averill, B. A.; Eldredge, P., *General Chemistry: Principles, Patterns, and Applications*. Prentice Hall: Creative Commons License, 2007; Vol. 1.
125. Aurbach, D., *Nonaqueous Electrochemistry*. CRC Press: 1999.
126. Cathcart, W. Bath for Manufacture of Sodium. 1958.
127. Loftus, W. Process for Producing Sodium. 1962.
128. Gilbert, H. Production of Alkali Metals. 1939.
129. S. Yoshizawa, N. W., T. Morimoto, M. Miura, Y. Yamada Production of Alkali Metals from Alkali Amalgam. 1966.
130. Heredy, L. Electrolytic System for Production of Alkali Metals. 1969.
131. Annual Energy Review, Nuclear Energy Administration, E. I., Ed. US Government: Washington DC, 2012; Vol. Department of Energy.
132. Revere, M.; Tosi, M. P., Structure and dynamics of molten salts. *Reports on Progress in Physics* **1986,** *49* (9), 1001.
133. McGreevy, R. L.; Pusztai, L., The Structure of Molten Salts. *Proceedings of the Royal Society of London. Series A: Mathematical and Physical Sciences* **1990,** *430* (1878), 241-261.
134. Sequeira, C. A. C., High Temperature Corrosion in Molten Salts. Trans Tech Publications Ltd: 2003; p 356.
135. Nishikata, A.; Numata, H.; Tsuru, T., Electrochemistry of molten salt corrosion. *Materials Science and Engineering: A* **1991,** *146* (1–2), 15-31.
136. Janz, G. J.; Solomons, C.; Gardner, H. J., PHYSICAL PROPERTIES AND CONSTITUTION OF MOLTEN SALTS - ELECTRICAL CONDUCTANCE, TRANSPORT, AND CRYOSCOPY. *Chemical Reviews* **1958,** *58* (3), 461-508.
137. Janz, G. J.; Dampier, F. W.; Lakshminarayanan, G. R.; Lorenz, P. K.; Tomkins, R. P. T., Molten Salts: Volume 1, Electrical Conductance, Density, and Viscosity Data. Standards, N. B. o., Ed. NSRDS: Troy, NY, 1968.
138. Jager, F., *Zeitschrift für Anorganische und allgemeine Chemie* **1917,** *101* (1).
139. Winterhager, H.; Werner, L., Forschungber. *Wirtsch* **1957,** *438*.
140. Murgulescu, I. G.; Zuca, S., *Z. physik. Chem.* **1961,** *218*, 379.
141. Vanartsdalen, E. R.; Yaffe, I. S., ELECTRICAL CONDUCTANCE AND DENSITY OF MOLTEN SALT SYSTEMS - KCL-LICL, KCL-NACL AND KCL-KI. *J. Phys. Chem.* **1955,** *59* (2), 118.
142. Yaffe, I. S.; Artsdalen, E. R. v., *J. Phys. Chem* **1956,** *60*, 1125.
143. Lorenz, R.; Hochberg, A., *Z. anorg. Chem.* **1916,** *94*, 288.
144. Janz, G. J.; Saegusa, F., MOLTEN CARBONATES AS ELECTROLYTES - VISCOSITY AND TRANSPORT PROPERTIES. *Journal of The Electrochemical Society* **1963,** *110* (5), 452-456.
145. Janz, G. J.; Lorenz, M. R., MOLTEN CARBONATE ELECTROLYTES - PHYSICAL PROPERTIES, STRUCTURE, AND MECHANISM OF ELECTRICAL CONDUCTANCE. *Journal of The Electrochemical Society* **1961,** *108* (11), 1052-1058.
146. Bloom, H.; Knaggs, I. W.; Molloy, J. J.; Welch, D., MOLTEN SALT MIXTURES .1. ELECTRICAL CONDUCTIVITIES, ACTIVATION ENERGIES OF IONIC MIGRATION AND MOLAR VOLUMES OF MOLTEN BINARY HALIDE MIXTURES. *Transactions of the Faraday Society* **1953,** *49* (12), 1458-1465.
147. Protseko, P. I.; Shokina, A. V.; Razumouskaya, O. N., *Russ. J. Inorg. Chem* **1965,** *10*, 405.
148. Byrne, J.; Fleming, H.; Wetmore, F. E. W., MOLTEN SALTS - ELECTRICAL CONDUCTIVITY IN THE SYSTEM SILVER NITRATE-SODIUM NITRATE. *Can. J. Chem.-Rev. Can. Chim.* **1952,** *30* (12), 922-923.
149. Dantuma, R. S., *Z. anorg. Chem.* **1928,** *175* (1).
150. Jaeger, F. M., The temperature dependency of the molecular free surface energy of fluids in temperature area from-80 to+1650(o) C. *Zeitschrift für Anorganische und allgemeine Chemie* **1917,** *101* (1/3), 1-214.

151. Kvist, A., ELECTRICAL CONDUCTIVITY AND DENSITY OF SOLID AND MOLTEN LI2SO4-AG2SO4. *Zeitschrift Fur Naturforschung Part a-Astrophysik Physik Und Physikalische Chemie* **1967,** *A 22* (2), 208-&.
152. Jaeger, F. M.; Kapma, B., Announcements from the laboratoryof anorganic and physical chemistry of the National University in Groningen (Holland) II The exact measurement of electrical conductibility of electrolytes at temperatures until 600 degrees. *Zeitschrift für Anorganische und allgemeine Chemie* **1920,** *113* (1), 27-58.
153. Plester, D. W.; Rogers, S. E.; Ubbelohde, A. R., MELTING AND CRYSTAL STRUCTURE - MECHANISMS OF MELTING OF ALKALI THIOCYANATES. *Proceedings of the Royal Society of London Series a-Mathematical and Physical Sciences* **1956,** *235* (1203), 469-481.
154. Arndt, K.; Ploetz, G., Conductivity and viscosity of melted sodium- and potassium hydroxide. *Zeitschrift Fur Physikalische Chemie--Stochiometrie Und Verwandtschaftslehre* **1926,** *121* (5/6), 439-455.
155. Masset, P.; Guidotti, R. A., Thermal activated (thermal) battery technology - Part II. Molten salt electrolytes. *J. Power Sources* **2007,** *164* (1), 397-414.
156. Guidotti, R. A.; Masset, P., Thermally activated ("thermal") battery technology: Part I: An overview. *J. Power Sources* **2006,** *161* (2), 1443-1449.
157. Lai, G. Y., Liquid Metal Corrosion and Embrittlemtn. In *High-Temperature Corrosion and Materials Applications*, ASM: 2007; p 461.
158. Ganesan, V.; Ganesan, V., Corrosion of annealed AISI 316 stainless steel in sodium environment. *Journal of Nuclear Materials* **1998,** *256* (1), 69-77.
159. Wriedt, H. A., *Al-Na Phase Diagram*. II ed.; ASM: 1990.
160. Ishitsuka, T.; Nose, K., Solubility study on protective oxide films in molten chlorides created by refuse incineration environment. *Mater. Corros.* **2000,** *51* (3), 177-181.
161. Bale, C. W.; Pelton, A. D.; Thompson, W. T., FactSage 6.3. GTT-Technologies, T. a., Ed. 2012.
162. Bredig, M. A.; Johnson, J. W.; Smith, W. T., Miscibility of Liquid Metals with Salts. I. The Sodium-Sodium Halide Systems1. *Journal of the American Chemical Society* **1955,** *77* (2), 307-312.
163. Johnson, J. W.; Bredig, M. A., Miscibility of Metals with Salts in the Molten State. III. The Potassium-Potassium Halide Systems. *The Journal of Physical Chemistry* **1958,** *62* (5), 604-607.
164. Bredig, M. A.; Bronstein, H. R., Miscibility of Liquid Metals with Salts. IV. The Sodium-Sodium Halide Systems at High Temperatures. *The Journal of Physical Chemistry* **1960,** *64* (1), 64-67.
165. Bronstein, H.; Bredig, M. A., ELECTRICAL CONDUCTIVITY OF SOLUTIONS OF METALS IN THEIR MOLTEN HALIDES .2. SODIUM-SODIUM IODIDE, POTASSIUM-POTASSIUM IODIDE, AND POTASSIUM-POTASSIUM FLUORIDE. *J. Phys. Chem.* **1961,** *65* (7), 1220-&.
166. Miles, M. H., Exploration of molten hydroxide electrochemistry for thermal battery applications. *Journal of Applied Electrochemistry* **2003,** *33* (11), 1011-1016.
167. Haarberg, G. M.; Thonstad, J., Electrochemical properties of metal-molten salt mixtures. *Journal of Applied Electrochemistry* **1989,** *19* (6), 789-801.
168. Yeager, E., Fuel Cells: Basic Considerations. In *Proceedings of the 12th Annual Battery Research and Development*, Army Signal Research & Development Laboratory: Fort Monmouth, NJ, 1958; p 2.
169. Agruss, B., The Thermally Regenerative Liquid-Metal Cell. *Journal of The Electrochemical Society* **1963,** *110* (11), 1097-1103.
170. Agruss, B. Regenerative Battery. 1960.
171. Kim, H.; Boysen, D. A.; Newhouse, J. M.; Spatocco, B. L.; Chung, B.; Burke, P. J.; Bradwell, D. J.; Jiang, K.; Tomaszowska, A. A.; Wang, K.; Wei, W.; Ortiz, L. A.; Barriga, S. A.; Poizeau, S. M.; Sadoway, D. R., Liquid Metal Batteries: Past, Present, and Future. *Chemical Reviews* **2012,** *113* (3), 2075-2099.
172. Cairns, E.; Crouthamel, C.; Fischer, A.; Foster, M.; Hesson, J. *Galvanic Cells with Fused Salts*; Argonne National Labs: Chicago, 1967.
173. Shimotake, H.; Rogers, G. L.; Cairns, E. J., In *Extended Abstr. Battery Div.*, Electrochemical Society: Chicago, 1967; Vol. 12.

174. Shimotake, H.; Cairns, E. J., In *Comite International de Thermodynamique*, Detroit, 1968; p 254.
175. Cairns, E. J.; Steunenberg, R. K.; Ackerman, J. P.; Feay, B. A.; Gruen, D. M., *Development of high-energy batteries for electric vehicles : progress report for the period July 1970-June 1971*. Argonne, Ill.: Argonne National Laboratory, 1971.
176. Balaish, M.; Kraytsberg, A.; Ein-Eli, Y., A critical review on lithium-air battery electrolytes. *Physical Chemistry Chemical Physics* **2014,** *16* (7), 2801-2822.
177. B, A.; HR, K., The Thermally Regenerative Liquid Metal Concentration Cell. In *Regenerative EMF Cells*, Crouthamel, C.; Recht, H., Eds. American Chemical Society: Washington DC, 1967; Vol. 64, pp 62-81.
178. Oldenkamp, R.; Recht, H., Development of a Thermally Regenerative Sodium-Mercury Galvanic System - Part 3. In *Regenerative EMF Cells*, Crouthamel, C.; Recht, H. L., Eds. American Chemical Society: Washington DC, 1967; Vol. 64, pp 53-61.
179. Groce, I.; Oldenkamp, R., Development of a Thermally Regenerative Sodium-Mercury Galvanic System - Part 2. In *Regenerative EMF Cells*, Crouthamel, C.; Recht, H., Eds. American Chemical Society: Washington DC, 1967; Vol. 1967, pp 43-52.
180. Heredy, L.; Iverson, M.; Ulrich, G.; Recht, H., Development of a Thermally Regenerative Sodium-Mercury Galvanic System - Part 1. In *Regenerative EMF Cells*, Crouthamel, C.; Recht, H. L., Eds. American Chemical Society: Washington DC, 1967; Vol. 64, pp 30-42.
181. Citation Report for "beta-alumina" OR "beta-Al2O3" OR "B-Al2O3" OR "b-alumina" OR "beta alumina" AND published between 1960-2013. Reuters, T., Ed. Web of Knowledge, 2013.
182. Heredy, L. Fusible Alkali-Metal Salt Electrolyte. 1969.
183. Lu, X.; Li, G.; Kim, J. Y.; Lemmon, J. P.; Sprenkle, V. L.; Yang, Z., The effects of temperature on the electrochemical performance of sodium–nickel chloride batteries. *J. Power Sources* **2012,** *215* (0), 288-295.
184. Lu, X.; Lemmon, J.; Sprenkle, V.; Yang, Z., Sodium-beta alumina batteries: Status and challenges. *JOM* **2010,** *62* (9), 31-36.
185. Wesoff, E., Exploding Sodium Sulfur Batteries From NGK Energy Storage. 2011.
186. Fukunaga, A.; Nohira, T.; Kozawa, Y.; Hagiwara, R.; Sakai, S.; Nitta, K.; Inazawa, S., Intermediate-temperature ionic liquid NaFSA-KFSA and its application to sodium secondary batteries. *J. Power Sources* **2012,** *209* (0), 52-56.
187. Li, G. S.; Lu, X. C.; Coyle, C. A.; Kim, J. Y.; Lemmon, J. P.; Sprenkle, V. L.; Yang, Z. G., Novel ternary molten salt electrolytes for intermediate-temperature sodium/nickel chloride batteries. *J. Power Sources* **2012,** *220*, 193-198.
188. Sakabe, S. *NAS Battery fire Incident and Reponse*; NGK Insulators, Ltd.: Tokyo, October 28,2 011, 2011.
189. Watarai, A.; Kubota, K.; Yamagata, M.; Goto, T.; Nohira, T.; Hagiwara, R.; Ui, K.; Kumagai, N., A rechargeable lithium metal battery operating at intermediate temperatures using molten alkali bis(trifluoromethylsulfonyl)amide mixture as an electrolyte. *J. Power Sources* **2008,** *183* (2), 724-729.
190. Nitta, K.; Inazawa, S.; Sakai, S.; Fukunaga, A.; Nohira, T.; Hagawara, R. Molten Salt Battery. 2011.
191. Alibaba Price for Sodium Hydroxide. http://www.alibaba.com/showroom/price-for-sodium-hydroxide.html (accessed 27 June 2015).
192. Sangster, J., Thermodynamics and phase diagrams of 32 binary common-ion systems of the group Li, Na, K, Rb, Cs//F, Cl, Br, I, OH, NO3. *J. Phase Equilib.* **2000,** *21* (3), 241-268.
193. Dessureault, Y.; Sangster, J.; Pelton, A. D., Coupled Phase Diagram/Thermodynamic Analysis of the Nine Common-Ion Binary Systems Involving the Carbonates and Sulfates of Lithium, Sodium, and Potassium. *Journal of The Electrochemical Society* **1990,** *137* (9), 2941-2950.

194. Dessureault, Y.; Sangster, J.; Pelton, A., Evaluation critique des données thermodynamiques et des diagrammes de phases des systèmes AOH-AX, ANO3-AX, ANO3, AOH-BOH où A, B. *Journal de chimie physique* **1990,** *87* (3), 407-453.
195. Dessureault, Y.; Sangster, J.; Pelton, A. D., Coupled Phase Diagram-Thermodynamic Analysis of the 24 Binary Systems, A2CO3-AX and A2SO4-AX Where A= Li, Na, K and X= Cl, F, NO3, OH. *Journal of Physical and Chemical Reference Data* **1990,** *19* (5), 1149-1178.
196. Sangster, J.; Pelton, A. D., Phase diagrams and thermodynamic properties of the 70 binary alkali halide systems having common ions. *Journal of Physical and Chemical Reference Data* **1987,** *16* (3), 509-561.
197. Alibaba prices for sodium bromide. (accessed 27 June 2015).
198. Alibaba prices for sodium iodide. (accessed 27 June 2015).
199. Lyday, P. A., Iodine and Iodine Compounds. In *Ullmann's Encyclopedia of Industrial Chemistry*, Wiley-VCH Verlag GmbH & Co. KGaA: 2000.
200. Sigma Aldrich Reagant-Grade Acids. (accessed 27 June 2015).
201. Newell, L. C., *Descriptive Chemistry*. D.C. Heath and Company: 1903.
202. Okada, S.; Yoshizawa, S.; Watanabe, N., Metal Deposit from Amalgam: Investigation of the equilibrium diagram of the NaOH-NaBr-NaI system. *Kogyo Kagaku Zasshi* **1953,** *56* (2), 79-80.
203. Okada, S.; Yoshizawa, S.; Watanabe, N., Solubilities of several materials in melted alkali sodium amalgam at higher temperature. *Kogyo Kagaku Zasshi* **1957,** *60*, 675.
204. Okada, S.; Yoshizawa, S.; Watanabe, N.; Omote, Y., Density and electrical conductivity of fused NaOH-NaBr-NaI system. *Kogyo Kagaku Zasshi* **1957,** *60*, 670-675.
205. Demidov, A.; Morchevskii, A.; Mitkina, N., Electrical Conductivity of Melts of the System NaOH-NaI. *Journal of applied chemistry of the USR* **1979,** *52* (5), 1132-1134.
206. Yoshizawa, S.; Watanabe, N. *Solubility of Metallic Sodium in Molten Alkali Salts*; Kyoto University: 1960.
207. J, O. M.; S, W. E., Differential microcalorimeter. Google Patents: 1966.
208. Yoshizawa, S.; Watanabe, N.; Ohara, Y., Differential thermal analysis of the binary systems in the system NaOH-NaCN-NaI. *Denki Kagaku* **1964,** *32*, 162.
209. Sangster, J., Thermodynamics and phase diagrams of 32 binary common-ion systems of the group Li,Na,K,Rb,Cs//F,Cl,Br,I,OH,NO3. *J. Phase Equilib.* **2000,** *21* (3), 241-268.
210. Scarpa, G., *Atti Real. Accad. Lincei* **1915,** *24* (II), 955.
211. Janz, G. J., *Molten Salts Handbook*. Academic Press: London, UK, 1967.
212. Lovering, D.; Gale, R., Molten salt techniques. Volume 3. **1987**.
213. Lovering, D. G.; Gale, R. J., *Molten salt techniques*. Plenum Pub Corp: 1987; Vol. 3.
214. Stull, D. R., Vapor Pressure of Pure Substances. Organic and Inorganic Compounds. *Industrial & Engineering Chemistry* **1947,** *39* (4), 517-540.
215. Yurkinskii, V. P.; Firsova, E. G.; Proskura, S. A., Thermal Dissociation of Sodium Hydroxide upon Evacuation. *Russ J Appl Chem* **2005,** *78* (3), 360-362.
216. Smith, G. P., Corrosion of Materials in fused Hydroxides. Oak Ridge National Lab: Oak Ridge, Tennessee, 1955.
217. Gunnarsson, G.; Johannesson, B., Corrosion of Sodium beta '- Alumina Membranes in Molten Sodium Hydroxide. *J. Am. Ceram. Soc.* **2011,** *94* (4), 988-990.
218. Davis, J. R., *Nickel, Cobalt, and their Alloys*. ASM International: 2000.
219. Schmid-Fetzer, R.; Andersson, D.; Chevalier, P. Y.; Eleno, L.; Fabrichnaya, O.; Kattner, U. R.; Sundman, B.; Wang, C.; Watson, A.; Zabdyr, L.; Zinkevich, M., Assessment techniques, database design and software facilities for thermodynamics and diffusion. *CALPHAD* **2007,** *31* (1), 38-52.

220. Gheribi, A. E.; Robelin, C.; Digabel, S. L.; Audet, C.; Pelton, A. D., Calculating all local minima on liquidus surfaces using the FactSage software and databases and the Mesh Adaptive Direct Search algorithm. *The Journal of Chemical Thermodynamics* **2011,** *43* (9), 1323-1330.
221. Audet, C.; J. E. Dennis, J., Mesh Adaptive Direct Search Algorithms for Constrained Optimization. *SIAM Journal on Optimization* **2006,** *17* (1), 188-217.
222. Chase, M. W., NIST-JANAF thermochemical tables. Technology, A. I. o. P. f. t. N. I. o. S. a., Ed. American Chemical Society: Woodbury, N.Y., 1998.
223. Bale, C. W.; Bélisle, E.; Chartrand, P.; Decterov, S. A.; Eriksson, G.; Hack, K.; Jung, I. H.; Kang, Y. B.; Melançon, J.; Pelton, A. D.; Robelin, C.; Petersen, S., FactSage thermochemical software and databases — recent developments. *CALPHAD* **2009,** *33* (2), 295-311.
224. Predel, B., Li-Mg – Nd-Zr In *Phase Equilibria, Crystallographic and Thermodynamic Data of Binary Alloys*, Madelung, O., Ed. Landolt-Börnstein - Group IV Physical Chemistry: 1997; Vol. 5.
225. Pelton, A. D., The Ag–Na (Silver-Sodium) system. *Bulletin of Alloy Phase Diagrams* **1986,** *7* (2), 133-136.
226. Predel, B., Na-Ni (Sodium-Nickel). In *Li-Mg – Nd-Zr*, Madelung, O., Ed. Springer Berlin Heidelberg: 1997; Vol. 5H, pp 1-1.
227. Barlage, H.; Jacobs, H., Na7I2(OH)5 - A hydroxide iodide int he system NaOH/NaI. *Zeitschrift für Anorganische und allgemeine Chemie* **1995,** *621* (7), 1189-1192.
228. Gulliver, G., The quantitative effect of rapid cooling upon the constitution of binary alloys. *J. Inst. Metals* **1913,** *9*, 120-57.
229. Scheil, E., Bemerkungen zur schichtkristallbildung. *Zeitschrift Fur Metallkunde* **1942,** *34* (3), 70-72.
230. Hillert, M.; Jansson, B.; Sundman, B., APPLICATION OF THE COMPOUND-ENERGY MODEL TO OXIDE SYSTEMS. *Zeitschrift Fur Metallkunde* **1988,** *79* (2), 81-87.
231. Hillert, M.; Jansson, B.; Sundman, B.; Agren, J., A 2-SUBLATTICE MODEL FOR MOLTEN SOLUTIONS WITH DIFFERENT TENDENCY FOR IONIZATION. *Metallurgical Transactions a-Physical Metallurgy and Materials Science* **1985,** *16* (2), 261-266.
232. Temkin, M., Mixtures of fused salts as ionic solutions. *Acta Physicochim. URSS* **1945,** *20* (4), 411-420.
233. Barin, I.; Kubaschewski, O.; Knacke, O., *Thermochemical properties of inorganic substances: supplement*. Springer: 2014.
234. Okada, S.; Yoshizawa, S.; Watanabe, N., Equilibrium diagram of ternary mixtures of NaOH-NaBr-NaI system in neighborhood of eutectic point. *Kogyo Kagaku Zasshi* **1957,** *60*, 377-379.
235. Vila, J.; Ginés, P.; Pico, J. M.; Franjo, C.; Jiménez, E.; Varela, L. M.; Cabeza, O., Temperature dependence of the electrical conductivity in EMIM-based ionic liquids: Evidence of Vogel–Tamman–Fulcher behavior. *Fluid Phase Equilibria* **2006,** *242* (2), 141-146.
236. Yasuda, K.; Kobayashi, S.; Nohira, T.; Hagiwara, R., Electrochemical formation of Dy–Ni alloys in molten NaCl–KCl–DyCl3. *Electrochimica Acta* **2013,** *106* (0), 293-300.
237. Machado, S. A. S.; Avaca, L. A., The hydrogen evolution reaction on nickel surfaces stabilized by H-absorption. *Electrochimica Acta* **1994,** *39* (10), 1385-1391.
238. Plambeck, J. A., *Encyclopedia of Electrochemistry of the Elements: Fused Salt Systems/JA Plambeck*. Dekker: 1976.
239. Murakami, T.; Nohira, T.; Ogata, Y. H.; Ito, Y., Electrochemical window of a LiCl-KCl-CsCl melt. *Electrochem. Solid State Lett.* **2005,** *8* (1), E1-E3.
240. Anderson, D. L. An Evaluatino of Current and Future Costs for Lithuim-Ion Batteries for use in Electrified Vehicle Powertrains. Duke University, 2009.

Appendix I – Cost Modeling

The cost modeling of the liquid metal battery (LMB) is accomplished via a highly functionalized spreadsheet model of the various processes (Figure 10) required for the production of a core (Figure 9). The objective of the model is to output the total cost to manufacture a user-input amount of annual storage production on a $/kWh basis. This cost is inclusive of materials, tooling and equipment, labor, facilities, and energy. Prior to walking through the modeling process, there are few key assumptions that are made at the outset that create some limitations in predictive power. These assumptions are shared below

Model Assumptions	Description
Cell Geometry	The shape of a cell is assumed to be square with the length and width determined by the desired area and the height being functional on the capacity required, material densities, and internal device spacings.
Chemistry	A Li-Pb/Sb device is assumed because detailed thermodynamic and kinetic studies provide information to account for discharge and overpotentials. Also, existing cost "ground truth" data only exists for this system. Moving to new chemistries can be approximated by changing input material costs and densities though accurate calculations require experimental discharge curves.
Material Preparation	Aside from the drying, melting, and homogenizing of electrodes and electrolytes, all material preparation is assumed to be controlled by the material supplier. This includes active material purity and size as well as inactive material (e.g. containers) creation and forming.
Distribution	Distribution costs are not calculated in this cost model as these costs are intimately tied to business model decisions made by an LMB company regarding satellite assembly plants vs. central assembly. Further, it is assumed that the distribution of LMB devices will not vary much from other batteries and as a result is not consider a distinguishing characteristic.

It is important to note that it is quite easy to modify these assumptions by modifying certain calculations in the spreadsheet. For example, the decision of use a Li-Pb/Sb chemistry battery was made in order to allow for a higher-resolution model that could

leverage the much greater availability of system information currently available in the publicly disclosed literature as well as knowledge that has been internally accumulated within the research group. For example, a deep knowledge of the functionality of lithium utilization, overpotentials, electrolyte costs and ohmic losses, and kinetic limitations of the system are all critical pieces of information that exist for Li-Pb/Sb but are not available for most other binary systems. Adapting this model to a Na-X type system would require a more comprehensive investigation of cell performance characteristics and limitations.

With assumptions in mind it is now possible to describe the general calculation flow of the cost model.

Step	Input (Sheet Location)	Output (Sheet Location)
1	Material Prices and Properties (9, 10)	Material costs functionalized by scale, type, and/or temperature (9,10)
2	Model Input Parameters and "Other Data" (1)	Dependent Parameters Set Automatically (1)
3	Capital Equipment Staffing Ratios (6,7,8) Process time estimates (5)	Limiting Step Calculation (5) Max Unit and Total Line Calculation (5)
4	Total Storage Request Input (1)	Total Cost per kWh/cell/pack/core (1) BOM breakouts (2)
5	Various Temperatures or Storage Requests (4)	TCOE as a function of volume and temperature (4)
6	10% confidence sensitivity variables (3)	Sensitivity tornado plot (3)

Prior to any meaningful calculations, reliable estimates on active and inactive materials must be input by the user. Common sources for these information are large suppliers like McMaster Carr, MSC Direct, Alfa Aesar, Sigma Aldrich, or Alibaba. Other items may require quotes from specialized vendors though care should be taken to acquire large volume pricing. The prices used in the current model are shown below:

Active Material Prices/ Properties	Molar Mass (g)	Density (g/cm^3)	Price/mole
Lithium	6.941	0.534	$0.43
Lead	207.20	6.697	$0.52
Antimony	121.76	11.34	$1.83
Salt (LiCl)	42.394	2.068	$0.85

Inactive Material Prices	Price ($)	Unit	Source
Stainless 304 sheet (1/8")	area < 250,000 in^2, -0.027*ln(area) + 0.3446 area > 250,000 in^2, $0.0086	Per in^2	Aksteel.com
Weld Filler	$7.00	Per pound	Ckworldwide.com
Tungsten Tip	$40.00	tip	WeldingSupply.com
Argon	$84.93	tank (49 liters)	Airgas.com
Insulation	Area*$1.06*Temp/400°C	Per ft^2	Mscdirect.com
Copper/Nickel Disc	Temp > 250, $0.52 Temp < 250, $0.15	each	McMaster Carr
Teflon O-Ring	$0.10	each	McMaster Carr
Glass-Ceramic Seal	$5.00	each	Shp-seals.com
Graphite Sheath	$2.00	each	graphitestore
Wiring	Temp > 450, $20.00 250 < Temp < 250, $14.78 200 < Temp < 250, $11.62	Per ft^2	Cablemaster.com
Pack/Core Racking	$75 / $750	Per pack/core	estimate
Bus Bars	Temp > 450, $300 250 < Temp < 250, $249 200 < Temp < 250, $116	Per core	MSC Direct
Pack TMS	$100	Per pack	estimate
Core TMS	$1400	Per core	estimate
Core BMS System	$1000	Per core	estimate

With data in place, it is now possible to begin specifying the parameters of the LMB device, operation, labor, and production facilities. These values can be easily reset and changed and the entire cost model will recalculate based on the new values. The two types of inputs are shown below:

Model Inputs	Value	Units	Typical Range	Description
Active Surface Area	230	cm^2	200 - 300	Defined as the surface area of positive electrode touching the electrolyte. The area sets the length and width of the battery.
Battery Capacity	300	Ah	250 -350	Defined as the total amount of passable charge in a battery. The capacity sets the number of moles of lithium metal required.
Cells per pack	24	cells	12 - 36	Defined as the number of individual batteries (cells) in each pack. This number influences the assembly time, pack costs, and labor required.
Packs per core	32	packs	N/A	Defined as the number packs in each core. This number influences the assembly time, core costs, and labor required.
Cells per core (200 kWh)	768	cells	N/A	Defined as the number of individual batteries (cells) in each pack. This number is a restatement of the previous two numbers.
Temperature	450.00	C	400 - 500	The temperature of operation of a Li-based LMB. This is usually chosen to be 25°C above the melting temperature of the high melting component.
Lithium Capacity	50%		33 - 66	Defined as the molar percent of lithium that the positive electrode is to accommodate at full discharge. This number influences the amount of positive electrode material required.
DC-DC Efficiency (System)	93.00%		90 - 95	Defined as the amount of electrical energy that can be obtained on the core terminals as a percentage of the total that exited each individual cell. This number influences total energy per cell.

Model Inputs Cont.	Value	Units	Typical Range	Description
C-rate	1/5	(C)	1/10 - 1	Defined as the rate at which a cell's fully capacity is to be discharged. This number helps set the current density and determine the overpotential losses.
Alloy Composition (Sb%)	40.00%	mole %	20 - 60	Defined as the amount of antimony in the Pb/Sb positive electrode. This number impacts the voltage profile used and the cost and height of the positive electrode.
Cost of Energy (from grid)	0.15	$/kWh	0.10 – 0.15	Defined as the cost of local energy used in at the production facility. This number impacts the cost of energy per process.
Electrolyte Thickness	0.75	cm	0.5 – 1.0	Defined as the thickness of the electrolyte between the positive and negative electrodes. This height impacts the resistance and efficiency of the battery as well as the overall height of the battery.
Container Thickness	0.13	inch	.0625 - .375	Defined as the thickness of container material used in the cell housing. This number impacts the cost of cell assembly costs and welding.
Product Life	10	years	5 - 10	Defined as the nameplate lifetime of an LMB product (cell, pack, or core). This number impacts the total $/kWh.cycle metric.
Capital Equipment Life	10	years	5 - 10	Defined as the lifetime of a piece of capital equipment at the production facility. This number impacts the annual capex cost via repayment period.
Staff Wages (w/ benefits)	$20	$/hr	15 - 30	Defined as the cost of bachelor's level engineers and technicians. This value impacts the cost of labor.
Admin wages (w/ benefits)	$50	$/hr	40 - 100	Defined as the cost of Masters or PhD level engineers or executives. This value impacts the cost of labor.
Total Storage Requested / year	10	MWh	1 - 50	Defined as the total amount of storage production required/requested per year. This value impacts the number of assembly lines required and therefore the total amount of capital equipment that must be purchased.

Other Data	Value	Unit	Description
Downtimes (input)			
No Operations	16	hours	Hours per day staff are not working
Planned Paid	1	hours	Hours per day staff are not working but paid
Administrative Labor (output)			
Total Admin	1	admin	Total Number of administrators. Functional on the number of production lines
Working Days/Yr	240	days/year	Workable days less weekends and holidays
Yearly Payment	$84,000.00	$/year	Total payment to all administrative staff
Salaries / unit	$1.85	$/unit	Payment to staff per unit production
Building Data (input)			
Property Value	$12.00	$/ft^2	Commercial real estate in Marlborough, MA
Property Upkeep and Taxes	$8.00	$/ft^2	Liberal estimate for taxes and other property charges
Safety Equipment	$0.33	$/line	Price of safety equipment per line per unit produced on that line
Floor Plate (fixed + variable line)	2000	ft^2	Total floor plate needed for assembly line
Total Value of Bldg	$40,000.00	Total Value	Total value of building
Discount Rate	0.06	%	Rate for capital repayment
Building Life	10	years	Repayment period on building
Payment/year	$5,434.72	$/year	Total payment for building per year
Payment/unit	1.21	$/unit	Payment for building per unit plus the cost of safety equipment for each line per unit.

With this data input, there are a number of key dependent variables that become set. The next table shares these variables as well as their descriptions and dependencies. These variables are used along with the Model Inputs and Other data in each of the sub-process sheets to calculate the cost of production of cells, packs, and units.

Dependent Parameters	Value	Unit	Description
Cell Volume	565.54	cm^3	The total internal volume of the cell based on the active surface area, the amount of negative and positive electrode materials required, current collectors, and required space.
Cell Height	4.91	cm	The total internal cell height required as a result of the area calculated above. Thickness of container material not included.
length and width (square)	15.16	cm	The symmetric length and width dimensions resulting from the active area requirement. Thickness of container material not included.
Current per cell	60.00	A	The current resulting from running the specified capacity cell at the specific C-rate.
Current Density	260.87	mA/cm^2	The current density experienced as a result of the current being run over the specified active area.
Voltage	0.78	V	The operational discharge voltage of a device accounting for the overpotential losses incurred at the specific current density. Voltage vs. current density functionalization from work by Wang[23].
Round Trip Efficiency	83.01%		A ratio of the discharge to charge voltages. Accounts for energetic overpotential losses experienced during a full cycle.
Energy per cell	220.25	Wh	The total energy of an individual cell at operational discharge voltage and accounting for DC-DC losses.

With these variables in hand the next step is to identify the important pieces of capital equipment that will be required for the production line, confirm their rough price estimates, and establish worker-to-line ratios for each step in the process. For example, the production line for cells may require more or less workers per line than for packs or cores. These numbers are important to set to ensure an accurate prediction of the assembly line process time (step 3). The following table shares the fixed equipment required for each step and also shares the staffing ratios for each portion of the assembly line.

Cell Assembly Line Capital Equipment	Costs	Number per line	Workers per cell line
Laser Welder	$15,000.00	1	2
Robotic Assembly Machine	$250,000.00	1	
Large Melting Furnaces	$50,000.00	2	
Melting Crucibles	$200.00	2/week	
Pack Assembly Line Capital Equipment	**Costs**	**Number per line**	**Workers per pack line**
Battery Pack Assembly Device	$100,000.00	1	2
Thermal Assembly Desk Equipment	$2,500.00	1	
Management Systems Capital Equipment	**Costs**	**Number per line**	**Workers per core line**
Core Assembly Station	$25,000.00	1	1 per 30 cores

With knowledge of the staffing ratios we are now able to estimate the time it takes each process to produce a core-equivalent. This time is defined as the time it takes to produce 768 cells, 32 packs, or 1 core. In the case of cells, there are two major steps that occur – the creation of pre-melted salts, metals, and seals and the construction of the cell. Because the pre-melting steps occur in large batch processes away from the assembly machine, these are assumed to not be rate limiting. This assumption is valid when considering the fact that each individual cell will contain on the order of hundreds of grams of salt whereas batch melting processes here utilize furnaces and crucibles that can contain kilograms worth of material each run. As a result dozens of cells can be supported from each salt pre-melting step. In addition, melting steps can be conducted overnight to further the supply of material to input into the assembly line. For these reasons, pre-melting steps are not further explored here as it is unlikely the cell assembly machine would be able to outpace the supply of raw material. The second process, cell assembly, must occur in a linear fashion. As a result, the time it takes to produce one cell is the sum of the time it takes for each step. In addition, a delay factor is added in to account for production realities.

Cell Assembly Time Calculation	Step	Individual Time (min)	Total Time (min)
Active Material Processing			
1a	Pre-melt salt	15.00	
1b	pretreat negative current collector	5.00	
1c	Electrode dielectic Seal	30.00	
Cell Assembly			
1	weight out lead and antimony	0.20	
2	negative electrode measurements	0.20	
3	weigh out salts	0.20	
4	Insert sheaths and hardware	0.20	
5	setting current collector height	0.20	
6	pouring in Pb/Sb, electrolyte, and NCC	0.20	
	TOTAL		1.20
Cell Sealing			
1	Circumference Weld Sealing	0.16	
	TOTAL		0.16
		time of rate limiting step (cell)	1.36
		Experimental Delays	0.2
		Per Cell time with Delays	**1.56**

In a similar manner, the pack and core assembly processes can be estimated and summed to identify the time it takes to produce their respective units as well as the cell-equivalent. The key difference between these two steps and the cell assembly step is that these steps are less automated and require more human inputs to complete. A single pack or core assembly can be done by multiple workers at once and, as a result, the individual processes can be done in parallel and therefore the total time can be reduced. In the following examples, both pack and core assembly use two workers for their respective assembly lines and the total time is therefore halved.

Pack Assembly	Step	Individual Time (min)	Total Time (min)
INDIVIDUAL PROCESSES (PER UNIT)			
1	Cell Racking per cell	0.25	6.00
2	Cell Wiring per cell	0.50	12.00
3	Cell Insulation per cell	0.50	12.00
4	Thermal Oversight unit	3.00	3.00
5	Enclosure	5.00	5.00
		time of rate limiting step (pack)	38.00
		total time per pack with n workers	19.00
		experimental delays	3.50
		Total with Delays for each pack	**22.50**
		per cell time	**0.94**

Core Assembly	Step	Individual Time (min)	Total Time (min)
INDIVIDUAL PROCESSES (PER UNIT)			
1	Pack racking per pack	10.00	320.00
2	Pack wiring per pack	10.00	320.00
3	Pack Insulation per pack	10.00	320.00
4	Thermal Management System	60.00	60.00
5	BMS System	120.00	120.00
6	Enclosure	60.00	60.00
		time of rate limiting step (core)	1200.00
		Time per core for n workers/machine	600.00
		experimental delays	150.00
		Total with Delays for each core	**750.00**
		per cell time	**0.98**

In order to compare these production times they are all converted to the time it takes to produce a core-equivalent. The table below shares these aggregated results and, for the model inputs we've entered, shows that cell assembly is the slowest step at 3.33 days per core equivalent (768 cells).

Process	Time for Core Equivalent (days)	Rate Limiting?
Cell Assembly	3.33	YES
Pack Assembly	2.00	No
Core Assembly	2.08	No

This limiting step can then be combined with some manufacturing efficiency information to yield a production volume per line per year as well as the number of lines needed to support the total storage requested in the model inputs section.

Production/year - one line		
	days/year	240
	hours/day	8
	Machine Efficiency (Working Rate)	93%
	workable hours/year	1440
	workable min/year	86400
	cells/year/line	55408
	reject rate	0.02
	good cells/year/line	54299
Lines Needed		
	Total Capacity Chosen	45403
	Number of Lines Required	1

The calculated number of lines then feeds back into the calculations for each of the process costs. Total volume and the number of lines impact the number of employees, capital equipment, and bulk discounts available for some parts. Below are the values calculated for the variable and fixed costs for the cell assembly process. It is important to note that any Costs values are on a per unit (cell) basis. This allows for a direct comparison and summing of costs across processes later on. Another important point is that variable costs are broken out by materials, energy, and labor while fixed costs only include that capital equipment that is used during the cell assembly process. Other equipment and shared facilities are not included here. A final point to note is that many of the cells in the table below are actually functionalized or conditioned to result in different values depending on a variety of different parameters. For instance, the negative current collector price varies between copper and nickel prices depending on the temperature input in the model input sheet.

Cell Assembly Variable Costs		**Values**	**Costs**
Active Materials Costs	Moles of X (moles)	11.19	
	Mass of X (g)	77.69	
	Volume of X (cm^3)	145.49	
	Price of X per unit ($)	0.43	
	Total Cost of X		**$4.79**
	Total Moles of MN alloy (moles)	11.19	
	Moles of M (moles)	4.48	
	Weight of M (g)	545.16	
	Moles of N (moles)	6.72	
	Weight of N (g)	1391.57	
	Total Cost of M and N		**$11.69**
	Total Cost Electrolyte		**$5.35**
	ACTIVE MAT. COST / UNIT		**$21.83**

Inactive Materials Costs			
Container	container area (in^2)	35.65	
	container height (in)	1.94	
	Container length/width	5.98	
	container thickness (in)	0.13	
	container circumference (in)	18.77	
	Total Area of one container	117.61	
	Total # containers needed/year	45403.00	
	Total area for all containers (in^2)	5339905	
	Discount price Steel ($/in)	0.01	
	cost of container ($)		**$1.01**
Negative Current Collector	Copper disc or lead		**$0.52**
Insulating Seals	Cost of Glass-Ceramic Seal / UNIT		**$5.00**
	Cost of Teflon o-ring seal		**$0.10**
Sheath	Graphite Sheath		**$2.00**
Argon	Argon Gas Flow rate (ft^3/hr)	20.00	
	Argon Gas per part (liters/unit)	1.50	
	Argon Gas per tank (liters,1 atm)	8000.00	
	Cost of Argon per unit		**$0.02**
	INACTIVE MATERIALS COST PER UNIT		**$8.55**
	TOTAL MATERIALS COST / UNIT		**$30.38**

Energy Costs			
Robot	Robot Energy consumption (kW)	1.5	
	All Robots Op. Time (hrs)	1792	
	Reboot/ warmup robots (hrs)	16	
	Total Energy consumed (kWh)	2760	
	Cost of Energy		$414.00
	Cost of Energy per Unit		**$0.00911834**
Laser Welder	Voltage (V)	25	
	Amperes (A)	300	
	Power (W)	7500	
	Cost of Power ($/kWh)		$0.15
	Welder Power Cost ($/minute)		$0.019
	Weld Travel Speed (in/min)	150	
	Time per part (min)	0.159341489	
	Energy cost per part		**$0.003**
	ENERGY COST / UNIT		**$0.01**
Human Capital			
	Labor and Overhead ($/hour)		$20.00
	Workers/machine	2	
	Total Workers	2	
	Hours per year	2880	
	Total Labor Cost	$57,600.00	
	LABOR COST / UNIT		**$1.27**
CELL ASSEMBLY TOTAL VARIABLE COST/UNIT			**$31.66**

Unlike the variable costs which are consumed for each device made, fixed costs are not directly consumed per unit and as a result require an amortization before being summed together with the variable costs. The next table will therefore show total rather than unit costs.

Cell Assembly Fixed Costs	Costs	Number needed	Total Cost
Laser Welder	$15,000.00	1	$15,000.00
Robotic Assembly Machine	$250,000.00	1	$250,000.00
Large Melting Furnaces	$50,000.00	2	$100,000.00
Melting Crucibles	$200.00	96	$19,200.00

In a similar manner, the pack and core variable and fixed costs can be shown. Because pack costs can be found in Table 8 we will here only provide the core costs.

Core Assembly Variable Costs		Values	Costs
BMS	Battery Management System per core		$1,000.00
	Battery Management per pack		$31.25
	Battery Management per cell		**$1.30**
Insulation	Total core insulation area (ft^2)	69.57	
	Thermal Core Insulation total cost		$77.99
	Thermal Core insulation cost per cell		**$0.10**
TMS	Thermal Management System per core		$1,500.00
	Thermal Management per pack		$46.88
	Thermal Management per unit		**$1.95**
Wiring	Total wiring per core (ft)	65.98	
	Cost of wiring/ft as fxn of temp	14.78	

		Total wiring cost per pack		$975.63
		Total wiring cost per cell		**$1.27**
	Racking	Core Racking		$750.00
		Racking per cell		**$0.98**
	Bus Bars	Bars needed	8	
		Bus Bar Price	249.18	
		Total Cost of Bars		1993.48
		Cost of bars per unit cell		**2.59**
	Enclosure	Steel Needed (in2)	2789.96	
		Total Cost Steel for Enclosure		363.77
		Cost of enclosure per unit		**0.47**
	Welding	Filler Length (in)	562.80	
		Filler Metal per food (lb/ft)	0.15	
		Filler Metal per part (lb)	7.04	
		Filler Metal cost per lb ($/lb)		$7.00
		Filler Metal cost per core ($)		$49.25
		Tungsten Tips / Unit	0.50	
		Tungsten Tip Cost / unit		$20.00
		Total Welding Cost per cell		**$0.09**
		MATERIALS COST / UNIT		**$8.76**
Energy Costs				
	Laser Welder	Voltage (V)	25	
		Amperes (A)	300	
		Power (W)	7500	
		Cost of Power ($/kWh)		$0.15
		Welder Power Cost ($/minute)		$0.019
		Weld Travel Speed (in/min)	150	
		Time per part (min)	15.01	
		Energy cost per part		**$0.28**
		ENERGY COST / UNIT		**$0.28**

Human Capital			
	Labor and Overhead ($/hour)		$30.00
	Core Assembly Workers (30 cores a year)	2	
	Hours worked per year per staff	1440	
	Total Hours Worked	2880	
	Total Cost Staff		$86,400.00
	LABOR COST / UNIT		**$1.90**
	CORE ASSEMBLY VARIABLE COST PER UNIT		**$10.95**

Core Assembly Fixed Costs

Item	Costs	Number needed	Total costs
Core Assembly Station	$25,000.00	1	$25,000.00

The cell, pack, and core assembly costs can then be aggregated once fixed costs are amortized over their lifetimes

Cell Assembly Costs 45403 cells

Variable Costs	Material Cost	$30.38		
	Energy Cost	$0.01		
	Labor Cost	$1.27		
		Total	**Per Year**	**Per Unit**
Fixed Costs	Laser Welder	$15,000.00	$2,038.02	$0.04
	Robotic Assembly Machine	$250,000.00	$33,966.99	$0.75
	Large Melting Furnaces	$100,000.00	$13,586.80	$0.30
	Melting Crucibles	$19,200.00	$2,608.66	$0.06
	TOTAL CELL ASSEMBLY COST PER UNIT			**$32.81**

Pack Assembly Costs		1892 packs		
Variable Costs	Material Cost	$11.54		
	Energy Cost	$0.15		
	Labor Cost	$1.90		
		Total	**Per Year**	**Per Unit**
Fixed Costs	Battery Pack Assembly Device	$100,000.00	$13,586.80	$0.30
	Thermal Assembly Desk Equipment	$2,500.00	$339.67	$0.01
TOTAL PACK ASSEMBLY COST PER UNIT				**$13.90**

Core Assembly Costs		60 cores		
Variable Costs	Material Cost	$8.76		
	Energy Cost	$0.28		
	Labor Cost	$1.90		
		Total	**Per Year**	**Per Unit**
Fixed Costs	Core Assembly Station	$25,000.00	$3,396.70	$0.07
TOTAL CORE ASSEMBLY COST PER UNIT				**$11.02**

These total costs, when combined with facilities and labor numbers from the “Other Data” table and after conversion to energy allow for the calculation of cost per unit cell, unit pack, and unit core.

TOTAL CELL COST	**$60.79**	**$/cell**
TOTAL PACK COST	**$1,458.96**	**$/pack**
TOTAL CORE COST	**$46,686.73**	**$/core**
TOTAL COST OF ENERGY	**$276.00**	**$/kWh**
ELECTRODE COST OF ENERGY	**$74.81**	**$/kWh**
ACTIVE MATERIAL COST OF ENERGY	**$99.10**	**$/kWh**

These values form the basis for comparison when changing input variables. For instance, simply be changing the temperature, volume requested, price of input materials, or even things like lithium capacity, the entire model will update and provide new total costs such as those in the above table. It is in this way that the Cost Model can be used to investigate the relationship of TCOE and temperature, volume, voltage, and other potential variables.